The Dissertation Committee for Engin Alkan Certifies that this is the approved version of the following dissertation:

EXPLORING HYDROCARBON-BEARING SHALE FORMATIONS WITH MULTI-COMPONENT SEISMIC TECHNOLOGY AND EVALUATING DIRECT SHEAR MODES PRODUCED BY VERTICAL-FORCE SOURCES

Committee:

Bob A. Hardage, Supervisor

Don Wagner,

Sergey B. Fomel

Clark R. Wilson

William L. Fisher

EXPLORING HYDROCARBON-BEARING SHALE FORMATIONS WITH MULTI-COMPONENT SEISMIC TECHNOLOGY AND EVALUATING DIRECT SHEAR MODES PRODUCED BY VERTICAL-FORCE SOURCES

by

Engin Alkan, Lisans Diplomasi, M.S.Geo.Sci

Dissertation

Presented to the Faculty of the Graduate School of
The University of Texas at Austin
in Partial Fulfillment
of the Requirements
for the Degree of

Doctor of Philosophy

The University of Texas at Austin
December 2012

Dedication

I would like to dedicate this doctoral dissertation to my mother, my sister and my wife. There is no doubt in my mind that without their continued support I could not have completed this difficult process.

Acknowledgements

First and foremost I would like to thank my advisor Dr. Bob A. Hardage for encouraging my research and development as a research scientist. It would not have been possible to complete this PhD work without his help and support, not to mention his advice on my research as well as on my career.

I would like to also acknowledge all the advice and technical support of Dr. Don Wagner. He assisted me on most of the technical work in this project. It would not have been possible for me to complete my work without his support with the computer programming software and overall data analysis.

Additionally, I would like to thank Dr. Clark Wilson who counseled with me great advice and important critiques about the data analysis and processing results. His advice helped me to re-evaluate my work and was imperative to this dissertation.

I am most grateful to Dr. Sergey Fomel for providing me with great references that helped me to understand the theories underlying the technical work as well as his many suggestions with regards to the data analysis results. I was able to use his advice to re-evaluate my analysis and the results of my work.

I would like to thank Dr. William Fisher for his guidance and assistance which helped me understand how important it is to focus on the geological aspects of my analysis as well as the geophysical concepts used in my dissertation.

I would like to express my special appreciation and thanks to Michael De Angelo, Paul Murray and Rosalba Mendoza for their tremendous help during my data analysis. Their support helped me to learn various software programs that were used to analyze data.

EXPLORING HYDROCARBON-BEARING SHALE FORMATIONS WITH MULTI-COMPONENT SEISMIC TECHNOLOGY AND EVALUATING DIRECT SHEAR MODES PRODUCED BY VERTICAL-FORCE SOURCES

Engin Alkan, Ph.D.
The University of Texas at Austin, 2012

Supervisor: Bob A. Hardage

It is essential to understand natural fracture systems embedded in shale-gas reservoirs and the stress fields that influence how induced fractures form in targeted shale units. Multicomponent seismic technology and elastic seismic stratigraphy allow geologic formations to be better images through analysis of different S-wave modes as well as the P-wave mode.

Significant amounts of energy produced by P-wave sources radiate through the Earth as downgoing SV-wave energy. A vertical-force source is an effective source for direct SV radiation and provides a pure shear-wave mode (SV-SV) that should reveal crucial information about geologic surfaces located in anisotropic media. SV-SV shear wave modes should carry important information about petrophysical characteristics of hydrocarbon systems that cannot be obtained using other elastic-wave modes. Regardless of the difficulties of extracting good-quality SV-SV signal, direct shear waves as well as

direct P and converted S energy should be accounted for in 3C seismic studies. Acquisition of full-azimuth seismic data and sampling data at small intervals over long offsets are required for detailed anisotropy analysis. If 3C3D data can be acquired with improved signal-to-noise ratio, more uniform illumination of targets, increased lateral resolution, more accurate amplitude attributes, and better multiple attenuation, such data will have strong interest by the industry.

The objectives of this research are: (1) determine the feasibility of extracting direct SV-SV common-mid-point sections from 3-C seismic surveys, (2) improve the exploration for stratigraphic traps by developing systematic relationship between petrophysical properties and combinations of P and S wave modes, (3) create compelling examples illustrating how hydrocarbon-bearing reservoirs in low-permeable rocks (particularly anisotropic shale formations) can be better characterized using different S-wave modes (P-SV, SV-SV) in addition to the conventional P-P modes, and (4) analyze P and S radiation patterns produced by a variety of seismic sources.

The research done in this study has contributed to understanding the physics involved in direct-S radiation from vertical-force source stations. A U.S. Patent issued to the Board of Regents of the University of Texas System now protects the intellectual property the Exploration Geophysics Laboratory has developed related to S-wave generation by vertical-force sources. The University's Office of Technology Commercialization is actively engaged in commercializing this new S-wave reflection seismic technology on behalf of the Board of Regents.

Table of Contents

CHAPTER-3: TECTONIC AND STRATIGRAPHIC CHARACTERISTICS OF MARCELLUS SHALE AND STRUCTURAL HISTORY OF APPALACHIAN BASIN 89

List of Tables

List of Figures

CHAPTER 1: INTRODUCTION

This PhD research presents the results of a multicomponent seismic study involving data acquired at the Devine Test Site, Texas and in Bradford County, Pennsylvania. The study describes multicomponent seismic acquisition, processing, and interpretation in addition to borehole and well log analyses that were done during this project.

The general objective of this research was to demonstrate that multicomponent seismic technology has greater value than conventional, single-component compressional-wave seismic technology for characterizing geologic targets.

To achieve the general objective of establishing the value of multicomponent seismic technology in exploitation of unconventional reservoirs and characterizing geologic targets, several secondary objectives were embedded in this PhD research tasks. The purposes of these secondary objectives were to compile information and evidence describing the physics of compressional (P) and shear (S) wave propagation in layered Earth associated with different geologic targets.

To address these objectives, a seismic field test was done at the Devine test site using various seismic data-recording systems and seismic sources to analyze propagation patterns of different seismic wave-modes and to compare different seismic field systems. Chapter 2 provides the results of this test study and presents examples that compare data acquired with different seismic sources and recording systems.

One of the main focuses of my study was to demonstrate the value of multicomponent seismic technology and elastic seismic stratigraphy for characterizing shale-systems and surrounding geologic lithology. Multicomponent seismic data acquired in Bradford County, Pennsylvania were the principal data used for these investigations. I analyzed the Marcellus Shale, Tully Limestone, selected porous brine-filled sandstones and carbonates in this area of the Appalachian Basin of northeastern Pennsylvania in detail to document the value of elastic wavefield seismic stratigraphy.

Past studies (Engelder and Geiser 1980; Evans et al., 1989; Plumb et al., 1991; Engelder et al., 1980; Loewy 1995; Lash, G. et al. 2004) that have demonstrated joint development in the Marcellus formation and that have used direct engineering measurements, well log analysis, and stress studies to relate joint development with the tectonic history of the Appalachian Basin are reviewed in Chapter 3. This chapter discusses characteristics of fracture structures in shale formations based on relationships between tectonic history, in-situ stress variations, and lithological characteristics of shale formations in the Appalachian Basin.

The results of seismic data acquisition and processing of Bradford County multicomponent data are presented in Chapter 4. Chapter 5 provides examples of seismic attribute analyses that compare numerous seismic attributes and impedance inversion analyses extracted from multicomponent seismic data for different wave modes. Chapter 6 provides a summary of results for every analysis performed.

Unique Contributions of PhD work

(1) Field test data were acquired at the University's Devine Test Site to compare attributes of P and S wave modes produced by explosive, accelerated-weight impact, and vibratory energy sources, and to document the relative merits of these sources for illuminating geologic targets. These data led to the most important principle documented in this dissertation: full-elastic wavefield data can be generated with vertical-force seismic sources. This research finding is significantly important because it eliminates the need to use both vertical-force and horizontal-force seismic sources to generate full-elastic wavefield directly at a source station data and simplifies multicomponent seismic data acquisition.

(2) Both seismic recording systems (cable-based and cable-free) were used to acquire multicomponent seismic test data at the Devine Test Site. One system was the popular Sercel 428 which is used by many seismic crews around the world. Although cable-free seismic data acquisition is a relatively new technology (first tests date back to the early 2000's), these systems provide data comparable in quality to conventional cable-based recording systems (Mougenot D., 2010; Lansley M., 2012). However, some in industry still need evidence to fully accept cable-free data acquisition systems. My study provides examples of comparison of data results obtained from both cable-based and cable-free recording systems, demonstrates that there are negligible differences in the quality of multicomponent seismic data acquired with both systems, and documents the differences between the systems. This finding is an important contribution to exploration industry, because cable-free

systems allow multicomponent seismic data to be acquired in areas of high culture more easily than can be done with cable-based systems. Many shale-gas exploration studies involve data acquisition at areas located close to high levels of human activity.

(3) Conventional seismic surveys use standard 10-Hz moving-coil geophone as a sensor to acquire seismic data for evaluating geologic targets. However, new sensors MEMS (micro-electronic mechanical systems) accelerometers became popular in the last decade (Stoter et al., 2008; Mougenot et al., 2010; Sasaki et al. 2007). Although both sensor types have been used for seismic exploration, there are few public tests that compare these two sensor types. My research presents an analysis of data acquired by both sensor types. I demonstrate that data recorded by the two sensor types are equivalent and documented that MEMS accelerometers provide better low-frequency data (frequencies less than 8 Hz) than do standard 10-Hz geophones. This research finding is important in multicomponent data acquisition because S-modes tend to be lower frequency than P-wave data. When S waves are critical to evaluating shale targets, serious consideration should be given to using accelerometers for exploration survey.

(4) The geological information provided by multicomponent seismic data acquired in Bradford County was compared to the information content of single-component compressional-wave data in terms of stratigraphic resolution and the characterization of faults and fractures. My study demonstrated that shear-wave seismic data provided better vertical resolution of strata related to shale-gas systems and also detected and

resolved faults better than did P-wave seismic data. As documented in this dissertation, shear wave data revealed crucial reservoir features and internal architecture which could not have been extracted from single-component compressional wave data alone.

(5) There are several examples of multicomponent seismic technology being applied to unconventional reservoir characterization and modeling. My PhD research focuses on the data analysis that allows many seismic attributes to be used to interpret the Marcellus Shale and related stratigraphy. I discuss many seismic attributes that are sensitive to changes in layer thickness, layer impedance, and fracture intensity, which are properties related to the geomorphology of Marcellus Shale reservoirs. With this information, my study illustrates how to locate fractures and faulted zones based on different seismic attributes. The study also demonstrates the value of elastic wavefield seismic stratigraphy by interpreting different seismic volumes (compressional and shear wave volumes).

(6) Although previous studies (Evans et al., 1989, Plumb et al., 1991, Engelder and Geiser, 1980) have attempted to define links between the deformation of Marcellus Shale and the structural nature and geomechanical properties of shale formations, there is no direct link between characteristics of joint development within the Marcellus Shale and in-situ stress conditions and lithological features that are observed in the Marcellus. My study investigates this connection using multicomponent down-hole data, surface seismic data, and log data.

CHAPTER-2: COMPARISON OF VERTICAL-FORCE SEISMIC SOURCES AND RECORDING SYSTEMS

As a part of my PhD project, I analyzed multicomponent seismic test data acquired by the Exploration Geophysics Laboratory, Bureau of Economic Geology. These data were collected at the Devine Test Site located in Medina County, Texas to evaluate the quality of data generated by three types of vertical-force sources: vertical vibrator, shot-hole explosive, and vertical-impact weight. The field-test program was done to: (1) quantify the relative strengths of compressional (P) wave and shear (S) wave modes produced by a variety of vertical-force seismic sources, (2) compare the relative merits of cable-based and cable-free data recording systems, and (3) document and compare the quality of 3C data acquired with moving-coil geophones and MEMS solid state accelerometers.

Elastic P- and S- wave modes propagating away from source stations located at the surface were recorded by a downhole vertical array of three-component geophones as well as by several surface-planted horizontal arrays of three-component geophones and accelerometers. Data acquired at the Devine Test Site demonstrate that each vertical-force source generated elastic wave modes consisting of a compressional wave mode, as well as radial- and transverse shear modes.

The purpose of this study was to demonstrate the presence of elastic wave modes on multicomponent seismic data created by vertical-force seismic sources, and to prove the effectiveness and efficiency of elastic wavefield stratigraphy. In this section, the amplitude and frequency characteristics of each elastic wave mode generated by different seismic sources and recorded by different recording systems are analyzed and evaluated.

Theory and Overview of Different Recording Systems

Most seismic surveys use velocity geophones to acquire seismic data. Regardless of instrument type, the sensitivity of a recording sensor and the level of background noise are the main factors that affect a recording system's ability to define reflection signal.

Accelerometers exhibit large amplitudes at low frequencies (5-8 Hz), and tend to have better signal quality for high frequencies due to their flat amplitude response. As a result, industry and geophysical community interest in accelerometers has been increasing (Mougenot and Thorborn, 2004; Mougenot 2005; Laine and Mougenot, 2007; Hons et al., 2008; Stotter et al., 2008). Methods such as differentiation of conventional geophone data or frequency-domain inverse filter applications on geophone data (Hons et al., 2008) have been proposed as options for simulating ground acceleration from geophone data.

A geophone's response to ground motion can be considered as a simple harmonic oscillation function that senses the displacement of the internal mass mounted in a geophone. Similarly, an accelerometer's digital output can be described by a harmonic oscillation function of its mass movement relative to a reference position. Because both geophone and accelerometer transfer functions are based on the same physical principles and their input functions can be defined by the same mathematical relations, frequency responses and amplitude characteristics for both sensors can be described by damped harmonic-oscillation motion. Because there is a simple relationship among various types of ground motion (displacement, velocity, and acceleration), different outputs of recording systems can be compared, and differences among them can be discussed.

GEOPHONES AND ACCELEROMETERS

Geophones sense ground motion by converting the movement of its spring-mounted magnetic mass to electrical voltage. Most geophones used in industry sense only the vertical motion of the Earth's surface. However, elastic seismic waves propagating through the earth create three-dimensional particle displacements. Thus 3-component phones – consisting of three wire coils mounted in a frame in which each sensing element is orthogonal to the others - are used to acquire multicomponent seismic data.

A recording system's sensitivity must be high enough to detect the amplitude range that needs to be analyzed to investigate propagation of seismic events. Noise content, whether generated by a sensor itself, or by power-lines (~60 Hz), recording cables, radio frequency interferences, and other factors, must be low enough to ensure that ground movement created by reflected seismic events are not masked by background noise.

Although most geophones measure upward traveling reflected seismic events because of their vertical motion, horizontally-propagating surface waves also are recorded by vertical geophones because these waves create vertical motion which may mask reflection events of interest. Therefore, most data acquisition schemes involve receiver array designs which attenuate horizontally-propagating surface waves.

Regardless of sensor type, system sensitivity plays an important role in eliminating undesired events. Geophone arrays consisting of several geophones planted in a line or forming a circle are common practices to increase sensor sensitivity.

Velocity-sensitive geophones, accelerometers such as MEMS (Micro - Electro Mechanical Systems), force balance, crystal, and optical devices are used to acquire multicomponent land seismic data. Because their frequency response is linear, accelerometers can, in concept, detect high and low frequency signals better than conventional geophones. Bland (2006) indicated the importance of digitizer sensitivity.

Digitizers which convert geophone output signal to digital values contain an internal and external preamplifier between the analog-to-digital converter and sensor. Various 24-bit converters are used in current industrial applications. These converters have a full-scale range (FSR) of 3 volts, 5 volts, or 10 volts, and create data values ranging between negative 2^{23} to positive 2^{23} -1. The smallest measurable non-zero value is $1/2^{23}$.

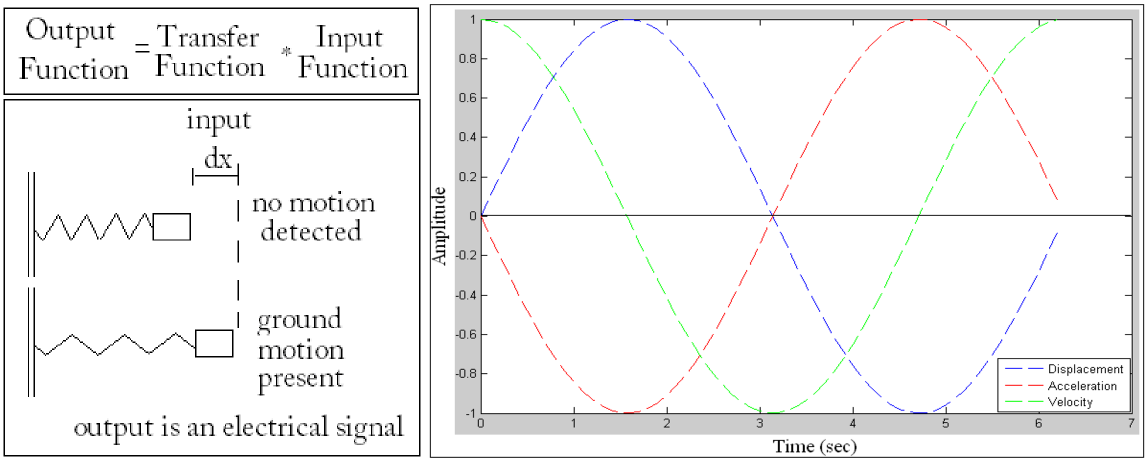

Figure 1: A model of a seismic recording system and phase differences between ground displacement, velocity, and acceleration.

One of the objectives of my research is to analyze data recorded by systems that capture these different ground motions and explain how these systems affect amplitude and frequency characters of signals and wavelets. Transfer functions of recording systems directly affect signal quality and noise content of recorded data.

The physics of transfer functions can be explained by describing the movement of a spring-supported mass mounted inside a measurement system (Figure 1). As a wave passes through the system, the mass moves relative to its original position. The sensor detects the displacement dx of the mass. The system output is an electrical signal created by the mass displacement. According to the system described on Figure 1, the transfer function represents the output function divided by the input function. If a seismic recording unit has only a single degree of freedom, the mathematical expression of the sensor movement can be described as a damped harmonic-oscillator function.

SEISMIC SOURCES

Selection of an optional seismic source can be daunting. The type and the number of vibrator sweeps, the size of explosives, source array design, and number of sources in an array are only a few of the parameters to be considered when selecting a seismic source. Using larger source arrays can improve signal strengths but doing so can also lower data quality if more noise is generated. A 3-db nonlinear sweep can generate less source-created noise than a linear sweep, but nonlinear sweeps may generate artificial events due to the low-cut frequency feature of nonlinear sweeps. A source array consisting of larger explosives can generate strong signals with a wide frequency spectrum, but implementation involves higher cost and labor.

Clearly it is crucial to select the most efficient source type in acquisition surveys. As part of Devine Test Study, the Exploration Geophysics Laboratory used several source types to evaluate source performance and to analyze elastic wave-modes produced by each source. Sources compared in this dissertation are vertical and horizontal vibrators, explosives, and weight impactors.

SEISMIC RECORDING SYSTEMS

Selection of seismic recording equipment is as important as the selection of seismic sources. The number of sensors planted at each receiver station, array distances and type of sensor are additional parameters to consider when selecting seismic recording equipment. Cable-free recording systems such as RSR (Remote Seismic Recorder), Sigma, and Sercel-Unite provide alternative approaches to traditional cable-based recording systems. Cable-free systems are becoming important for solving problems related to large channel counts, harsh environment conditions, and environmental footprint. Basically cable free recording systems are engineered to optimize operational efficiency.

On the other hand, traditional cable-based systems such as Sercel-428XL, 428XL DSU3, and 408UL bring great advantages to seismic surveys. Digital Sensor Units (DSU) serve as integrated sensor packages enabling accelerometer measurements based on MEMS (Micro-electro-mechanical-sensor) technology in addition to velocity data measured by conventional geophones. Even though MEMS accelerometers provide data with better-quality low and high frequencies, they require continuous electrical power and provide only a single-sensor point-receiver array data (Maxwell et al., 2001 and Dragoset et al., 2007). DSU sensors provide better signal-to-noise ratio due to less noise, less crosstalk, and broader frequency content. OYO Geospace GSR^{TM} sensors also present advantages such as high resolution recording with compatibility with all type of sources, and built-in GPS system. These comments illustrate the fact that the selection of components to use in a recording system can be daunting because of the number of options to consider.

Devine Test Side and Field Procedure

The University's seismic test site is located at Devine, Texas, and shown on the map displayed as Figure 2a. An aerial photo of the test site property is included as Figure 2b. The locations of the well where a vertical array deployed in is indicated by the solid circle labeled 4, on Figure 2b.

The stratigraphy penetrated by the test wells is labeled on the well log curves displayed in Figure 3. These logs were recorded in well 4 and define compressional velocity V_P, shear velocity V_S, and gamma-ray readings across the rock units that form the first 3000 ft of the seismic propagation medium beneath the property. These log measurements start immediately below the base of surface casing, which is at a depth of 532 ft in well 4 where these logs were recorded.

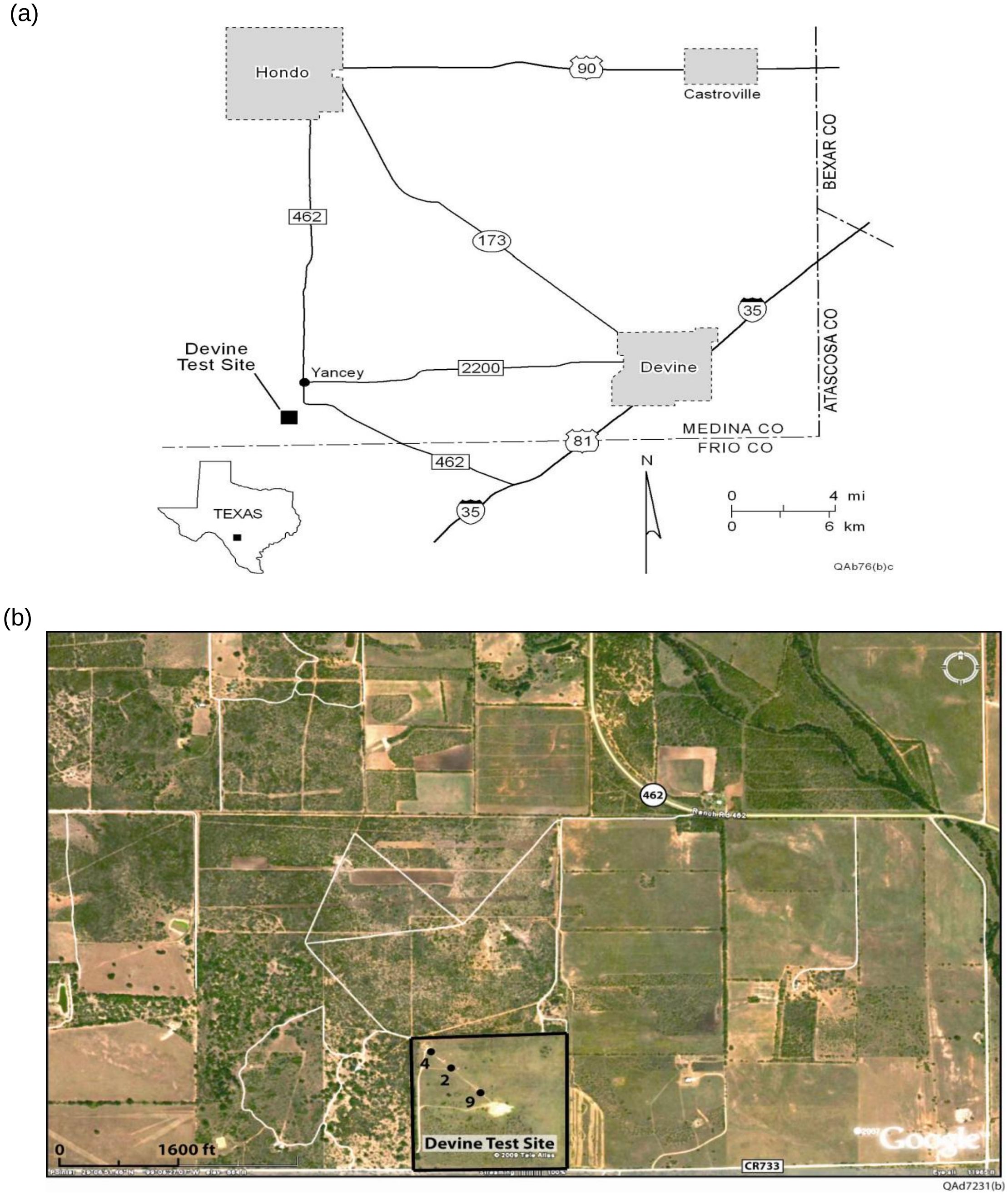

Figure 2: (a) Location of the Devine Test Site in Medina County, Texas. The city of San Antonio is approximately 50 km east of the town of Hondo shown on this map. (b) Aerial photo of the Devine Test Site. Test wells 4, 2, and 9 were constructed for the purpose of deploying downhole instrumentation, particularly seismic sources and receivers and well logging tools. All wells are 3000 ft (914 m) deep. The site spans 100 acres.

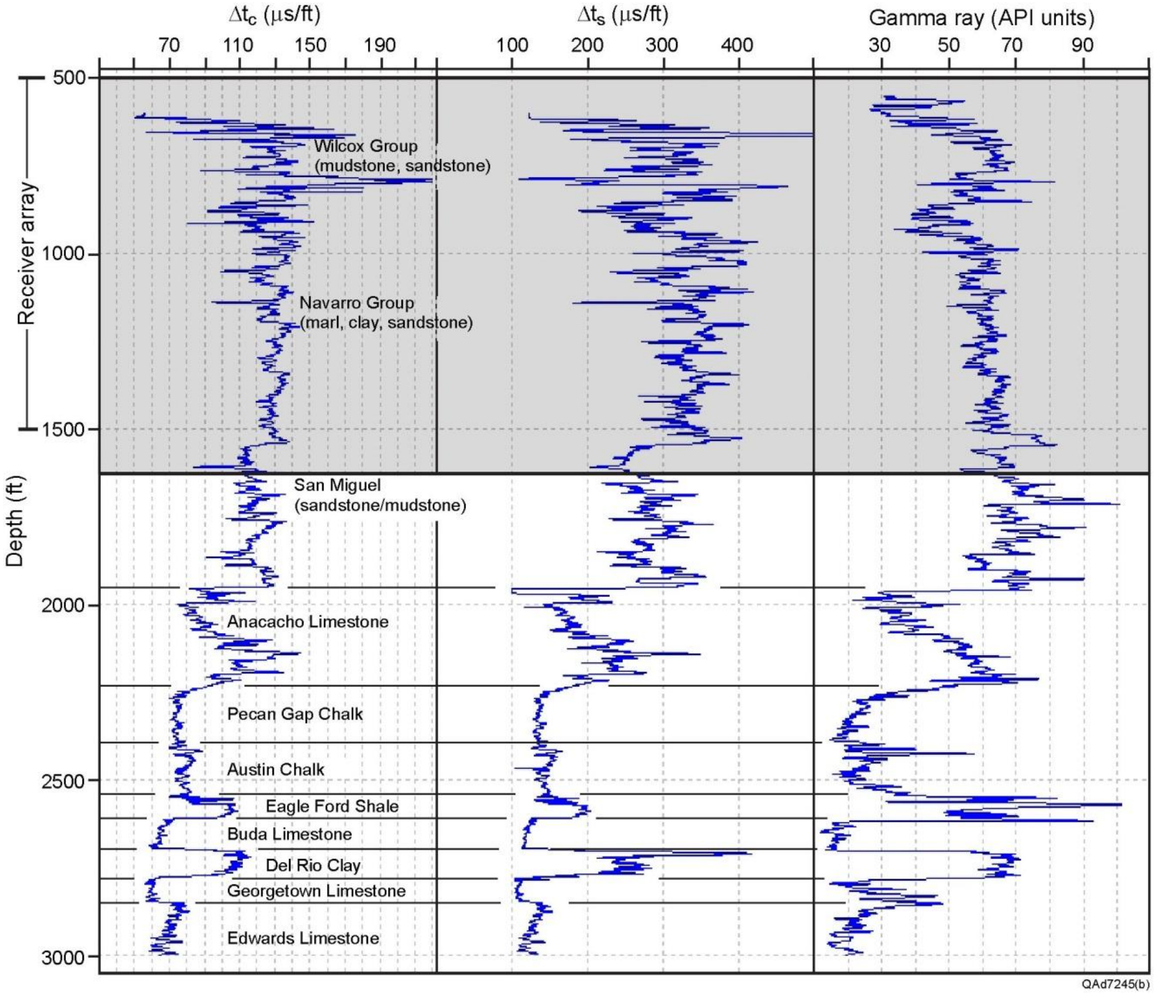

Figure 3: V_P and V_S velocity logs and gamma-ray log acquired in well 4 on the Devine Test Site. The shaded interval defines the depth range over which downhole geophones were deployed for source tests in this study.

In the Devine Test Site acquisition scheme, a cable-based Sercel 428XL DSU3 MEMS and 3C geophones, a Sigma cable-free recording system provided by Seismic Source, Sercel's Unite, and OyoGeospace cable-free recording units were used to detect seismic signals.

The source-receiver geometry utilized for these tests combined the concepts of horizontal wave testing (involving only a horizontal receiver array) and vertical wave testing (involving only a vertical receiver array) as described by Hardage (2009, 2010). A 24-station MaxiWave receiver system provided by Mitcham Industries was deployed in this well, with receiver stations spanning a depth interval extending from 500 to 1632 ft (152 to 497 m). The velocity layering local to this vertical sensor array is defined by the log character inside the shaded interval shown on Figure 3. Several parallel arrays of 2D horizontal sensors extended eastward 250 ft (76 m) from well 4, and a series of nine inline source stations continued eastward a distance of 1920 ft (585 m), as illustrated on Figure 4. Within each 250-ft (76 m) horizontal-receiver array (the heavy black line between source stations 1 and 2 on Figure 4), a single 3C sensor was buried at inline intervals of 10 ft (3 m) so that the top of each sensor case was flush with the ground surface. The X, Y, Z sensor elements at each 3C sensor station were recorded as individual data channels.

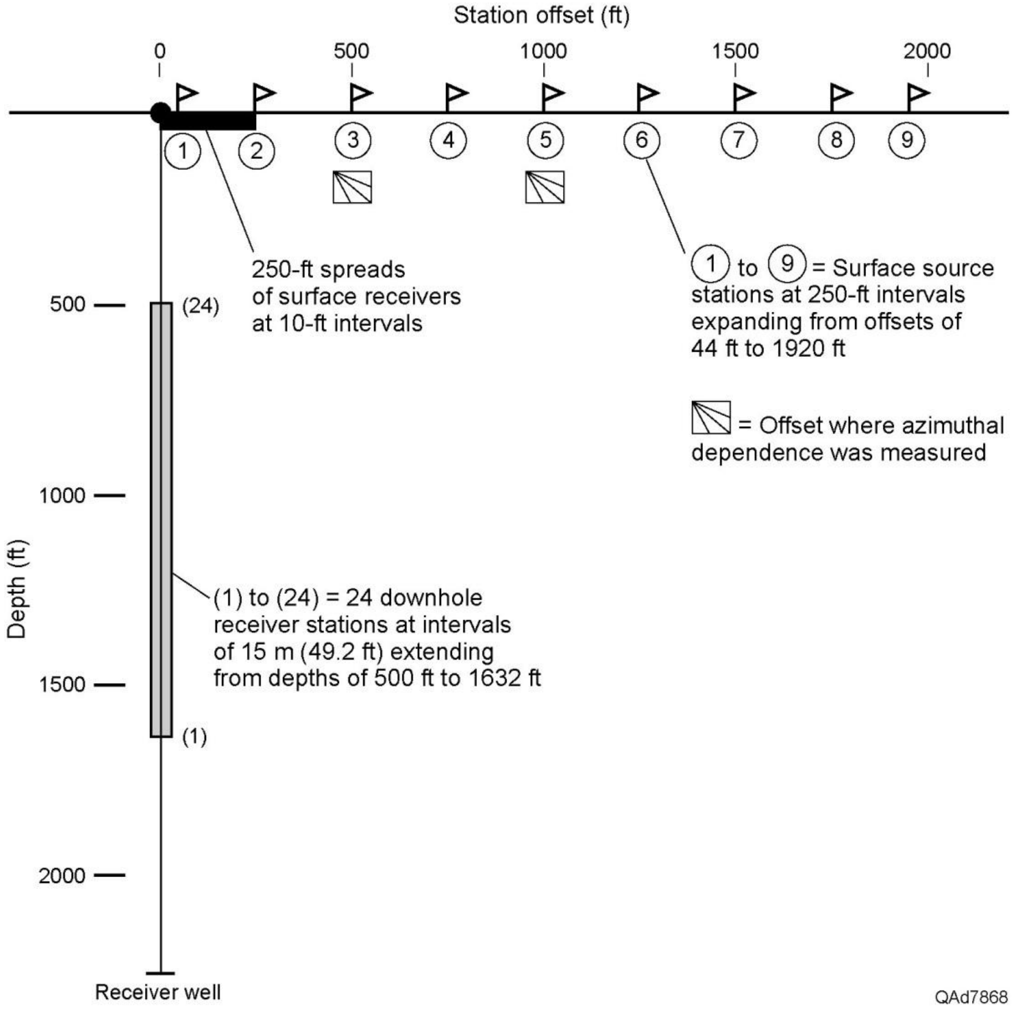

Figure 4: Source-receiver geometry used to compare relative merits of multicomponent seismic sources, sensors, and recording systems. A 24-station vertical array of 3C geophones spaced at intervals of 15 m (49.2 ft) spanned the depth interval from 500 to 1632 ft (152 to 497 m) in well 4. Several 25-station horizontal arrays of 3C sensors spaced 10 ft (3 m) apart spanned the offset range 0 to 250 ft (0 to 76 m) immediately next to well 4. Source stations were offset from the well at intervals of 250 ft (76 m), the linear dimension of the horizontal surface-receiver arrays.

Photographs of the surface equipment deployed for the tests are shown on Figure 5. Along each horizontal receiver array, the first sensor station was 10 ft (3 m) from well 4 and sensor station 25 ended at source station 2, offset 250 ft (76 m) from the receiver well (Fig. 5). As shown by the labeling on the photographs, the instrumentation deployed along these parallel arrays consisted of:

1. 25 stations of 3C geophones recorded by Sigma cable-free boxes provided by Seismic Source and i-Seis.
2. 25 stations of DSU3 MEMS sensors recorded by a Sercel 428 cable-based system. 25 stations of 3C geophones recorded by Sercel's EUnite cable-free boxes.
3. 25 stations of 3C geophones recorded by a Sercel 428 cable-based system.
4. 5 stations at which OyoGeospace deployed high-sensitivity geophones and special packaging of 3C geophones with all sensors recorded by OyoGeospace GSR cable-free boxes.

The 3C geophones utilized in surface spreads 1, 3, and 4 of this list were Oyo Geospace Model 20DX (10-Hz resonance) geophones.

(a)

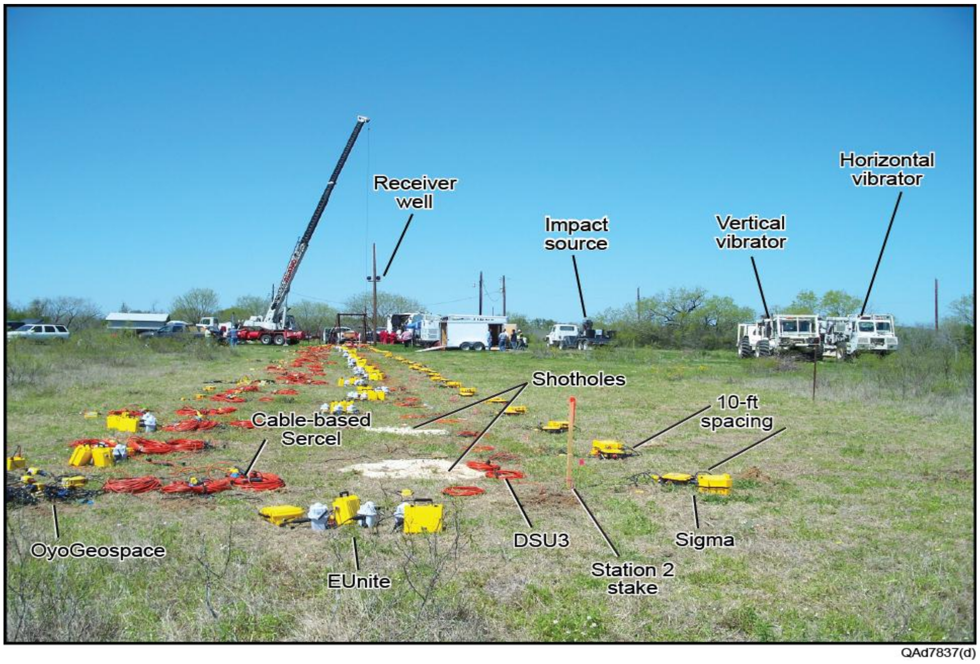

(b)

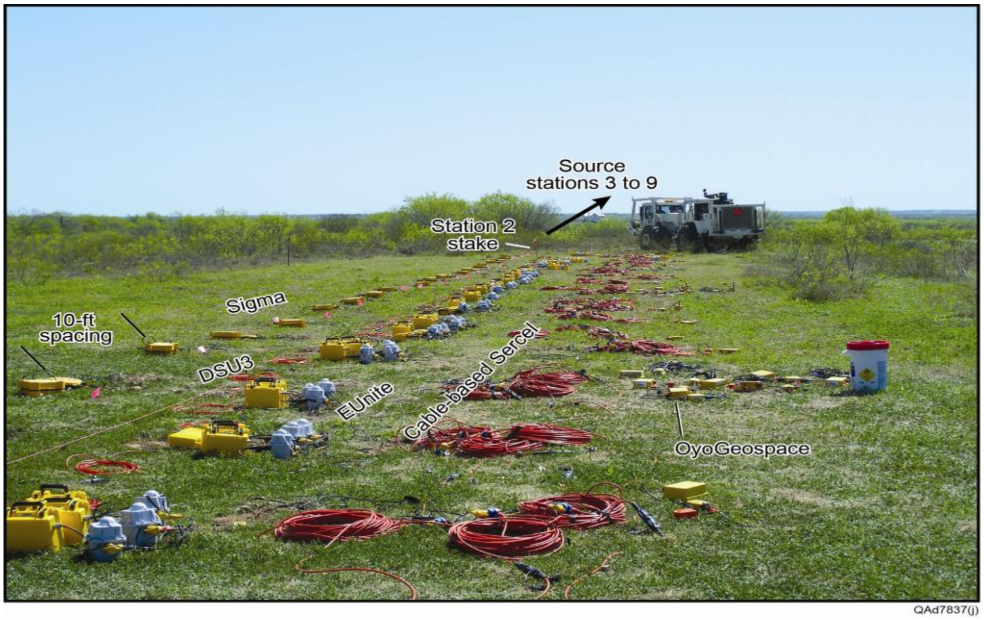

Figure 5: (a) View of the receiver well from a position near source station 2 on the source-station profile. This view shows parallel, 25-station arrays of horizontal-wave-test instrumentation deployed over the offset range 0 to 250 ft (0 to 76 m) and some of the source and data-acquisition technologies assembled for the test. (b) View from the receiver well looking down the source-station profile.

Comparison of Data Recording Systems and Data Analysis

One of the objectives of my study was to test performances of different types of seismic sources and various seismic sensors. The ground was a medium-hard condition when the sensors were deployed. Sensors were deployed with the top of each case slightly below ground level to ensure good coupling and to minimize wind noise during recording. Equipment layout created uniform sensor coupling that produced good seismic signal with good bandwidth. As a result, responses could be compared over a wide range of frequency spectra.

Energy-related characteristics of the sources used in the test were: (1) vertical vibrator (I/O AHV IV PLS 362 with a hold-down weight of 60,000 lbs), (2) explosive (2.2 lbs of dynamite placed at a depth of 20 ft [6 m]), and (3) vertical impact (33,000-lb vehicle with 1000-psi nitrogen-spring weight-acceleration system).

Sercel recording systems were incorporated into the Devine test program because they are widely used by seismic contractors. Sercel Systems provide great flexibility for surveys that require a large number of receiver stations to be deployed because two telemetry systems can be used: real-time modes or autonomous modes. The Sercel 428 system used at Devine was compatible with geophones, MEMS, and wireless recording systems which provided high-quality 3-component data with broad bandwidth. Cable-based Sercel-428 systems were also integrated into the test program. These systems also provide advantages for large surveys because the field equipment requires low power and provides long battery life for more reliable data. Up to 100,000 channels recording capacity enables real time recording at 2 miliseconds. Sigma, a cable-less seismic recording system manufactured by Seismic Sources, was also tested during the Devine study. Sigma recording systems are preferred by some contractors because the system provides a stakeless survey, enables fast and simple crew operations, and can download data loading via cable or WiFi during acquisition.

ANALYSIS OF SURFACE DATA

Comparisons of energy content and frequency bandwidth of P and S modes produced by vertical-force source types

Surface array measurements of wave-mode amplitudes and frequencies produced by test sources are analyzed. Except for the first (44 ft offset from Well 4) and the last station (1920 ft offset from Well 4), sources were offset at uniform distance increments of 250 ft (76.2 m) from the Well 4 (Fig. 4). With the source geometry, data acquired by orthogonal X,Y,Z sensors deployed across the 25-station surface receiver array can be represented as 192-trace, single-fold field records having trace spacings of 10 ft (3 m) and extending 1920 ft (585.2 m) from the vertical receiver array. Examples of field records produced when the vertical impact source was positioned at source stations 2 through 9 are displayed on Figure 6. For each sensor profile, static shifts occur in 25-trace blocks along the source line because no P or S source-station static corrections have been applied to the individual common-source gathers.

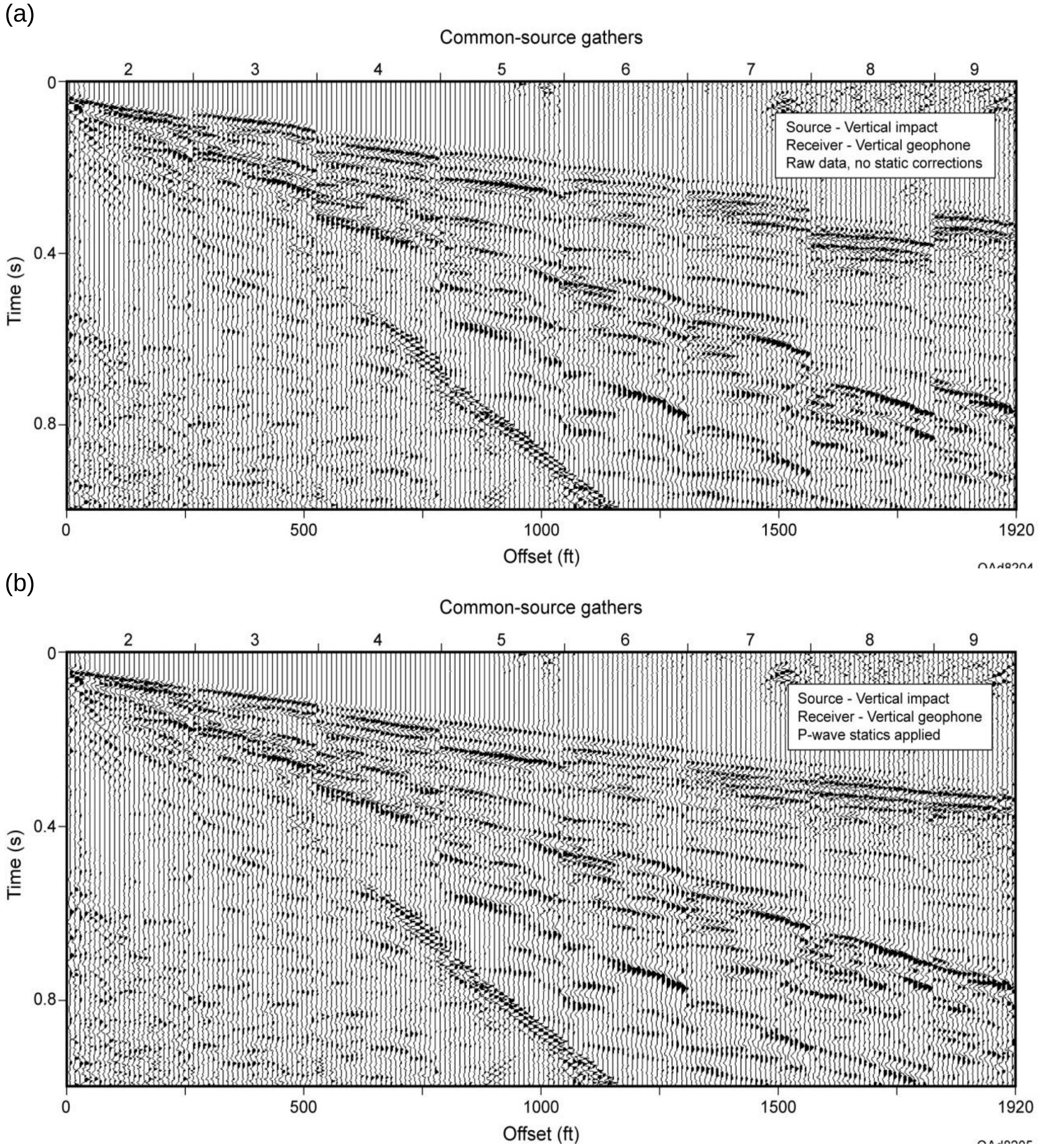

Figure 6: (a) Data generated by a vertical weight-impact source positioned at source stations 2 through 9 and recorded by surface vertical geophones. Discontinuities between each 25-trace group of source-station gathers are caused by source-station statics and variations in time-zero for this impact source. (b) Same data with adjustments made to align the earliest P-wave refraction arrivals.

Test data acquired with surface-based 3C geophones and Sigma cable-free boxes are analyzed in this section to compare the energy content and frequency bandwidth of P and S modes produced by each of the three tested vertical-force source types. The data windows illustrated on Figures 7 through 15 were acquired by a surface-positioned horizontal sensor array and contain not only P and S reflections and refractions, but also intrabed multiples and horizontally-traveling surface-wave noise. The signal-to-noise ratio of reflection data acquired with surface-based horizontal receiver arrays (Figs. 7 to 15) is low.

It is difficult to identify reflection signal in the data shown in Figures 7 through 15 by visual inspection because the surface-array data are only 1-fold and the short length of the profile does not allow significant reflection curvature. Therefore, amplitude strengths and frequency bandwidths are calculated for refracted P, S, and surface waves that sweep across the horizontal receiver array.

Analyses of vertical-vibrator data are shown as Figures 7 to 9; explosive source data are analyzed on Figures 10 to 12; and vertical-impact source results are presented as Figures 13 to 15. For each source, separate analyses are done for vertical geophones, inline-horizontal (radial) geophones, and crossline-horizontal (transverse) geophones. For each geophone orientation, wave-mode velocity and frequency characteristics are calculated in data windows constrained to span only interpreted P, S, or surface-wave modes.

Velocity and frequency behavior are displayed as frequency-wavenumber (FK) spectra. On these FK plots, the vertical axis defines how energy embedded in a wave mode is distributed as a function of frequency. The horizontal axis spans a positive half-plane of wavenumber space (K) and a negative half-space. The negative-K half-space defines events that propagate left-to-right from zero offset to an offset of 1920 ft. This left-to-right direction is the propagation direction for all wave modes that are analyzed. The positive half-plane defines events that propagate right-to-left, from an offset of 1920 ft back to zero offset. In this display format, no events propagate right-to-left, so no energy appears in positive wavenumber half-space in any figure. The slope of energy distribution on these FK plots defines the propagation velocity of a wave mode, with steeper slopes implying higher wave-mode propagation velocities.

Data acquired with vertical and radial-horizontal geophones have three embedded wave modes: a P-wave mode (labeled P), a radial shear mode (labeled SR), and a surface Rayleigh wave (labeled R). Data acquired with transverse-horizontal geophones have only two wave modes: a transverse shear mode (labeled ST) and a surface Love wave (labeled L). No effective P-wave energy appears on transverse horizontal geophones.

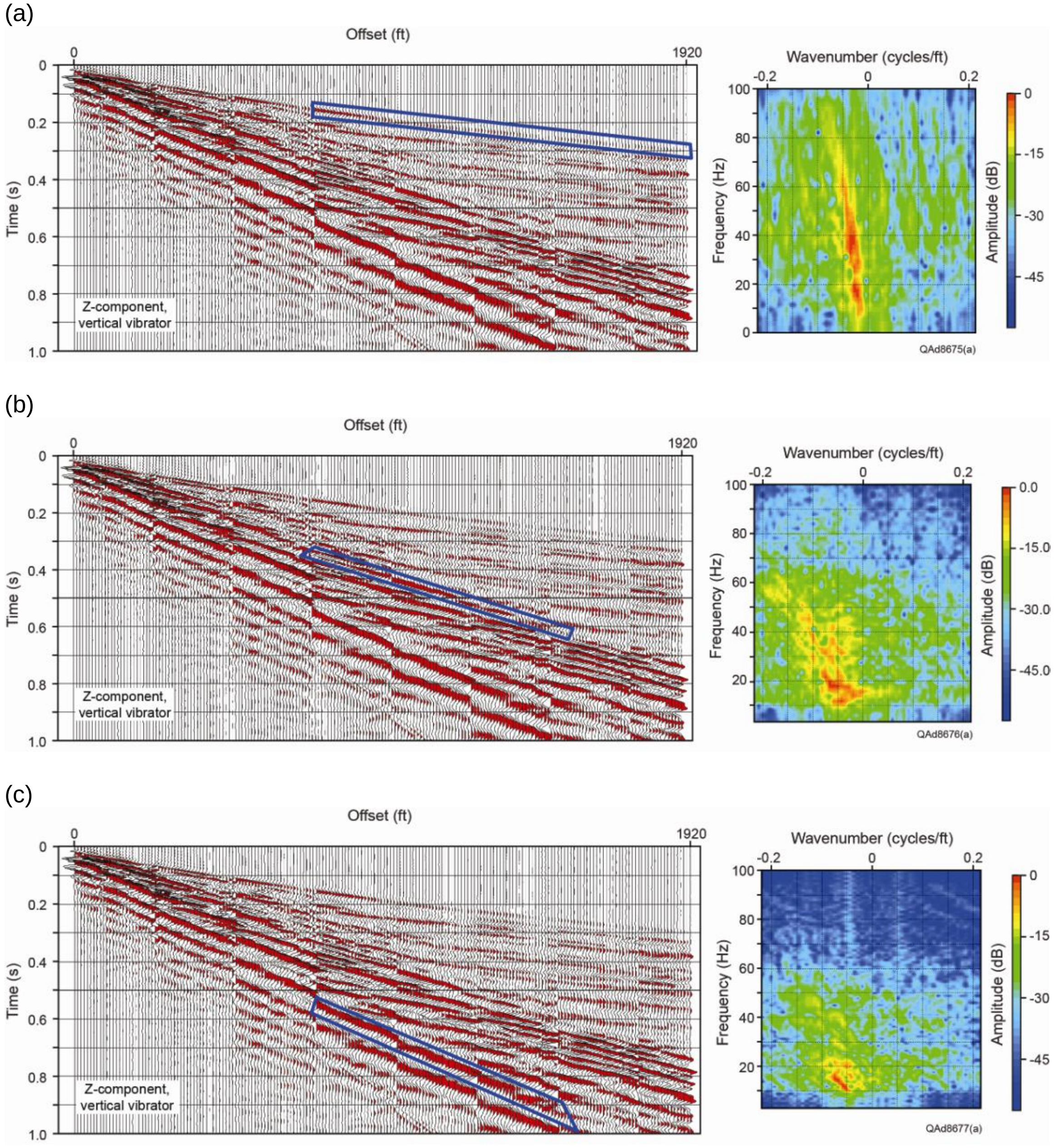

Figure 7: Analysis of refracted P, S, and Rayleigh wave modes produced by a vertical-vibrator source and recorded by vertical geophones deployed as a surface-based horizontal array. (a) Compressional mode, P. (b) Radial shear mode, SR. (c) Rayleigh wave mode, R. Data recorded by Sigma cable-free boxes.

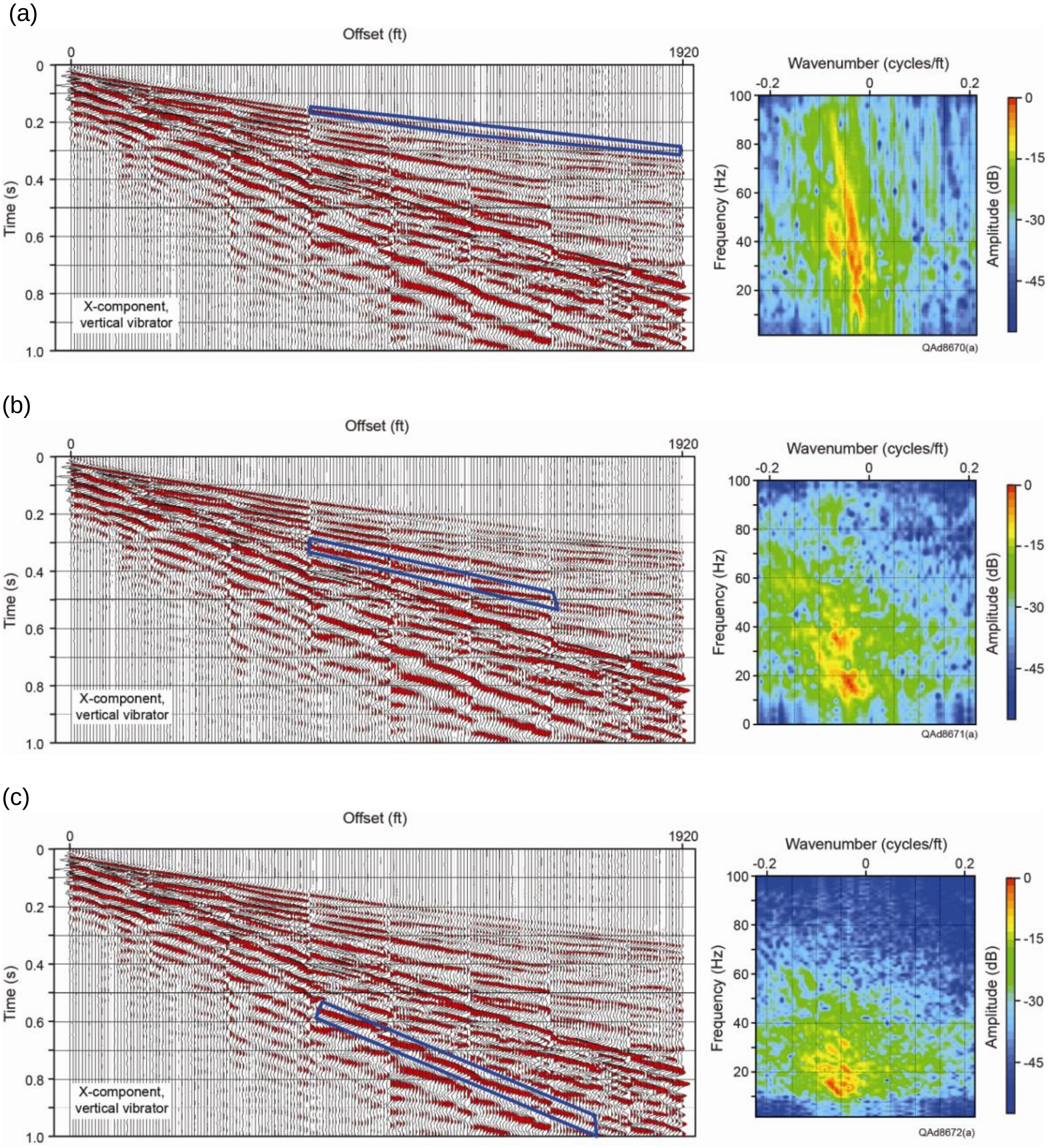

Figure 8: Analysis of refracted P, S, and Rayleigh wave modes produced by a vertical-vibrator source and recorded by inline-horizontal (radial) geophones deployed as a surface-based horizontal array. (a) Compressional mode, P. (b) Radial shear mode, SR. (c) Rayleigh wave mode, R. Data acquired by Sigma cable-free boxes.

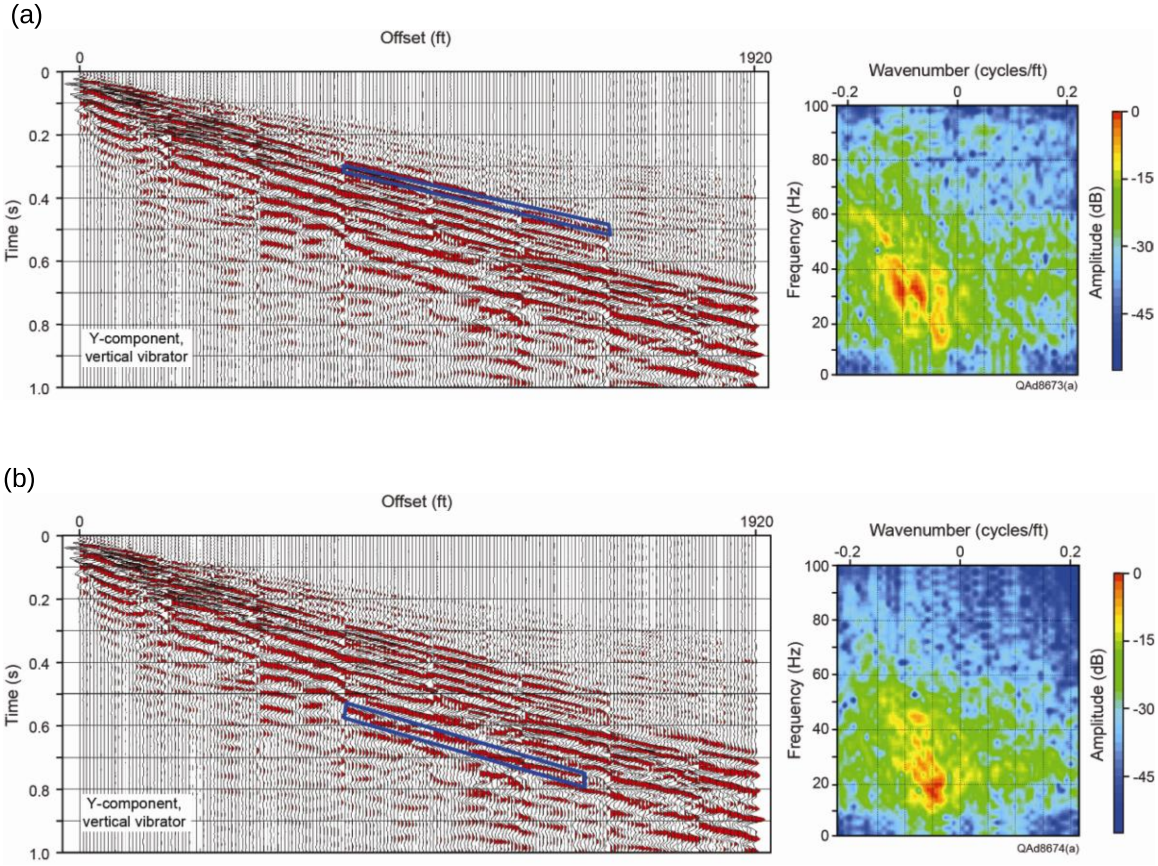

Figure 9: Analysis of refracted S and Love wave modes produced by a vertical-vibrator source and recorded by crossline-horizontal (transverse) geophones deployed as a surface-based horizontal array. (a) Transverse shear mode, ST. (b) Love wave mode, L. No P mode is recorded by transverse horizontal geophones. Data recorded by Sigma cable-free boxes.

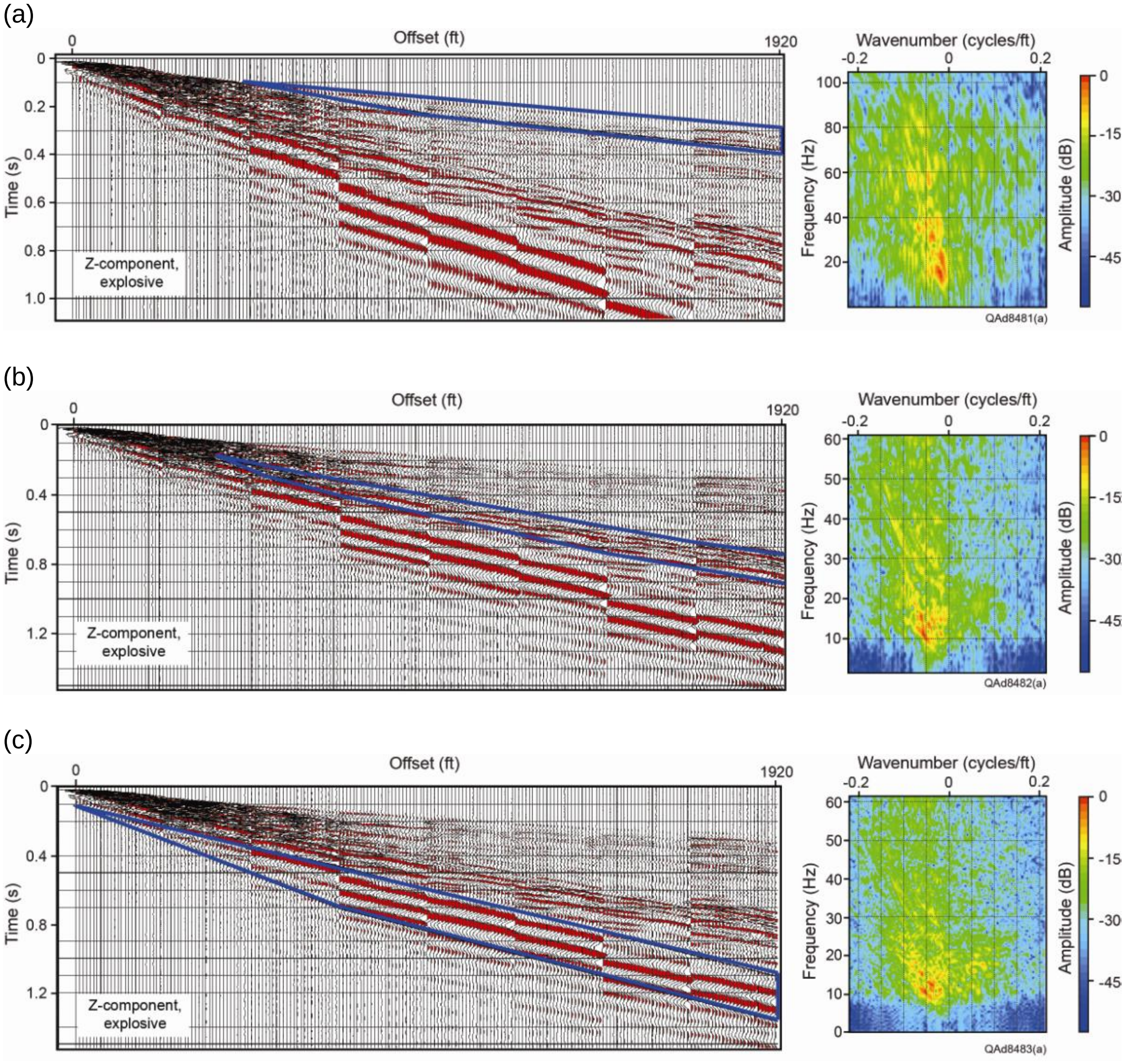

Figure 10: Analysis of refracted P, S, and Rayleigh wave modes produced by an explosive source and recorded by vertical geophones deployed as a surface-based horizontal array. (a) Compressional mode, P. (b) Radial shear mode, SR. (c) Rayleigh wave mode, R. Data recorded by Sigma cable-free boxes.

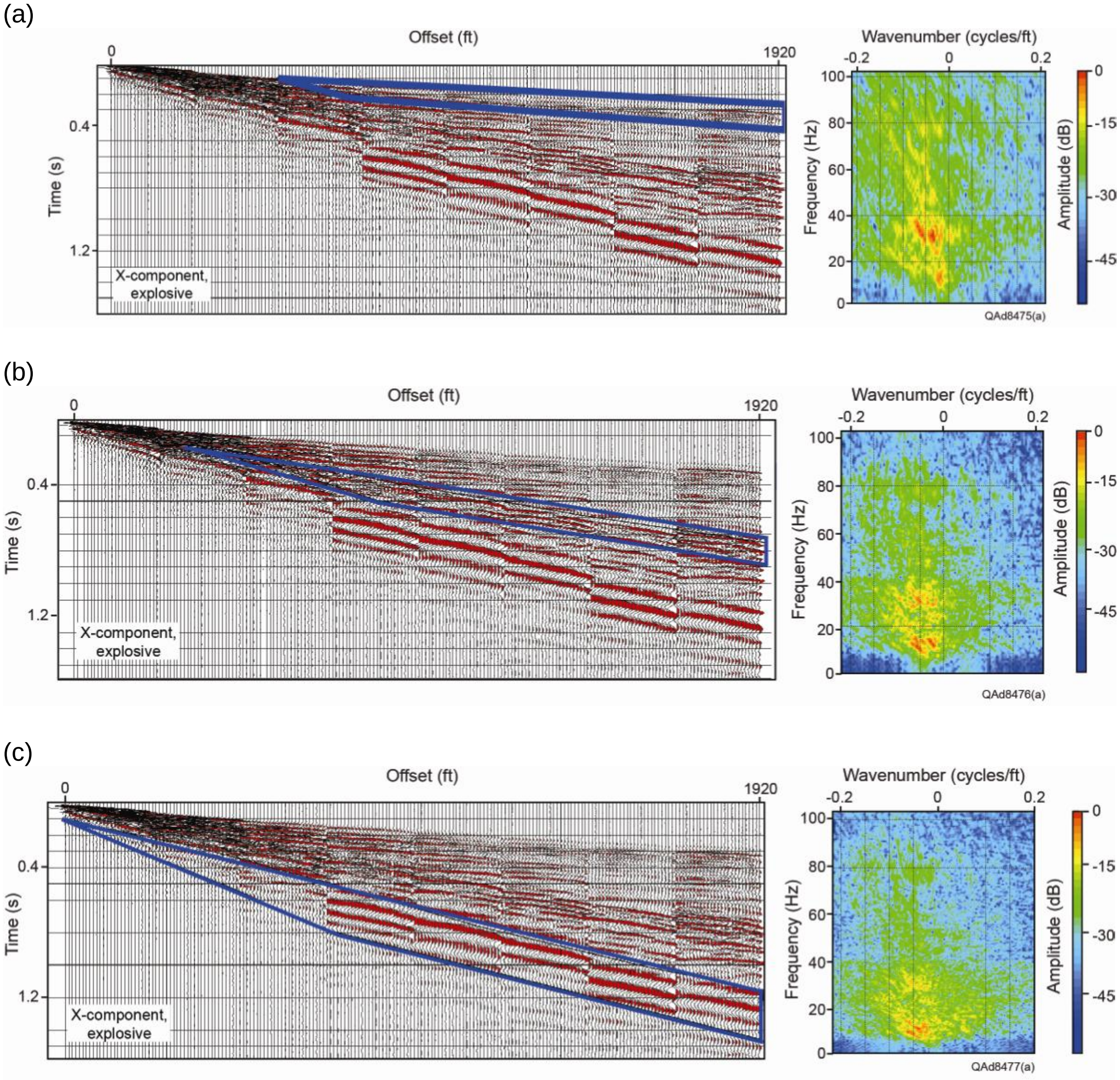

Figure 11: Analysis of refracted P, S, and Rayleigh wave modes produced by an explosive source and recorded by inline-horizontal (radial) geophones deployed as a surface-based horizontal array. (a) Compressional mode, P. (b) Radial shear mode, SR. (c) Rayleigh wave mode, R. Data recorded by Sigma cable-free boxes.

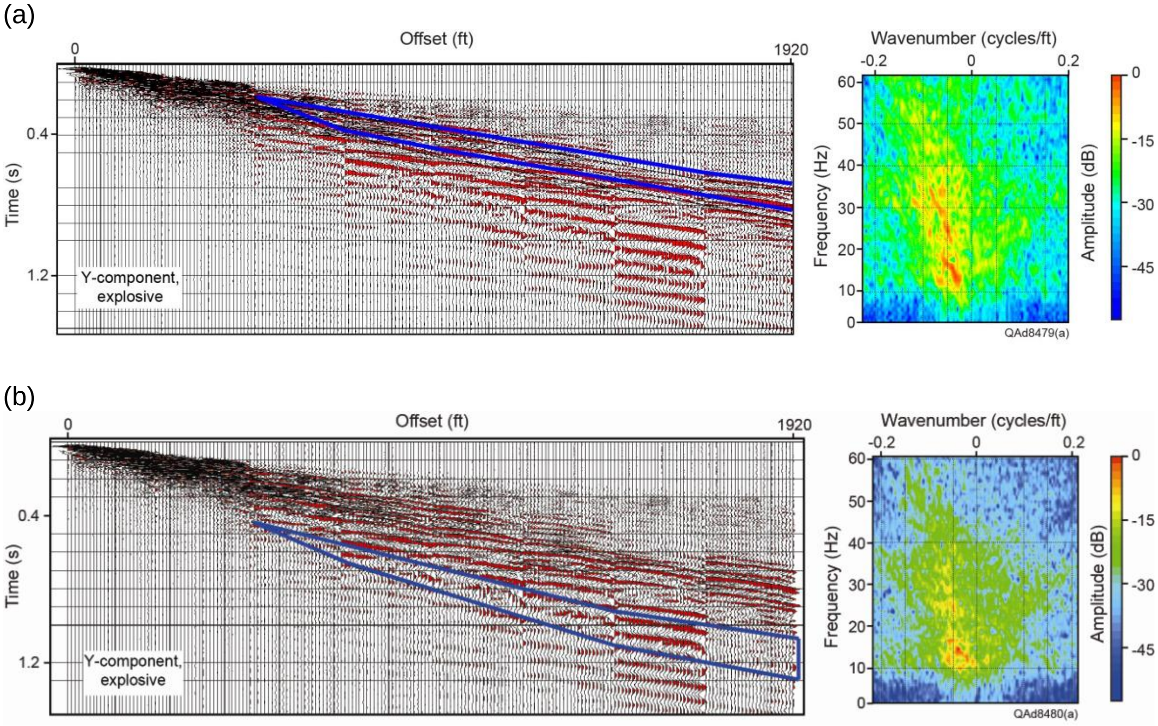

Figure 12: Analysis of refracted S and Love wave modes produced by an explosive source and recorded by crossline-horizontal (transverse) geophones deployed as a surface-based horizontal array. (a) Transverse shear mode, ST. (b) Love wave mode, L. No P mode is recorded by transverse horizontal geophones. Data recorded by Sigma cable-free boxes.

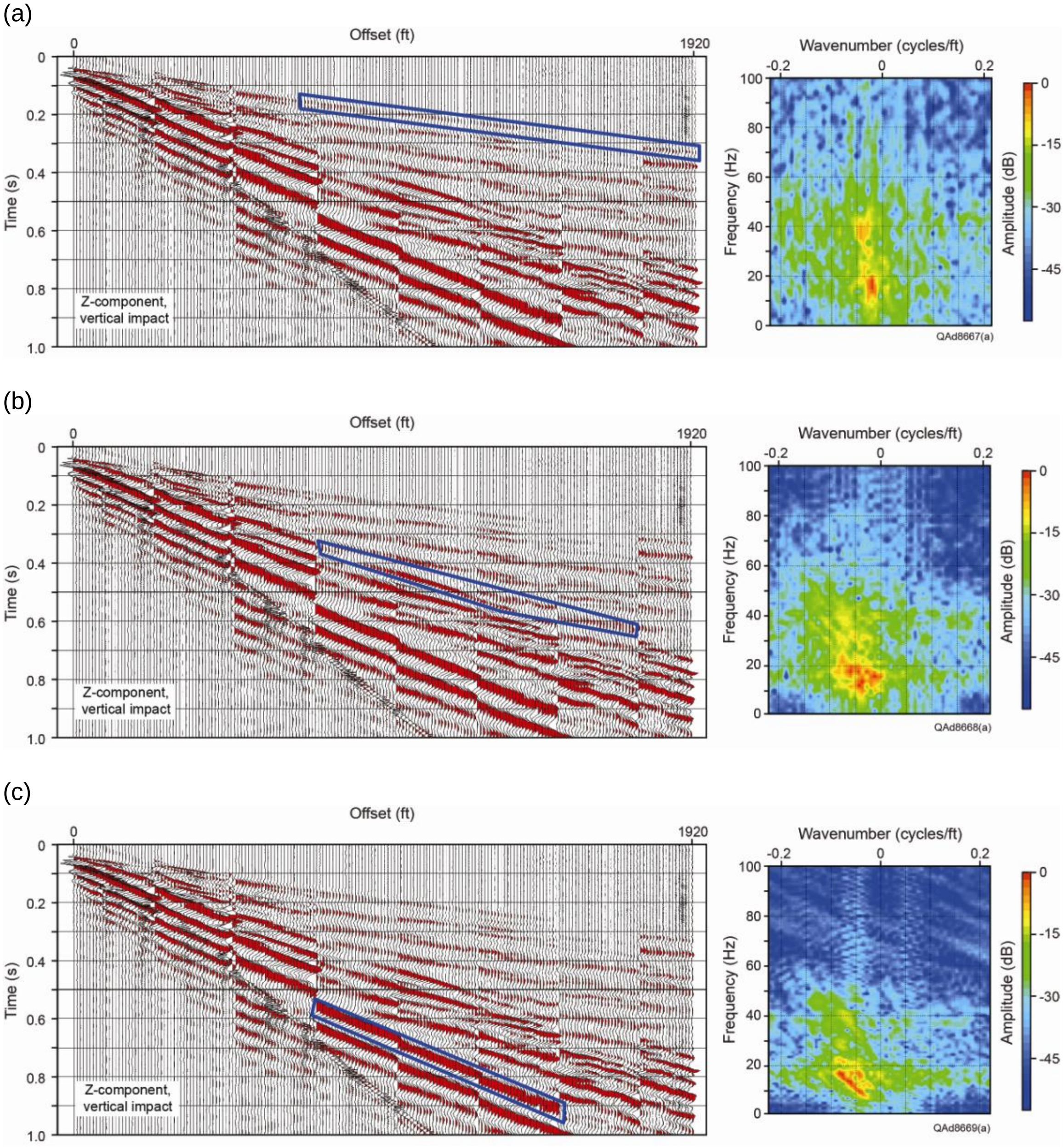

Figure 13: Analysis of refracted P, S, and Rayleigh wave modes produced by a vertical-impact source and recorded by vertical geophones deployed as a surface-based horizontal array. (a) Compressional mode, P. (b) Radial shear mode, SR. (c) Rayleigh wave mode, R. Data recorded by Sigma cable-free boxes.

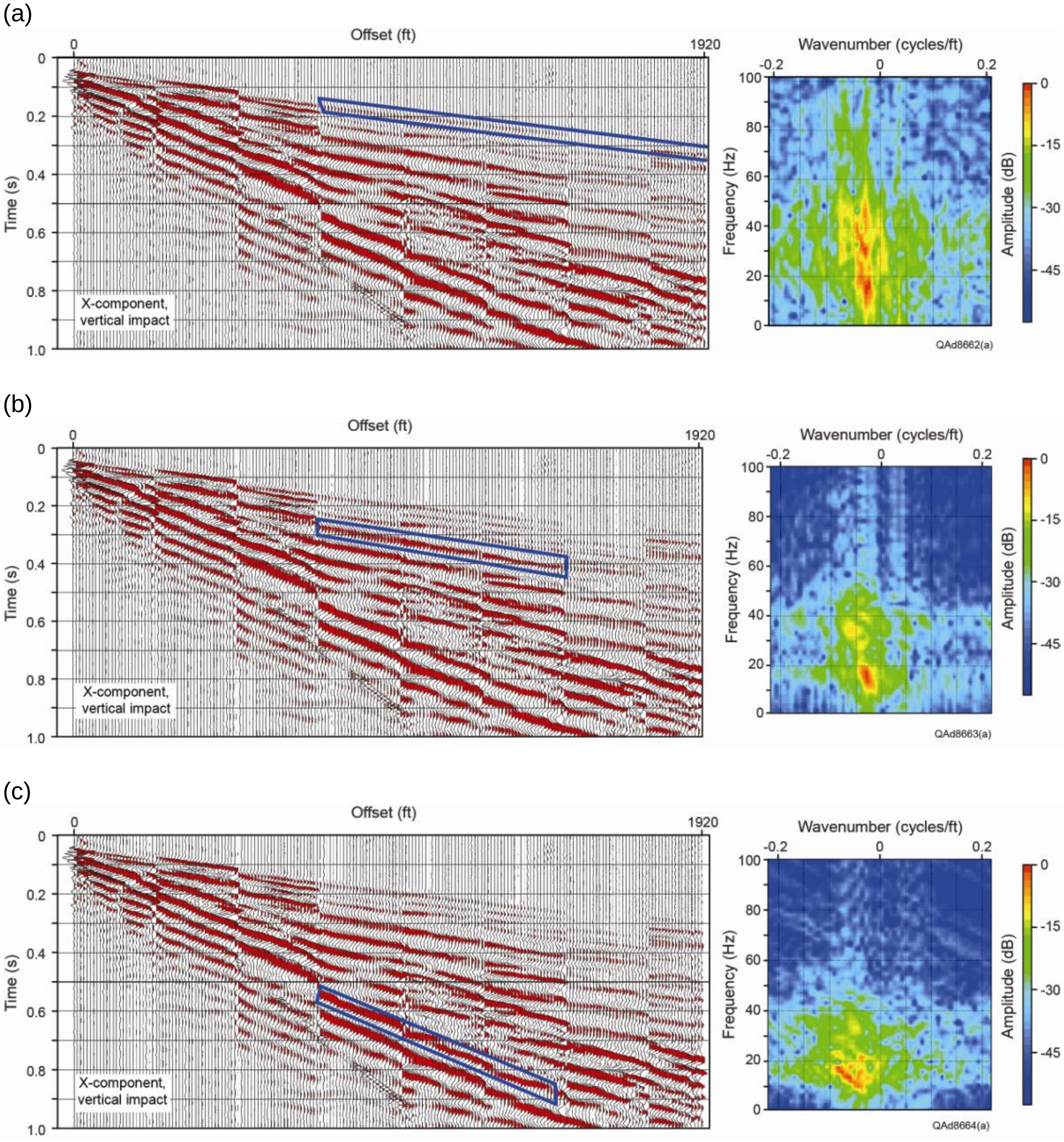

Figure 14: Analysis of refracted P, S, and Rayleigh wave modes produced by vertical-impact source and recorded by inline-horizontal (radial) geophones deployed as a surface-based horizontal array. (a) Compressional mode, P. (b) Radial shear mode, SR. (c) Rayleigh wave mode, R. Data recorded by Sigma cable-free boxes.

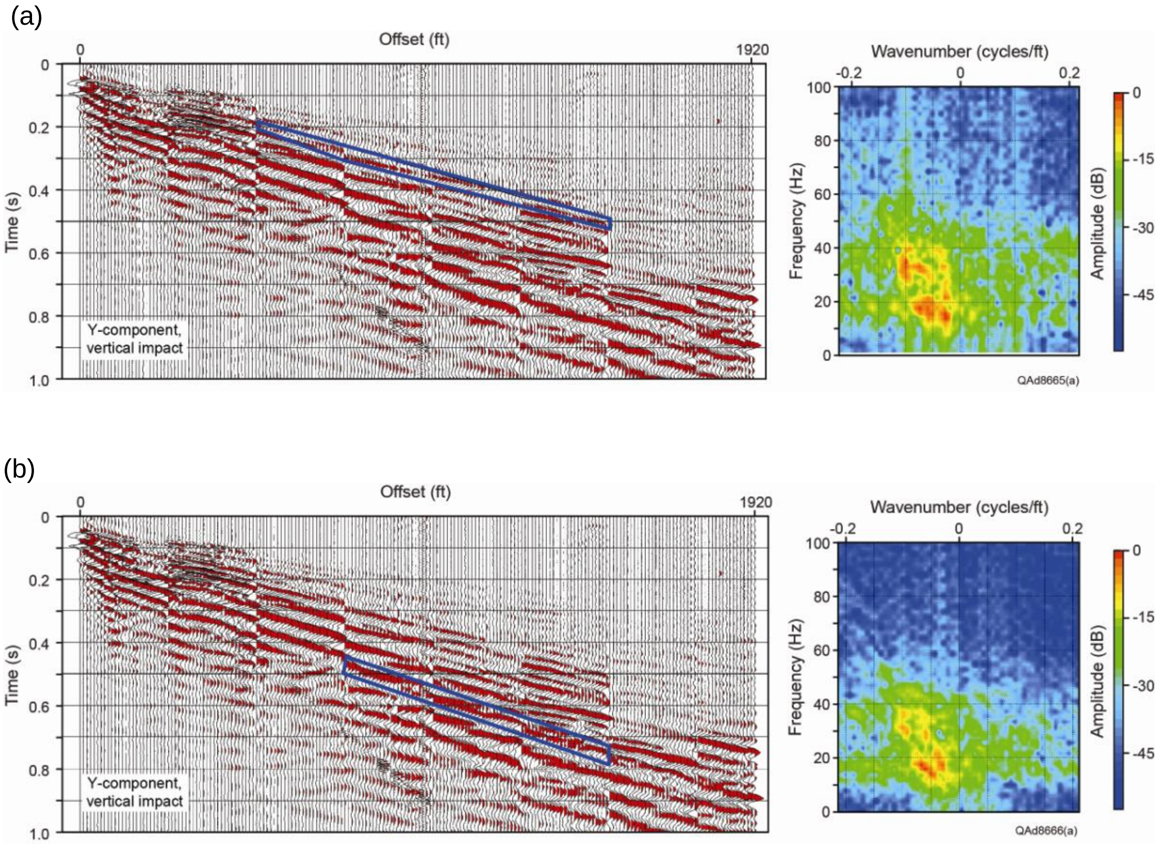

Figure 15: Analysis of refracted S and Love wave modes produced by vertical-impact source and recorded by crossline-horizontal (transverse) geophones deployed as a surface-based horizontal array. (a) Transverse shear mode, ST. (b) Love wave mode, L. No P mode is recorded by transverse horizontal geophones. Data recorded by Sigma cable-free boxes.

Source-specific amplitude and frequency characteristics of P, S, and surface-wave modes (either Rayleigh waves or Love waves) that can be inferred from these horizontal-array data are summarized below:

1. By visual inspection of the wiggle-trace data, refracted waves segregate into rather obvious P, S, and surface-wave modes for each source, allowing mode-specific data analysis windows to be positioned on the data.
2. FK spectra calculated for P, S, and surface-wave data windows vary from source to source.
3. Surface-wave modes are lower frequency than P and S modes for all sources, both by visual inspection of wiggle-trace data and by comparison of calculated FK spectra.
4. Examination of FK spectra shows P-mode spectra calculated for vertical geophones and inline-horizontal geophones are approximately equivalent for vertical vibrator and explosive sources (Figs. 7 and 12). P-mode spectra produced by the vertical impact source span a frequency band approximately 70-percent (one-third) less than that of the vertical vibrator and explosive sources, with diminished energy content occurring at the higher-frequency end of the impact-source spectra (Fig. 13).
5. FK spectra calculated from horizontal-transverse geophone data (Figs. 9a, 12a, 15a) show ST-mode spectra are roughly equivalent for the vertical vibrator and explosive sources. ST spectra for the vertical impact source span a frequency band slightly less than that of the vertical vibrator and explosive sources.

When horizontal vibrators are used to generate S-wave data, S-wave modes have frequencies that usually extend to only 50 Hz. This upper-frequency constraint is caused by mechanical limitations of horizontal vibrators. Although a horizontal vibrator can sweep to frequencies higher than 50 Hz, numerous mechanical problems develop if a large number of high-frequency sweeps are done. For this reason, S-wave data generated by horizontal vibrators typically have frequency spectra that span 4 to 48 Hz or 5 to 50 Hz so that S-wave data can be acquired at a large number of source stations with minimal down time for vibrator repair. In contrast to the S-wave frequency limitation imposed by traditional S-wave sources, an important research finding provided by these test data is that S modes produced by vertical-force sources have frequency spectra that exhibit appreciable energy for frequencies higher than 50 Hz. Examples of broadband S-wave data produced by vertical vibrator and explosive sources are displayed as Figures 7b, 8b, 9a, and 12a. S-mode spectra calculated for the impact source (Figs. 13 through 15) span a frequency bandwidth equivalent to that usually generated by horizontal vibrators.

Each of the vertical-force sources (vertical vibrator, shot-hole explosive, vertical impact) creates good-quality elastic wavefields. Specifically, each source produces more S-wave energy than P-wave energy, and although energy output varies from source to source, the ratio of S-wave energy to P-wave energy is approximately the same for each source. Some sources can image deeper geology simply because they are more energetic. For example, the 60,000-lb vertical vibrator used in these tests produced wave-modes having amplitudes approximately 1000 times greater than wave-mode amplitudes produced by the impact source and approximately 100 times greater than wave-mode amplitudes created by the explosive source. As a result, this particular vertical vibrator should image deeper geology than what can be imaged with the vertical-impact source or the shot-hole explosive source. However, any of the three vertical-force sources can provide P and S images extending to depths of principal targets across most oil and gas prospects. The test data do not cause me to conclude that one type of vertical-force source should be used to the exclusion of other vertical-force sources. Source selection will be dictated by factors such as surface conditions across a prospect, source availability, source cost, and target depth.

Comparisons of Geophones and Accelerometers

One objective of the equipment tests done at the Devine Test Site was to compare P and S wave modes acquired with 3C accelerometers and 3C geophones to determine if one type of sensor provided more attractive multicomponent data than the other. Several factors were considered when analyzing these sensor data, with key requirements being:

1. Geophones and accelerometers had to be planted in the same sediment,
2. All sensors had to be coupled to the Earth in the same manner,
3. All sensor outputs had to be recorded by the same recording system, and
4. Geophones and accelerometers had to record data generated by the same seismic source.

These four data constraints were addressed by: (Requirement 1) placing geophone stations and accelerometer stations side-by-side within 1 meter of each other (Fig. 5);

(Requirement 2) taking care to bury all sensors flush with the ground surface and tamping soil around each sensor with the same consistency; (Requirement 3) recording geophone and accelerometer data with the same data-acquisition system—a cable-based Sercel 428, and (Requirement 4) recording data generated by only an explosive source.

As a result of these field test procedures, it is reasonably correct to assume that differences in P and S wave modes observed in data outputs from test-site geophone arrays and accelerometer arrays should be caused by the type of sensor that recorded the seismic wavefields rather than by other factors.

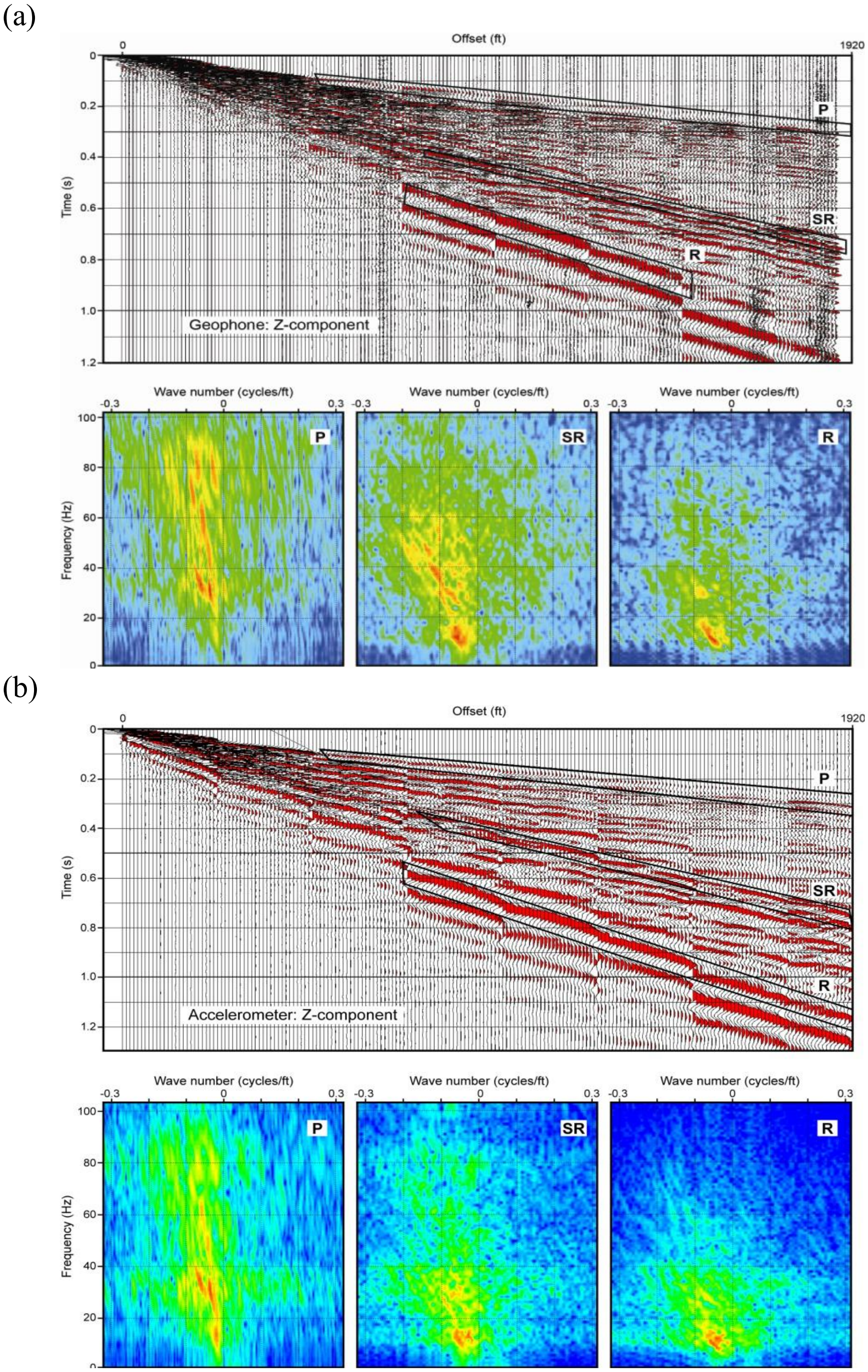

Figure 16: Comparison of seismic sensor data. (a) Response of vertical component of 3C geophones. (b) Response of vertical component of 3C accelerometers. P = P-wave mode. SR = radial shear mode. R = Rayleigh surface wave.

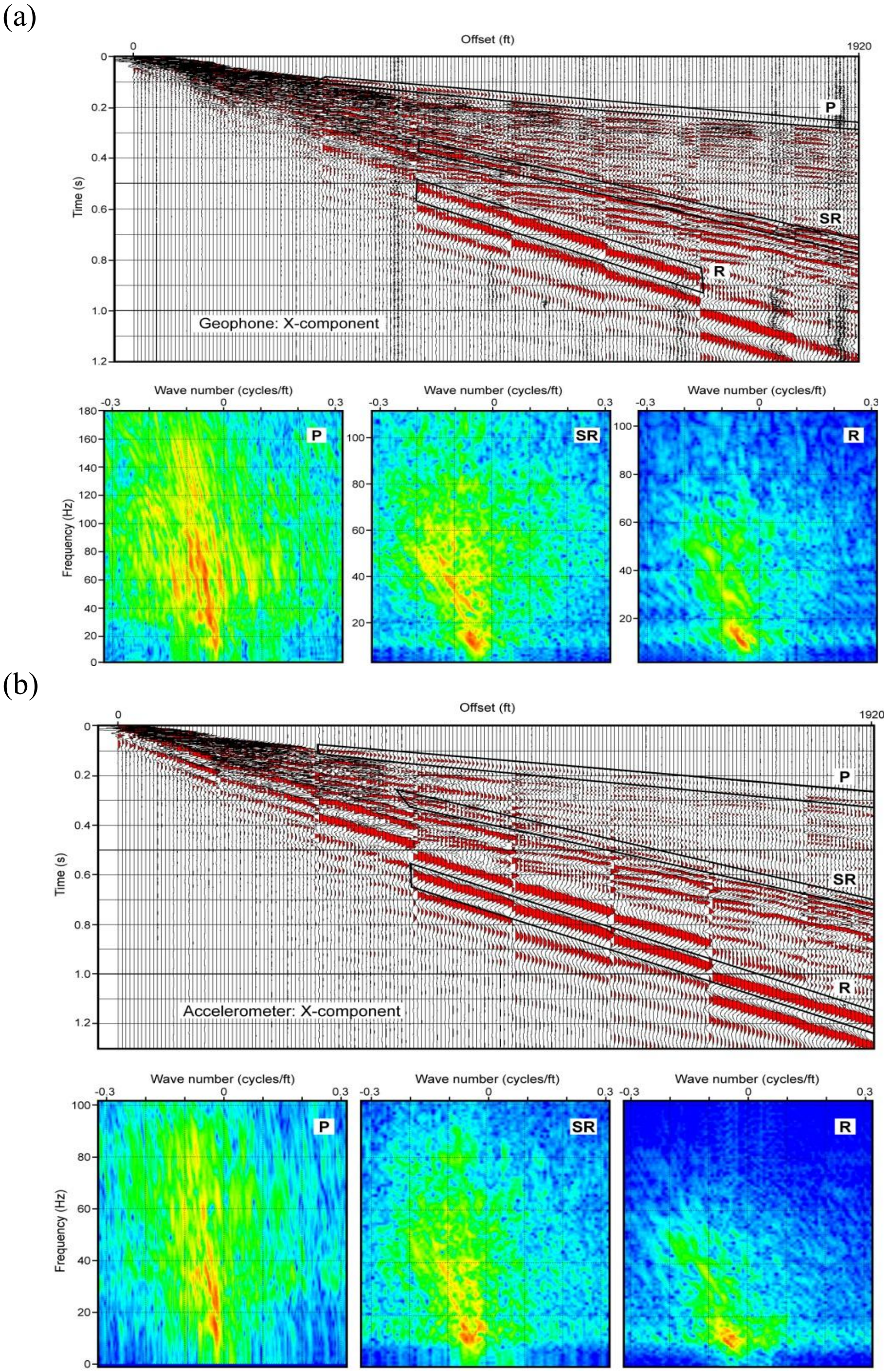

Figure 17: Comparison of seismic sensor data. (a) Response of horizontal-radial component of 3C geophones. (b) Response of horizontal-radial component of 3C accelerometers. P = P-wave mode. SR = radial shear mode. R = Rayleigh surface wave.

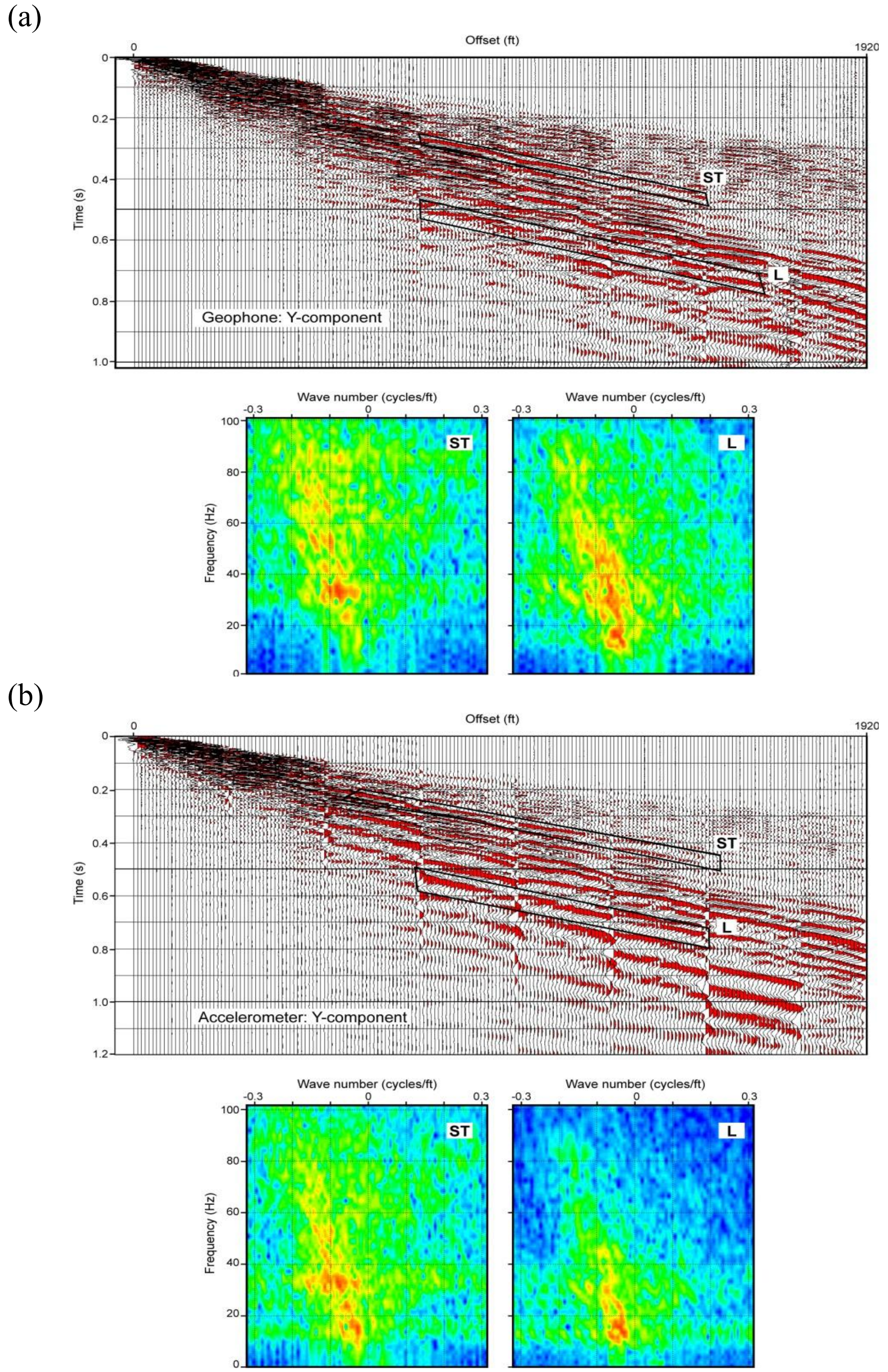

Figure 18: Comparison of seismic sensor data. (a) Response of horizontal-transverse component of 3C geophones. (b) Response of horizontal-transverse component of 3C accelerometers. ST = transverse shear mode. L = Love wave.

Test data acquired by 3C geophones and 3C accelerometers are compared on Figures 16 through 18. The geophones deployed for the test were Oyo Geospace Model 20DX types (10-Hz resonance suspension spring). The accelerometers were Sercel DSU3 MEMS solid-state sensors. The energy source that generated the sensor test data was a 1 kg (2.2 lb) explosive charge detonated at a depth of 6 m (20 ft).

Visual inspection of the wiggle-trace test data displayed on Figures 16 through 18 implies accelerometers record slightly more robust low-frequency components than do geophones. This distinction in sensor frequency response is verified by most (not all) of the FK spectra that accompany the wiggle-trace plots. In any multicomponent seismic application where it is essential to emphasize low frequencies, serious consideration should be given to using accelerometers rather than geophones for data acquisition.

A unique attribute of MEMS solid-state accelerometers is that they function as gravity meters when they are not reacting to Earth vibrations. The benefit of this gravity meter behavior is that a 3C accelerometer can identify which of its three sensors is in a vertical orientation. As a result, any of the three orthogonal accelerometers in a 3C accelerometer package can be the vertical sensor. An advantage of this sensor physics is that in situations where ground conditions make it difficult to plant a MEMS sensor package in its normal vertical orientation, the sensor package can be laid on its side, covered with a small sandbag or mound of dirt, and still record high-quality data. In these field tests, this property of MEMS sensors was utilized at two receiver stations located 20 and 30 ft (6 and 9 m) from the receiver well. At these locations, a thick layer of coarse gravel prohibited deploying a DSU3 sensor package in its normal vertical orientation. The DSU3 package was laid on its side at these two stations and covered with dirt-filled bags to make a reasonable sensor-to-Earth coupling. The internal electronics of the MEMS data-acquisition system switched the definitions of vertical, radial horizontal, and transverse horizontal to the appropriate accelerometers. The data acquired at these two receiver stations look identical to data acquired at all other receiver stations and cannot be identified when inspecting the wiggle-trace data on Figures 16 to 18. Thus there is considerable appeal to using MEMS 3C accelerometers to acquire multicomponent seismic data across areas where it is difficult to plant geophones in a vertical orientation, for example across prospects covered with hard rock outcrops.

In most seismic data-acquisition projects, vertical orientation of 3C geophones is not a serious handicap. Also for most studies, it is not necessary that amplitudes of low-frequency components (less than 10 Hz) be greater than the amplitudes provided by 3C geophones. In such conditions, there is no significant difference between multicomponent data acquired with 3C geophones and data acquired with 3C accelerometers.

An important principle of S-wave physics demonstrated on Figures 16 to 18 has nothing to do with the type of sensor that recorded the data. This principle is that FK spectra show the frequency bandwidth of an ST shear mode is significantly broader than the frequency bandwidth of an SR shear mode. Examples of this frequency difference are shown by comparing ST spectra on Figure 18, where high-energy frequency components extend from 10 to 100 Hz, with SR spectra on Figures 16 and 17, where high-energy frequency components extend from 10 Hz to only 40, 60, or 80 Hz, depending which sensor data are considered (vertical sensor data or horizontal-radial sensor data).

Comparisons of Cable-Based and Cable-Free 3C Data

The third objective of the equipment test program was to compare P and S wave modes acquired with cable-based and cable-free data acquisition systems to determine if equivalent data are acquired with each recording system. Constraints placed on data subjected to this analysis were:

1. Identical sensors (3C Oyo Geospace Model 20DX geophones [10-Hz resonance suspension spring]) generated the data inputs to the two recording systems, and
2. Sensor arrays recorded by each system were planted side-by-side in equivalent sediment and with equivalent sensor-to-earth coupling (Fig. 4).
3. The geophone responses that were input to each recording system were produced by the same source (a shot-hole explosive).

The cable-based recording system was a Sercel 428. Two cable-free systems were utilized: EUnite boxes provided by Sercel and Sigma boxes provided by Seismic Source and iSeis.

As a result of the three field test procedures listed above, any differences in P and S wave modes observed in the test data should be caused only by the type of data-acquisition system that recorded the wave modes and not by differences in sensor type, sensor coupling, source wavefields, or other factors.

Test data acquired by these three data-acquisition systems are compared on Figures 19 through 21. In these displays, data are segregated according to geophone orientation. Vertical geophone responses are shown in Figure 19, horizontal-radial geophone responses are displayed on Figure 20, and horizontal-transverse geophone responses are on Figure 21.

As was the case for seismic sensor comparison (Figs. 16 to 18), the energy source that generated the data was 1 kg (2.2 lb) of explosive detonated at a depth of 6 m (20 ft).

Comparing FK spectra on each figure leads to the conclusion that data acquired with the 428 cable-based system have wider frequency spectra than data acquired with either cable-free system. This difference is particularly obvious for P-wave spectra where 428-system frequencies extend above 100 Hz (Fig. 20 in particular), but Sigma-system and EUnite-system frequencies extend to only 100 Hz (or less). Extensions of energy to higher-frequency components also occur for SR and ST shear modes acquired with the cable-based system.

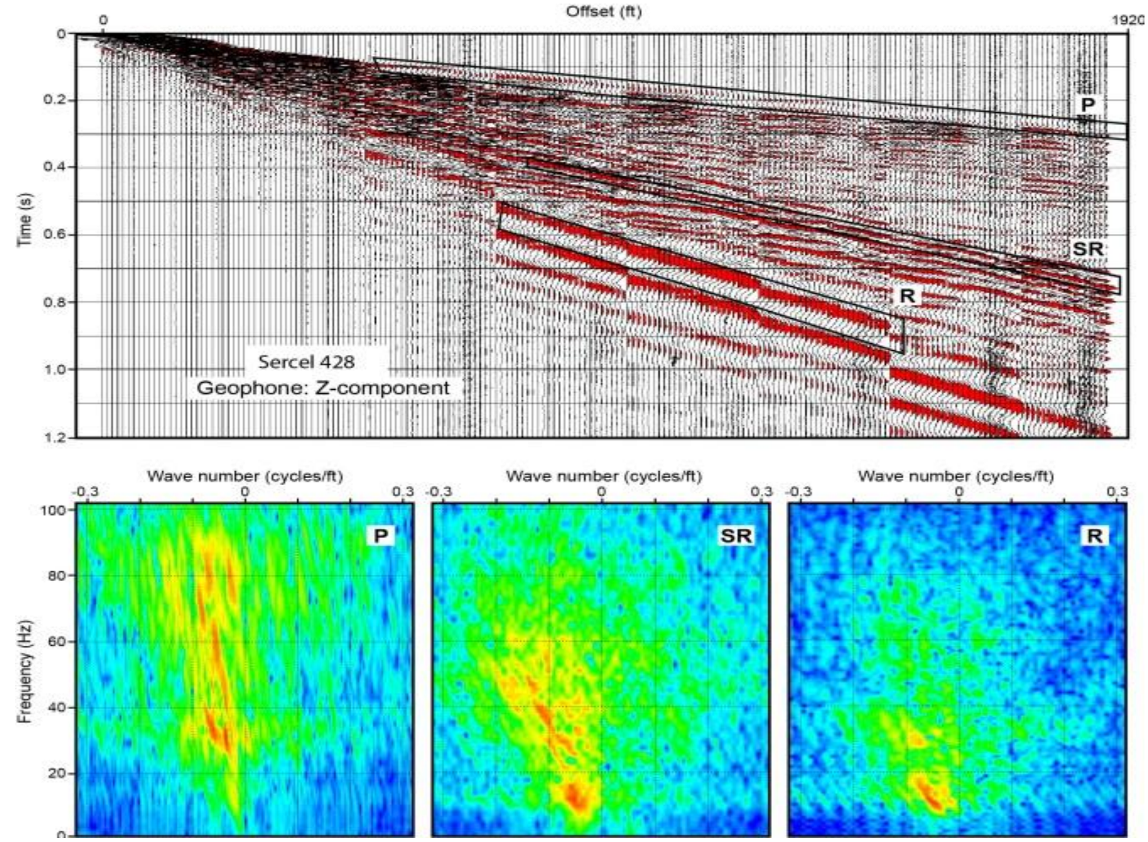

Figure 19 (a): Comparison of vertical-geophone data acquired with a cable-based recording system and cable-free recording systems. Vertical component data acquired with cable-based Sercel 428. P = P-wave mode. SR = radial shear mode. R = Rayleigh surface wave.

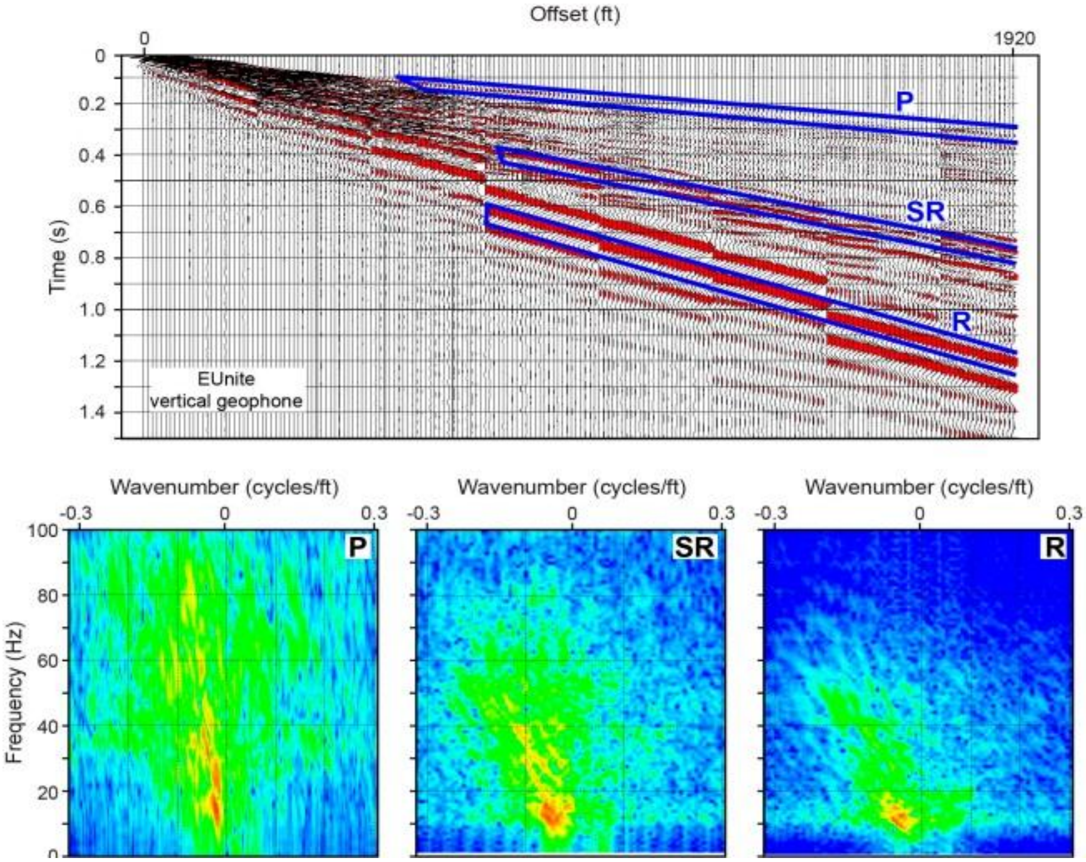

Figure 19 (b): Comparison of vertical-geophone data acquired with a cable-based recording system and cable-free recording systems. Vertical component data acquired with cable-free EUnite system. P = P-wave mode. SR = radial shear mode. R = Rayleigh surface wave.

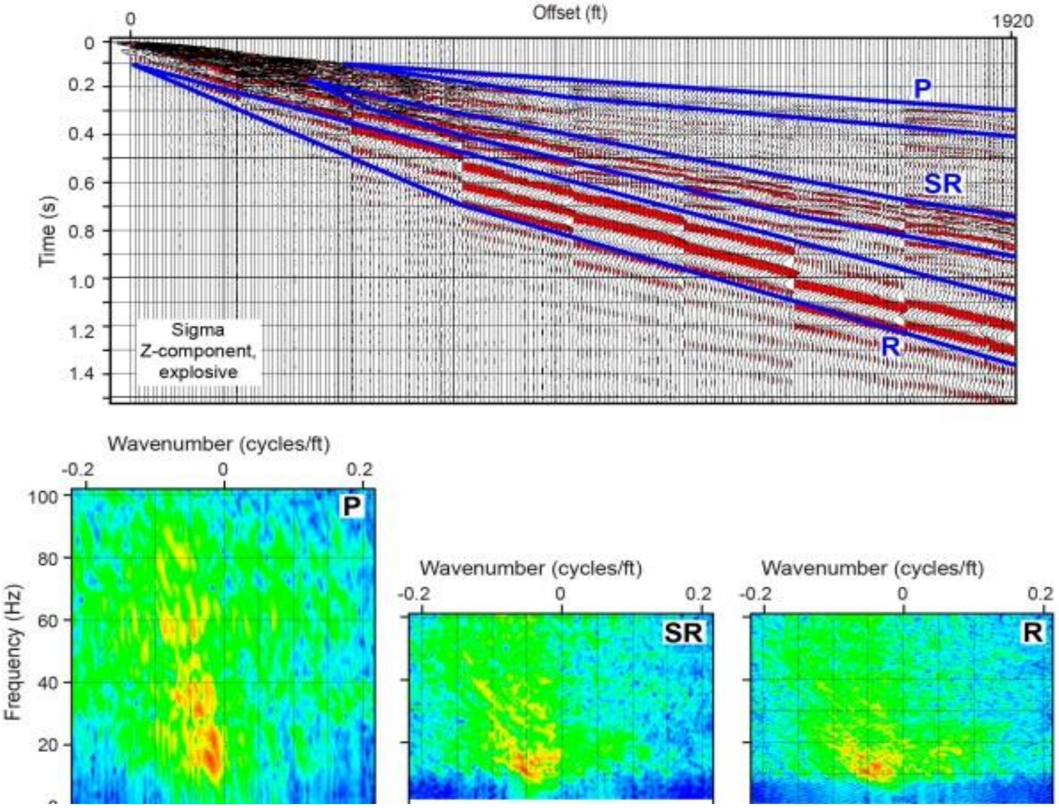

Figure 19 (c): Comparison of vertical-geophone data acquired with a cable-based recording system and cable-free recording systems. Vertical component data acquired with cable-free Sigma system. P = P-wave mode. SR = radial shear mode. R = Rayleigh surface wave.

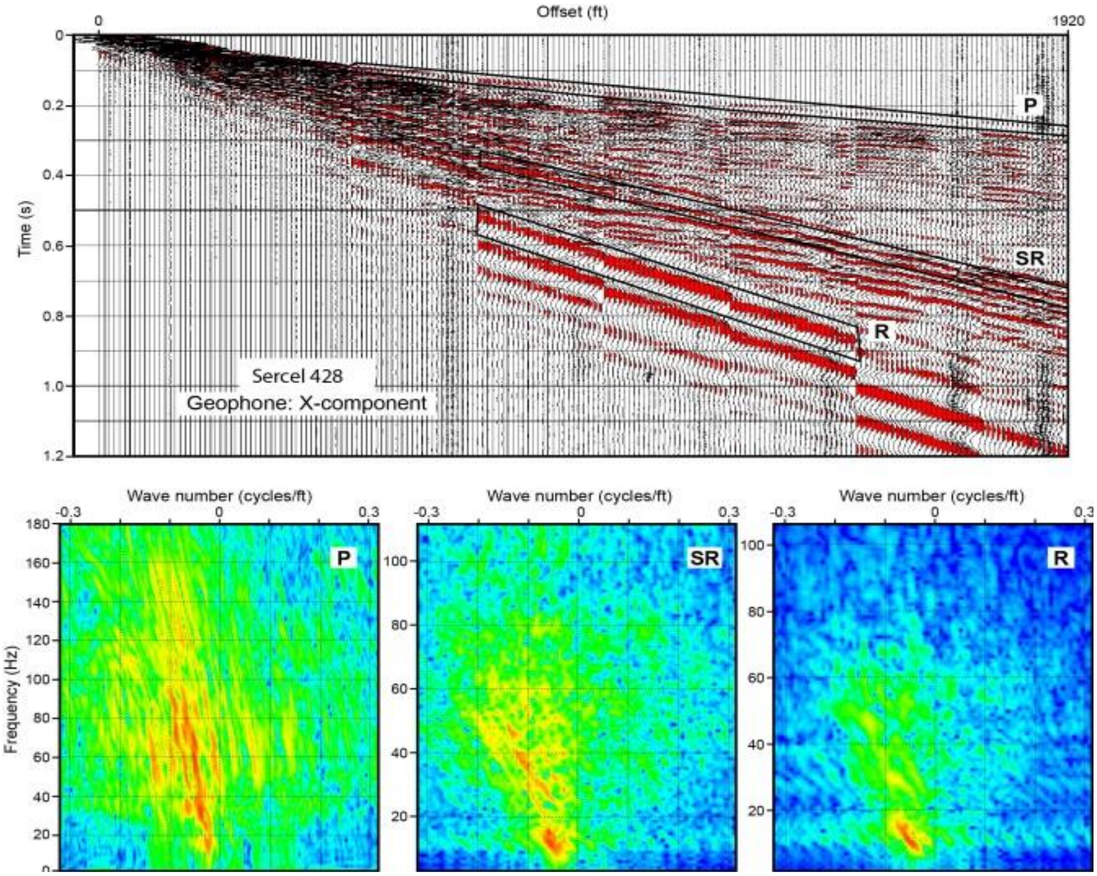

Figure 20 (a): Comparison of horizontal-radial-geophone data acquired with a cable-based recording system and cable-free recording systems. Horizontal-radial component data acquired with cable-based Sercel 428. P = P-wave mode. SR = radial shear mode. R = Rayleigh surface wave.

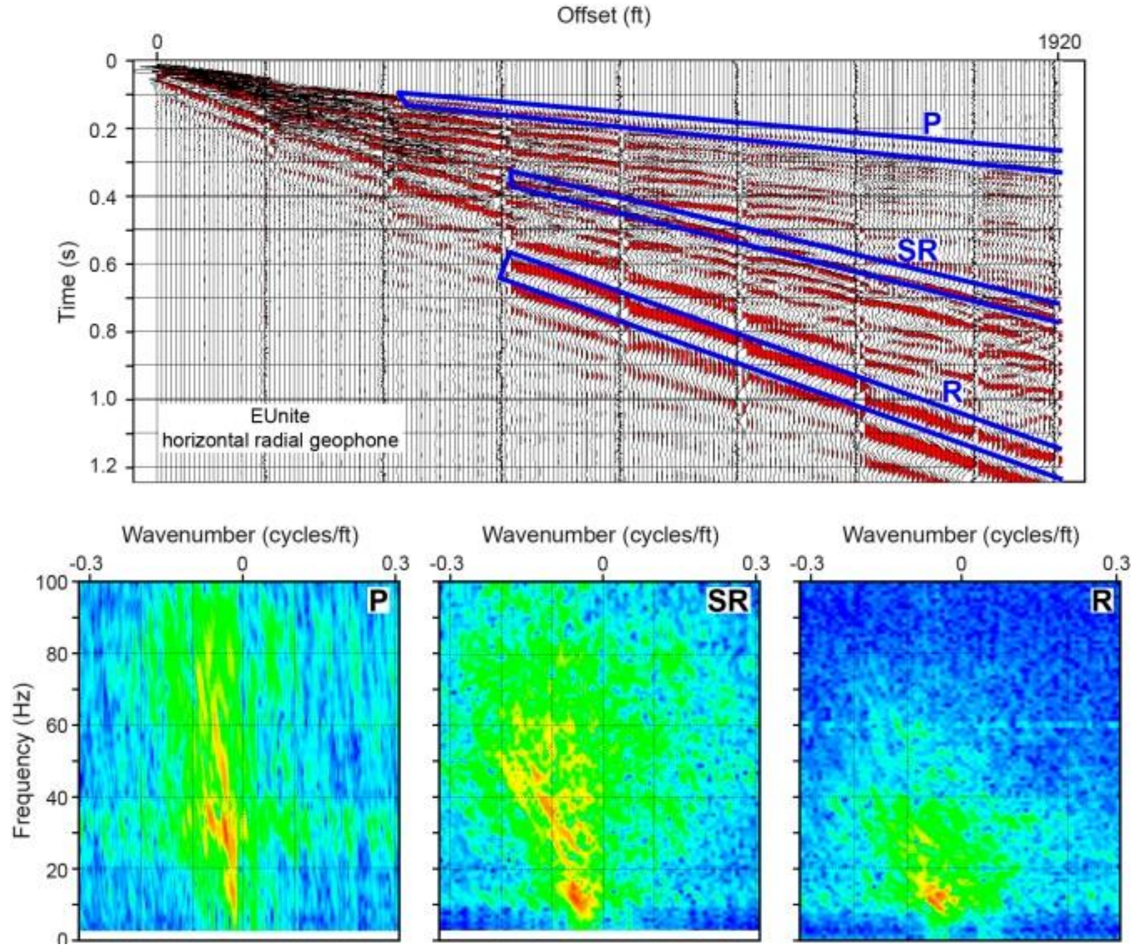

Figure 20 (b): Comparison of horizontal-radial-geophone data acquired with a cable-based recording system and cable-free recording systems. Horizontal-radial component data acquired with cable-free EUnite system. P = P-wave mode. SR = radial shear mode. R = Rayleigh surface wave.

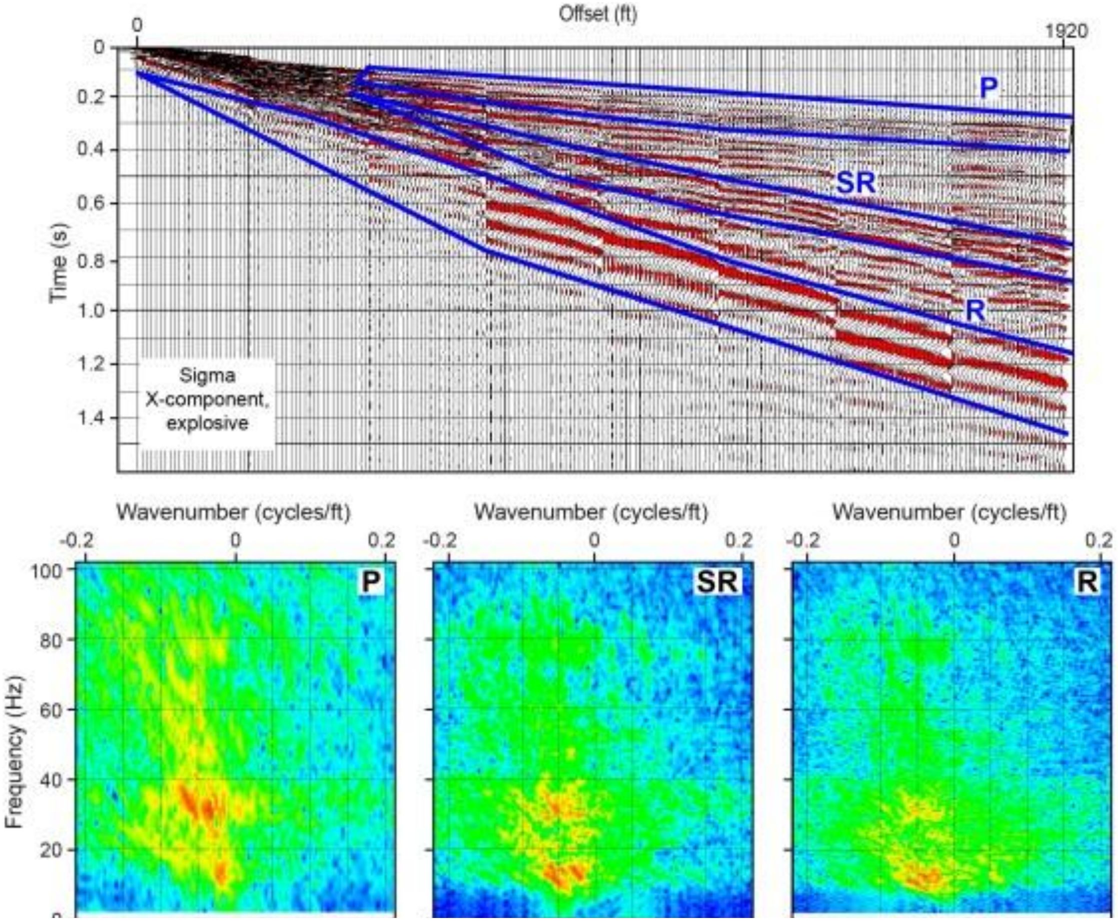

Figure 20 (c): Comparison of horizontal-radial-geophone data acquired with a cable-based recording system and cable-free recording systems. Horizontal-radial component data acquired with cable-free Sigma system. P = P-wave mode. SR = radial shear mode. R = Rayleigh surface wave.

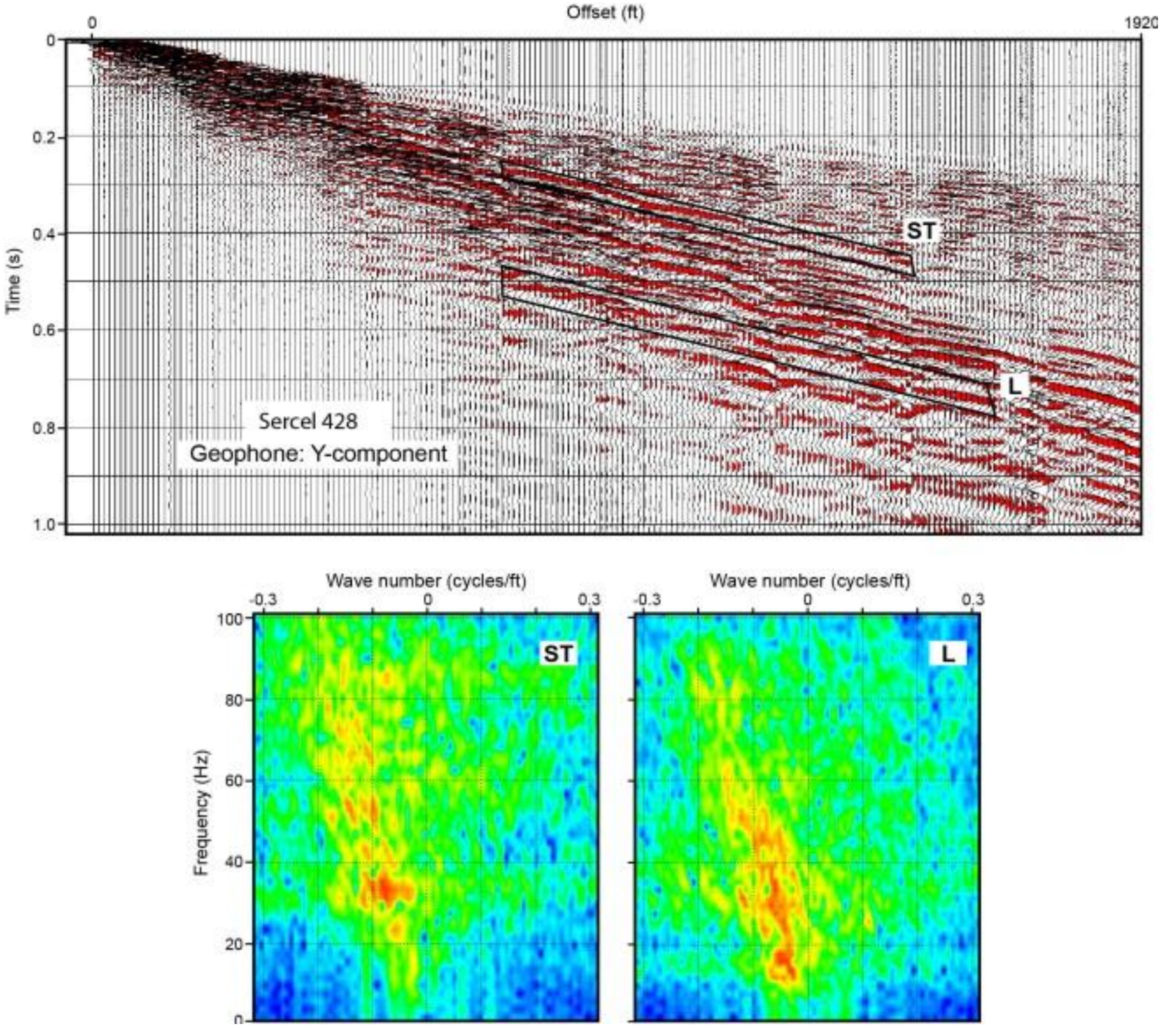

Figure 21 (a): Comparison of horizontal-transverse-geophone data acquired with a cable-based recording system and cable-free recording systems. Horizontal-transverse component data acquired with cable-based Sercel 428. ST = transverse shear mode. L = Love surface wave.

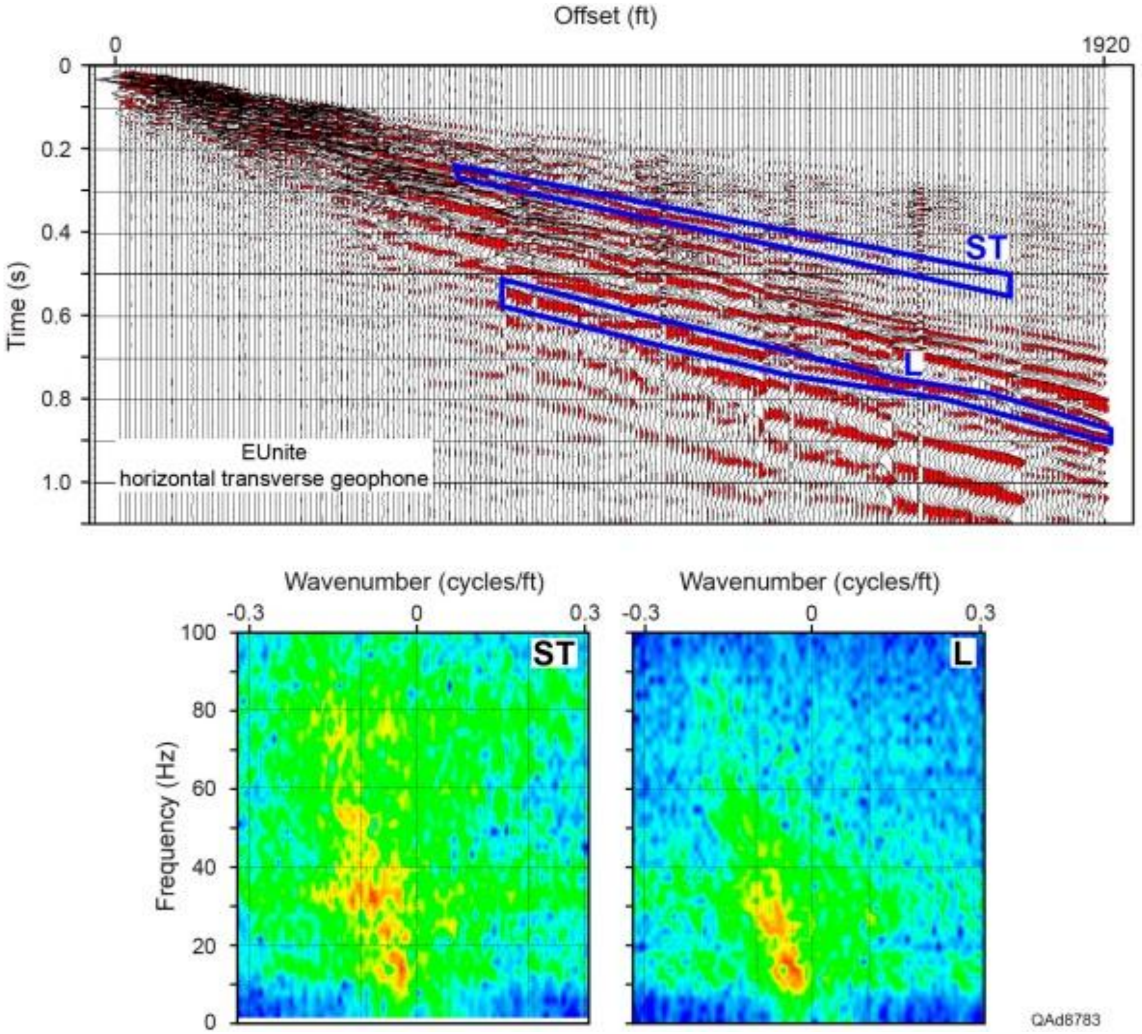

Figure 21 (b): Comparison of horizontal-transverse-geophone data acquired with a cable-based recording system and cable-free recording systems. Horizontal-transverse component data acquired with cable-free EUnite system. ST = transverse shear mode. L = Love surface wave.

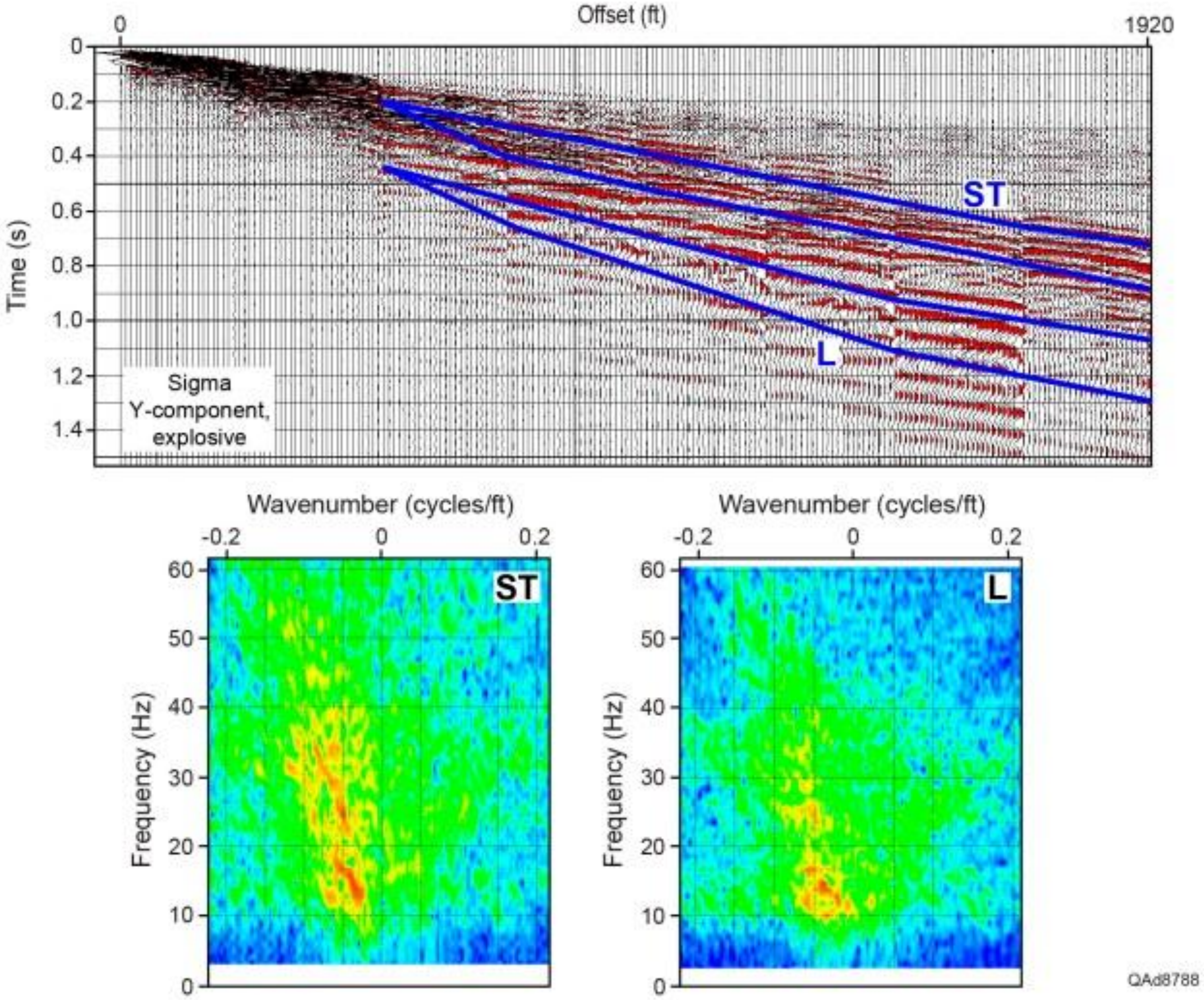

Figure 21 (c): Comparison of horizontal-transverse-geophone data acquired with a cable-based recording system and cable-free recording systems. Horizontal-transverse component data acquired with cable-free Sigma system. ST = transverse shear mode. L = Love surface wave.

ANALYSIS OF VSP DATA

The objective of this section is to compare data quality of different vertical-force seismic sources based on VSP data acquired during the Devine test program. Multicomponent seismic data generated by vertical vibrator, seismic explosive, and vertical impact sources are compared for all three sensor components.

Vertical Aperture of Test Geometry

An important requirement of the test was to record downgoing P and S modes over a wide aperture of vertical takeoff angles from surface source stations. This requirement allowed the maximum amount of energy contained in each wave mode propagating away from source stations to be captured for analysis. The shallowest takeoff angle involved data generated at source station 9 (offset 1920 ft [585 m]) and recorded at downhole receiver station 24 (depth of 500 ft [152 m]). The steepest takeoff angle involves source station 2 (offset 250 ft [76 m]) and downhole receiver station 1 (depth of 1632 ft [497 m]). A first-order approximation of the aperture range created by the source-receiver geometry can be done by assuming straight raypaths from source to downhole receiver, which yields the result shown on Figure 22 (a).

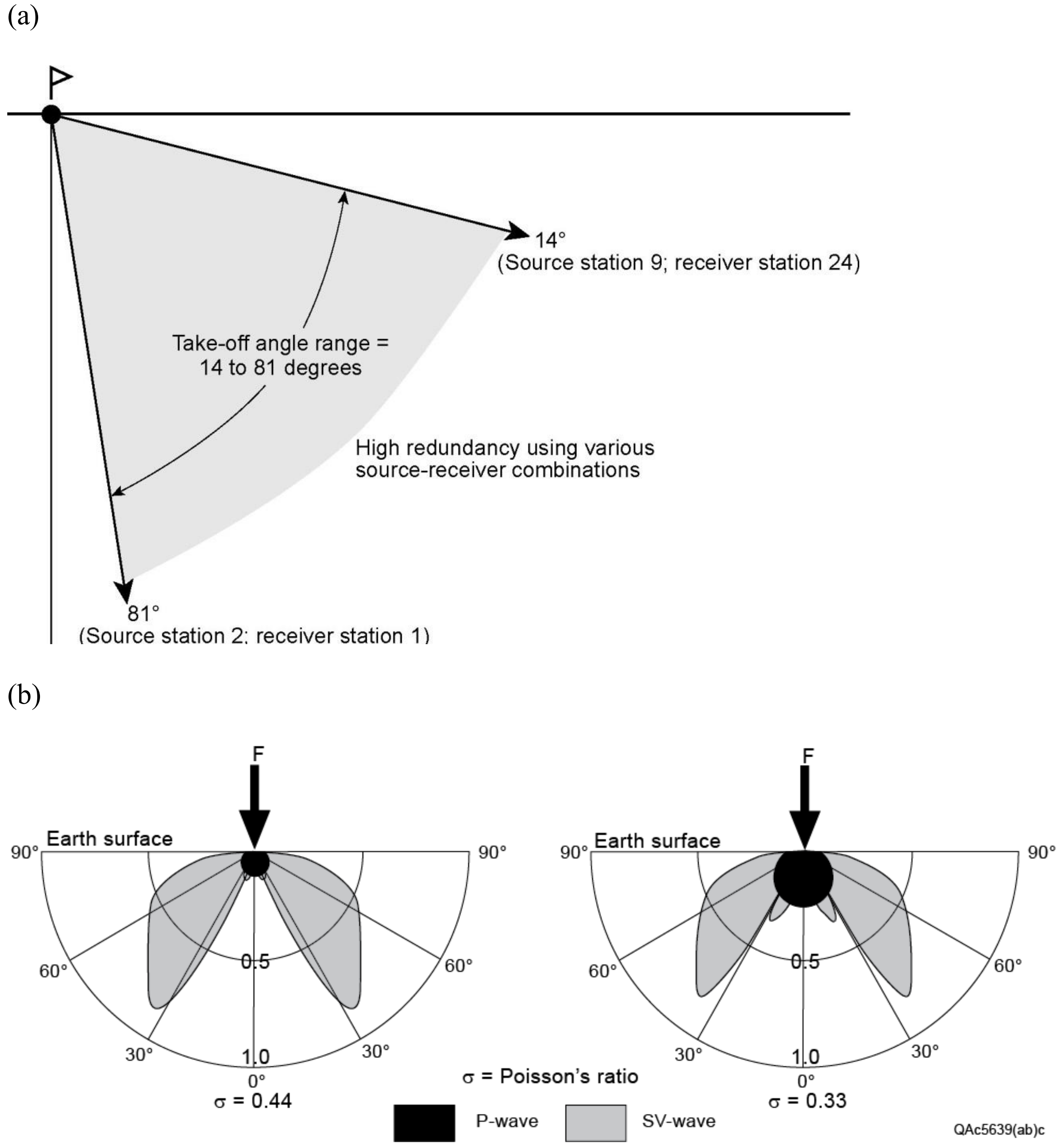

Figure 22: (a) Takeoff angle aperture when straight raypaths are assumed between surface sources and downhole receivers, (b) P and SV radiation patterns produced when a vertical force is applied to the surface of a homogeneous Earth. A soft Earth surface (bottom-left). A hard Earth surface (bottom-right). In both cases more SV energy radiates from the source station than does P energy. (Modified from Hardage et. al, 2011)

Wave Components Embedded in Test Data

Three independent, vector-based, seismic wave modes propagate in a simple homogeneous Earth**:** a compressional mode, P, and two shear modes, SV and SH (Fig. 23 (a)). These are the wave modes the seismic industry creates when wavefields produced by three orthogonal source-displacement vectors are recorded with three orthogonal vector sensors. These are the wave modes that were evaluated in the wavefields generated by the seismic sources evaluated at the Devine Test Site.

Each mode of an elastic wavefield travels through the Earth at a different velocity, and each mode distorts the Earth in a different direction as it propagates. In a homogeneous medium, the orientations of the P, SV, and SH displacement vectors relative to the propagation direction of each mode are defined on Figure 23 (a). The propagation velocities of SH and SV shear modes differ by only a few percent, but both shear velocities (V_S) are significantly less than P-wave velocity (V_P). The velocity ratio V_P/V_S can vary by an order of magnitude in Earth media, from a value of 50 or more in deep-water, unconsolidated, near-seafloor sediment to a value of approximately 1.5 in a few dense, well-consolidated rocks.

A convenient way to distinguish between SH and SV shear modes in a homogeneous medium is to imagine a vertical plane passing through a source station and a receiver station. SV vector displacement occurs in this vertical plane; SH vector displacement is normal to the plane (Fig. 23 (b)). This vertical plane passing through the coordinates of a source station, a receiver station, and a reflection point produced by that source-receiver pair is called a sagittal plane.

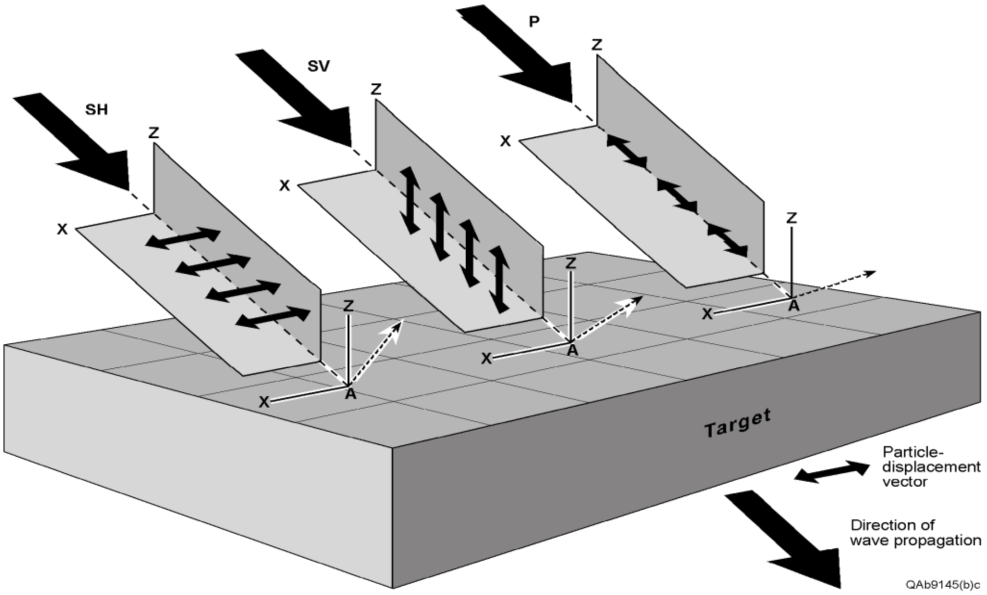

Figure 23 (a): A full-elastic, multicomponent seismic wavefield propagating in a homogeneous Earth consists of a compressional mode P and two shear modes, SV and SH. A key distinction among these wave modes is that each mode distorts the Earth in a different direction along its propagation path. The direction in which each mode displaces the Earth is indicated by double-headed arrows. (Modified from Hardage et. al, 2011)

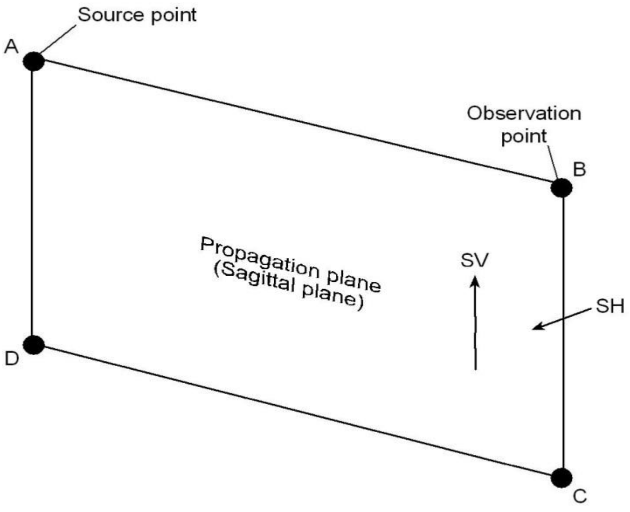

Figure 23 (b): Distinction between SH and SV shear wave displacements in a homogeneous medium. SV displacement occurs in the vertical plane that passes through a source station and an observation point. SH displacement is normal to this plane. (Modified from Hardage et. al, 2011)

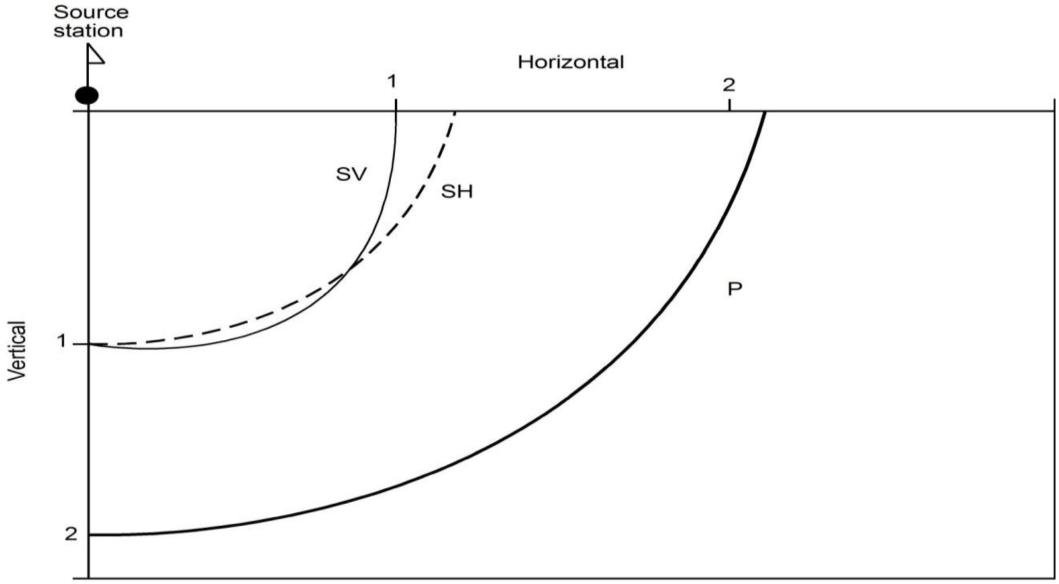

Figure 23 (c): Comparison of SH, SV, and P velocity behavior for elastic wave propagation in horizontally layered [vertical transverse isotropic (VTI)] media. From Levin (1979, 1980).

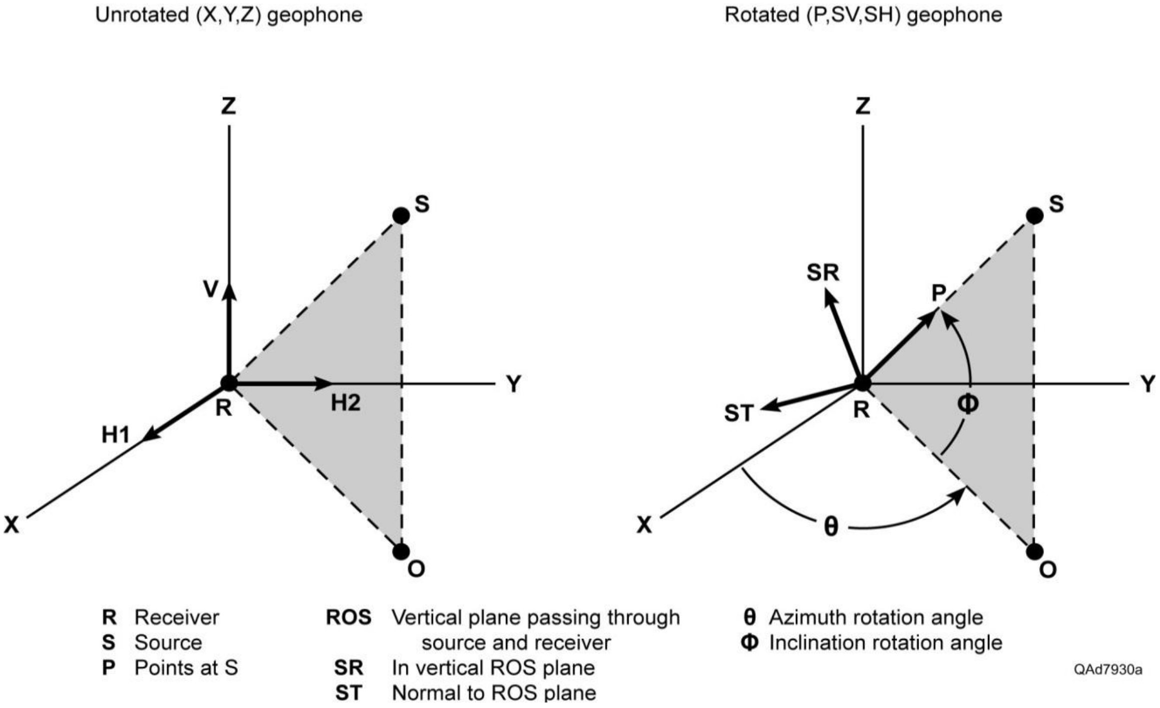

Figure 23 (d): Reorientation of X, Y, Z receivers to P, SR, and ST receivers. (Modified from Hardage et. al, 2011)

Because SV and SH modes cause orthogonal displacements with these orientations, some geophysicists prefer to use the terms radial-S (SR) and transverse-S (ST) when describing S-wave propagation in layered media and to restrict the terms SV and SH to S-wave propagation in homogeneous media, or to S-wave modes that propagate only in symmetry-axis planes. Both styles of nomenclature are used in this study.

Levin (1979, 1980) expanded the physics of S-modes from a homogeneous Earth to a layered Earth and found SH and SV modes propagating through a layered medium exhibit velocity behaviors like those displayed on Figure 23 (c). An important point to note is that at all take-off angles from the source station, except for true vertical and for the one angle that points to the subsurface coordinate where the SH and SV wavefronts intersect, SV and SH modes propagate with different velocities, with the SH mode having a significantly faster velocity at shallow take-off angles from a source station. This wave physics will be important when examining seismic test data shown later.

In a vertical receiver well, azimuth orientations of X, Y horizontal geophones differ at each downhole station because sensor packages are deployed on twisted-wire cable that rotates as it spools off a cable reel. As a result, sensors rotate by different amounts when they reach different deployment depths. Phase shifts and amplitude variations introduced into horizontal-sensor data by station-to-station variations in receiver orientation do not allow individual events or distinct wave modes to be recognized, particularly S-wave events that dominate horizontal-sensor response.

Receivers must be mathematically oriented to consistent azimuths and to proper inclinations to define downgoing and upgoing P and S modes.

Transformations of borehole receivers from in situ X, Y, Z orientations to a data space where receivers are oriented to emphasize P, radial-shear (SR), and transverse-shear (ST) events have been practiced in VSP technology for several decades (DiSiena, et al., 1981; Hardage, 2000). A graphical description of the transformation of receivers from X, Y, Z data space to P, SR, ST data space is shown on Figure 23 (d). In this approach, the downgoing P-wave first arrival is analyzed at each receiver station to determine azimuth rotation angle θ and inclination angle Φ such that when the 3C sensors are rotated by these angles, one sensor is aligned with the downgoing P-wave displacement vector oriented along raypath RS. A second sensor is then aligned with radial-S displacement vector SR, which is assumed to be orthogonal to RS and to be in vertical plane ROS. The third sensor is aligned with the transverse-S displacement vector ST, which is assumed to be orthogonal to plane ROS (Fig. 23 (d)).

This receiver orientation procedure applied to vertical-impact, shot-hole explosive, and vertical-vibrator sources positioned at selected source stations are illustrated on Figures 24, 25, and 26. The data windows used to determine geophone azimuth θ and inclination angle Φ (Fig. 23 (d)) to apply at each receiver station spanned 40 ms immediately following the onset of the interpreted P-wave direct arrival (top row of Figures 24, 25, and 26).

Because each of the three seismic sources (explosive, vertical vibrator, vertical impact) generated a different amount of seismic energy, a different plot gain was used to display data produced by each source. However, a constant plot gain is used within individual figures (Figures 24, 25, and 26) so that P, SR, and ST wave mode amplitudes produced by each specific source can be compared visually to judge their relative energy levels. Such comparisons confirm S modes radiating away from a vertical-force source often have amplitudes greater than their companion P mode (for example, Figs 24 and 25). Because data-display gains differ for each source, P and S amplitudes produced by one source should not be visually compared with P and S amplitudes produced by other sources.

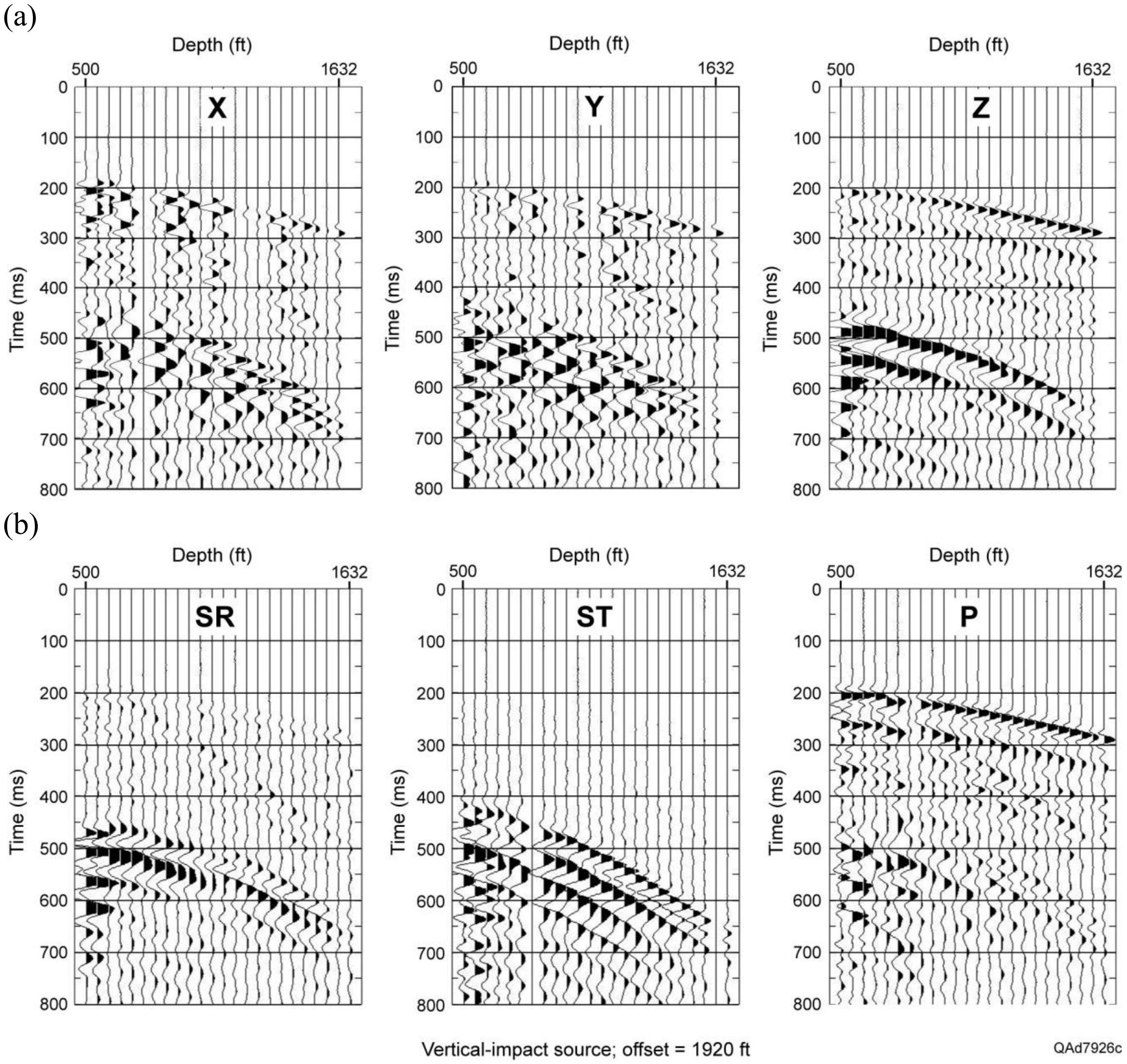

Vertical-impact source; offset = 1920 ft

QAd7926c

Figure 24: (a) Example of X, Y, Z data acquired with the test-site vertical sensor array when a vertical-impact source was positioned at source station 9, offset 1920 ft (585 m) from the array. (b) Data rotated to P, SR, and ST data space. All data panels are shown with a constant display gain.

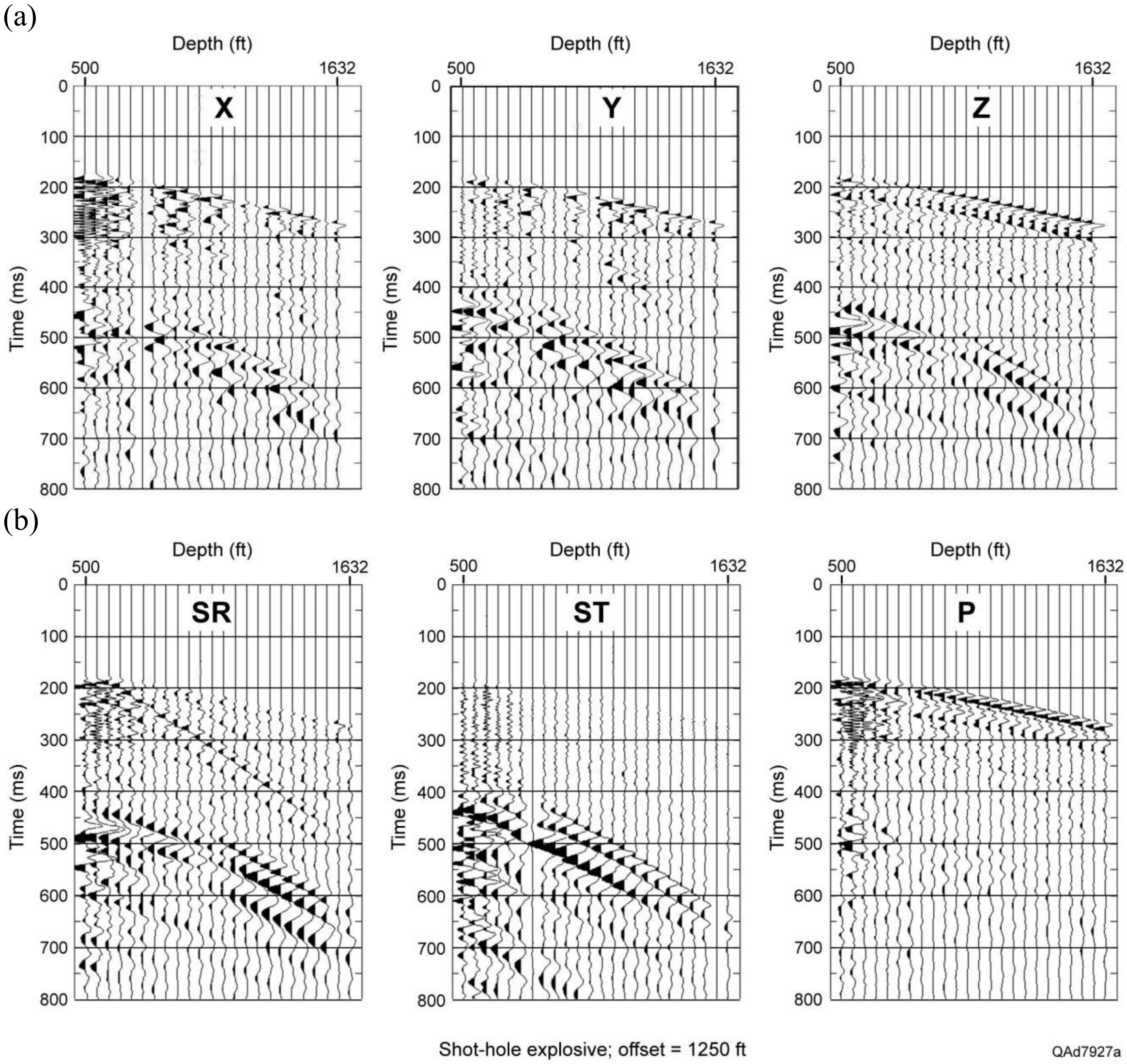

Figure 25: (a) Example of X, Y, Z data acquired with the test-site vertical sensor array when a shot-hole explosive source was positioned at source station 5, offset 1250 ft (381 m) from the array. (b) Data rotated to P, SR, and ST data space. All data panels are shown with a constant display gain.

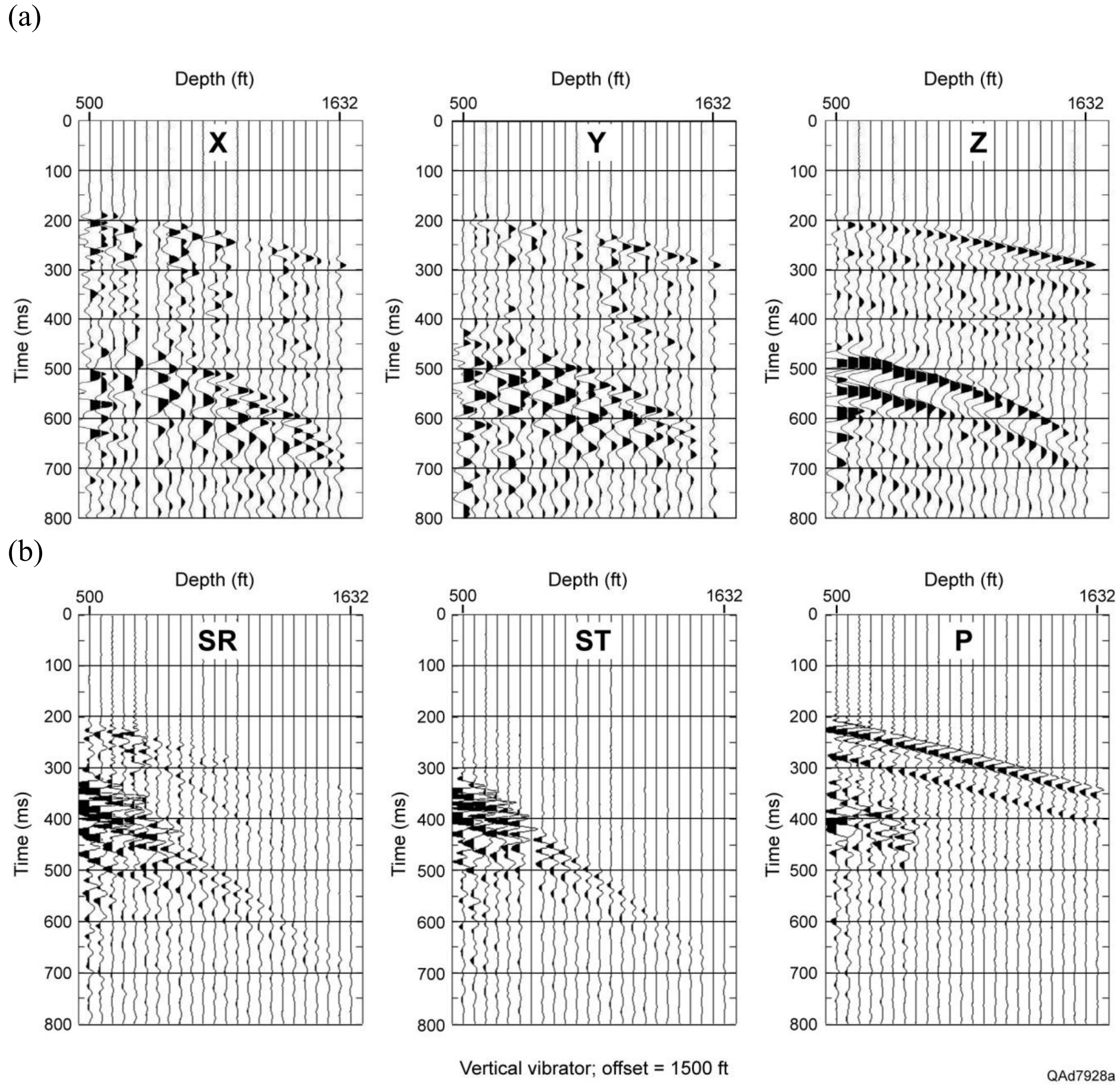

Figure 26: (a) Example of X, Y, Z data acquired with the test-site vertical sensor array when a vertical-vibrator source was positioned at source station 6, offset 1500 ft (457 m) from the array. (b) Data rotated to P, SR, and ST data space. All data panels are shown with a constant display gain.

Only data rotated to coordinate axes that isolate downgoing P, SR, and ST modes (the bottom rows of Figures 24, 25, and 26) were analyzed for energy content. Examination of these rotated data shows it is reasonably simple to define narrow windows that span the downgoing first arrivals of P, SR, and ST modes.

After defining first-arrival times at each receiver station for each wave mode produced by each source, wavelet amplitudes were analyzed in 40-ms windows starting at the interpreted first-break times of each arriving mode. Wavelets inside these data windows represent the downgoing illumination wavelets for each wave mode. Curves of root-mean-square (rms) wavelet amplitudes calculated in these first-arrival windows for data generated at various source stations are exhibited on Figures 27 through 29.

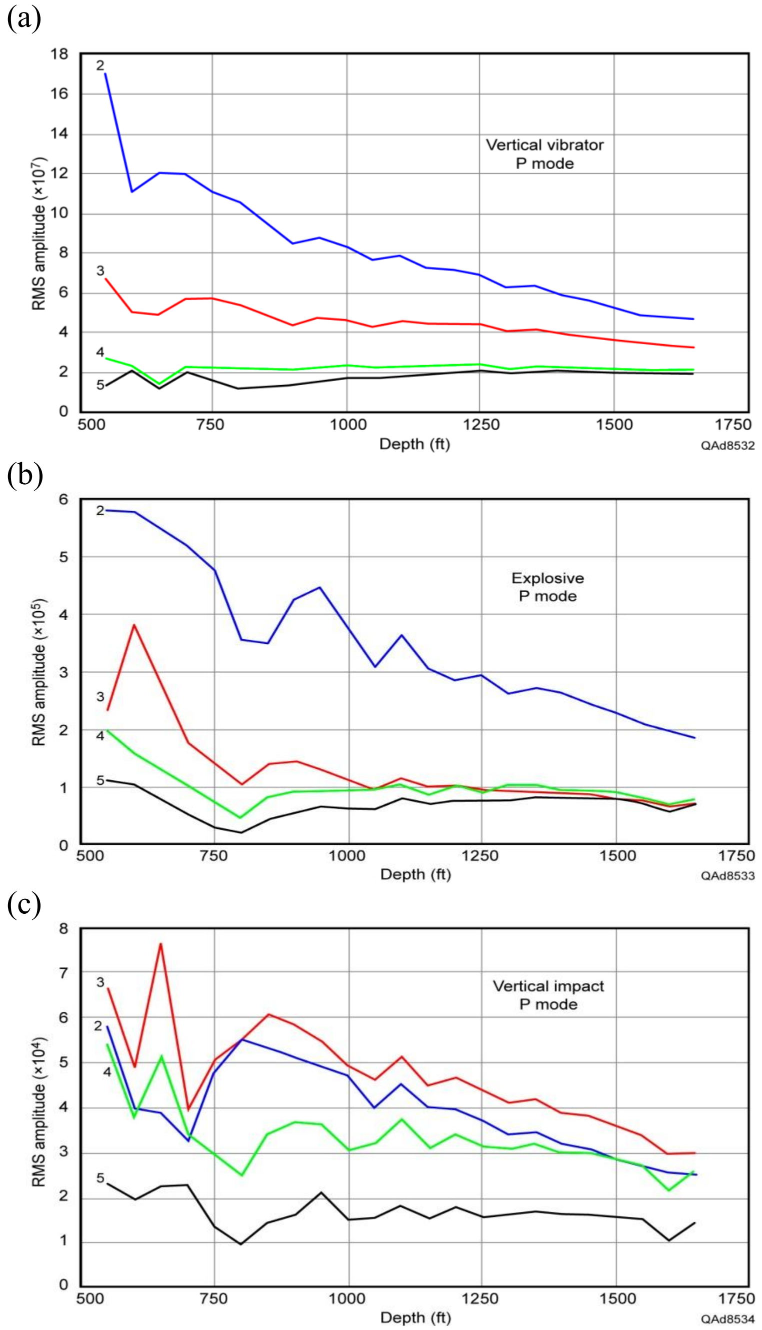

Figure 27: Root-mean-square (rms) amplitudes of downgoing P modes measured across the downhole vertical sensor array when sources are positioned at offset stations 2 through 5 (Fig. 4). Source station locations are indicated by the numbers on the curves. (a) Source is 60,000-lb (27,733-kg) vertical vibrator. (b) Source is 1 kg charge at depth of 6 m. (c) Source is an accelerated-weight impact delivering 22,276 ft-lb (30,202 joules) to the Earth.

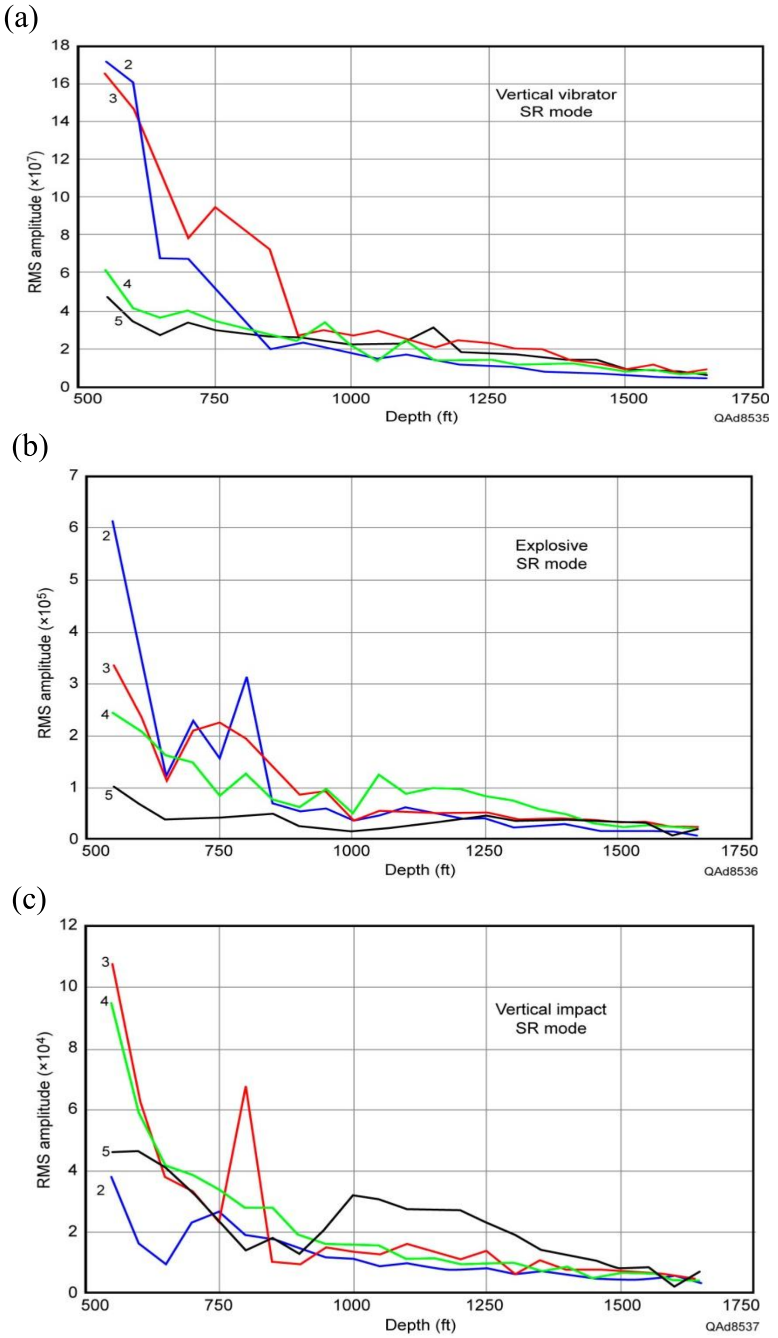

Figure 28: Root-mean-square (rms) amplitudes of downgoing SR modes measured across the downhole vertical sensor array when sources are positioned at offset stations 2 through 5 (Fig. 4). Source station positions are indicated by the numbers on the curves. (a) Source is 60,000-lb (27,733-kg) vertical vibrator. (b) Source is 1 kg charge at depth of 6 m. (c) Source is an accelerated-weight impact delivering 22,276 ft-lb (30,202 joules) to the Earth.

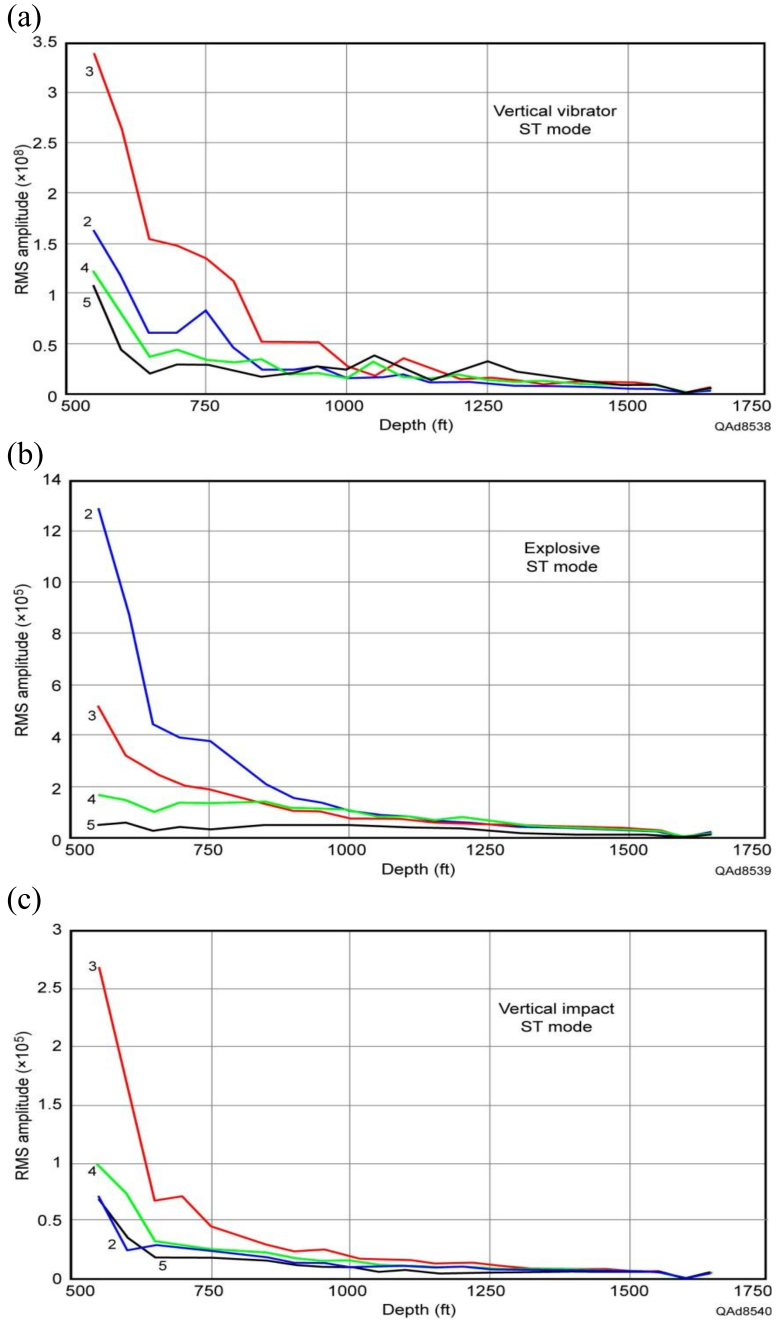

Figure 29: Root-mean-square (rms) amplitudes of downgoing ST modes measured across the downhole vertical sensor array when sources are positioned at offset stations 2 through 5 (Fig. 4). Source station positions are indicated by the number on the curves. (a) Source is 60,000-lb (27,733-kg) vertical vibrator. (b) Source is 1 kg charge at depth of 6 m. (c) Source is an accelerated-weight impact delivering 22,276 ft-lb (30,202 joules) to the Earth.

Important energy-related characteristics of the sources that were tested which should be kept in mind as data on Figures 24 through 29 are examined include the following specifications:

- Vertical vibrator: I/O AHV IV PLS 362 with a hold-down weight of 60,000 lb (27,733 kg). Linear 8-seconds sweep from 8 to 96 Hz.
- Explosive: One kilogram (2.2 lb) placed at a depth of 6 m (20 ft).
- Vertical impact: 33,000-lb vehicle with 1000-psi nitrogen-spring weight-acceleration system that delivers impact energy of 22,276 ft-lb (30,202 joules).

Figure 30: VSX^{TM} accelerated-weight impact source provided by Vecta Technology and United Services Alliance. This source can deliver a vertical impact to the Earth, or an inclined force vector can be applied in any azimuth direction and at any incident angle between 0 and 45 degrees without moving the vehicle. Vehicle weight is 33,000 lbs. Its compressed-nitrogen spring system delivers 22,276 ft-lb (30,202 joules) of energy to the Earth.

The vertical vibrator used in the test is shown in both photos of Figure 5. The accelerated-weight impact source from United Service Alliance, which is powered by a compressed-nitrogen spring, is shown as Figure 30. These photos, together with the source characteristics just listed, imply the vertical vibrator is quite powerful and should put more energy into the ground than does either the explosive shot or the vertical-impact source. Test data exhibited as Figures 27 through 29 confirm this expected energy advantage of the vibrator, with the amplitudes of vibrator-produced wave modes being approximately 1000 times larger than the amplitudes of corresponding modes produced by the weight-impact source and approximately 100 times stronger than amplitudes of modes produced by a 1-kg explosive detonated at a depth of 6 m.

Frequency attributes of the wave modes produced by the sources are illustrated as Figures 31 through 33. These analyses show the narrow data windows spanning the downgoing illumination wavelets where frequency spectra were calculated. These data windows differ slightly from those used to measure the wavelet amplitude curves exhibited as Figures 27 through 29. The data within each shaded analysis window are almost pure wave-mode signal and have a minimal amount of non-mode noise. For this reason, each frequency spectrum is assumed to be a reasonable indication of the signal-frequency content in each downgoing illumination wavelet. Amplitudes that are more than 20 dB below the peak of an amplitude spectrum are assumed to be too small to make significant contributions to images and are ignored. The position of the -20 dB cutoff line that indicates frequency bandwidth is labeled on each spectrum. The effective signal-frequency content of each wave mode is defined as the frequency spectrum extending above each 20 dB cutoff line. Defining effective signal frequency with a 20 dB cutoff is only an approximation, because this assumption results in some signal energy extending beyond the limits of the 8 to 96 Hz sweep of the vertical vibrator (Fig. 31).

Frequency and amplitude-strength characteristics of wave modes measured by the downhole vertical-receiver array are summarized on Table 1. On this table, the amplitude measures displayed on Figures 27 to 29 are listed as "order of magnitude" quantities rather than as specific numerical values. In contrast to the amplitude information that was analyzed at four source stations (stations 2, 3, 4, 5) on Figures 27 to 29, the frequency characteristics summarized on Table 1 relate to data generated only at source station 3. Key principles defined by these tabulated amplitude and frequency characteristics are:

1. The ST (transverse S) mode is the most energetic mode produced by each source, with ST amplitudes often tending to be almost 10 times larger than P and SR amplitudes (Table 1).
2. Explosive-source wave modes have amplitudes approximately 100 times smaller than the amplitudes of vertical-vibrator wave modes (Table. 1).
3. Vertical-impact wave modes have amplitudes approximately 1,000 times smaller than the amplitudes of vertical-vibrator wave modes (Table 1).
4. All three vertical-force sources (vibrator, explosive, impact) produce robust P and S wave modes, and each source would be effective for many P and S imaging objectives.
5. For the vertical vibrator, the signal frequencies of SR and ST wave modes are essentially the same as the signal frequencies of the P mode. The frequency

bandwidths of all vibrator wave modes are constrained by the 8–96 Hz sweep used to generate the data (Fig. 31).

6. For the explosive source, the signal frequency bandwidth of the P mode (approximately 5 to 200 Hz) is approximately twice the signal bandwidths of the SR and ST shear modes (Fig. 32). However, the 5 to 80 Hz (approximate) bandwidths of the SR and ST signal frequencies exceed the bandwidths of S modes that can be produced with horizontal vibrators, which tend to be about 4 to 50 Hz (or less).
7. The vertical-impact source (Fig. 33) produces a P mode that has a bandwidth (5 to 130 Hz) that is approximately twice that of the bandwidths of the SR mode (5 to 60 Hz) and the ST mode (5 to 70 Hz). However, P-mode frequencies greater than 50 Hz are significantly weaker in amplitude than frequency components less than 50 Hz (Fig. 33), causing all three modes (P, SR, ST) generated by the impact source to have approximately the same "effective" bandwidth. The ST shear mode has much of its energy concentrated in the frequency range between 30 and 50 Hz, which interestingly causes the amplitude of that mode to be 4 dB to 6 dB greater than the amplitudes of the P and SR modes.

Source	P mode		SR mode		ST mode	
	Amplitude	Freq (Hz)	Amplitude	Freq (Hz)	Amplitude	Freq (Hz)
Vertical vibrator	10^7	8–96	10^7	8–96	10^8	8–96
Explosive	10^5	5–200	10^5	5–80	10^5	5–80
Vertical impact	10^4	5–130	10^4	5–60	10^5	5–70

Table 1: Amplitude and frequency attributes of wave modes measured by downhole sensors. Amplitude properties taken from Figures 13 - 15 for source stations 2, 3, 4, and 5. Frequency properties taken from Figures 17 – 19 for source station 3 only.

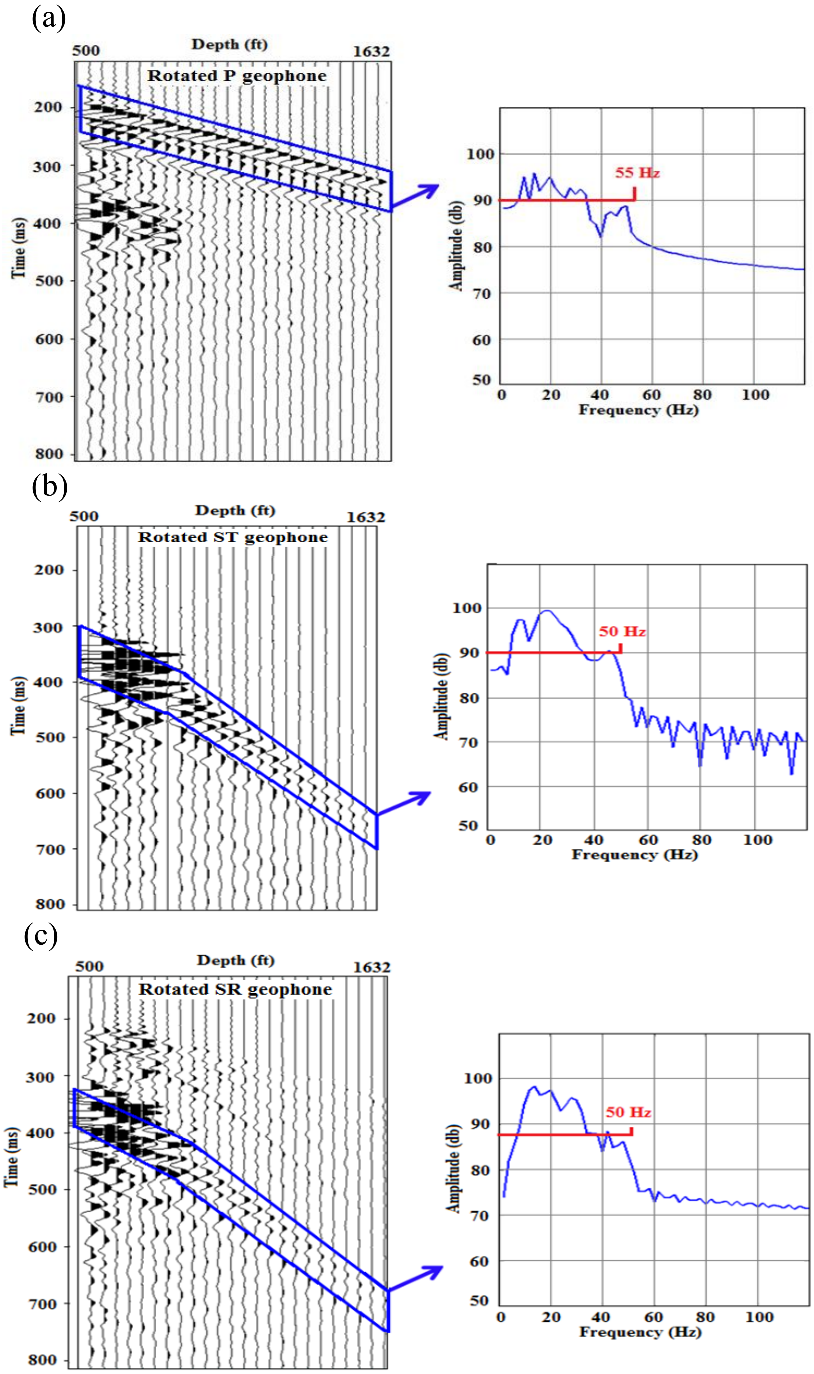

Figure 31: Frequency analysis of elastic wave modes produced by the 60,000-lb (27,733-kg) vertical vibrator at source station 3 and recorded by the downhole vertical array. (a) P mode. (b) ST mode. (c) SR mode. Amplitudes of the frequency spectra indicate relative strengths of the wave modes propagating away from the source station.

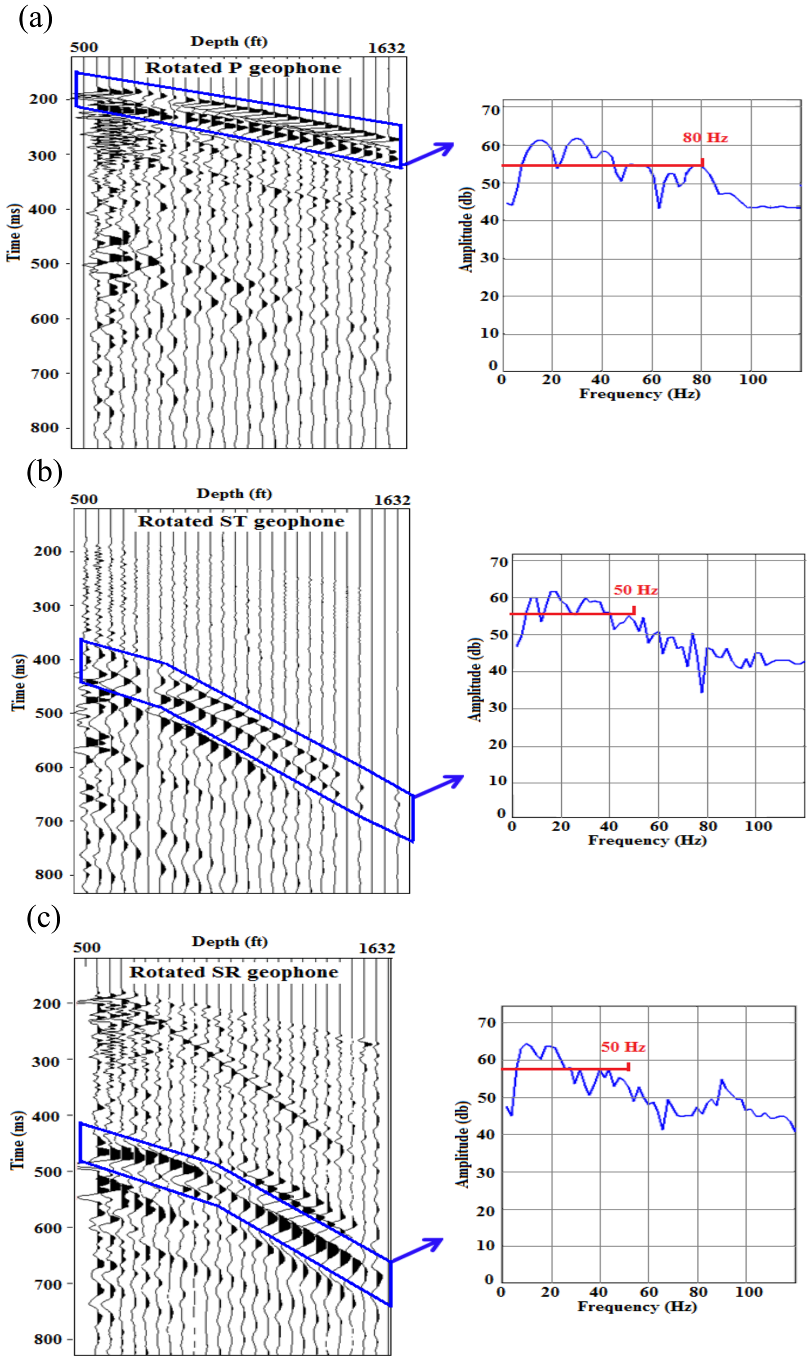

Figure 32: Frequency analysis of elastic wave modes produced by a 1-kg explosive shot at a depth of 6 m at source station 3 and recorded by the downhole vertical array. (a) P mode. (b) ST mode. (c) SR mode. Amplitudes of the frequency spectra indicate relative strengths of the wave modes propagating away from the source station.

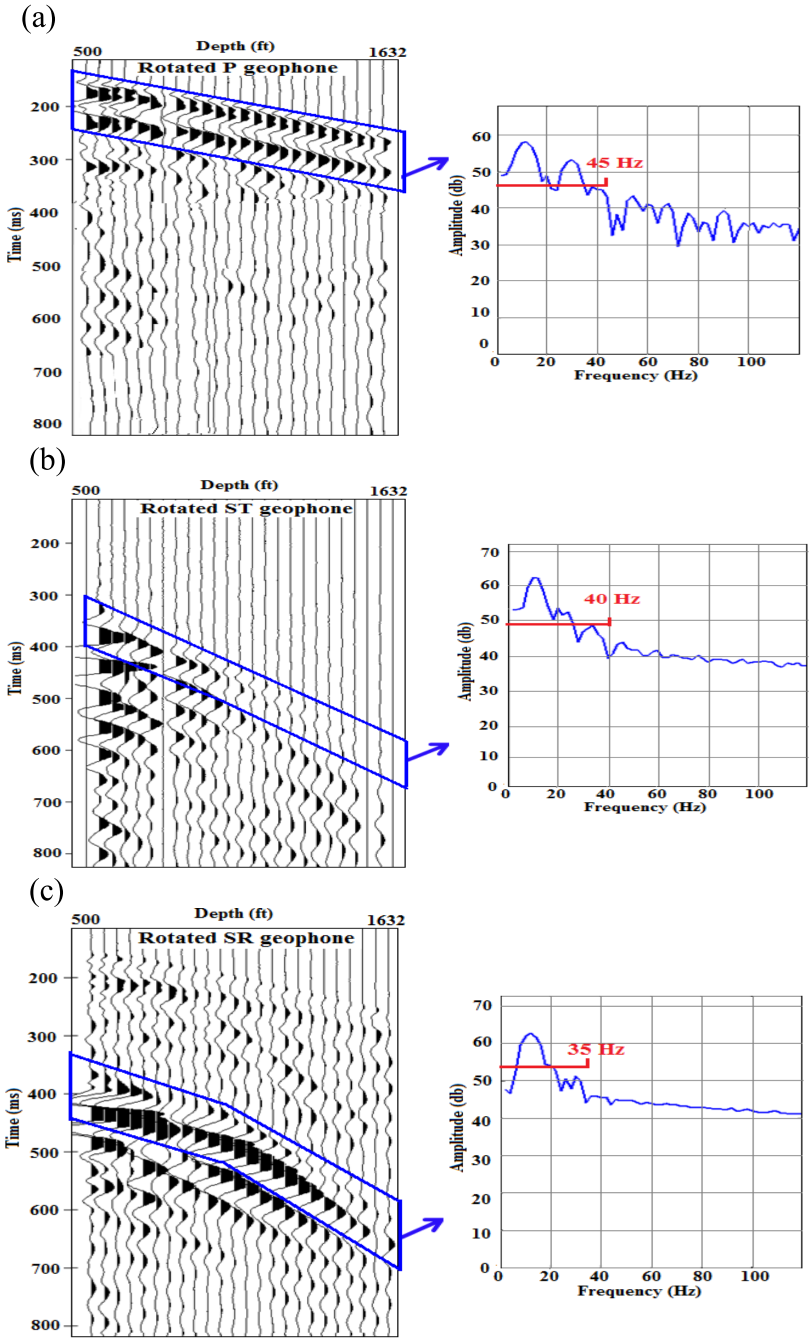

Figure 33: Frequency analysis of elastic wave modes produced by a vertical-impact source delivering 22,276 ft-lb (30,202 joules) of energy at source station 3 and recorded by the downhole vertical array. (a) P mode. (b) ST mode. (c) SR mode. Amplitudes of the frequency spectra indicate relative strengths of the wave modes propagating away from the source station.

Comparing Direct-S Modes Produced by Vertical and Horizontal Vibrators

Prudent field practice is to limit the highest frequency of a horizontal-vibrator sweep to approximately 50 Hz. Horizontal vibrators can sweep to frequencies higher than 50 Hz, but tend to have an unacceptable number of mechanical problems when forced to operate at high frequencies because of undue stress on hydraulic systems and structural supports. It is also challenging to maintain proper phase locking of horizontal vibrators at high frequencies. For these reasons, the sweep range of the horizontal vibrators used in these field tests was constrained to a bandwidth of 4 to 50 Hz, which is a common sweep range people use when deploying horizontal vibrators in exploration programs. In contrast, vertical vibrators can sweep to frequencies well above 100 Hz without undue mechanical problems or phase-locking issues. In these field experiments, the sweep range of the vertical vibrators was set at a modest interval of 8 to 96 Hz. When utilizing vertical and horizontal vibrators in data-acquisition projects, it is common practice to set sweep parameters so that the start and stop frequencies and frequency bandwidths used for vertical vibrators are a factor of 2 greater than the equivalent sweep parameters used for horizontal vibrators. I followed this common field practice in our field tests.

Quantifications of the differences in frequency content of direct-S modes produced by vertical-force and horizontal-force vibrators are illustrated on Figures 34 and 35.

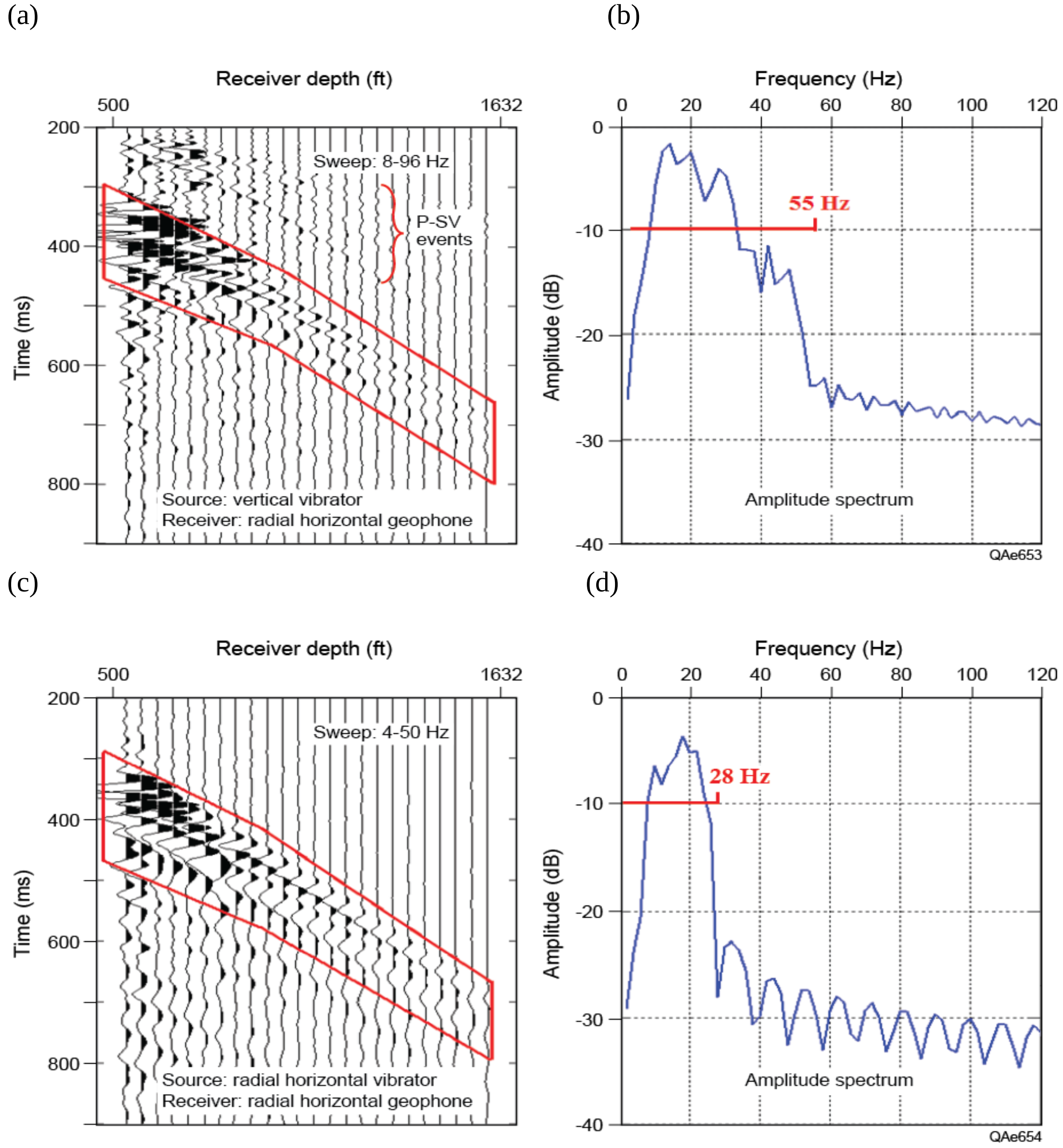

Figure 34: Comparison of radial-S data generated by (a) a vertical vibrator and (c) an inline horizontal vibrator positioned at the same source station. Data were recorded by the same vertical array without altering receiver orientations or couplings. The amplitude spectrum of these direct-S wavefields are shown as (b) and (d). Data recorded at receiver stations above 800 ft (243.8 m) are distorted by critical refractions and interbed reverberations.

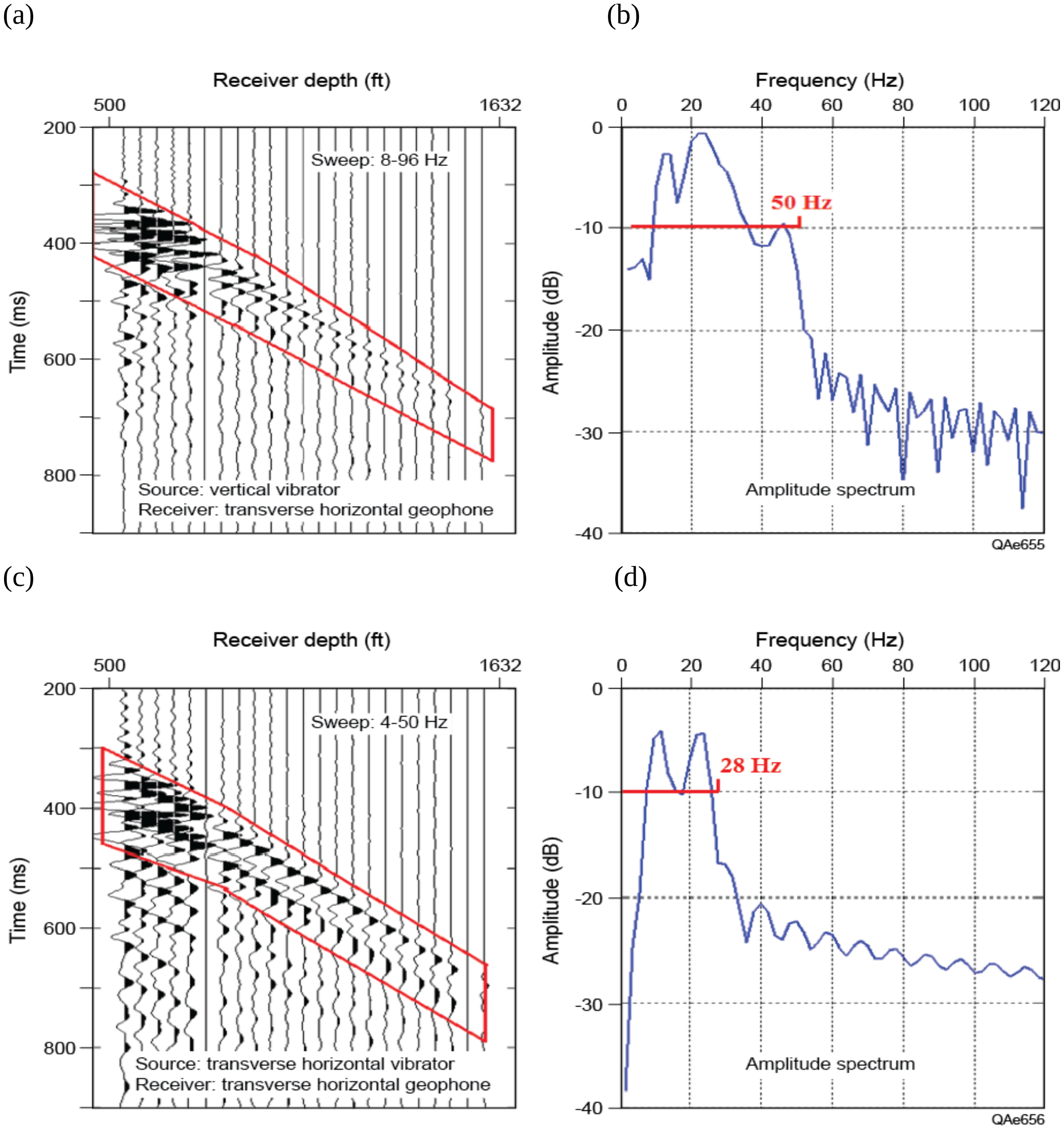

Figure 35: Comparison of transverse-S data generated by (a) a vertical vibrator and (c) a crossline horizontal vibrator positioned at the same surface station. Data were recorded by the same vertical array without altering receiver orientations or couplings. The amplitude spectrum of each direct-S illuminating wavelet is shown as (b) and (d). Data recorded at receiver stations above 800 ft (243.8 m) are distorted by critical refractions and interbed reverberations.

The radial component of the direct-S mode generated by a vertical vibrator is compared with the radial component of the direct-S mode produced by a horizontal vibrator on Figure 34; the transverse components of direct-S modes radiating from these two vibratory sources are compared on Figure 35. Some important wave physics principles are exhibited by these data:

1. For both vertical and horizontal vibrators, the highest frequency in the propagating direct-S wavelet observed at our test-site was 50 percent to 55 percent of the highest frequency used in the vibrator sweep. For example, a 50-Hz upper sweep limit for the horizontal vibrator resulted in an upper frequency of approximately 28 Hz in the downgoing direct-S wavelet for that source, and a 96-Hz upper sweep limit for the vertical vibrator created an upper frequency of 50 to 55 Hz in the direct-S illuminating wavelet for that vertical-force source.
2. In terms of octaves, the bandwidths of direct-S wavelets propagating from both horizontal and vertical vibrators are approximately the same, with wavelets from each source spanning slightly less than three octaves (4 to 28 Hz for the horizontal vibrator, and 8 to 55 Hz for the vertical vibrator).
3. Because the bandwidth of the direct-S wavelet generated by a vertical vibrator spans higher frequencies than does the bandwidth of the direct-S wavelet produced by a horizontal vibrator, a vertical vibrator should provide better S-wave resolution of geologic targets than can a horizontal vibrator.

Item 3 of this list is particularly important and may result in wider use of vertical-force-source direct-S wavefields in future seismic evaluations of prospect areas.

Radiation patterns of a shear-wave generated by a vertical vibrator and horizontal vibrators were previously analyzed and compared by several authors (Robertson and Corrigan, 1983; Dankbaar, 1983; Easley 1992; Sun and Jones, 1993). I illustrate the similarity between direct-S modes produced by horizontal vibrators and vertical vibrators by overlaying the downgoing direct-S modes produced by each source so the arrival times and wavelet attributes of the modes can be more easily compared. These wavefield comparisons are displayed on Figure 36. The direct-S radial wavefield propagating from the horizontal vibrator (Fig. 36 (a)) has a polarity opposite to that of the radial direct-S mode produced by the vertical vibrator because the horizontal vibrator was oriented North, causing the first motion of its baseplate (the direction of its radial-S polarity) to be away from the receiver well. In contrast, the radial-S vector produced by the vertical vibrator was oriented toward the receiver well. Rather than reverse the polarity of one of the wavefields displayed on Figure 36 (a), I left them as shown because this dual-color display of opposite-polarity data helps some people better judge the equivalence of the two modes for undistrorted data recorded by receivers below 800 ft (243.8 m). The polarities of the transverse component of the vertical-vibrator and horizontal-vibrator direct-S wavefields are identical (Fig. 36 (b)) and are essentially exact copies of each other when data above 800 ft (243.8 m) are ignored.

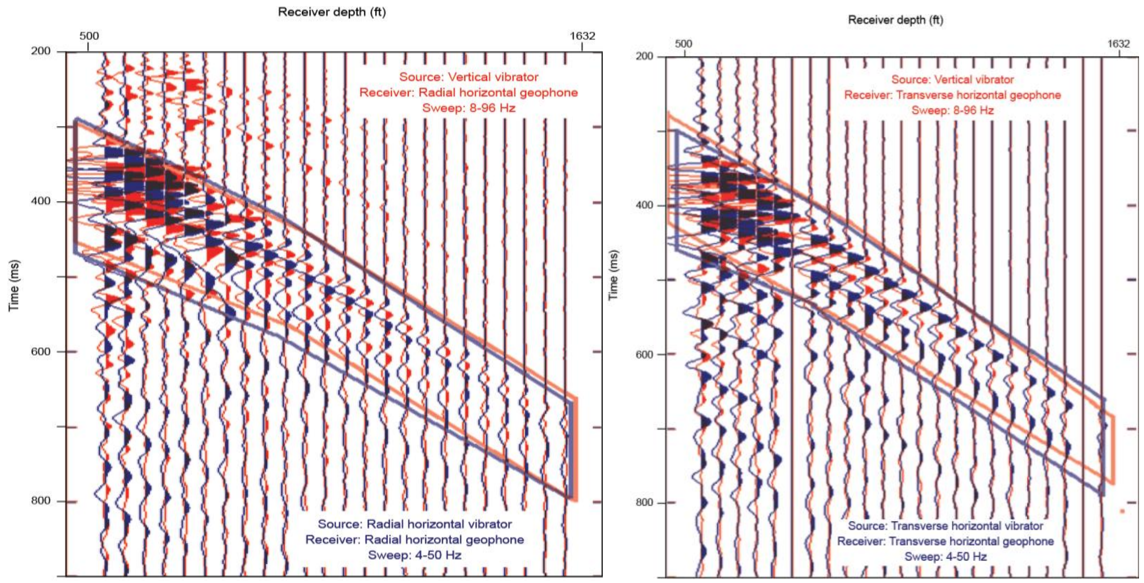

(a) (b)

Figure 36: (a) Radial direct-S wavefield produced by a vertical vibrator (red traces) overlain by the radial direct-S wavefield produced by a radial horizontal vibrator (blue traces). (b) Transverse direct-S wavefield produced by a vertical vibrator (red traces) overlain by the transverse direct-S wavefield produced by a transverse horizontal vibrator (blue traces). Vibrators were positioned at the same surface source station. Data were recorded by the same vertical array without altering receiver orientations or couplings. Data recorded at receiver stations above 800 ft (243.8 m) are distorted by critical refractions and interbed reverberations.

The comments above focus only on data within the outlined windows on each display, which define the downgoing direct-S modes produced by each vibrator. When data character outside these direct-S data windows are considered, there are several downgoing P-to-S converted events in the vertical vibrator data that are absent in the horizontal-vibrator data. The most obvious downgoing converted-SV mode is the event that originates near a depth of 500 ft (152 m) that precedes the direct-S data window (Fig.

36 (a)). These downgoing converted-S events contribute noise in radial-S data produced by a vertical vibrator that does not have to be dealt with when a horizontal vibrator is used. No downgoing converted modes exist in transverse-S data produced by a vertical vibrator (Fig. 36 (b)). Visual examination of both of these dual-wavefield displays causes me to conclude that, except for the different frequency bandwidths documented on Figures 34 and 35, the downgoing direct-S wavefields produced by a vertical vibrator are reasonably equivalent to the downgoing direct-S modes produced by a horizontal vibrator.

Azimuthal Anisotropy

I emphasize the P and SV radiation patterns on Figure 22 (b) apply for wave propagation in a homogeneous elastic half space. When azimuthal anisotropy exists in shallow Earth layers, wave propagation needs to be described in terms of natural coordinate axes. Many researchers have stated that any S-wave response observed in transverse receiver components is most likely due to S-wave splitting in an azimuthally anisotropic medium, and results from the interference of fast and slow S-waves (Crampin and Kirkwood 1981; Alford 1986; Banik, 1987; Winterstein and Meadows 1991; Winterstein and Meadows 1991a; Crampin 1991; Thomsen 1988; Simmons and Backus 2001; Thomsen 2002).

Because shear wave modes are sensitive to anisotropy, they split into fast and slow modes with orthogonal polarizations, and therefore shear wave velocity anisotropy is larger than compressional wave anisotropy (Thomsen et al., 1999; Bale et al., 2009; Tsvankin and Grechka, 2011). To rule out splitting, seismic experiment should be done in multiple azimuths centered around the well. This study would sample many propagation azimuths and show the full-azimuth response of shear-waves on the radial and transverse receiver components with respect to the source. As shown by Lewallen (2008), detailed multi-azimuth survey would allow me to correlate shear wave birefringence to possible anisotropy caused by the stress field. However, the 2D data collected at the Devine Test Site do not allow multi-azimuth analysis.

Although my analysis does not rely on multi-azimuth experiment, others have analyzed VSP data acquired at the Devine Test Site where my data originate and concluded a weak S-wave anisotropy is present in the local rock layering. Raikes (1991) used an inclined-impact source to produce horizontal-force source VSP data and concluded S-wave anisotropy was less than 3-percent across the property. She found a time delay of 12 ms between fast and slow modes at geophone depths of 900 m, and estimated cracks were oriented at an azimuth of 10 degrees from North. The same data were later studied by Li et al. (1998) who confirmed S-wave anisotropy was less than 3-percent, found fast and slow modes travel times differed by 10 ms at deep (900 m) receiver stations, and estimated one natural coordinate axis was oriented 60 degrees from North.

The P and SV radiation patterns shown by Figure 22 (b) are replications of analyses published by Miller and Pursey (1954) and White (1983). Both P and SV modes are generated directly at the point where vertical force vector F contacts the Earth surface. The relative strengths of P and SV modes propagating at any take-off angle from the source station are indicated by the radial distances from the origin point to the outer edges of the P and SV radiation patterns.

Edelmann (1981) analyzed S displacement vectors associated with raypaths slanted at arbitrary takeoff angles in the SV lobes of Figure 22 (b) to conclude that a vertical vibrator should create SH illumination in addition to SV illumination. Fertig and Krajewski (1989) used the same radiation diagram in their study and made the important declaration that not only does a vertical vibrator produce direct-S modes, but so does a shot-hole explosive and an air gun in a pit. Lynn and McCardle (1990) also state direct-S waves are produced by air guns operating in rectangular pits and show direct-S modes labeled as SV and SH produced by vertical vibrators.

The radiation of direct-S modes from shot-hole explosives has been documented by Wright and Carpenter (1962) following investigations to determine how to detect tests of buried nuclear devices. They made plaster casts of shot-hole cavities that showed asymmetric deformation generated by explosive detonations. They state that "on no occasion has an underground firing failed to give rise to significant transverse seismic waves". Fertig (1984) also concludes a shot-hole explosive generates direct-S modes but associates the generation of these modes to P-to-SV conversion at the Earth-air interface above a shot. Zhou et al. (2005) show VSP data in which they propose azimuthal anisotropy local to a source station as being the reason they observe both direct SH and qSV modes propagating away from vertical-vibrator stations. Yang et al. (2007) present excellent data examples of direct-S modes produced by both vertical vibrators and shot-hole explosives and refer to pure-S (SH) modes radiating from these vertical-force sources in addition to SV modes.

The important distinction between my study and all of these that are cited is that none of the above studies used a combination of vertical-force and horizontal-force sources in the same test so direct-S modes produced by both sources types could be directly compared. My approach relies on the deployment of vertical vibrators and horizontal vibrators at the same surface coordinates and on recording downgoing direct-S modes generated by these sources with the same vertical receiver array. I do not delve into the effects of azimuthal anisotropy on P and SV radiation in my data analyses. I describe only a straightforward field experiment in which a vertical vibrator and a horizontal vibrator were positioned at the same source station and the direct-S wavefields produced by each vibrator were recorded with a vertical array of downhole 3C geophones.

I ignore the issue of whether the downgoing direct-S wavefields do or do not propagate in an azimuthally anisotropic medium and simply compare the character of the direct-S wavefields recorded by radial geophones and transverse geophones for each type of vibrator source. The end result is that I observe a strong similarity between direct-S modes produced by vertical and horizontal vibrators at the Devine Test Site (Figs. 34-36).

Conclusions

One of the secondary goals of this PhD study was to analyze different source and recording systems and document the differences and similarities among data acquired with different recording systems. Data recorded by velocity and acceleration sensors at the Devine Test Site have been compared. Amplitude, frequency, and phase characteristics of various recording units were evaluated, and appropriate spectra illustrated coherency and frequency characteristics among sensors. I focused on geophone and accelerometer data recorded by Sercel E-Unite, Sercel 428XL, and Sigma systems, and found data recorded by these systems were similar. Accelerometer data had different amplitude and phase characteristics over certain frequencies, especially low-frequencies, and for some high-frequencies.

At stations where both geophone and accelerometer sensors recorded the same events, accelerometer records contained a wider frequency spectra as well as larger amplitude values over these frequencies. In conventional seismic surveys using geophones, the output of the system is the average of all phones planted in an array; whereas, the output of present accelerometer systems represents individual sensor results. Therefore, issues regarding individual geophones in an array cannot be detected from seismic data. However, any problem related to the planting of an accelerometer unit can be detected in the raw data. Accelerometer data provide traces recorded at high-precision over high frequencies, and such data will be preferable for surveys requiring high-frequencies. I can state that velocity, displacement, and acceleration independently preserve approximately the same frequencies, and each type of sensor data presents certain advantages because of its distinct frequency and amplitude characteristics. However, accelerometers provide better low-frequency data (frequencies < 8 Hz) than do geophones. This research finding can be important when it is important to acquire optimal-quality S-wave data because S-modes tend to be lower frequency than P-wave data. When S waves are critical to evaluating a shale-gas target, serious consideration should be given to using accelerometers. Essential benefit of MEMS accelerometers is their ability to record full wavefield with providing better vector fidelity and more accurate amplitude because their accurate and stable calibration. This is important for AVO and inversion studies.

Data acquired at the Devine Test Site demonstrated that planting 3-component MEMS sensors needed attention to get proper coupling, but ensuring exact verticality was not mandatory. This is sensor flexibility result because of a unique feature of MEMS accelerometers; this being its ability to measure the continuous effect of the gravity vector. As a result, any one of the three MEMS sensors can be used as the vertical sensor of a 3-component XYZ sensor configuration.

Comparing FK spectra leads to the conclusion that data acquired with the 428 cable-based systems have wider frequency spectra than data acquired with either cable-free system. This difference is particularly obvious for P-wave spectra where 428-system frequencies extend above 100 Hz, but Sigma-system and EUnite-system frequencies extend to only 100 Hz (or less).

One focus of my PhD research was to demonstrate that valuable S-wave modes are produced directly at the point where a vertical-force source applies its force vector to the Earth, which allows S-wave modes other than P-SV data to be utilized in shale-gas studies. The recognition and use of these direct-S modes introduce new seismic imaging options into shale-gas studies and provide expanded suites of seismic attributes that can be used to infer rock and fluid properties across shale-gas prospects.

The analysis of VSP data acquired at the Devine Test Site confirmed that all elastic wave modes (compressional, radial and transverse shear) are generated by vertical-force sources directly at the source station. Different elastic wave-modes are clearly identified from VSP seismic data after the seismic energy was transformed to principal coordinates by vector rotation of data to the directions that maximized P, radial, and transverse S-wave particle displacements. The implication of this principle is significant because, when proven to be true, it is no longer necessary to use only horizontal-force sources (either horizontal vibrators or inclined-impact sources) to generate S-wave modes directly at a source station.

As a conclusion, the work presented in this chapter demonstrated that acquisition cost of multicomponent seismic data can be reduced by using direct shear waves generated by vertical-force sources and multiple shear-wave attributes can be created without relying on converted-shear data only. With proper job flows, processing of shear wave data can be simplified because direct shear wave-data processing is based on CMP concepts which are easier to implement than CCP concepts that have to be used for converted-shear data processing.

CHAPTER-3: TECTONIC AND STRATIGRAPHIC CHARACTERISTICS OF MARCELLUS SHALE AND STRUCTURAL HISTORY OF APPALACHIAN BASIN

Introduction

In many parts of the world, as in the Appalachian Basin area of Pennsylvania, fractured shale reservoirs are effective production reservoirs despite their low permeability and lack of trapping structures associated with conventional reservoirs. Research has demonstrated three joint sets are present in the Marcellus formation (Engelder et al., 1980; Engelder, 2009). Some sets are aligned parallel to the direction of maximum horizontal stress direction. Thus stress fields explain some joint development within the formation and their relationship to the tectonic history of the basin. If natural fractures are detected successfully, permeability is significantly enhanced when these natural fractures are connected to form a network. Detailed fracture characterization within shale reservoirs improves hydrocarbon recovery and enables more effective reservoir management. Determination of stress field directions and estimation of fracture parameters within the Marcellus Shale and its surrounding rock units can be done using shear wave anisotropy data and elastic wavefield stratigraphy technology.

This chapter discusses the characteristics of fracture structures in shale formations, assessment of hydraulic fracturing treatment based on the relationships between tectonic history, and in-situ stress variations and lithological characteristics of shale formations located in the Appalachian Basin. Many studies have been done to estimate stress field orientations, magnitudes, and their relationships with fractures. This chapter uses well log data and direct engineering measurements to define links between the deformation of Marcellus Shale and the structural nature and geomechanical properties of shale formations.

Geologic and Petrophysical Characteristics of Shale Reservoirs

The slow deposition of fine-grained particles in low energy environments, clay-rich mineral structures laminations formed as thin layer sequences, complicated fracture structures, and small pore spaces within the reservoir interval combine to reduce the permeability of shale formations. Technological advances such as horizontal drilling and hydraulic fracturing now make it possible to develop unconventional shale reservoirs even though limited permeability makes it difficult to transmit hydrocarbons to a wellbore. Significant amounts of hydrocarbon are now produced from shale reservoirs.

Unique depositional, structural, and geologic properties of shale formations created a strong anisotropy in which laminated clay sheets with rich organic material content and fractures oriented in multiple directions occur. Knowing patterns of stress over geologic time provides valuable information regarding tectonic and physical processes that reveal relationships between material properties of shale and stress distribution. Identification of stress distribution within a shale reservoir is crucial for pore pressure estimation; however, formation pore pressures in shale are not known with certainty because of the low permeability and extremely small pore spaces. Stress field distribution and pore-pressure information are vital in the petroleum industry because such information can lead to identification of formations yielding hydrocarbons.

Several researchers (Evans et al., 1989, Plumb et al., 1991; Engelder et al., 1980) have demonstrated the properties of formations located across the Appalachian Basin based on direct engineering measurements (open hole stress measurements), geophysical log responses, and structural analysis from core and outcrop analysis. These studies explain why significant joint development is present in the basin and how these joint structures are related to stress field distribution within the formations and their tectonic history. These research findings also explain the occurrence of other major structures such as salt detachment, thrust faults, and the distribution of limestone and sandstone units.

Several studies have been done to estimate stress variation from borehole log data (Evans et al. 1989; Plumb et al., 1991). These studies describe the orientation of maximum stress directions and magnitudes and variations of such stress-related attributes among adjacent rock formations. All studies had one common goal which was to relate stress variation to the tectonic and stratigraphic history of rock formations across the Appalachian Basin.

Only recently have seismic surveys been done across the Appalachian Basin to study geophysical attributes of the Marcellus Shale. Seismic data are essential in shale plays because of its importance in imaging permeable zones in formations. Seismic studies can provide detailed mapping of the quality of hydrocarbon-bearing shale reservoirs located across the Appalachian Basin. Seismic studies can also provide information about in-situ stress conditions of fault structures and nearby fracture networks. As a result, it is important to utilize seismic and other geophysical methods to attain useful information about the structure and lithological variation of Marcellus Shale reservoirs.

Uniqueness of the Marcellus Shale and Statement of Problem

Unlike other shale formations, the Marcellus Shale contains not a set of single natural fractures but two (and sometimes three) joint sets oriented in different azimuths. These joint patterns are cumulative and carry information related to tectonic events that occurred in the basin in the past. The relationship between joint development and past stress regimes is not complete (Engelder et al., 1980; Engelder, 2009), and numerous companies and researchers are engaged in ongoing studies.

Observations of Marcellus outcrops may not reflect exact conditions present in deep reservoirs because outcrops exposed to surface conditions no longer provide same reservoir conditions such as high temperatures, high pressures caused by loading from the overburden, and stress produced by compaction of surrounding formations. If one can define the orientations of joints developed within the reservoir rock, it may be possible to define the sequence of stress fields that created joint sets across a study area and their relationships to each other.

Precise stress-magnitude measurements are rarely obtained in shale formations, and relationships between rock physical properties and stress fields can be observed only if the contrasts between properties are large. Thus separation between shale units within the same shale formation based on correlations between geophysical log parameters and estimated or measured stress values is low. Previous studies (Plumb et al., 1991; Engelder et al., 1980) have shown that shale formations do not always have low-strength in a near-lithostatic state of stress and may sustain significantly high shear stress. Therefore, hydraulic fracturing is not always successful in shale formations if the contemporary stress field is affected by active tectonic compression.

Despite the fact that relationships between stress field distribution and the development of joint patterns in rock formations have been attempted by in-situ strain measurements using relaxation methods, the poorly understood mechanism of the method has hindered the success of these studies. Even though tests provided direct measurements, the recovery of elastic strains imposed by far-field stresses, multiple strain elements influence on relaxation (such as residual elastic strains), thermal strains induced by near temperature gradients, and strain induced by chemical processes occurring within the rock all combined to cause complexity (Engelder et al., 1980). As a result of their study, Engelder, (1980) could not find any indication of the physics that governs the pattern of joint sets and their development across study area. Also because of the complexity generated by multiple joint sets, in which there is no certain relation among all individual sets, joint development did not explain the relationship between joints, subsurface stress distributions, and the influence of stress on joint orientation.

Some researchers have proposed that the relationship between rock properties and stress field variations within the some formations may depend on bed-to-bed stress differences (Evans et al., 1989; Engelder et al., 2009). Therefore stress field–to-lithology correlation is not straightforward in shale formations. The observed low stress values in shale formations do not agree with gravitational loading used in Earth stress models. Therefore simple gravitational loading models are not able to predict bed-to-bed stress variations as expected (Plumb et al, 1991).

Because of horizontal bedding in the Marcellus, it is difficult to recognize near-horizontal fractures, and it is impossible to image such fractures by televiewer logs alone (Evans et al. 1989). All direct engineering measurements performed in both vertical and horizontal wells are spatially limited. Thus such data will not reflect spatial variations in lithology and stress fields as well as will seismic data.

Geologic Setting and Tectonic and Depositional Background

The Marcellus Shale is one of the eight major shale formations located within the Appalachian Basin that contain organic-rich black shale. Engelder et al., (1980) asserted that major shale formations in the Appalachian basin were deposited in deeper sections of the basin during the collision of two boundary plates (Figure 37). This plate collision is also responsible for the orogeny that created the Appalachian Mountains as well as many thrust faults across the area. Some authors (Evans et al., 1989; Engelder et al., 1980) state deposition and other orogenic events caused rapid burial of organic material in the Marcellus Shale. The high amount of natural gas trapped in the Marcellus Shale is attributed to this rapid sedimentation and its related circumstances.

The Marcellus Shale is a black shale formation across a wide area of the Appalachian Basin that was formed at, or near, the bottom of the Devonian Hamilton stratigraphic group. The total organic carbon fraction in the lower Hamilton group, whose thickness is as much as 500 ft, is greater than 10-percent. Almost all gas shales deposited during Devonian and Mississippian time have joint sets which differ in orientation and density compared to other types of shale and siltstone formations in the Appalachian Basin (Boyce et al., 2010; Sageman et al., 2003; Engelder et al, 2009).

Interbedded shales, massive fine-grained sandstones formed as 2-m thick beds, and siltstones are major components of Upper Devonian rock formations located in the Appalachian Basin (Engelder et al., 1980). Figure 37 shows the stratigraphic column of Devonian rock formations and other major groups including the Marcellus Shale. According to the study by Engelder et al. (1980), all of the formations contain joints that may be present in as many as three different individual sets in some units; whereas, these may be only one nonsystematic joint set in other units. According to past researchers (Evans et al., 1989; Engelder et al., 1980; Plumb et al., 1991) joints formed in shale units tend to be more irregularly spaced than joints in sandstone and siltsone units. Researchers have demonstrated that shale joints terminate at shale-siltsone boundaries and cut across folds at high angles (Evans et. al., 1989). Some joints have planar surfaces, but some have non-planar. Furthermore, some joints can be aligned vertically or horizontally relative to bedding.

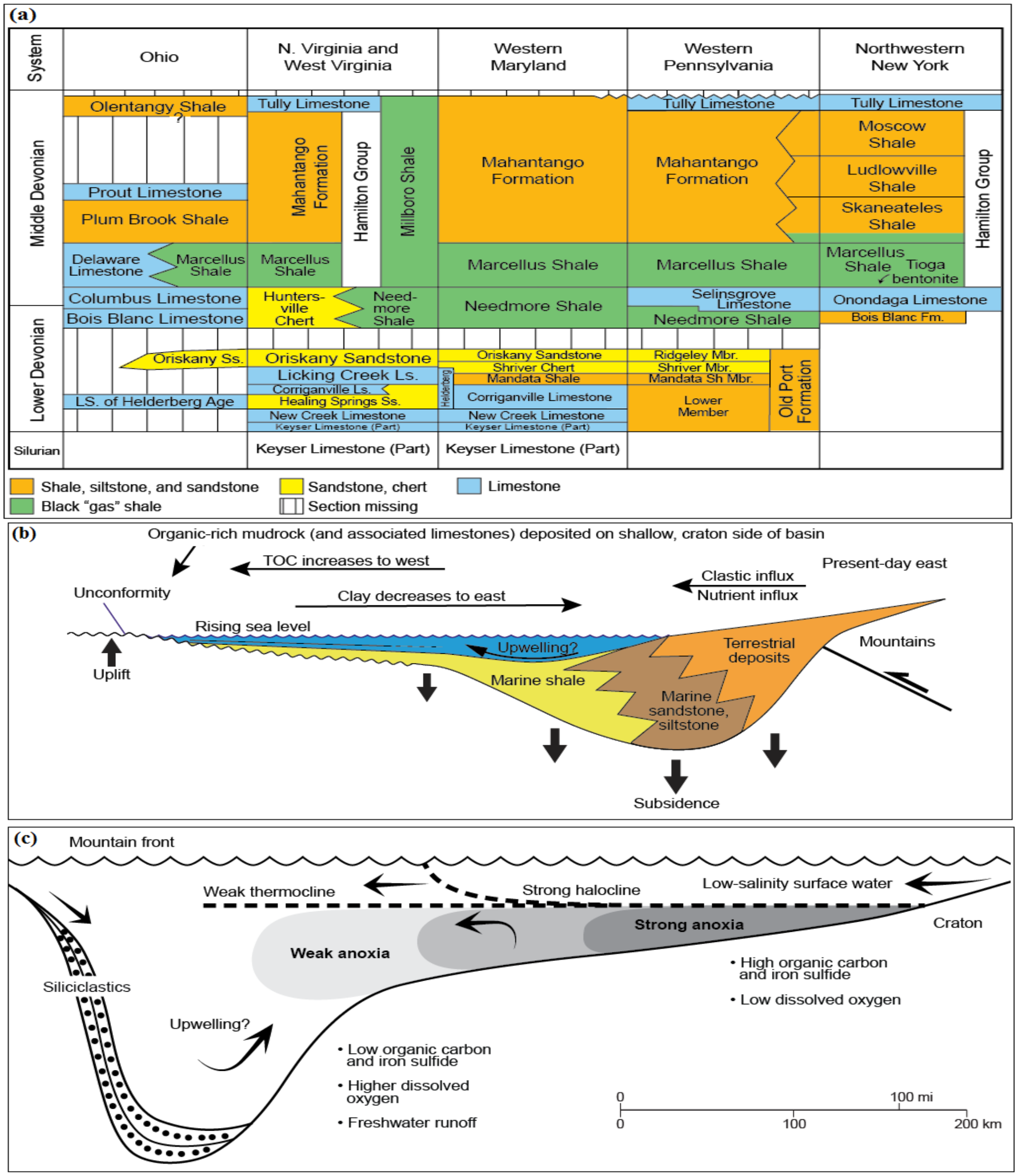

Figure 37: (a) Stratigraphy of the Lower and Middle Devonian of the Appalachian Basin, with emphasis on the Hamilton Group (Modified from USGS, 2006.), (b) shallow water depositional model for Devonian organic-rich black shales, (c) Hydrographic details of development of a shallow sediment depositional environment Modified from Smith and Leone (2010).

There are three locations where thermogenically sourced natural gas reside in the Marcellus Shale formation: (1) within naturally occurring fractures (joint sets), (2) adsorbed on mineral structure, and (3) within the small pore spaces of the shales. Overall, the Marcellus near my study area in Bradford County, PA (Figure 38a) has limited permeability because of the compacted, sheet-like, clay laminations seen in outcrop (Figure 38b, 38c, and 38d).

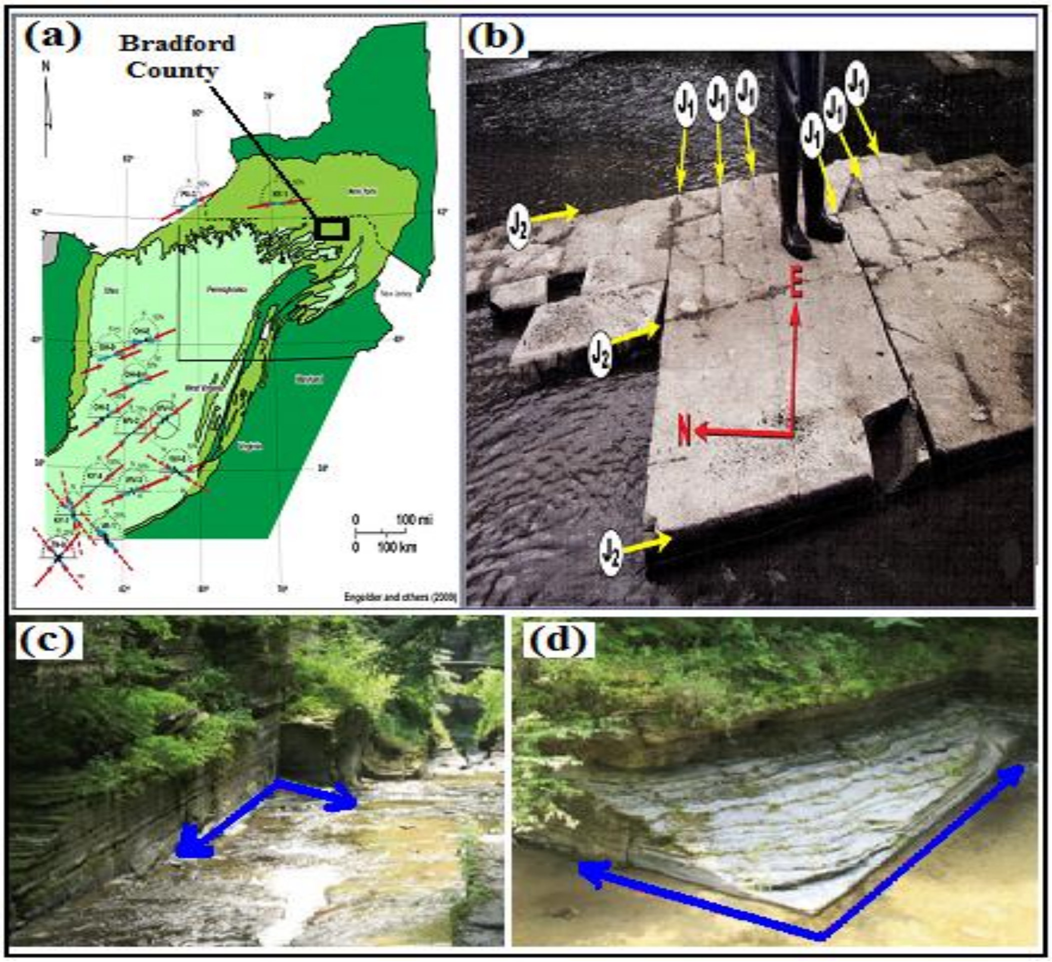

Figure 38: Naturally occurring fracture network (joint sets) as seen on outcrops of Marcellus Shale formation (b), (c), and (d) near Bradford County, PA (a). Joint sets define stress field directions (modified from Engelder et al., 2009).

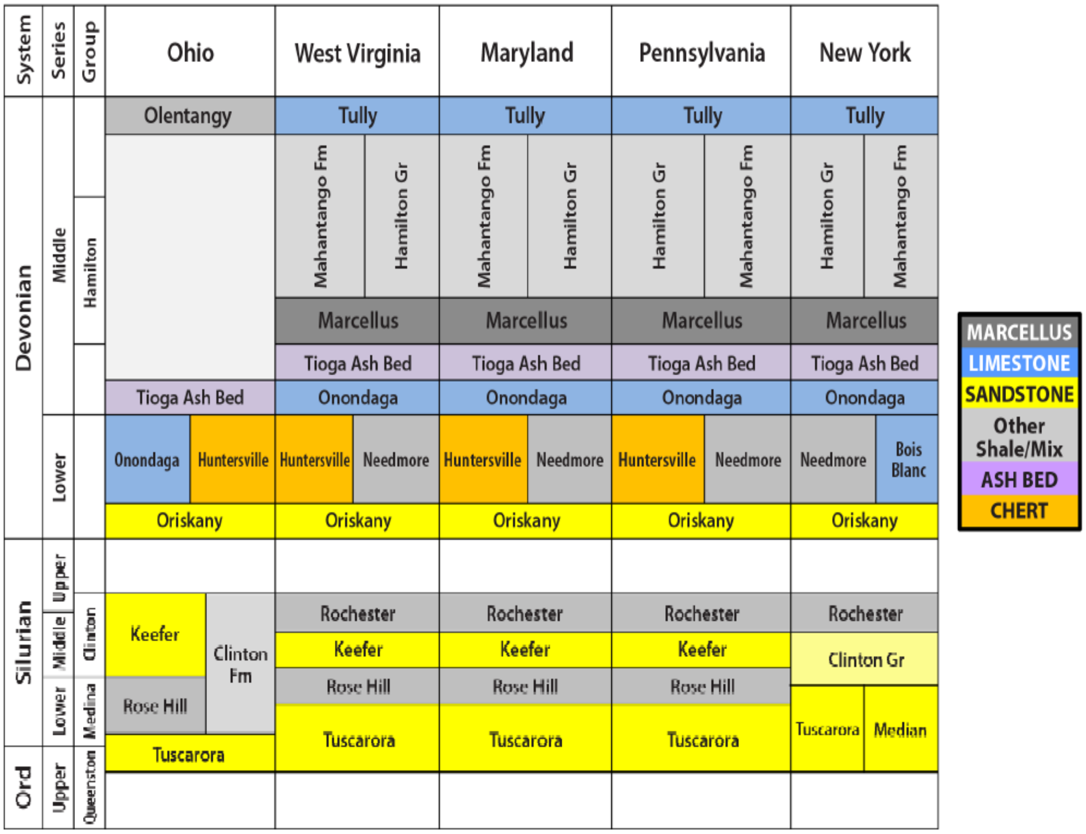

Figure 39: Stratigraphic column for the Marcellus Shale and other major facies (modified from Zagorski et al., 2011).

Research by Zagorski et al., (2011) showed there are significant differences among Marcellus Shale formations in various states (Figure 39). As displayed in Figure 40 – 42, major characteristics of Marcellus Shale and important reservoir parameters significantly differ between the northeast part of the Appalachian Basin and the southwest part. Their study illustrates how tectonic and structural history can affect the characteristics of depositional sequences and reservoir parameters associated with sequences.

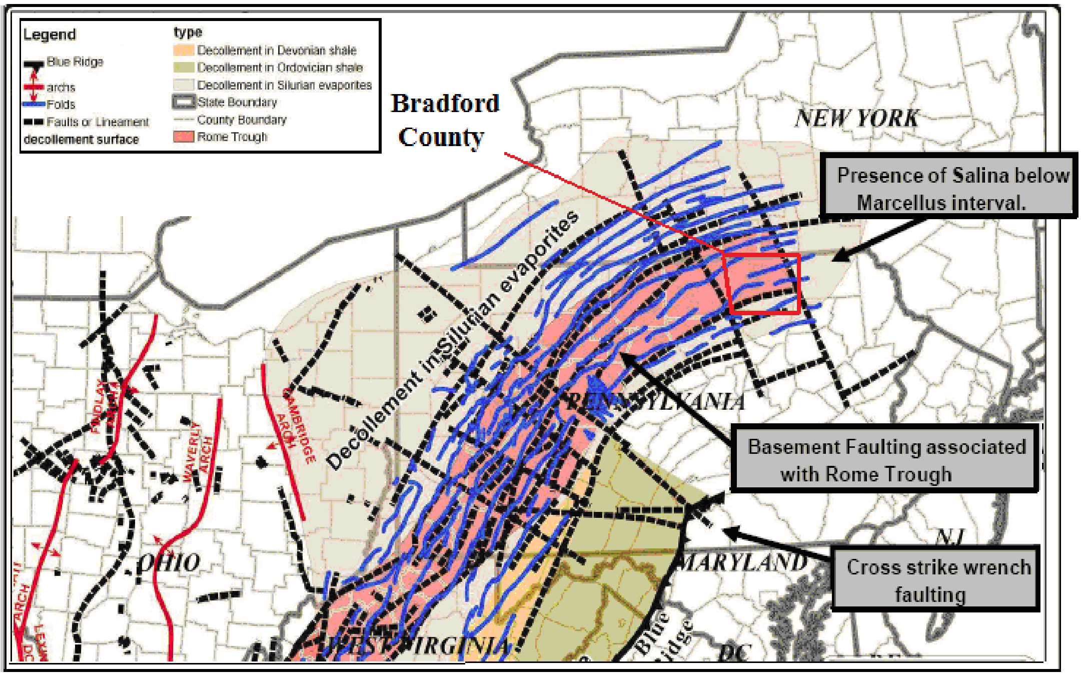

Figure 40: Major structural features affecting Marcellus Shale (modified from Zagorsky et al., 2011).

Figure 40 demonstrates major structural features related to the tectonic history of the basin. These features affect the geological and structural characteristics of the Marcellus Shale across Pennsylvania, New York, West Virginia, Maryland and Ohio. Clay and calcite volume and distribution statistics are example of these influences (Figure 41). As presented on the map of Figure 40, major evaporates, Salina and basement faulting associated with the Rome Trough, and cross-strike wrench faulting are three major tectonic structures shaped the current structural pattern across the Appalachian Basin.

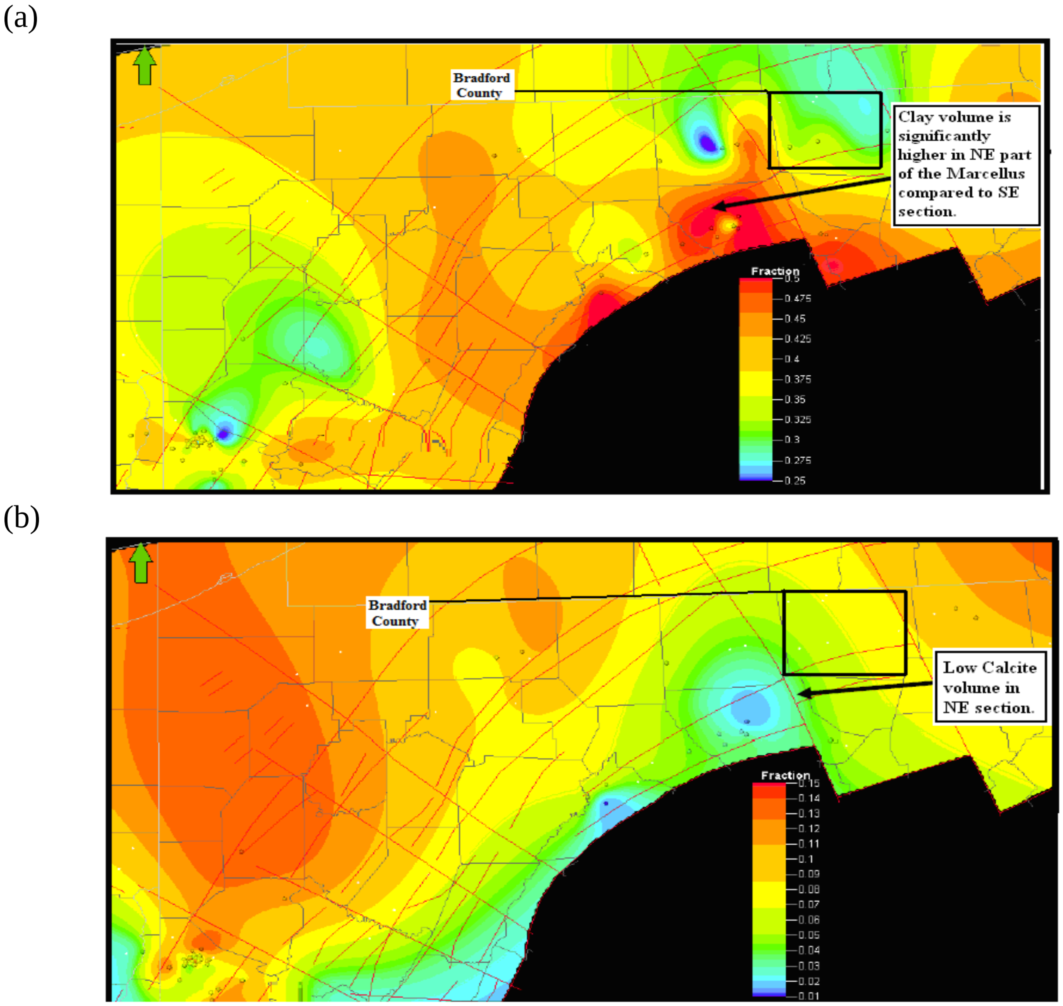

Clay volume is significantly higher in NE part of the Marcellus compared to SE section.

Low Calcite volume in NE section.

Figure 41: Clay (a) and calcite (b) volume maps (modified from Zagorsky et al., 2011).

Figure 42 shows other maps which indicate high pressure zones and thermal maturity across the basin. As seen on these maps, our survey area (Bradford) is located close to an over pressure area. This pressure trend is related to the burial history associated with tectonic events, presence of Salina evaporate interval, and other occurrences driven by tectonic and structural history of Appalachian Basin, which is approximately 300 miles wide and 600 miles long.

(a)

(b)

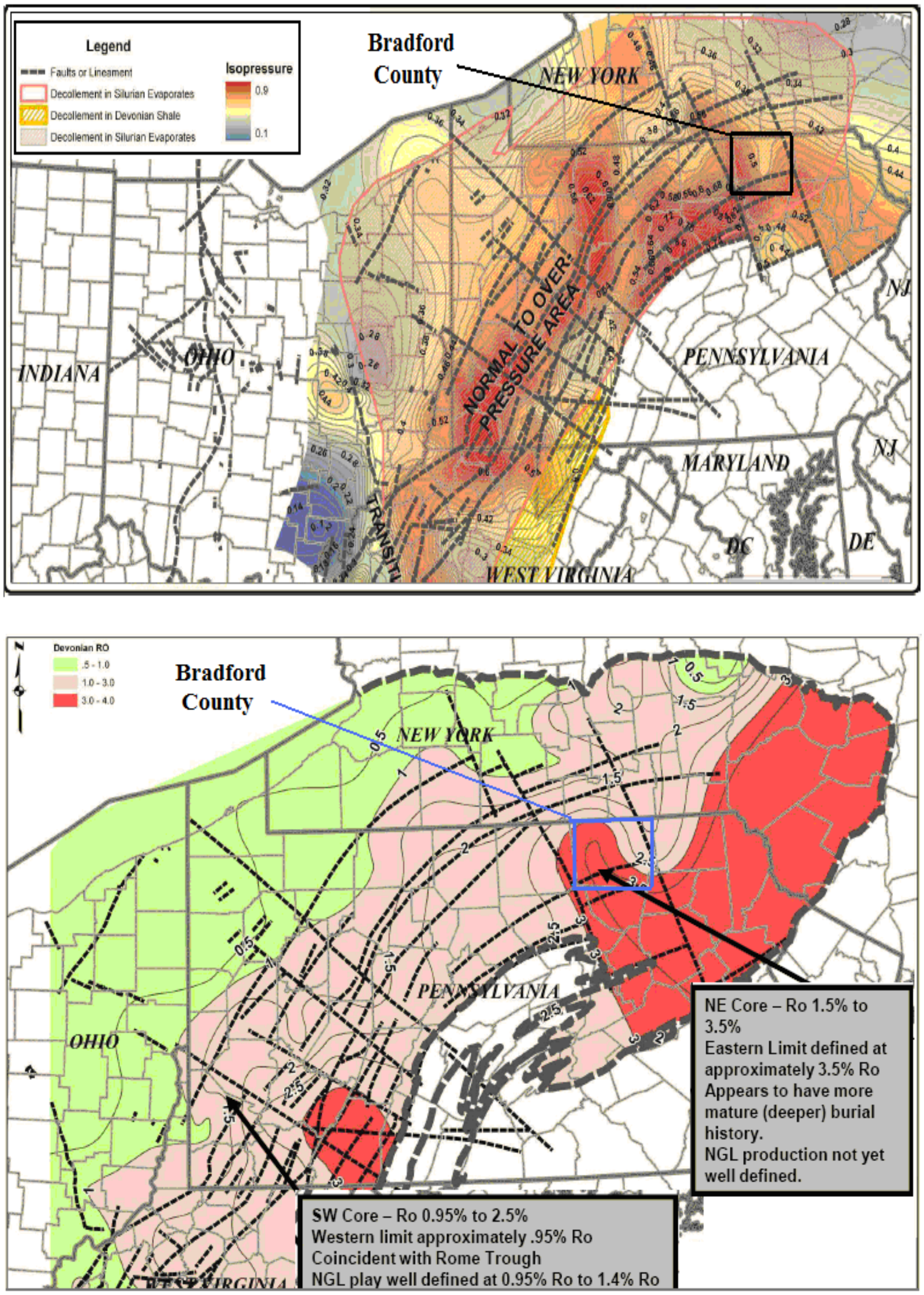

NE Core – Ro 1.5% to 3.5%
Eastern Limit defined at approximately 3.5% Ro
Appears to have more mature (deeper) burial history.
NGL production not yet well defined.

SW Core – Ro 0.95% to 2.5%
Western limit approximately .95% Ro
Coincident with Rome Trough
NGL play well defined at 0.95% Ro to 1.4% Ro

Figure 42: Regional pressure (a) and thermal maturity (b) maps (modified from Zagorsky et al., 2011).

Field studies performed in New York revealed major tectonic events and their concomitant influences on the development of shale formations within the Appalachian Basin and upon stress field distributions within the Marcellus Shale and surrounding limestone and sandstone formations (Evans et al., 1989 I and II). Evans et al. (1989) asserted that Devonian Shale formations located in western New York are mostly prodeltaic and contain sequences constructed by gray and black mudstone and siltstone turbidites. Lithology varies vertically and horizontally, and consists of calcareous siltstones, limestones, quartzic clastics, and black-shale formations. Salt detachment had an impact on the mechanical response of this sedimentation and on tectonic stress in the Appalachian Basin. Thrust faults, which cut limestone formations, occurred in response to compression during Alleghanian and Acadian orogeny.

Regional stress field studies of the Appalachian Basin have demonstrated that stress field variations have strong influence on the entire stratigraphic section as did Alleghanian compression. Crustal straining and major salt formations caused remnant stress and bed-to-bed stress variations which affect correlations between geomechanical properties of rock formations and stress measurements.

Deposition of shale sequences in the region occurred during the erosion of surrounding high lands to the east. Sediments were transported via delta systems, were deposited on alluvial plains, and formed black shale formations in deep marine basins extending south and west. As a result four main depositional environments formed: alluvial plain, shelf-delta front, base of slope, and deep basin (Hill D.G., and Lombardi T.E., 2002).

Strain and Stress Relationships and Their Effects on Joint Pattern Occurrence

In this section, several approaches to stress variation measurements will be compared, and results of several studies performed in the Appalachian Basin will be presented. Results will be evaluated to derive links between mechanical and structural properties of formations and to propose alternative approaches to characterizing fracture structures and estimating fracture parameters for the Marcellus Shale.

From numerous studies of stresses and fracture characterizations, the following studies were selected for inclusion in this thesis. Engelder et al., (1980) performed a thorough study relating sequences of stress fields to joint development and joint patterns. They compared regional joint patterns with finite strain to infer the orientations of strain and joints and how they are related to each other. In a study by Evans, K.F., Engelder, T., and Plumb, R.A. (1989), tectonic and stratigraphic processes that caused deformation in shale formations were investigated. They showed stress variations and discontinuities within the shale formations were related to structural history. In a study performed by Plumb, et al. (1991), geophysical log responses were evaluated to identify stress contrasts in certain formations across the Appalachian Plateau. The effects of mineralogical, chemical, and physical properties on Devonian black-shale burial history and on development of joint mechanisms were thoroughly investigated in a study done by Lash, G. et al. (2004).

Engelder's study (2009) investigated how joint sets contribute to the permeability enhancement and cause abnormal fluid pressures during thermal maturation of organic matter.

RELATIONSHIP BETWEEN STRESS REGIME AND REGIONAL FOLDS

Major structural components of structural deformations across the Appalachian Plateau are characterized by major joint sets. Folds identified near my study site also help understand the region's structural history. In addition to joint sets located across the region, a series of small-scale folds (dipping approximately 2-degrees and associated with the main Appalachian Fold Belt) extend southwest towards neighboring Tioga County and also infer stress-strain components related to the structural and tectonic history of the region. The stress-regime associated with these folds highlights major structural properties of two major plateaus within the region – the Allegany and Appalachian - where Paleozoic rocks overlay Precambrian crystalline basement outcrops that dip southwest to the Pennsylvania – New York State border (Figure 43).

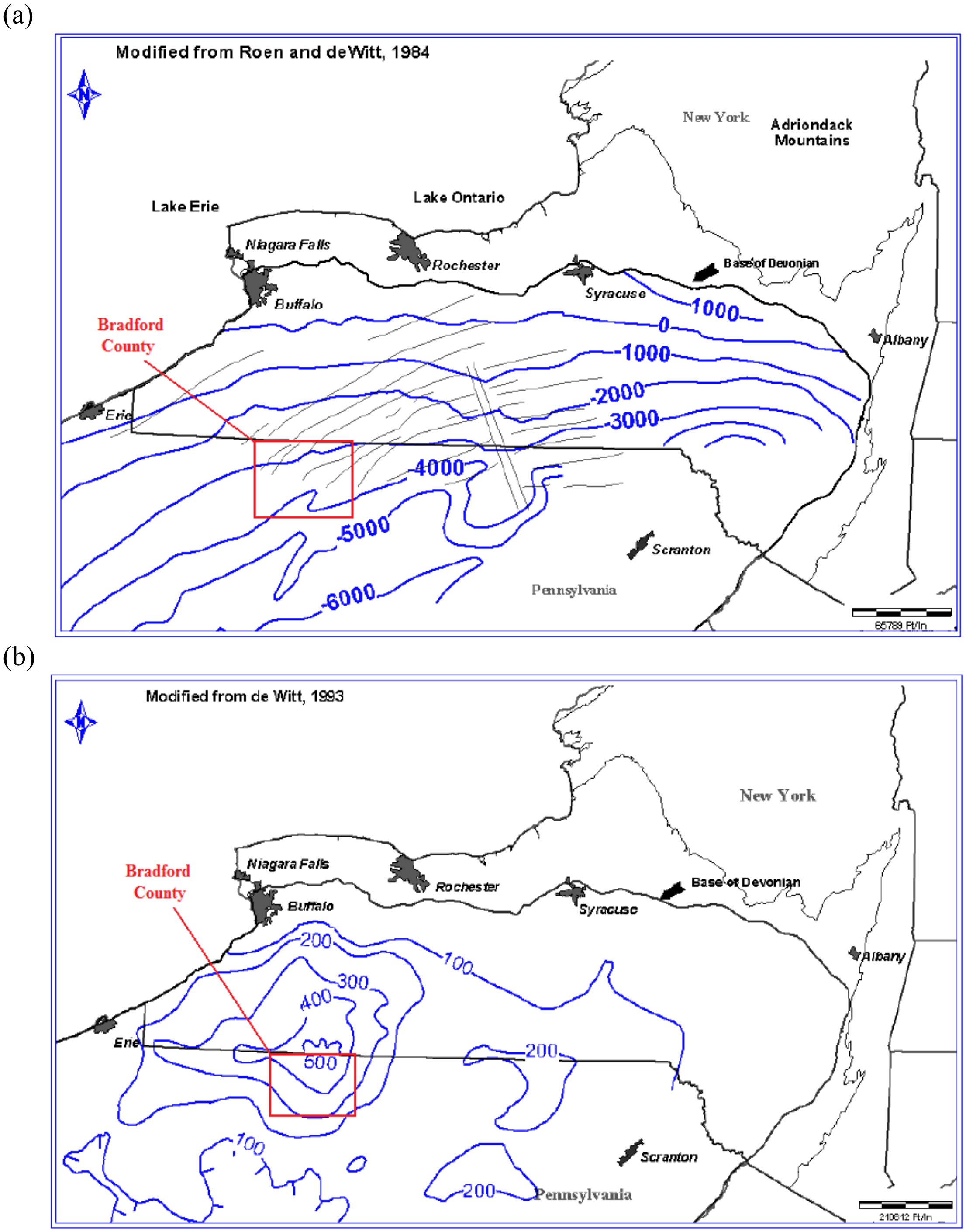

Figure 43: Structural setting of New York and northern Pennsylvania: structure contour on the base of (a) and the thickness of radioactive Devonian black-shale (b) (modified from Roen and deWitt, 1984; deWitt et al., 1993; Milici R.C. et al., 2006).

DEFINITION OF THE RELATIONSHIP BETWEEN STRAIN AND REGIONAL JOINT SETS

Geologic formations of the Appalachian Basin were strongly affected by the stress regimes driven by orogenic events that caused natural fracturing in the plateau. Stress regime and associated natural fracturing have been studied by numerous researchers including Engelder (2009), Evans (1989), Gross (1991), Lash (2004), and Loewy (1995). These geologic studies documented the presence of various vertical joint sets in Devonian formations. These joint systems were formed by various mechanisms in different geologic time periods.

After detailed outcrop studies and measurements, Engelder and Geiser (1980) attempted to correlate joint patterns with strain and stress components in shale, sandstone, siltstone, and limestone formations in the Appalachian Basin. They measured the orientations of joint surfaces for three joint sets with a Brunton compass and determined the mean joint plane using an averaging procedure described in the magnetic anisotropy measurement study. The results of their measurements are shown on the map of southern New York included as Figure 44 through 47.

Engelder and Geiser (1980) observed three major joint sets referred to as Ia, Ib, and III sets. Ia and Ib sets have different orientations and different filling minerals (Ia joint sets in Tully limestones have calcite filling whereas Ib sets are not calcite-filled). They divided outcrop data into several groups based on their stratigraphic boundary, strike orientations, ages and geographic properties.

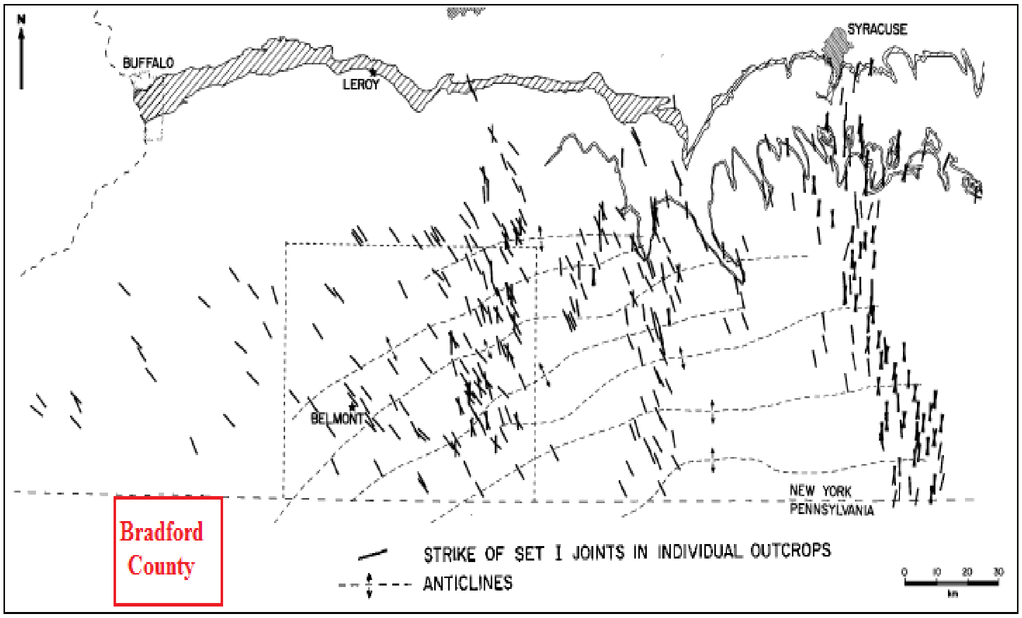

Figure 44: Map view of strike of cross-strike joints observed in outcrops of Middle and Upper Devonian rocks located across the southern New York and northern Pennsylvania States (modified from Engelder and Geiser, 1980).

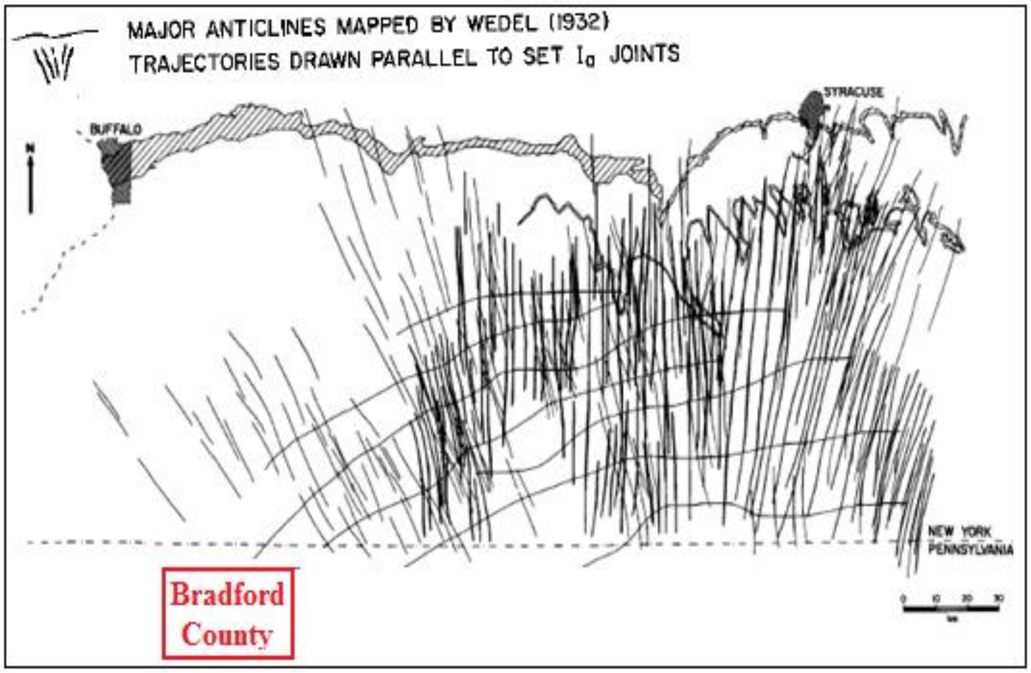

Figure 45: Plot of trajectories drawn parallel to the measured strike of Ia joint sets (modified from Engelder and Geiser, 1980).

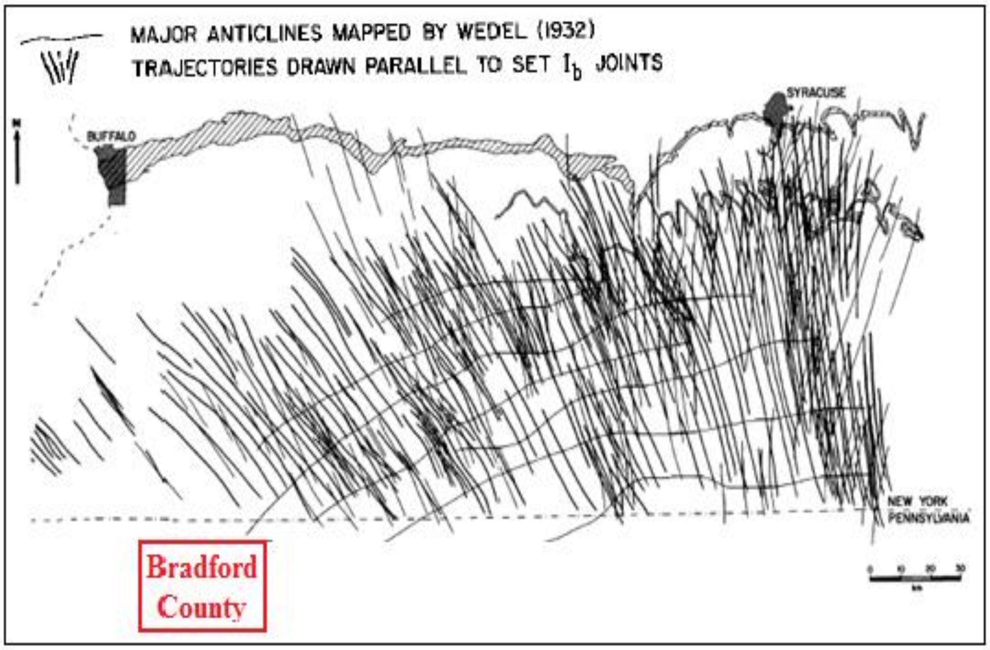

Figure 46: Plot of trajectories drawn parallel to the measured strike of Ib joint sets (modified from Engelder and Geiser, 1980).

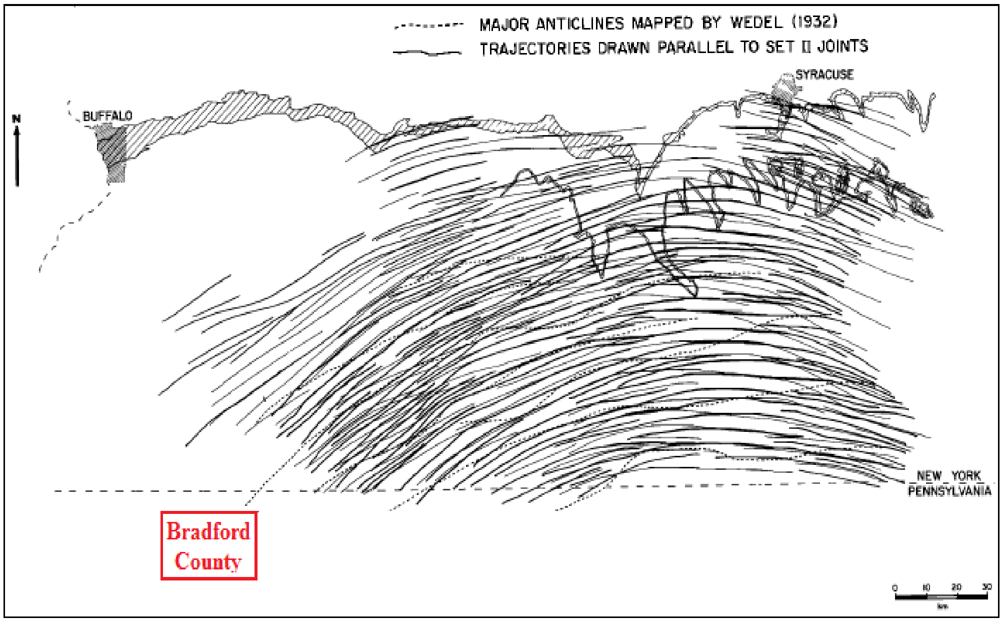

Figure 47: Plot of trajectories drawn parallel to the measured strike of joint sets II and III (modified from Engelder and Geiser, 1980).

One of the most important parts of their study was the relationship they described between folds and joints. They defined the continuous strike direction of joints conforms to the fold axes found in the Appalachian Basin. However they did not find any consistent orientation of joints relative to the folds (Figure 45 through 47). Figure 45 also shows the trajectories drawn parallel to the maximum horizontal compression. Presence of joint sets III and joint sets unique to individual outcrops (set II) introduces additional complexity to the joint pattern of the Appalachian Basin. Figure 47 displays trajectories drawn parallel to joint sets II and III, respectively. Even though Engelder and Geiser (1980) asserted that joints sets Ib and II have the widest coverage, they could not detect any consistency regarding to their alignment any distribution pattern.

In addition to determining orientation and distribution of individual joint sets, Engelder and Geiser (1980) defined the relationship between in-situ stress field distributions and joint development patterns through in-situ strain measurements provided by strain relaxation tests. They described the term "recoverable strain" (order of 10^{-3} to 10^{-4}) based on the change in shape of the rock, distinguishing this type of strain from non-recoverable finite strain (order of 10^{-1}).

Because several strain components affect relaxation, the dependence of relaxation method measurements on certain parameters is not fully understood. However, relaxation tests provide direct measurements. These measurements revealed the inversely proportional relationship between (1) recoverable-strain magnitude and the joint density of an outcrop, and (2) the proportional relationship between the volume of joint-free rock sections and the strain relaxation associated with that part of the rock.

According to their measurements and observations, Engelder and Geiser (1980) concluded that rocks which have residual elastic strain tend to have fractures parallel to maximum compression, and in situ stresses are oriented with residual strain and joint propagation. However, their study did not assert clear evidence which indicates whether residual strain or rock fabric is the main controlling element on joint development (Engelder and Geiser, 1980). Likewise, they could not prove that in situ strain is genetically related to maximum horizontal compression. However, they identified the orientation of maximum stress fields and their positions relative to joint sets for major rock units, including Machias formations consisting of interbedded shale and siltsone with deformed fossils, and the Onondaga Limestone which is highly fractured and contains many joint sets (Figure 48).

As stated in the Engelder and Geiser (1980) study, none of the unique individual joint sets located in the Onondaga limestone is related to joint sets I or II identified in Devonian Shale formations. Even though they were not certain about nature of stress field that affected the Onondaga Limestone, they were able to infer that the propagation direction of joints in the Onondaga Limestone is controlled by stress fields.

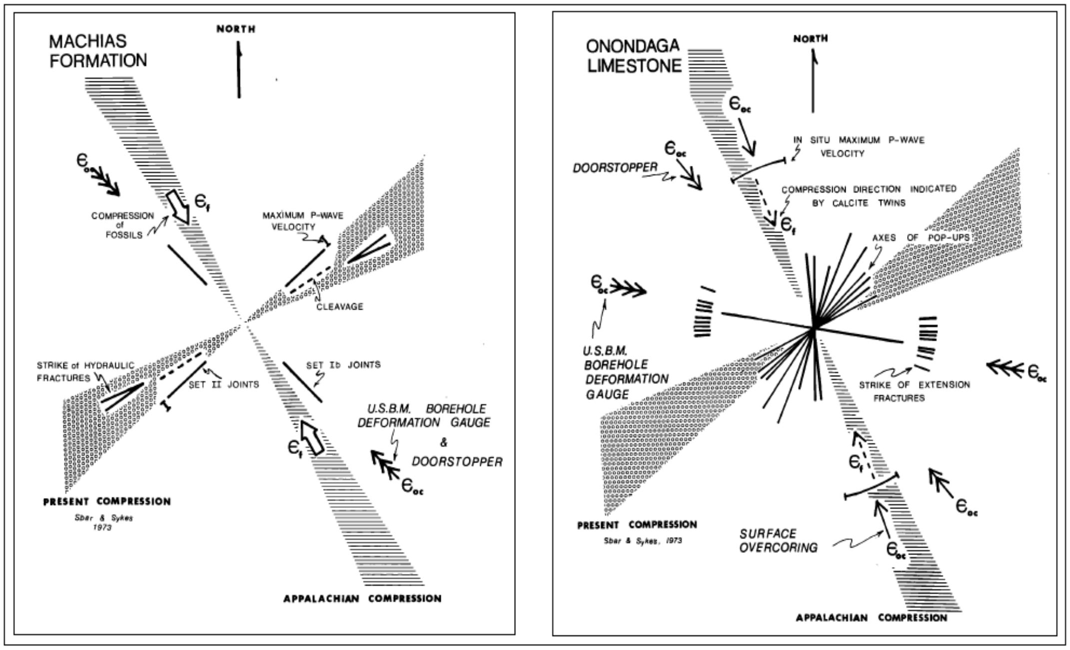

Figure 48: Orientation of joint sets, stress fields, and strains for major rock formations: Machias Formation (left), and Onondaga Limestone (right) (modified from Engelder and Geiser, 1980).

The rotation of mica minerals during sediment deformation indicates the impact of rock fabric on rock deformation. Engelder and Geiser's study (1980) showed mica fabric is not coaxial with strain. Also, they indicated that compression direction is parallel to the Ia joint sets. The fact that calcite veins identified in the Tully Limestone are parallel to the Ia joint sets is additional evident that there is a clear relationship between rock fabric and joint development. Engelder and Geiser (1980) documented the relationship that indicates the orientation of Ib joint sets is normal to mica fabric. Furthermore, they stated that Ib joint sets occurred during overburden removal and thermal cooling and resulting contraction. Because contraction does not require a large tectonic stress, rock fabric may play a major role on the occurrence of Ib joint sets.

Using the relationship between calcite and quartz-filled joints identified in the Tully Limestone and open joints which have no filling, Engelder and Geiser (1980) asserted that strain by shortening was not volume constant. Early formed joints, which were thought to be a major sink, actually served as conduits.

As a result of studying thin sections, outcrops, and calcite fillings, Engelder and Geiser (1980) suggested that Ia joint sets are early-formed joints and were formed before joint sets II. They asserted that joint sets II and folds formed simultaneously, and Ib joint sets formed later than other sets. Their study demonstrated that using rock fabric, mechanical properties, tectonic history, and stress fields, it is possible to understand the mechanism and time when fractures and joint sets are developed.

Loewy (1995) documented five major joint sets categorized based on their morphological structure, geologic time when they were formed, and the orientation of joint clusters. He indicated the variation of joint orientation followed folds associated with the Appalachian Fold Belt orientation. Engelder (2009) also indicated the influence of fold structures on natural fracturing and pressure variations caused by compaction and compression.

In summary, various studies done in different regions of the Appalachian Basin indicate the presence of various naturally-occurring joints driven by various tectonic and depositional forces.

ISIP MEASUREMENTS AND DETERMINATION OF STRESS VARIATION

The presence of stress discontinuity, complicated structural settings and time-varying tectonic and gravitational loading conditions controlled the pattern of stress variations within shale formations across the Appalachian Basin. In their stress study, Evans, et al. (1989) observed multiple structures: basement sediment interfaces, faults, detachments, volcanic intrusions and salt formations that grew during the main orogenic process that constructed the Appalachian Mountains. They described the main elements controlling stress patterns based on stress measurements in several wells (a kilometer apart) located on top of Devonian shale, sandstone, and limestone sequences in western New York.

Their study was based on borehole televiewer logs and ISIP (instantaneous shut-in pressure) measurements conducted using wireline systems during hydraulic-fracturing. These data revealed the important facts that: (1) stress varies according to the rock type in a sequence, and (2) major drops in horizontal stress magnitude occur in shale formations. They used borehole televiewer data to identify zones which do not contain natural fractures and calibrated other borehole logs such as gamma ray, density etc. inside these intervals. They related local tectonic and geologic-setting information to stress measurements to demonstrate how accurate stress measurements can be made in certain rocks, and which stress component can be related to measured rock-property values. Although they related stress component orientation and magnitude to lithology and structural features, they could not find a strong correlation between stress orientation and lithology because of the different orientations obtained for successive tests when they performed identical ISIP measurements.

Induced fracture geometry at wellbores was determined based on the assumption that the best characterization of fractures can be made by penny-shaped equilibrium cracks in an idealized elastic medium. In addition to constraints attributed by this model assumption, intermittent blockage and leakage in downhole equipment during pumping operation also hampered their study. Under these constraints, they concluded that ISIP measurements reflect least principal stress values. They recognized two distinct stress regimes separated by the transition zone between shale formations and two major sandstone formations. They obtained different ISIP values for these two main stress regimes. ISIP values were lower than overburden in lower stress regimes, while ISIP values higher than overburden were observed in higher stress regimes. Equal ISIP values in each well suggested a laterally uniform subsurface horizontal stress regime. Televiewer images indicated the main orientation of induced fractures aligned vertical to the wellbore.

Even though Evans et al (1989) observed fractures aligned with maximum horizontal stress, they did not find any correlation between lithology and stress zones. In lower stress regimes, ISIP measurements were less than vertical stress values. This indicated that the magnitude of least horizontal stress can be larger than vertical stress, which causes vertical fractures to turn to a horizontal direction (Evans, et al., 1989). Evans et al (1989) also indicated the impact of topography on stress measurements in their study. Using the assumptions that Poisson’s ratio equals 0.33 and plane strain conditions, they asserted that topography influences on stress measurements are larger on vertical stress than it is on horizontal stress. The impact of topography on stress is shown in Figure 49. As a part of their evaluations, Evans et al (1989) concluded stress variations relate not only to tectonic orogenic process (Alleghanian deformation), but also to abnormal pore pressure in response to limited drainage of fluid.

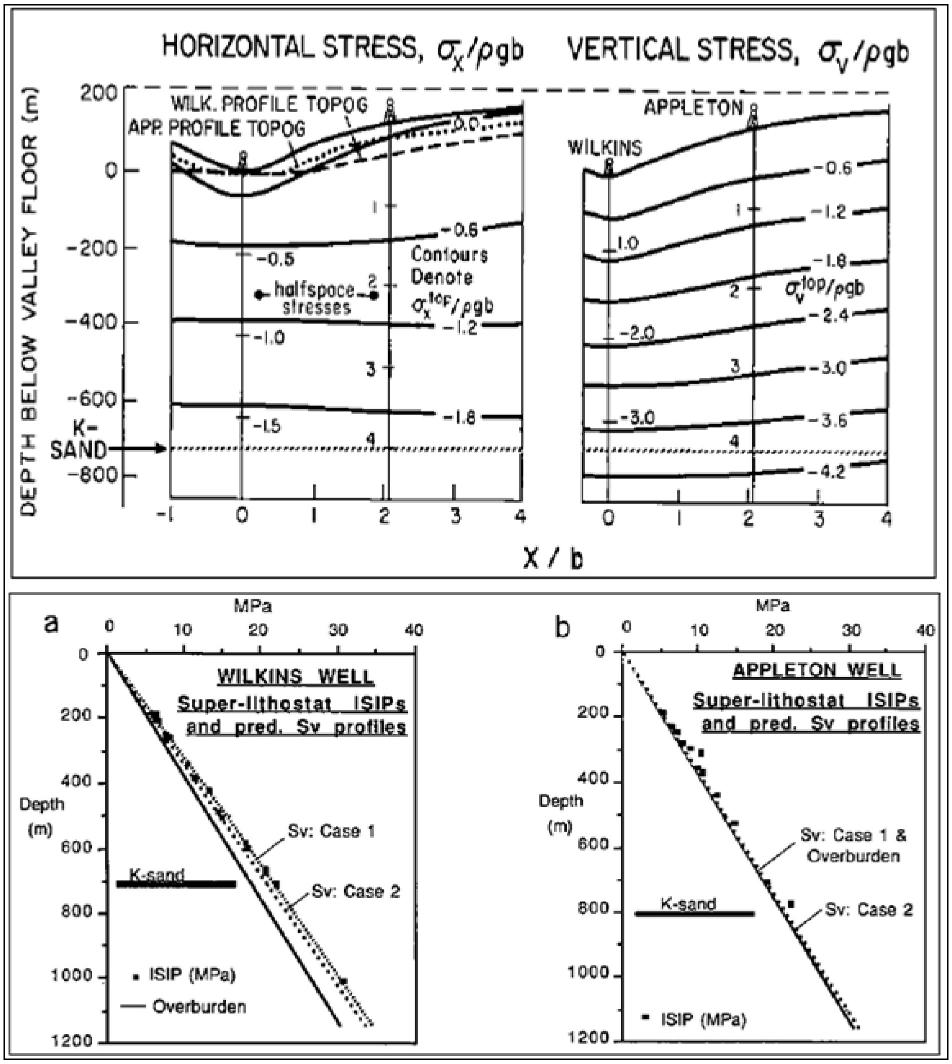

Figure 49: The effect of topography on stress measurements (top). Vertical stress is more sensitive to topography. The near-lithostat trend tends to be closer to vertical stress profile (Modified from Evans, et al., 1989).

As a result, under some of the model constraints (such as using a two-dimensional model to represent three-dimensional topography), Evans et al (1989) concluded that ISIP measurements are identical at different well locations if they measure lateral variation in horizontal stress. However, ISIP measurements are not the same at different well locations if measurements represent spatial variation of vertical stress in which ISIP values are higher than overburden. Sandstone formations have higher ISIP values than shale formations (Figure 50).

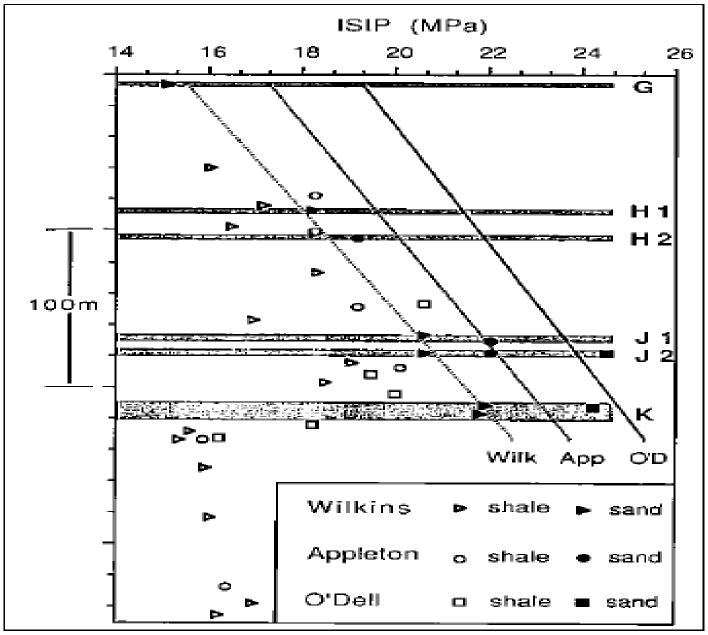

Figure 50: ISIP measurements indicating the lithology change at the transition zone between shale and sand formations (Modified from Evans, et al., 1989).

Estimation of Maximum Stress Components

Evans et al (1989) proposed two methods to estimate maximum horizontal stress from hydraulic fracturing data: (1) fracture reopening, and (2) breakdown. Both methods are based on the mechanism of vertical borehole rupture in the presence of horizontal stress. Both methods have limitations because of the requirement to estimate the tensile stress of the rock formation of interest. The assumption that fluid pressure within a fracture near a wellbore must be same as pore pressure helped overcome the issue of estimating tensile stress. Estimated horizontal stress values were used to calculate pore pressure of reservoirs; however, pore pressure estimation in shale formations is not as certain as for conventional reservoirs because of low permeability and small pore volume.

Geomechanical Properties of Shale Formations

Rock formations undergoing stress are characterized by mechanical properties which can be determined from stress conditions and the resulting strain. Based on the elastic modulus values they calculated in their study, Evans et al (1989) demonstrated that stiff shale formations with high clay content represent higher stress levels. This result explains why sand/shale stress contrast exists as a result of compression during tectonic loading. Although Evans et al (1989) related stress to elastic modulus, they did not state any correlation between stress and Poisson’s ratio.

GEOPHYSICAL LOG RESPONSES AND THEIR CORRELATION WITH STRESS CONTRAST

Plumb et al (1991) conducted comprehensive geophysical well log studies to identify physically different lithologies and to determine their stress values. Their analysis evaluated several types of log data, including electric resistivity, spectral gamma ray, bulk density, neutron porosity, and acoustic logs to determine the relationships between rock properties and in situ stress differences.

Plumb et al (1991) utilized apparent resistivity values which are sensitive to pore fluids, the tortuosity of pore space, and surface conductivity between clay minerals in shale formations. The radioactivity measured by spectral gamma ray log emitted by potassium, thorium, and uranium allowed them to distinguish shale formations from other rock units. With the tool irradiating the formation with gamma rays, they measured the bulk density which is used to estimate porosity and overburden stress. With neutron porosity logs, they attempted to identify porous rock units and to estimate porosities. Travel time measurements obtained from acoustic logs provided information about compressional and shear wave velocities. Using these velocities and densities they calculated averaged interval elastic moduli.

As a result of their analysis, Plumb et al (1991) indicated differences between stress values which coincide with variations in bed thickness and log responses. They interpreted a significant stress drop as an indicator of the separation between normally compacted formations and deeper undercompacted shale formations.

Plumb et al (1991) correlated their results with open-hole stress measurements performed by hydraulic fracturing operation which was explained in detail by Evans et al.

(1989). The greatest difficulty they faced was the small thickness of targeted formations. This thin-bed geology forced them to do careful depth matching between stress measurements and log responses before charactering physical properties of recorded stress values. After proper corrections, they computed arithmetic means of geophysical parameters. They were able to distinguish all lithologic units from geophysical logs.

Based on considerations resulting from horizontal tectonic strain, paleo-overpressure drainage, and rock shear strength, they analyzed stress-contrast mechanism using core and log data. Plumb et al (1991) stated that formations which have the highest Young’s modulus and lowest clay content are characterized by the greatest minimum horizontal stress. Using the ratio of minimum horizontal stress to vertical stress, they determined lithologic contrasts and lithostatic stress. Plumb et al (1991) observed the strongest correlations between log responses and stress values when the contrasts between stress and physical properties rocks were large. Large physical contrasts are observed at transition zones between shale-sandstone or shale-limestone sequences. Therefore, they could not define strong correlations between physical properties and stress values within shale groups. However, they found that stiffer rocks which have greater stress magnitudes are also characterized by lower clay content.

Cross sections

Figure 51 displays cross sections, depositional sequences, and lithological intervals studied for four locations located in Pennsylvania and New York which are close to my Bradford survey area. Tully, Onondaga, Stafford, Tichenor, Centerfield, and Cherry Valley limestones in addition to Marcellus Shale are identified in the Bradford survey as well. Analysis of these cross sections provides information regarding variations of thickness and depth of major limestone depositional facies and their progression across the basin.

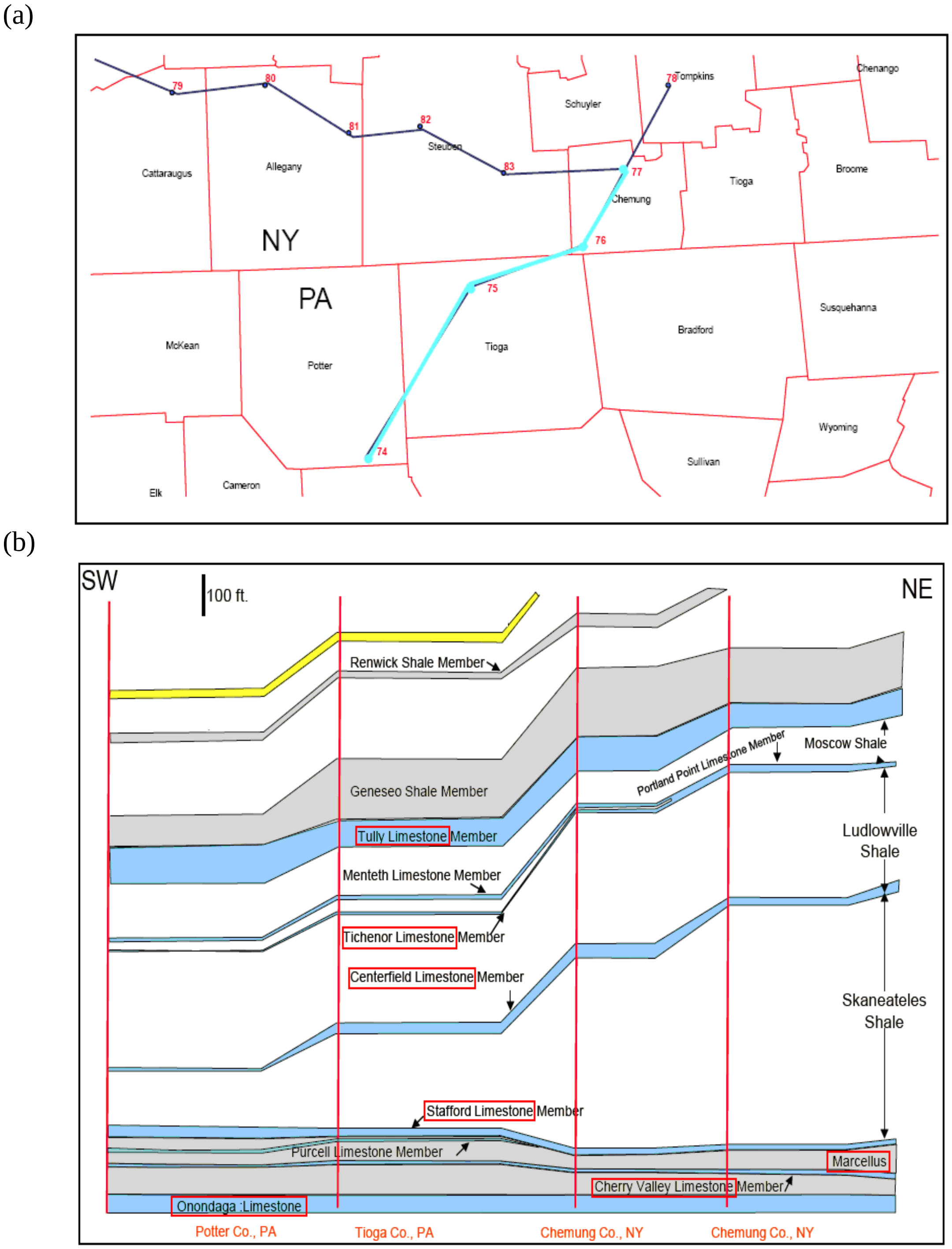

Figure 51: Location map (a) and cross section profiles (b) (modified from Avary K. L., 2010).

Conclusion

Because the internal architecture and connectivity of joint and fracture systems, together with stress regimes, control fluid flow in fractured unconventional shale formations, a geomechanical understanding of these properties provides important information and helps predict the nature and orientation of naturally-occurring fractures and joints. Heterogeneity of stress regimes, in addition to rocks properties, controls the initiation and propagation of joint and fracture systems in region.

This chapter reviewed geological and geomechanical insights into various fracture types and characterizes joint sets present in the region. Evidence of the stress regimes driven by tectonic, structural, and depositional processes across the Appalachian Basin is summarized. This chapter describes some of the most prominent modes of fracturing and joint structures for common geologic units by addressing various methods used to detect and characterize naturally-occurring fracture and joint systems. Particular emphasis is placed on direct engineering and geophysical measurements.

Both large-scale (surface) and small-scale (borehole) measurements provided important information regarding stress regimes and their relationship to joint-set generation. However, methods reviewed in this chapter relied on the following facts: (1) fractures create 2D anomalies that require fracture thickness to be extremely thin compared to length and height, (2) because of the deformation process, most fractures and joints are oriented nearly vertical and can be characterized by either a single azimuth or by two-orthogonal azimuth directions, and (3) because of tectonic and depositional forces, fractures and joint sets have different orientations which causes azimuthal anisotropy.

The scale of a measurement and the resolution of the measurement method are important factors that constrain the accuracy of predictions. Methods explained in this chapter include direct (e.g. relaxation test) and indirect (e.g. correlation between rock properties and fracture parameters) fracture measurements.

Methods reviewed here did not find any correlation between geologic lithologies and stress regime when fractures aligned with maximum horizontal stress. ISIP measurements from different well locations were inconsistent when measurements represented spatial variation of vertical stress. Even though relaxation-test data provided direct measurements, the dependence of relaxation method measurements on certain parameters were not fully understood because several strain components affect relaxation. Even though borehole measurements provided good understanding about several physical properties of various lithologies, they did not help understand the lateral extension of joint sets and other structures because of the lateral spatial limitation of well log data.

CHAPTER 4: DATA PROCESSING AND IMAGING

A 3C3D seismic survey and vertical seismic profile (VSP) data were acquired in Bradford County, PA and were processed by commercial data-processing companies. Geokinetics processed the 3C3D data, and Halliburton processed the VSP data. Geokinetics generated P-P, P-SV_1, and P-SV_2 data volumes to image naturally-occurring fractures and joint sets within the Marcellus interval. In addition to surface seismic data and VSP data, borehole well-log data acquired in the central image VSP well were provided by Chesapeake Energy. These logs defined petrophysical properties and geologic units used to calibrate seismic data and to establish depth registration for reflection events identified on seismic data.

One of the goals of this study was to investigate data processing and imaging procedures for multicomponent land data that optimize information describing fractured zones and the internal architecture of unconventional reservoirs. In many geologic settings, compressional wave data provide sufficient images; however, characterization of complex structures such as fracture networks and faulting within unconventional reservoirs such as the Marcellus Shale often fail when based on single-component compressional wave data.

Past researchers (Al-Anboori et al. 2005; Liu et al. 2003; Chapman et al. 2003) used shear-wave splitting to analyze fracture geometry, size, and orientation. However, their efforts were limited to microseismic data. In my study, shear-wave splitting analysis was done to determine stress directions by comparing two images: fast-shear and slow-shear wave volumes. If done properly, time shift correlations between the two S-wave data volumes indicate the location and intensity of fracture networks.

This chapter illustrates the 3C3D multicomponent dataset and discusses strengths and weaknesses of different wavefield types used in the study. Fracture detection and rotation analysis of multicomponent data are also discussed.

Multicomponent Data Sets and Data Processing Flows

3C3D SEISMIC DATA

Analyzing multicomponent surface-based seismic data was the essential part of this study. Survey design and acquisition statistics affect seismic data attributes because multicomponent data analysis depends on the stacking fold, offset distribution, and azimuth distribution created by the acquisition geometry. Data acquisition parameters affect both common-midpoint data (P-P and S-S wave-modes), and also common-conversion point data (P-SV and S-VP wave-modes). Using seismic data to detect fracture networks and to characterize stress fields and geomechanical properties of naturally-fractured unconventional reservoirs requires that data have high stacking fold, rich azimuth, and full offsets.

This PhD project used the high-density, wide-azimuth 3D multicomponent data acquired by Geophysical Pursuit and Geokinetics over the Marcellus Shale in Bradford County in northeastern Pennsylvania. Using these data, both compressional-wave and shear-wave data were analyzed to investigate the orientation and location of naturally-occurring fractures within the Marcellus Shale and associated formations.

SURVEY ATTRIBUTES AND DATA BINNING

The energy source used to generate the Bradford County seismic data was an explosive charge of 1 kg (2.2 lbs) positioned at a depth of 6 m (20 ft).The source used to generate VSP data was a vertical vibrator. Both surface and downhole data were recorded with three-component sensors. The survey design that was planned to be used to acquire surface-based 3C3D seismic data across the Bradford County study site is illustrated on Figure 52a. Because of surface conditions and operational limitations, actual acquisition did not follow survey design as originally planned (Figure 52b).

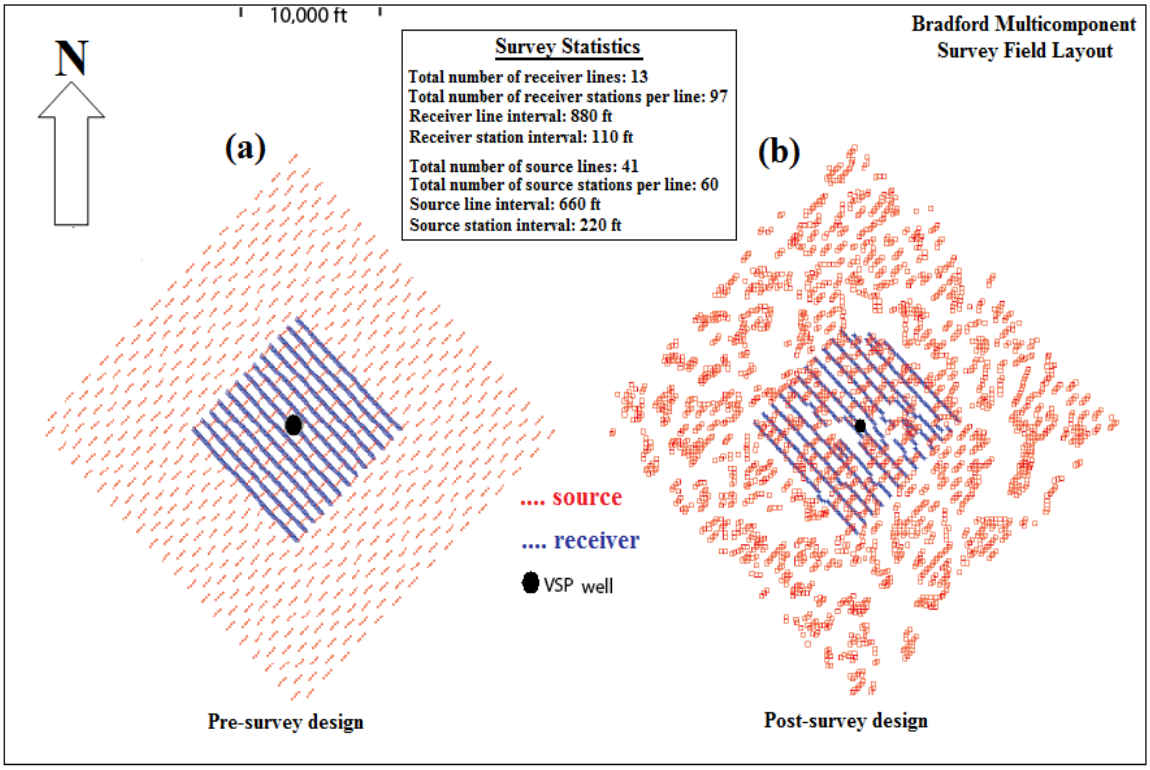

Figure 52: Map view of Bradford County multicomponent survey design showing location of VSP well relative to field equipment used for the surface-based seismic survey. (a) Intended source-receiver geometry. (b) Actual source-receiver geometry.

Stacking fold is one of the most important statistics of a 3D survey design that is directly linked to image quality. In 3D surveys, the first task is usually to examine the nominal fold and overall fold distribution across a survey area to decide if a design is appropriate for imaging geologic targets at specific depths. Inadequate nominal fold across an image area and drastic fold variation between adjacent stacking bins lower the quality of seismic images. Structural dip, target depth, and the architecture of target structures are factors that dictate what the magnitude of stacking fold should be. The strength and type of the energy source, as well as the nature of the signal-to-noise ratio of different elastic wave modes and the frequency content of reflection wavelets all contribute to decisions as to what nominal fold is sufficient to produce optimal images of geologic targets.

Because the objectives of this study were to compare different wave modes and images from multiple elastic wavefields, two types of stacking fold were considered in this study: (1) common-midpoint (CMP) fold for P-P (pure compresional) data, and (2) common-conversion point (CCP) fold for P-SV (downgoing P and upgoing converted S) data. Wave modes, such as P-P and S-S, that have the same propagation velocity for upgoing and downgoing wavefields are imaged based on CMP principles; whereas, wave modes, such as P-SV and SV-P converted modes that have a different propagation velocity for upgoing and downgoing wavefields require CCP principles (Hardage et al., 2011).

In the Bradford survey, CMP folds created by the proposed source-receiver geometry when offsets are restricted to 5,000 ft (1,524 m), 10,000 ft (3,048 m), and 26,000 ft (7,925 m), and when all source-to-receiver offsets are used, are shown in Figure 53. It is important to examine fold distributions associated with these three offset ranges because they indicate the image quality based on CMP stacking folds expected for target depths of 2500 ft (762 m), 5,000 ft (1,524 m), and 13,000 ft (3,962 m), respectively.

To highlight the influence of long offsets on fold distribution, I prepared CMP fold plots for different offset ranges. Near offsets (0-5000 ft), intermediate offsets (5000-10000 ft), and long offsets (over 15000 ft) affect nominal fold because different numbers of source-receiver midpoints fall into each stacking bin for each offset range (Figure 53). Long offsets are particularly important because long-offset data provide crucial information regarding anisotropy.

Operational limitations and surface constraints hamper regular source-receiver geometry layout in the field and affect survey attributes such as fold. These realities produce uneven fold distribution at some target depths and may cause fold variations in adjacent stacking bins. Figure 54 shows the post-survey CMP fold distribution. Randomization introduced by surface conditions and operational constraints caused modest variations of fold attributes over the survey area compared to attributes predicted by the pre-survey design (Fig. 53). Random stations result in aceptable fold variations between adjacent stacking bins and higher nominal fold values at the center of the image area (Figure 54). Alkan (2007) documented the effect of random survey design and acquisition geometry on survey attributes and demonstrated that random survey design can improve fold and offset distributions by removing acquisition imprints and other geometry-related effects. Alkan (2007) showed random survey designs are beneficial, compared to rigorous regular survey geometries, as long as randomization is constrained so that source and receiver station movements are limited to 10-25% of the station interval.

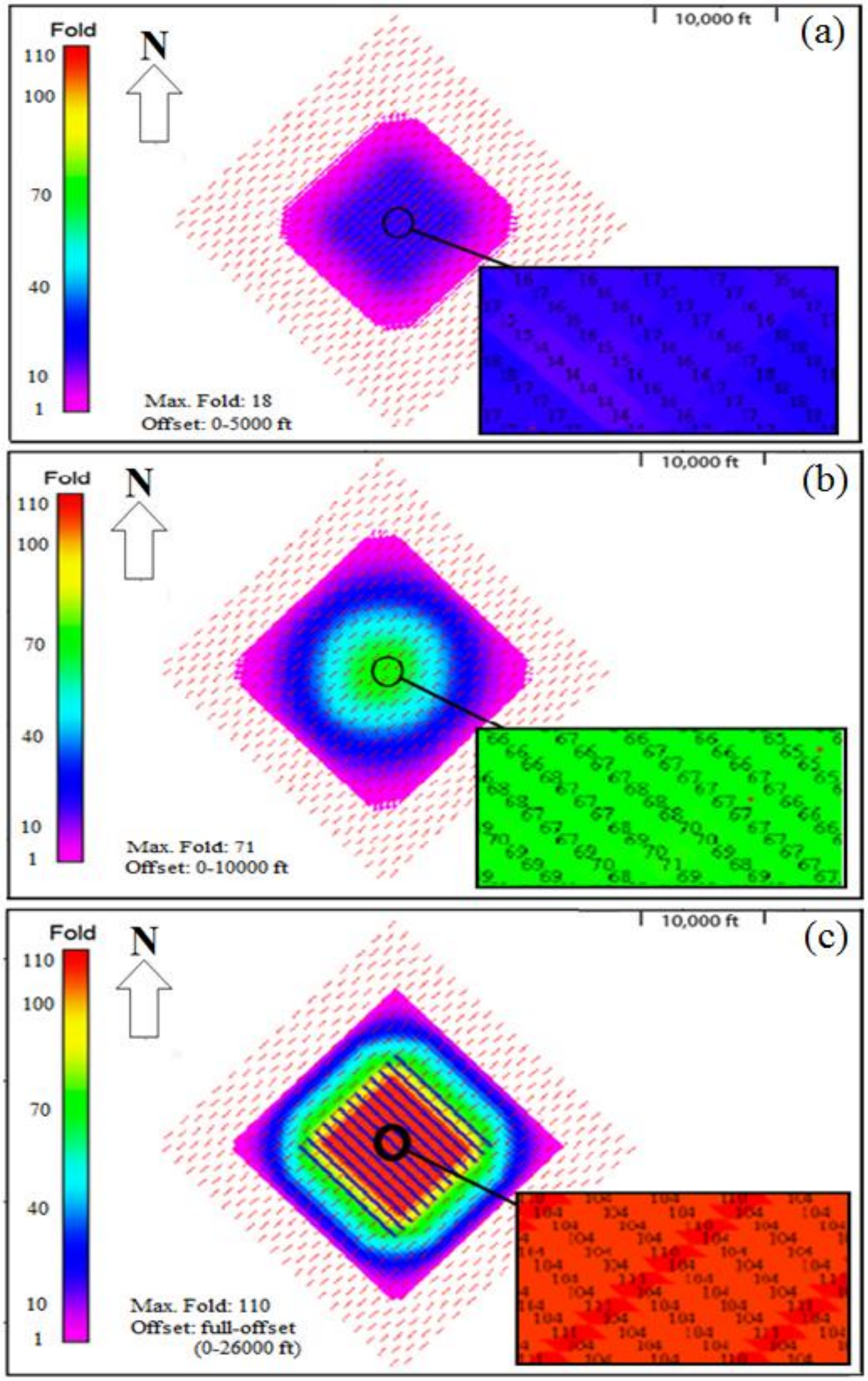

Figure 53: CMP fold statistics for different offset intervals: 0-5000 ft offset (a), 0-10000 ft offset (b), and full offset (c) used in pre-survey planning.

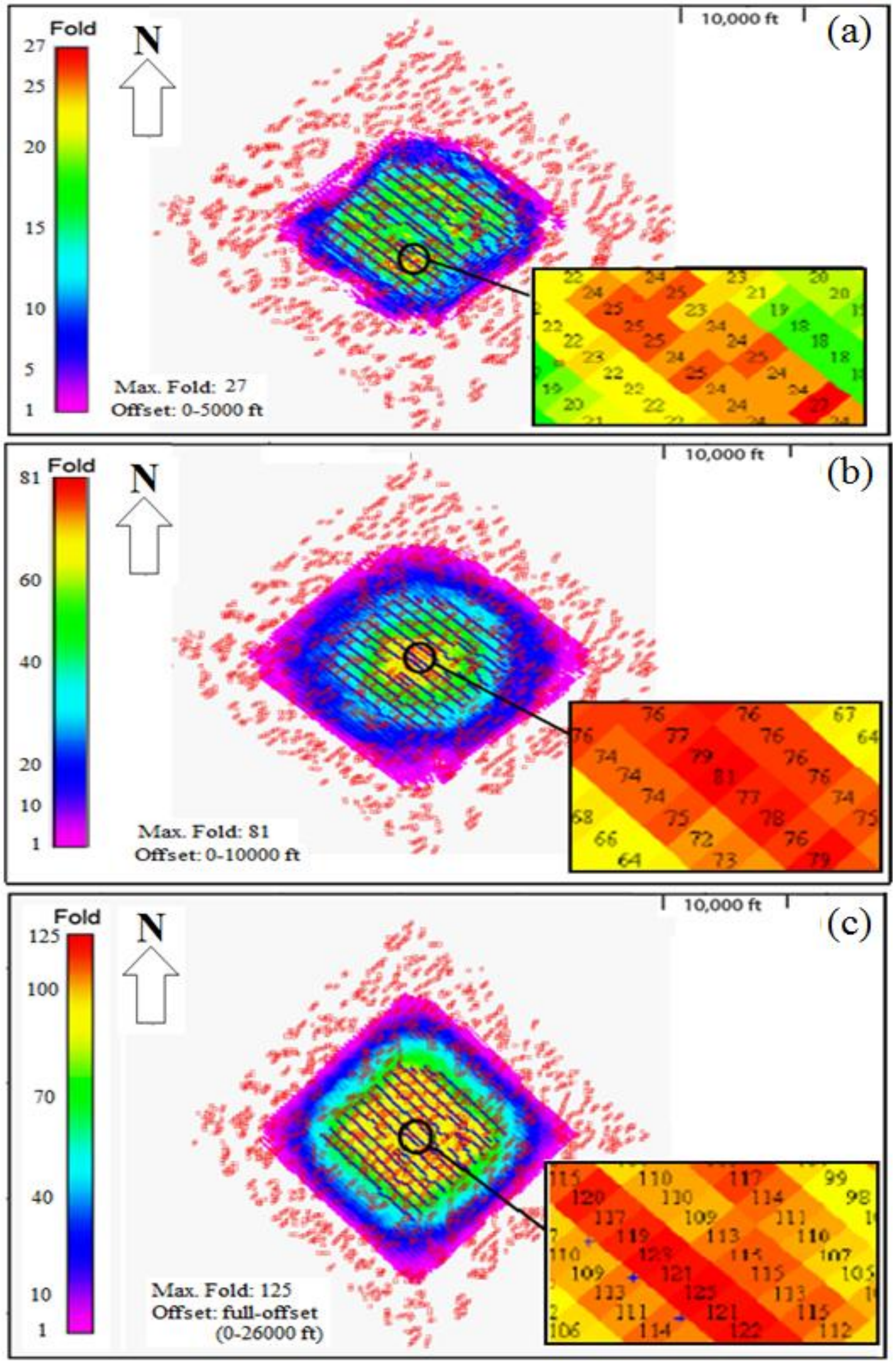

Figure 54: CMP fold statistics for different offset intervals: 0-5000 ft offset (a), 0-10000 ft offset (b), and full offset (c) for actual post-survey geometry that was used.

The effects of station randomization on survey attributes are more significant for converted-wave data than for CMP data. CCP data tend to have greater acquisition imprints than do CMP data. Thus the reduction of erratic CCP fold values caused by data-acquisition footprints is more obvious when station randomization is introduced into an acquisition geometry (Alkan, 2007). The most powerful evidence of the advantage of station randomization is the effect on source-receiver offset and source-receiver azimuths. Regular station geometry causes large offset outliers. Randomization of station coordinates eliminates these outliers. Distributions of source-receiver offsets for planned and actual acquisition geometries are demonstrated in Figure 55.

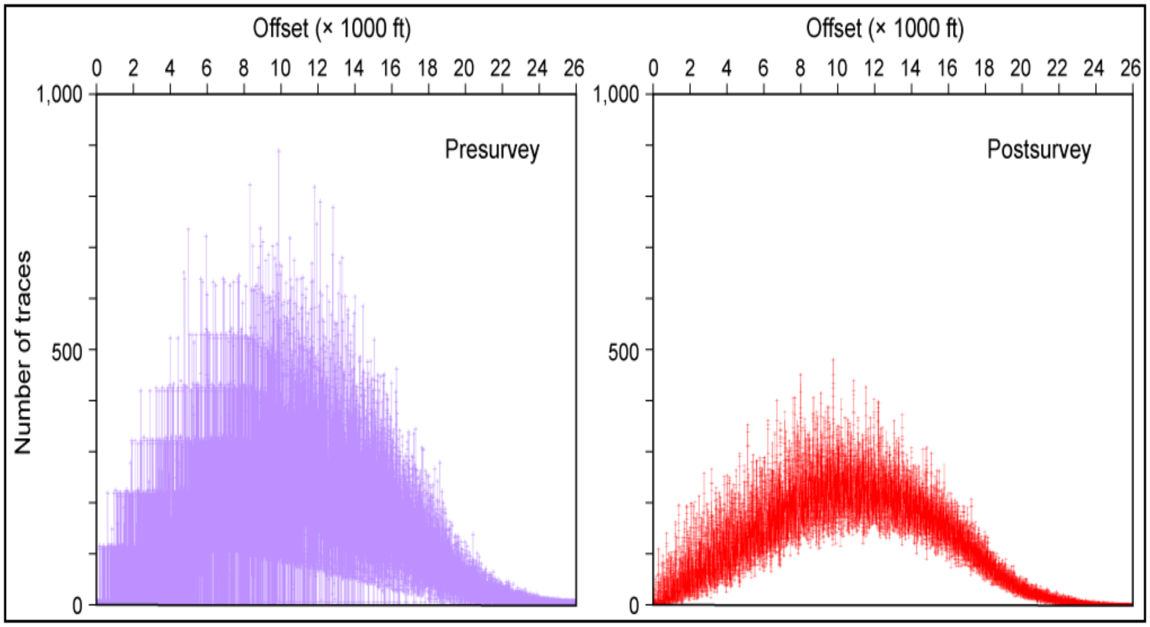

Figure 55: Distribution of source-receiver offsets for the pre-survey, regular-geometry design (left) that was planned for deployment, and for the post-survey, random-station geometry that was actually implemented (right).

Figures 56 and 57 present CCP stacking fold maps created by regular and random station geometry conditions (Figure 52). These displays demonstrate how fold varies between stacking bins for P-SV converted shear wave-mode data (fast and slow shear wave-modes).

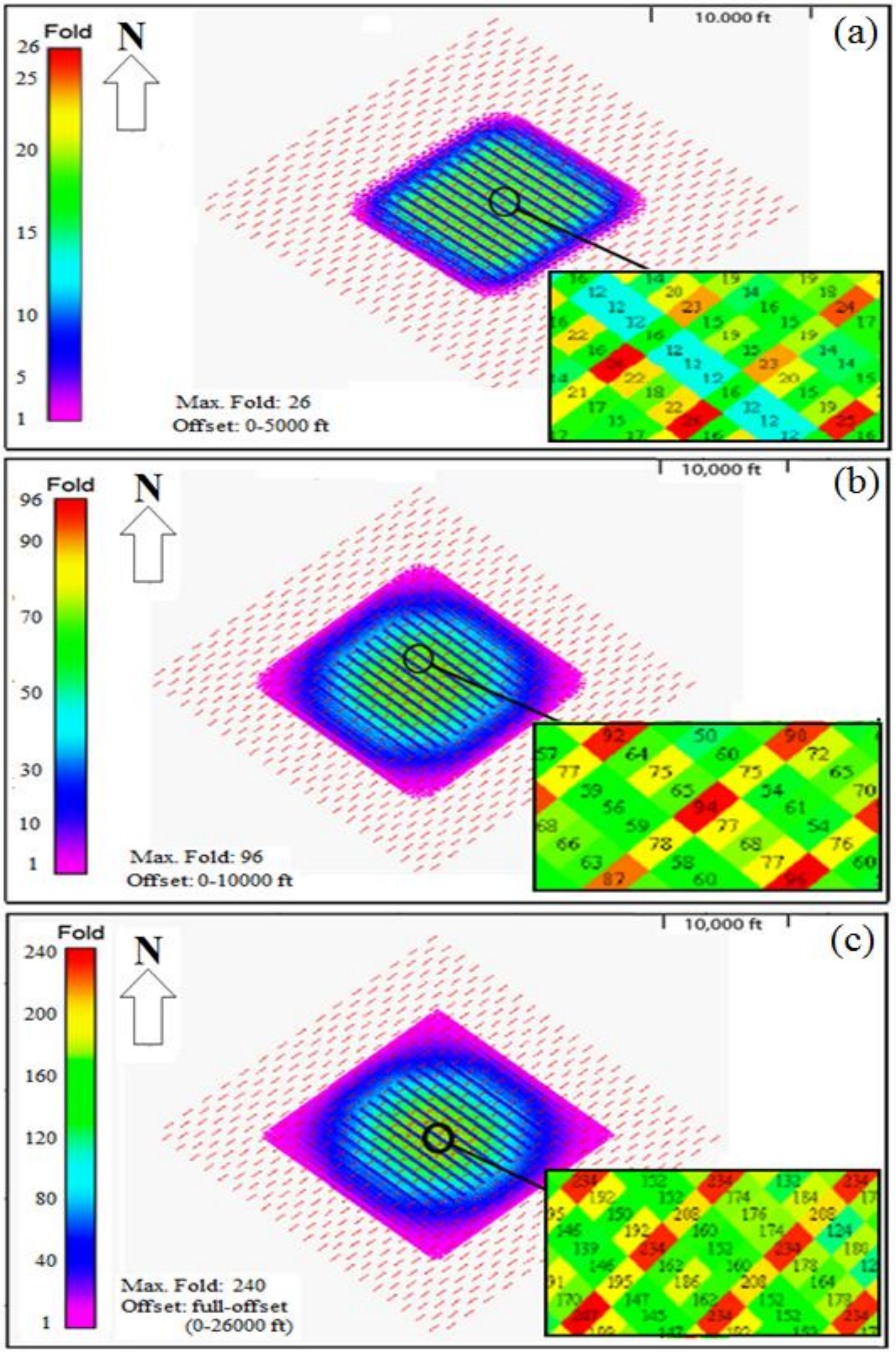

Figure 56: CCP fold statistics for P-SV data at different offset intervals: 0-5000 ft (a), 0-10000 ft (b), and full offset ranges (c) used for pre-survey planning.

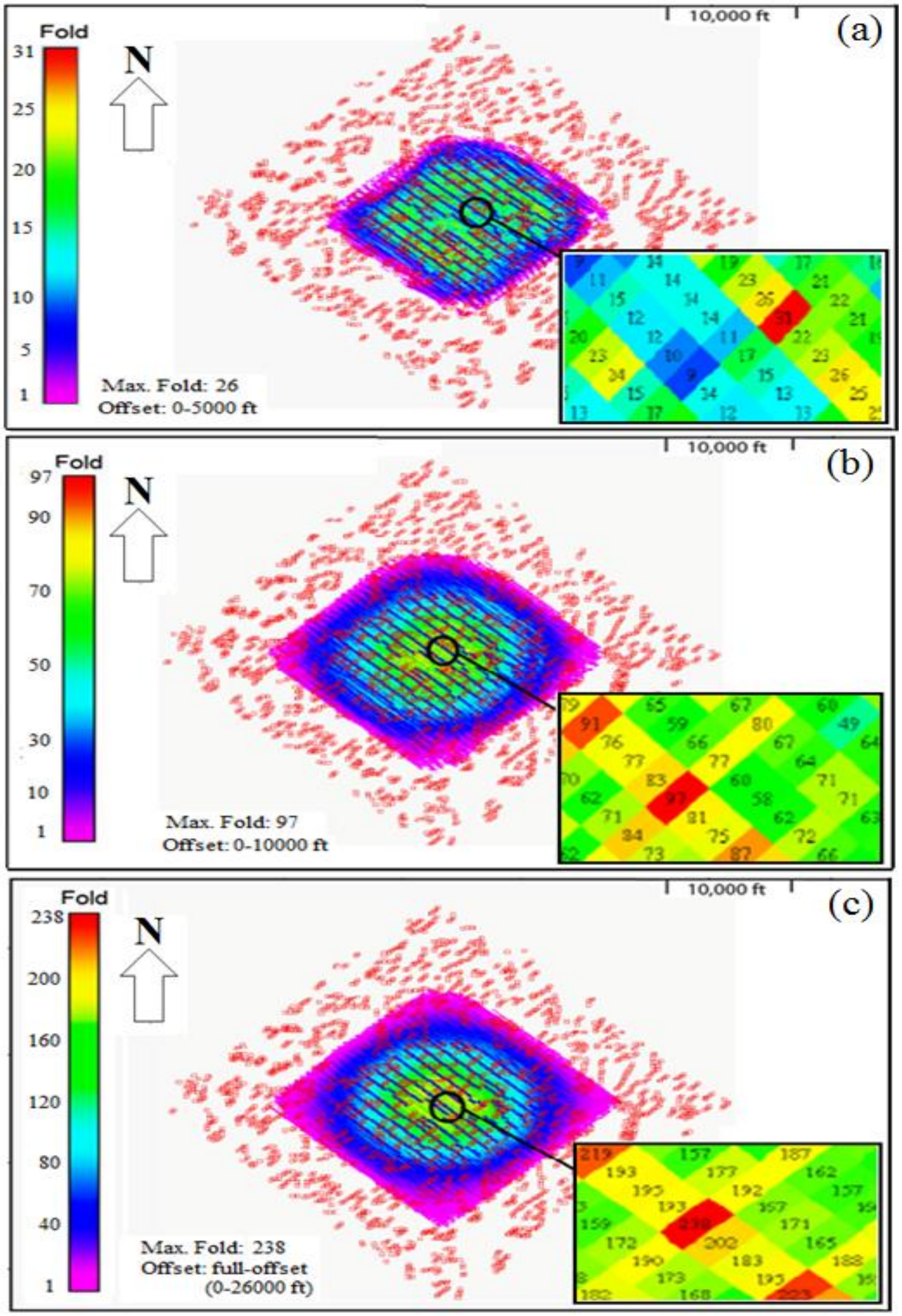

Figure 57: CCP fold statistics for P-SV data at different offset intervals: 0-5000 ft (a), 0-10000 ft (b), and full offset ranges (c) for actual post-survey geometry that was used.

As dictated by wave propagation theory, small variations in V_p/V_s may result in large variations on CCP fold maps. Several V_p/V_s values were assumed to examine the influence of velocity ratio on CCP fold distribution. A velocity ratio of 1.6 was finally used for CCP fold calculations because dipole sonic log data analysis suggested a velocity ratio of 1.6 is appropriate.

My PhD research included an analysis of one wave-mode, the SV-P mode that has not been investigated in the past. This analysis involved only a study of SV-P data acquisition and did not include processing and interpreting SV-P data. The SV-P converted wave mode propagates according to the same wave physics as does the P-SV mode. A V_P/V_S velocity ratio of 1.6 was also assumed for the calculation of SV-P fold, as was done for P-SV fold calculations.

A principal difference between P-SV and SV-P data generated by a given source-receive pair is that the common-conversion point for the P-SV mode is closer to the receiver station than to the source station; whereas, the common-conversion point for the SV-P mode is closer to the source station than to the receiver station.

As demonstrated in Figures 58 and 59, for the acquisition geometry used in Bradford County, the surface area where source stations are deployed is larger than the area where receivers are deployed. Therefore, the image area imaged by SV-P data is larger than the area imaged by P-SV data (Figs. 56 and 57). Fold values for SV-P data were calculated using commercial software designed for P-SV data and simply exchanging the coordinates of source stations and receiver stations were exchanged. Figures 58 and 59 show CCP fold maps calculated for the SV-P mode.

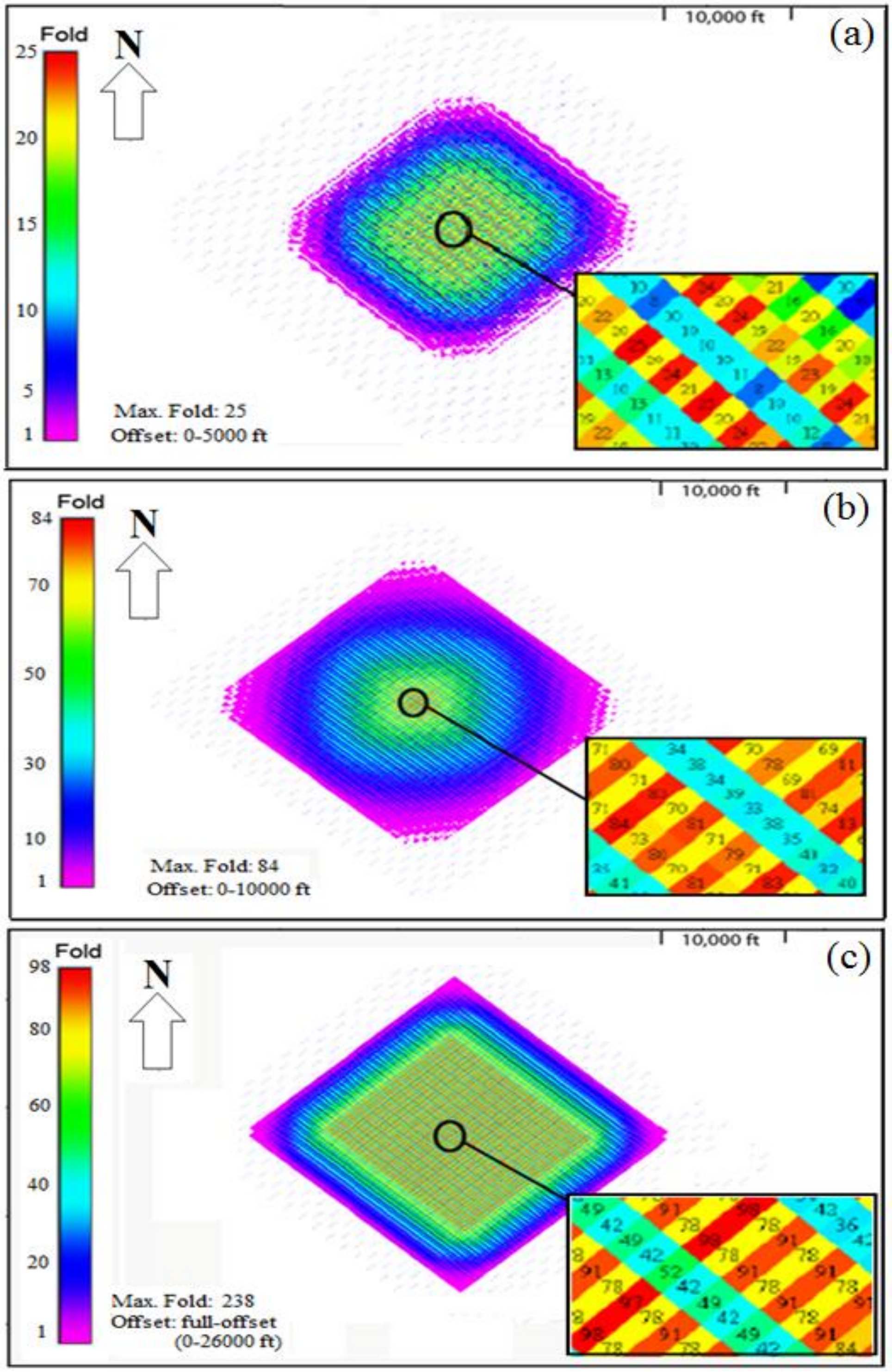

Figure 58: CCP fold statistics for SV-P data at different offset intervals: 0-5000 ft (a), 0-10000 ft (b), and full offset ranges (c) used for pre-survey planning.

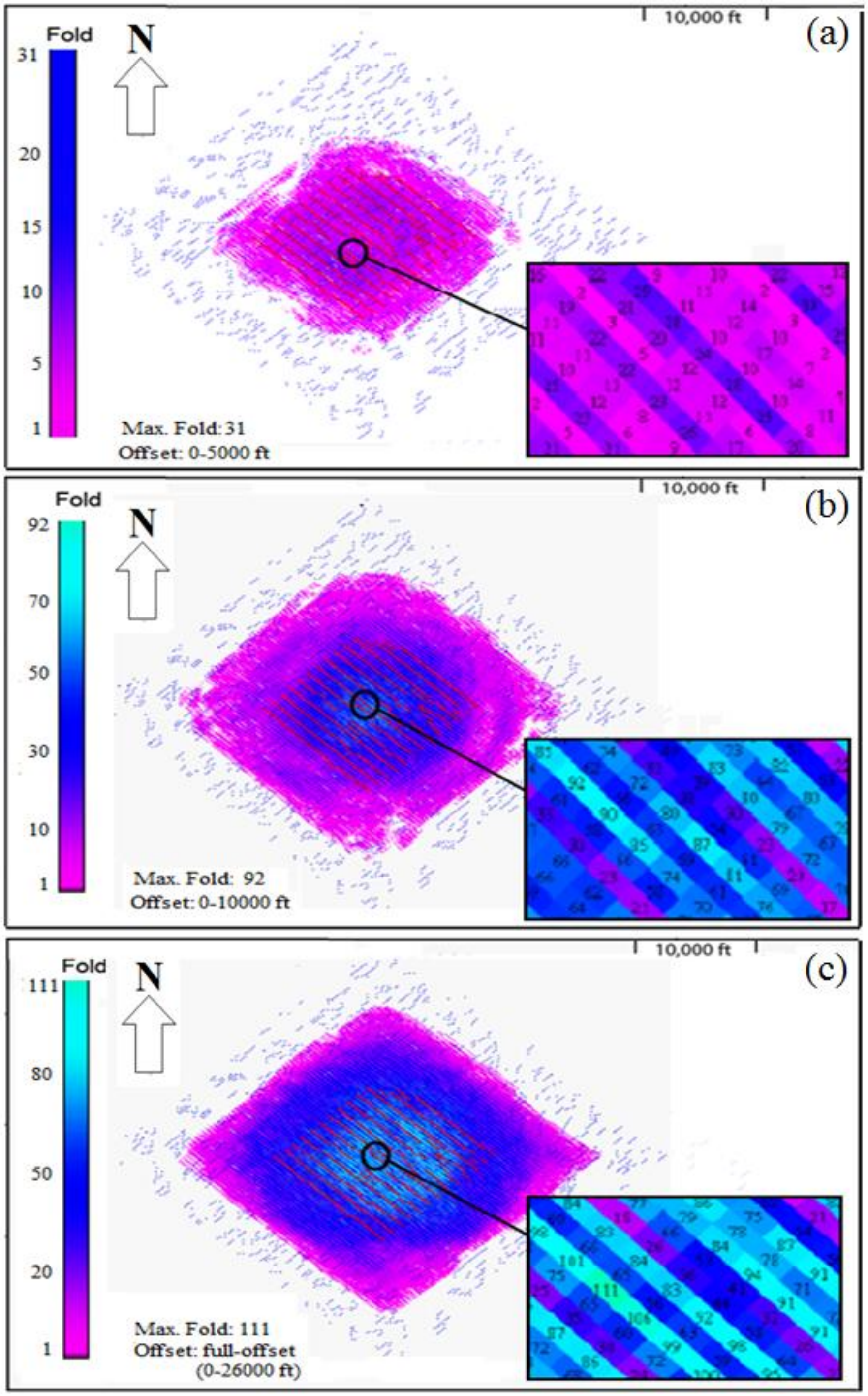

Figure 59: CCP fold statistics for SV-P data at different offset intervals: 0-5000 ft (a), 0-10000 ft (b), and full offset ranges (c) for actual post-survey geometry that was used.

SHOT GATHERS AND INITIAL DATA PROCESSING

Figure 60 illustrates common-shot gathers created from responses of three-component (vertical, radial-horizontal, and transverse-horizontal) surface geophones after rotation analysis is applied to orient radial geophones directly at a source station. The response of each component of the surface-based sensors and the interpreted target reservoir interval are illustrated on Figure 61.

Although it can be difficult to extract reflected P and S wavefields embedded in some multicomponent data, inspection of these shot gathers demonstrated that signal-to-noise ratio of S reflections is high for this particular seismic survey.

In addition to VSP and surface-based raw field data, P-P and two P-SV data volumes produced by Geokinetics were also analyzed. Interpretations and multi-attribute analysis of these 3D data volumes are illustrated and discussed in Chapter 5.

Figures 62 and 63 illustrate examples of vertical sections through the 3D image volumes. These vertical-section displays demonstrate the quality of two major wavefield images (compressional and converted shear-wave modes) and verify that the targeted Marcellus reservoir interval is imaged with high-quality data on both the P-P and the P-SV volumes. Selected horizons, faults, major lithologic facies, and other interpreted geologic units are presented in Chapter 5.

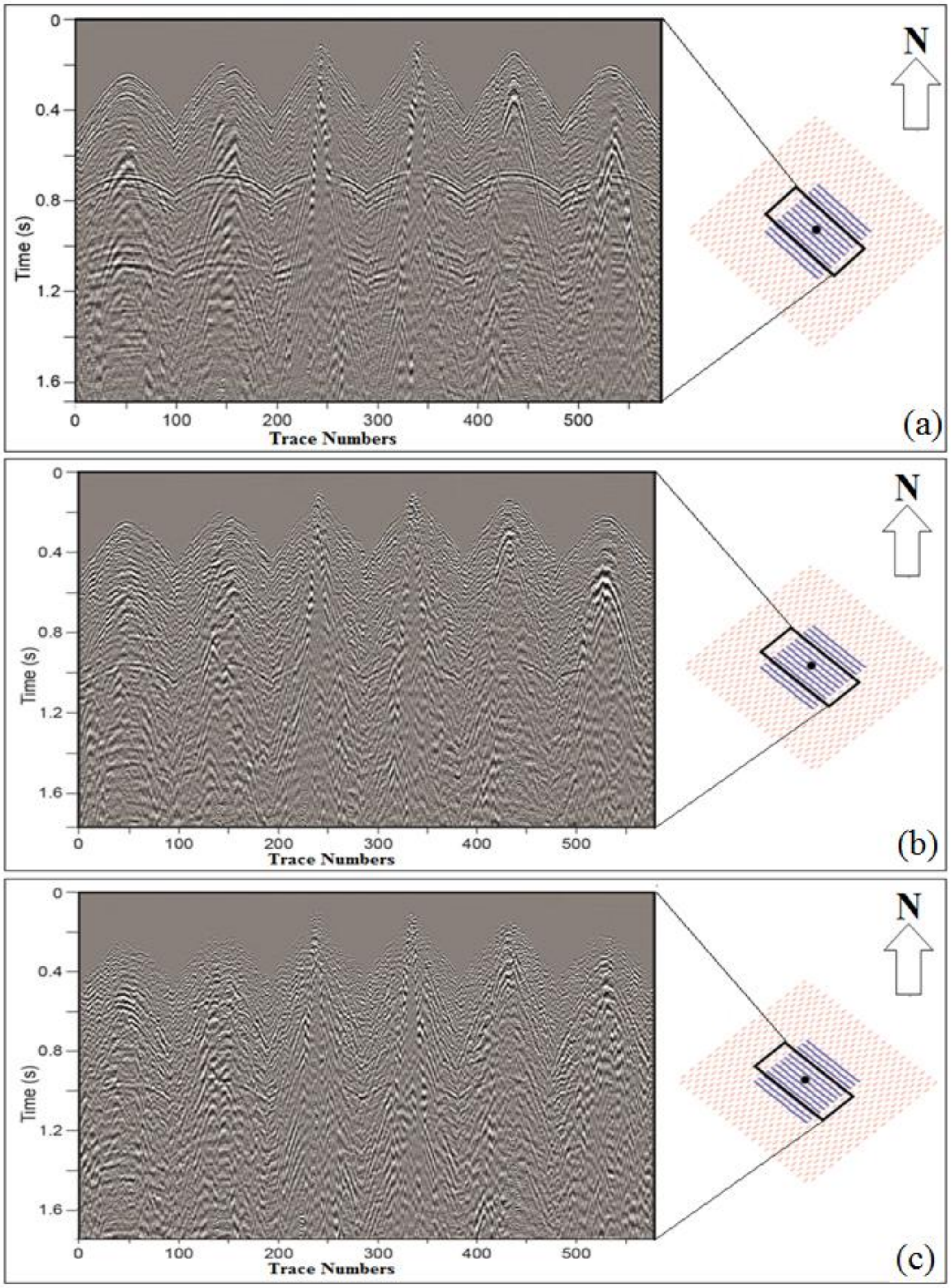

Figure 60: Shot gathers of responses of (a) vertical geophones, (b) radial-horizontal geophones, and (c) transverse-horizontal geophones. The solid dot in the data-acquisition grid defines the location of the calibration well.

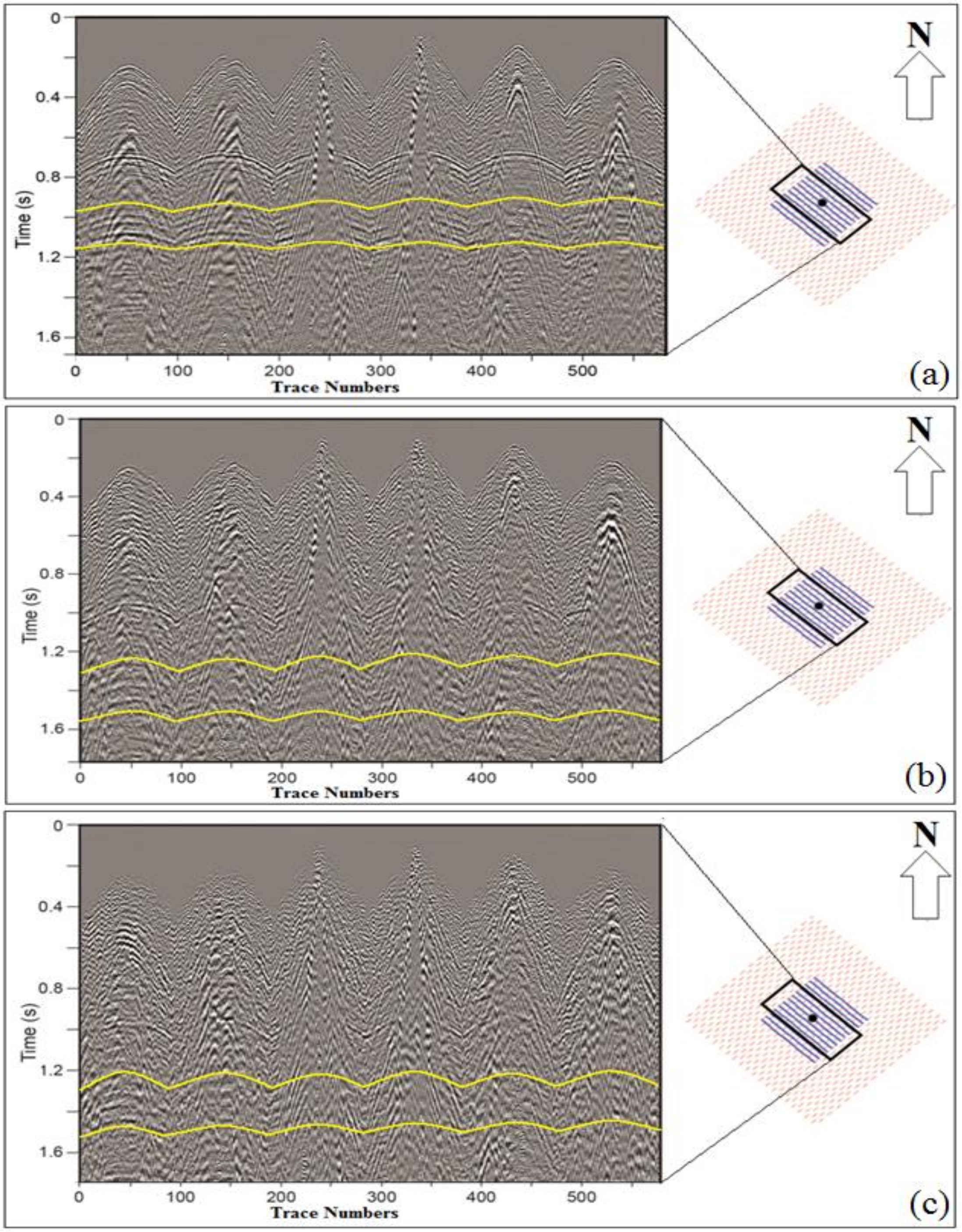

Figure 61: Marcellus reservoir interval interpreted from trace gathers of (a) vertical geophones, (b) radial-horizontal geophones, and (c) transverse-horizontal geophones. Uninterpreted data are shown as Figure 60. The solid dot in the data-acquisition grid defines the location of the calibration well.

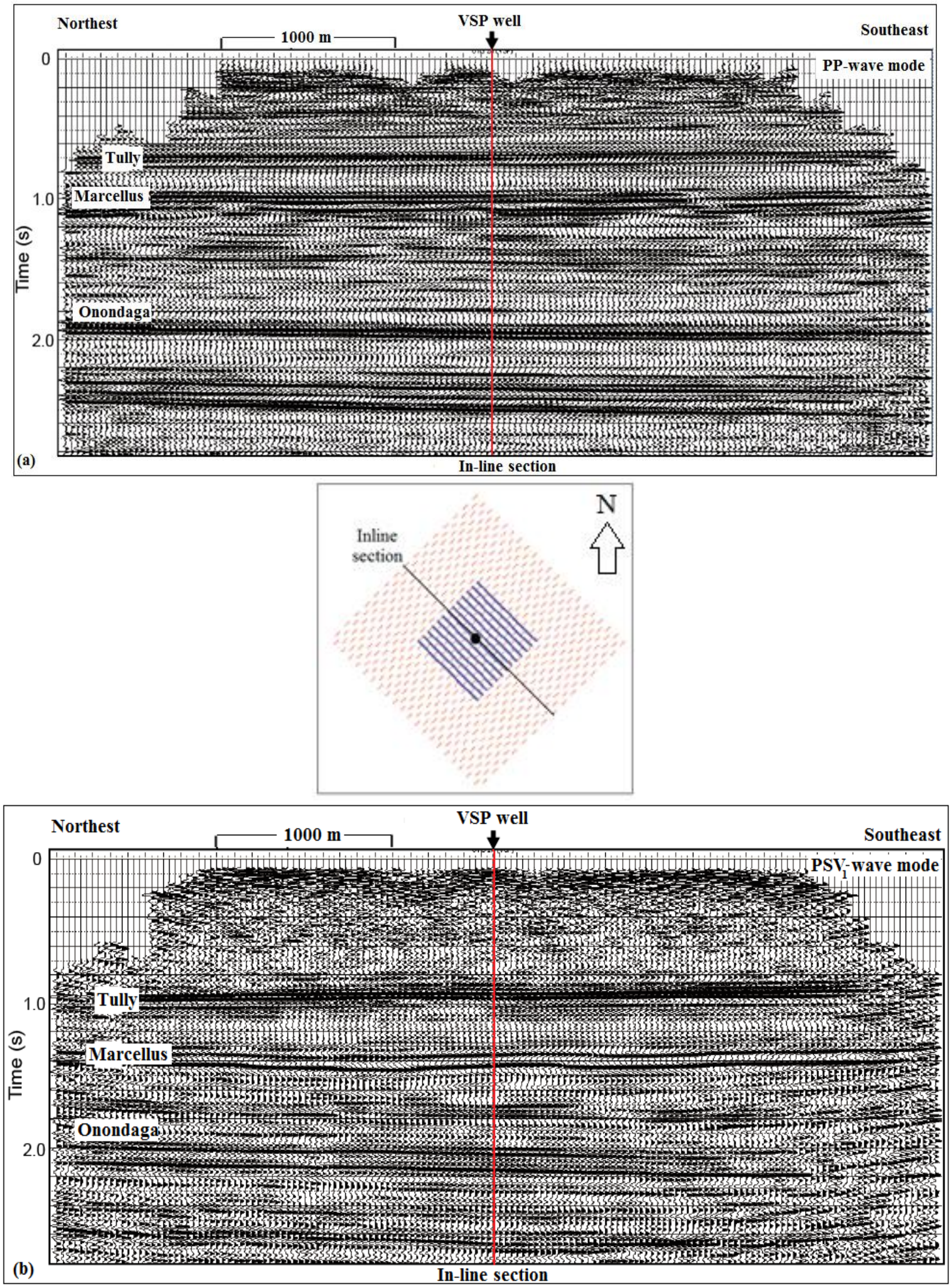

Figure 62: Vertical inline slices of (a) P-P, and (b) P-SV_1 volumes constructed from surface-based seismic data. Major geologic units interpreted from 3C3D seismic data are labeled. The solid dot in the data-acquisition grid defines the location of the calibration well.

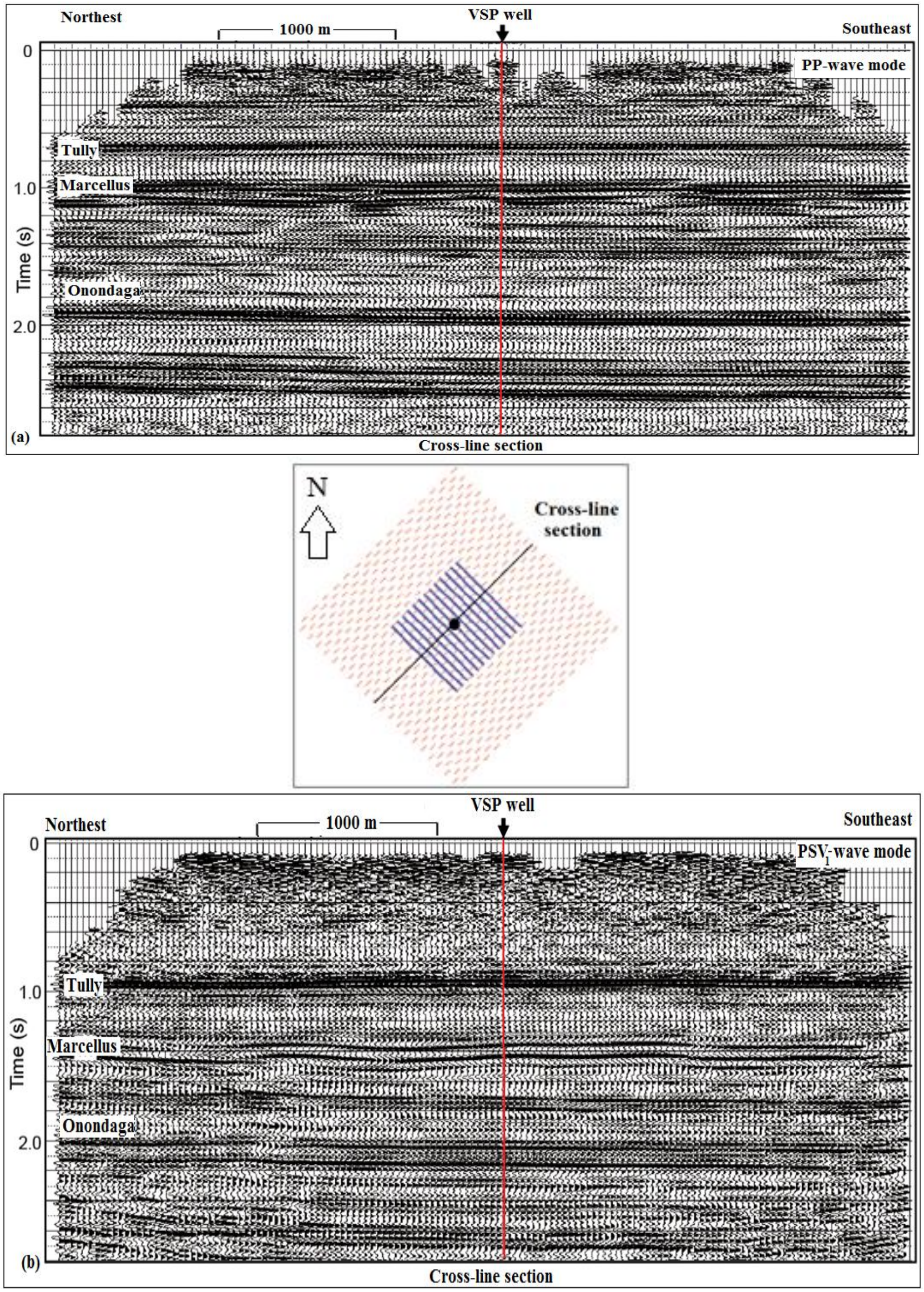

Figure 63: Vertical cross-line slices of (a) P-P, and (b) P-SV$_1$ volumes constructed from surface-based seismic data. Major geologic units interpreted from 3C3D seismic data are labeled. The solid dot in the data-acquisition grid defines the location of the calibration well.

DIRECT SHEAR WAVES FROM VERTICAL-FORCE SOURCES

As explained in Chapter 2, a direct SV-mode is generated by a vertical-force source (Figures 24-26, and 34-36). It is important to understand this concept because using vertical-force sources reduce multicomponent data-acquisition cost by providing all elastic wave modes (P, SV and SH). These direct wave modes have previously been provided only when both vertical-force and horizontal-force sources are deployed. The value of a direct SV-SV wave mode is that the data can be processed using simple CMP concepts. Figure 64 shows the vertical slice of a stacked section of a SV-SV data volume created by researchers in Exploration Geophysics Laboratory at the Bureau of Economic Geology. These data were not interpreted in this study because additional processing is needed to reach an acceptable level of image quality.

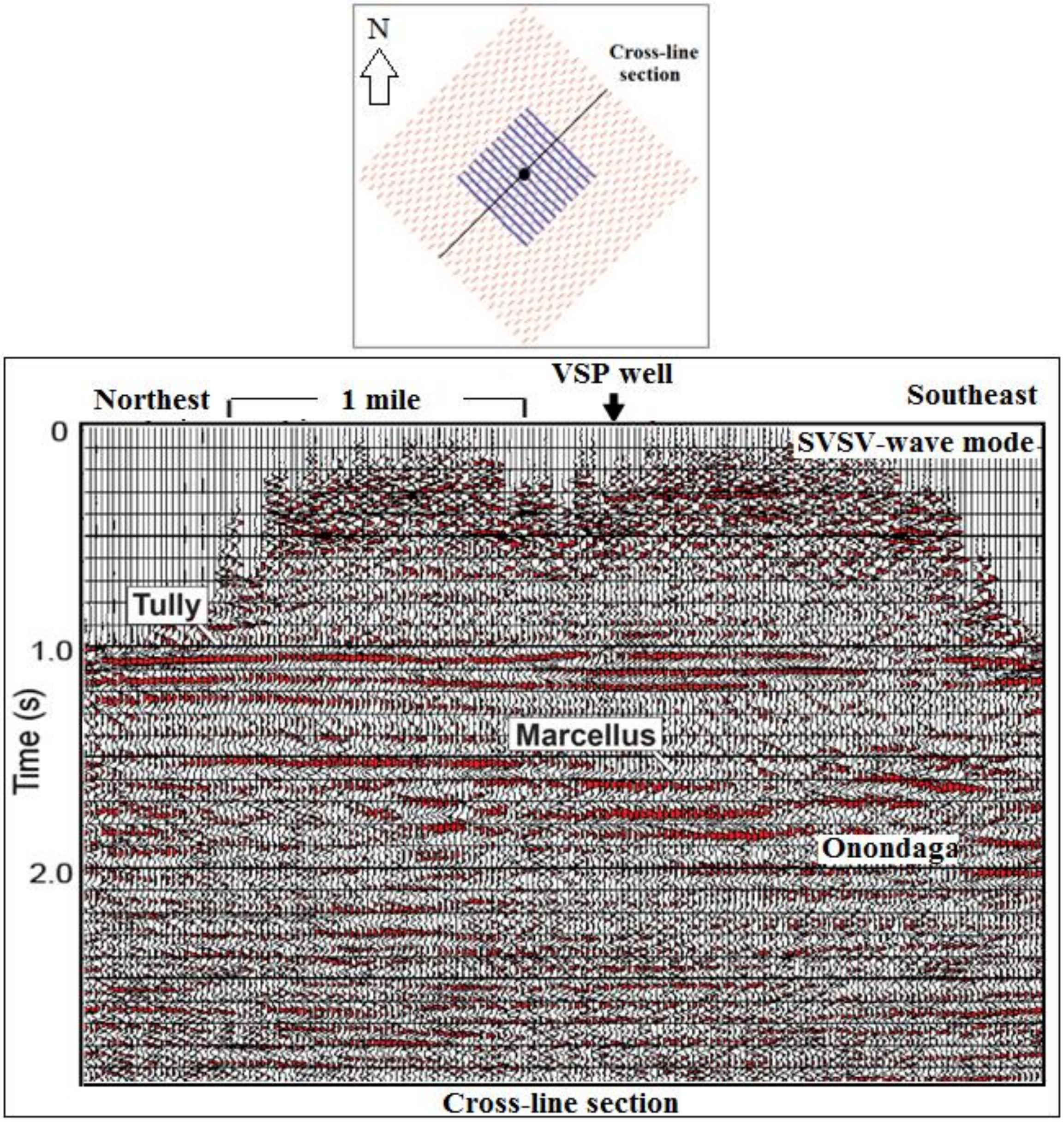

Figure 64: Vertical slices through cross-line direction SV-SV volume constructed from surface-based seismic data and major geologic units interpreted from 3C3D seismic data.

Vertical Seismic Profile Data

Vertical seismic profile (VSP) data are valuable for an accurate and effective interpretation of multicomponent seismic data (Hardage et al. 2011). Fundamental distinctions between compressional waves and shear waves are differences in P and S wave-mode propagation velocities and differences in P and S reflection character at targeted interfaces. Compressional-wave data position a geologic target in an image-time window that is significantly different from the image-time window where that geologic target is positioned by shear-wave data. As a result, one of the challenges in interpreting multicomponent seismic data are to depth register compressional and shear wave images and to correlate log-based stratigraphic depth intervals with their associated P- and S-wave image-time windows. Both of these challenges can be overcome using information provided by VSP data. VSP data allow interpreters to accurately position geologic depth on surface-based multicomponent data by defining P- and S-wave image times as a function of depth and by confirming phase and amplitude characteristics of and S reflection wavelets at interfaces of interest.

Figures 60-63 illustrate where the VSP well used in this study was positioned relative to the planned positions of source and receiver stations used to record the Bradford County survey. An extensive set of VSP data was acquired. Figure 65 shows source stations utilized in VSP data acquisition consisting of:

- An outer walk-around survey involving 73 source stations that allowed P and S wave propagation to be analyzed at large offsets of 1 to 1.5 mi (1.6 to 2.4 km) in azimuth increments of approximately 5 degrees. Source stations occupied by this walk-around are shown by red station labels on Figure 65.

- An inner walk-around survey involving six source stations that allowed P and S velocities and images to be created at moderate offsets of 0.5 to to.75 mi (0.8 to 1.2 km) in azimuth increments of approximately 60 degrees. These inner walk-around source stations are shown as yellow flags on Figure 65.
- An 18-station walk-away profile extending southeast from the receiver well approximately 1.5 mi (2.4 km). Walk-away source stations are shown as blue station flags (Fig. 65).
- An orthogonal-azimuth source station pair positioned approximately 0.8 mi (1.3 km) from the receiver well (green station flags, Fig. 65).
- A conventional zero-offset VSP with a source positioned at the walk-away station closest to the well.

A vertical vibrator was used to generate all of these VSP data. Wavefields generated by the orthogonal-azimuth vibrator pair (highlighted by the green flags on Figure 65) will be used to demonstrate the quality of the VSP data. Data generated at the southwest vibrator source are shown on Figure 66, and data generated at the southeast station are shown on Figure 67.

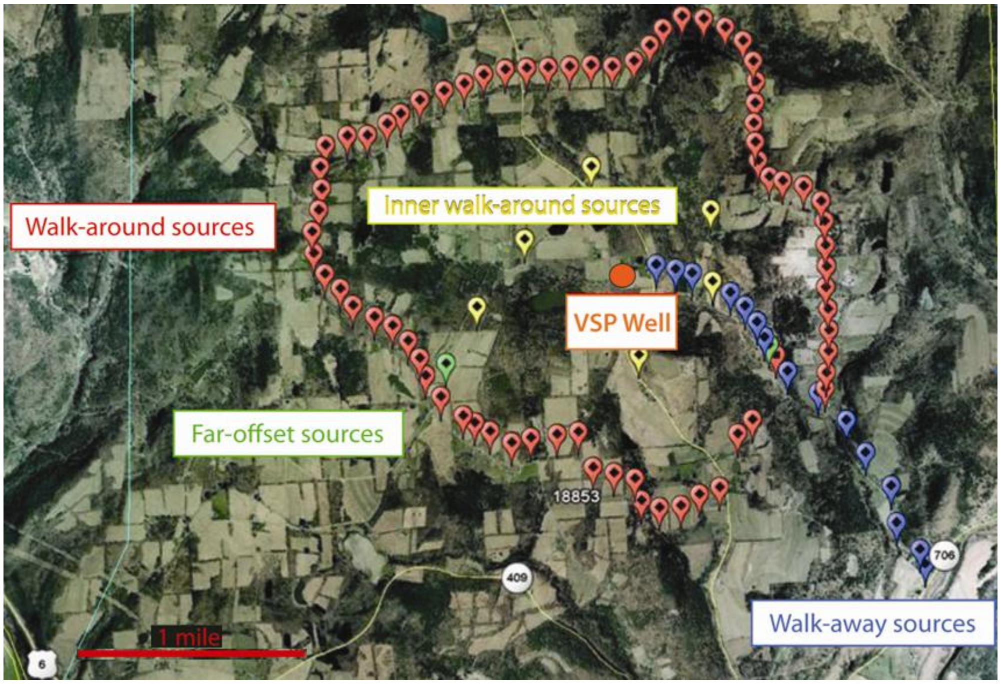

Figure 65: Source stations utilized in VSP data acquisition. Data acquisition included a 73-station outer walk-around (red stations), a 6-station inner walk-around (yellow stations), an 18-station walk-away (blue stations), a 2-station orthogonal-azimuth pair (yellow stations), and a zero-offset station (blue station closest to the well).

After receiver rotation was applied, VSP data were transformed to proper P and S coordinate systems. Compressional, radial-shear (SR), and transverse-shear (ST) wave modes obtained after receiver rotation are demonstrated in Figures 66b and 67b. Downgoing, and upgoing components of P- and S-wavefields are labeled to show the high quality of multicomponent seismic data at this location.

Walkway VSP data acquired in Bradford County are particularly important for defining behavior of the different seismic wave modes (P, SV, SH), because this data provide radiation patterns of elastic wave modes by repeating data acquisition by downhole receivers at several offset source stations. As described by Hardage et al.

(2011), velocity behavior of SH and SV shear wave modes can be illustrated by analyzing travel-time behavior along different takeoff angle from a same station. Figure 67 demonstrates that SH and SV wave modes recorded in radial and transverse receiver components propagate with different velocities at different takeoff angle from a source station. These results conform to the physics of wave propagation in horizontally layered media published by Levin (1979) as demonstrated in Figure 68 and 69 by Hardage et al. (2011).

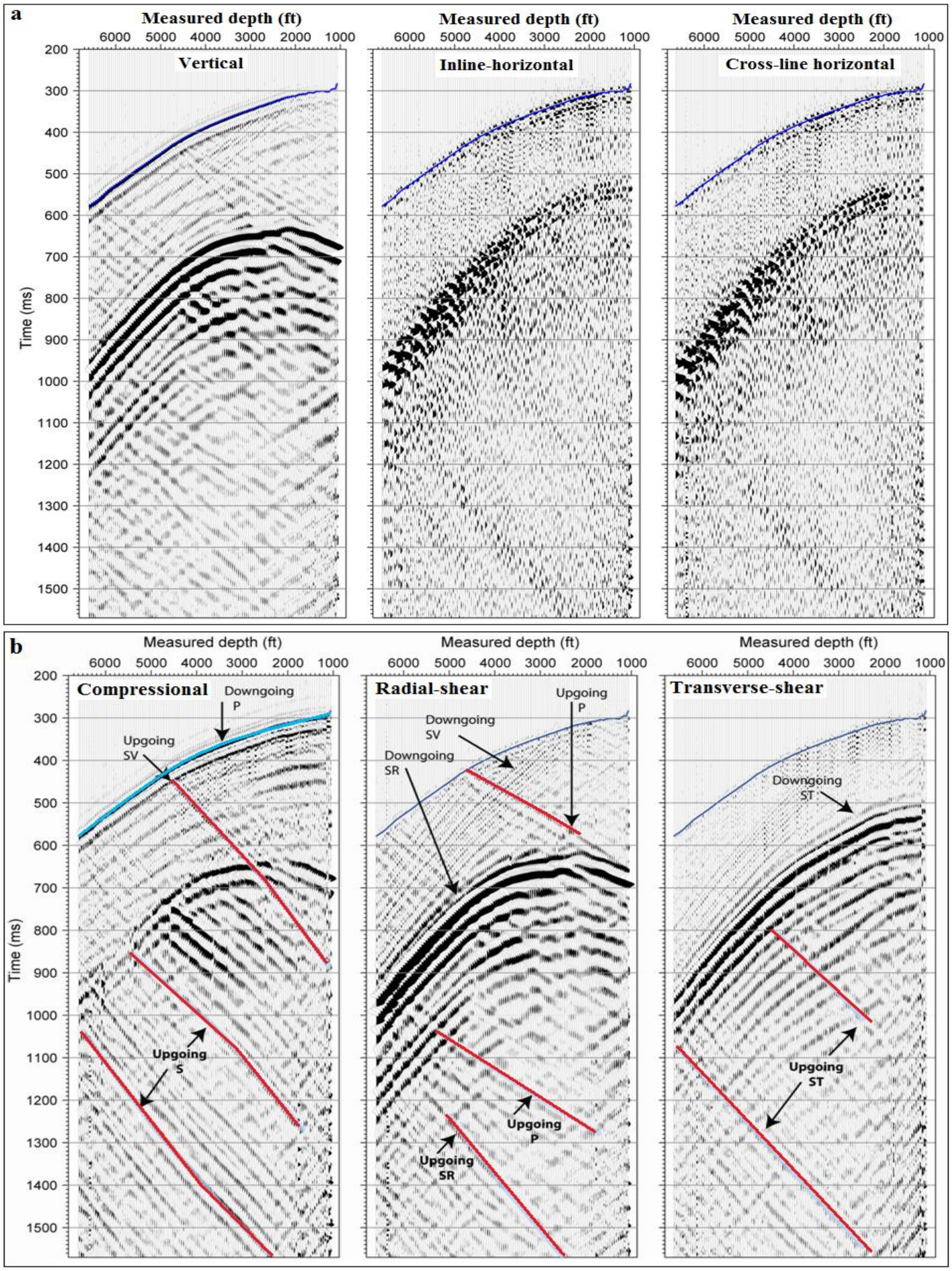

Figure 66: VSP data acquired when the source was at the green-flag station southwest of the receiver well. (a) Raw data as recorded. (b) Data after coordinate rotation to P, S-radial (SR), and S-transverse (ST) data space.

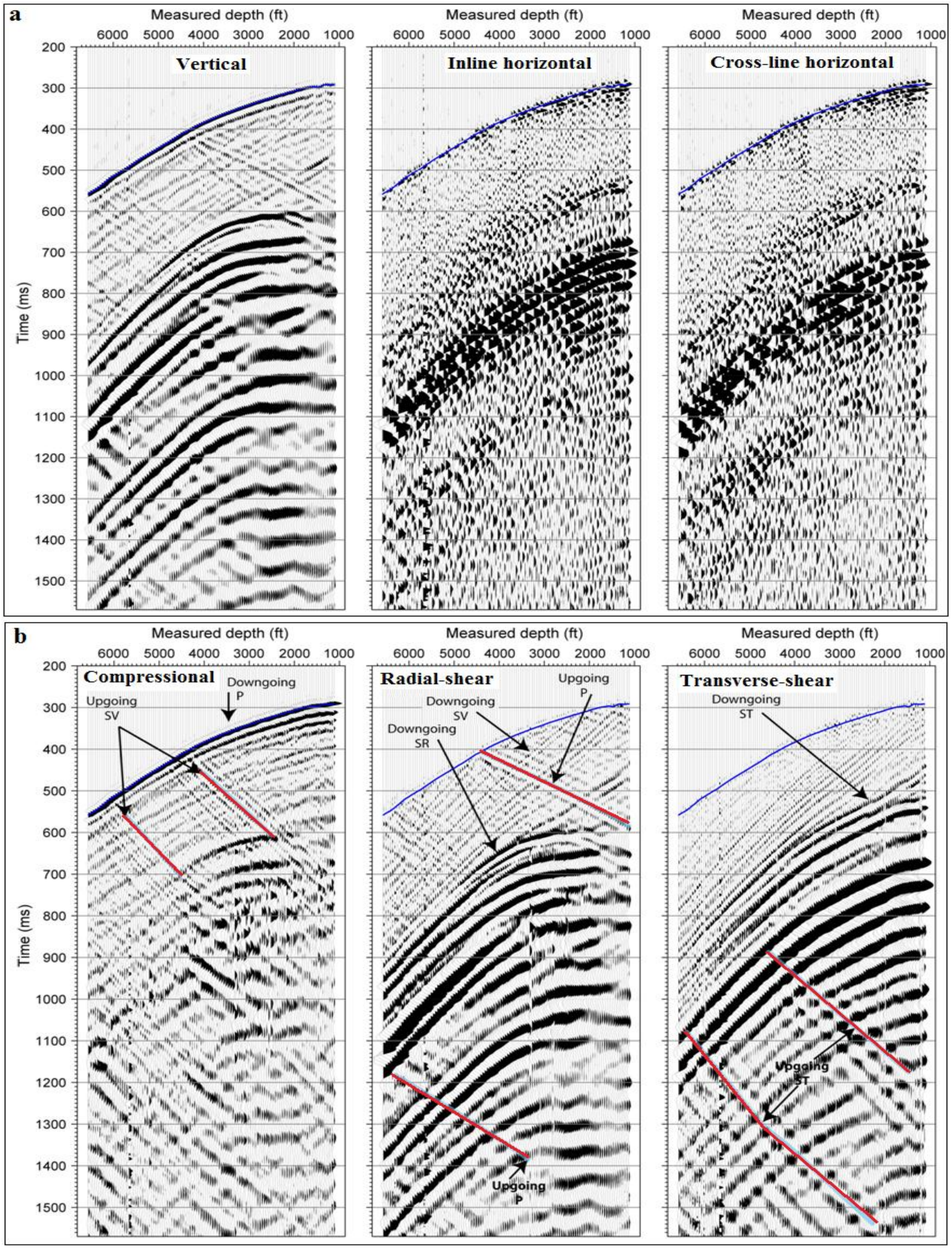

Figure 67: VSP data acquired when the source was at the green-flag station southeast of the receiver well. (a) Raw data as recorded. (b) Data after coordinate rotation to P, S-radial (SR), and S-transverse (ST) data space.

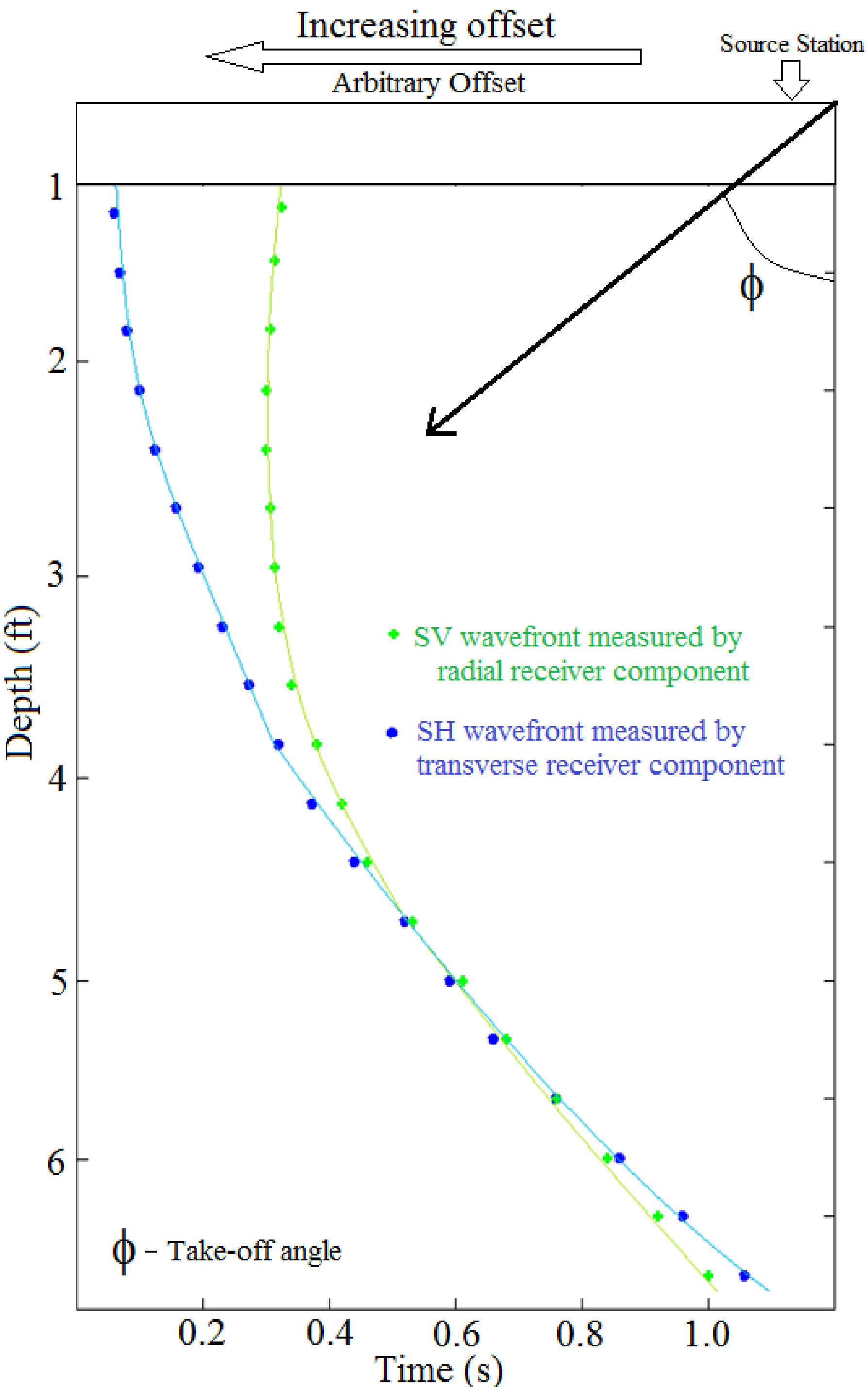

Figure 68: Comparison of SV and SH wavefronts recorded by radial and transverse receivers as shown in Figure 66 (a) and (b).

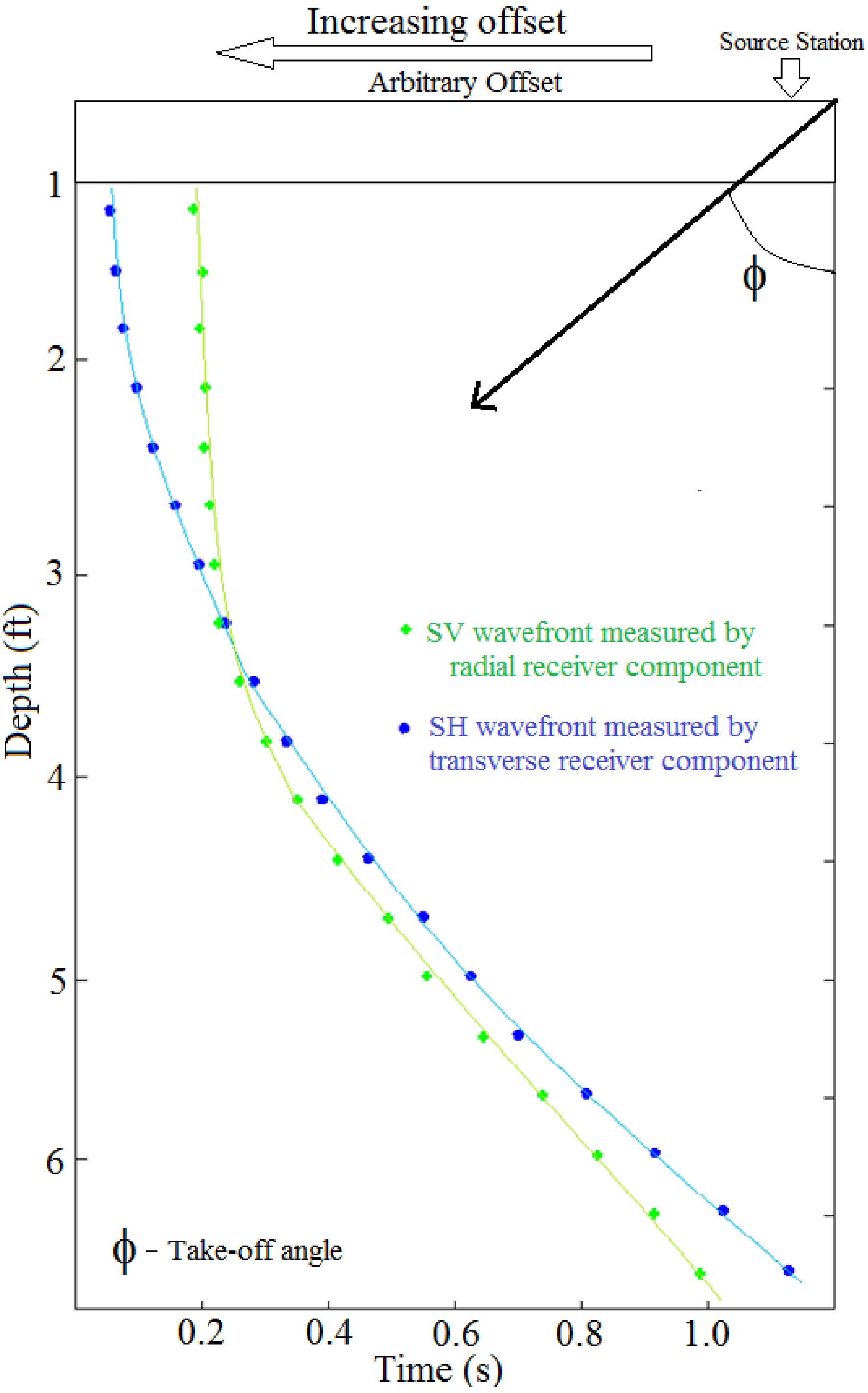

Figure 69: Comparison of SV and SH wavefronts recorded by radial and transverse receivers as shown in Figure 67 (a) and (b).

Data Processing Flows

The Free Unix Seismic Processing (Free USP) system released as an open source code by BP America Inc. was used to process Bradford County data. The data processing flow used to generate final volumes involved the following steps:

1. Determine wave-mode refraction statics separately for P and SV data and correct for the near surface.
2. Pick P-wave mode first arrivals and apply refraction statics. Repeat for SV mode.
3. Apply gain correction (geometrical spreading correction).
4. Apply 3D deconvolution.
5. Sort to CMP gathers
6. Perform velocity analysis
7. Apply NMO
8. Compute and apply residual statics.
9. Back out the NMO correction and compute residual statics again.
   (continue this loop to refine both NMO and residual statics).
10. Stack the data
11. Migrate the data after stack.

Picking P-wave direct arrivals was not as difficult as picking SV arrivals. Calculating refraction statics for SV data was difficult and results were poor. Essentially I have not been able to use the SV refraction picks to improve the statics computed by Geokinetics.

Therefore, RMS velocities were computed using supergathers that were 11x11 patches of CDPs centered on a specific CDP. This step provided 121 different CDP bins all added to form a single supergather. The statistics greatly improved the signal-to-noise ratio, and reflections were located and stacking velocities were computed.

Velocity filtering was applied to these super gathers to emphasize specific wavefields. The velocity filter was a hyperbolic Radon transform. Examples of shot gathers and semblance panels displaying NMO velocities for the pure compressional wave-mode (downgoing P and upgoing P wavefields), for the pure-SV shear wave-mode (downgoing SV and upgoing SV wavefields) and for the pure-SH shear wave-mode (downgoing SH and upgoing SH wavefields) are presented in Figures 70 - 75. These examples illustrate the characteristics of vertical, radial, and transverse gathers before and after velocity filtering. The P, SH, and SV velocity functions used to define the velocity-pass ranges of the hyperbolic radon transform velocity filter were derived from zero-offset VSP data acquired in the central-image VSP well.

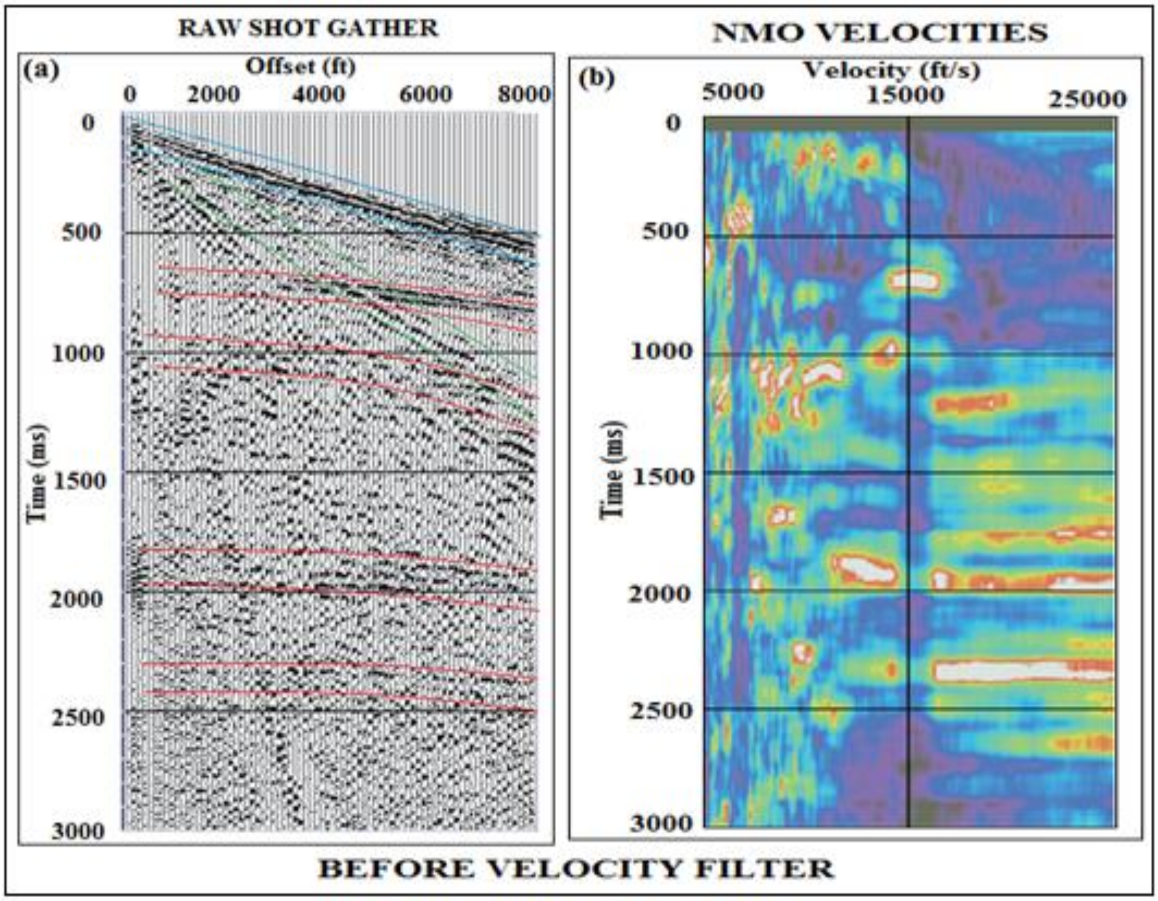

Figure 70: (a) Shot gathers of vertical-geophone data and (b) semblance panels displaying NMO velocity for pure compressional wave-mode (down-going P and up-going P wavefields) before velocity filtering.

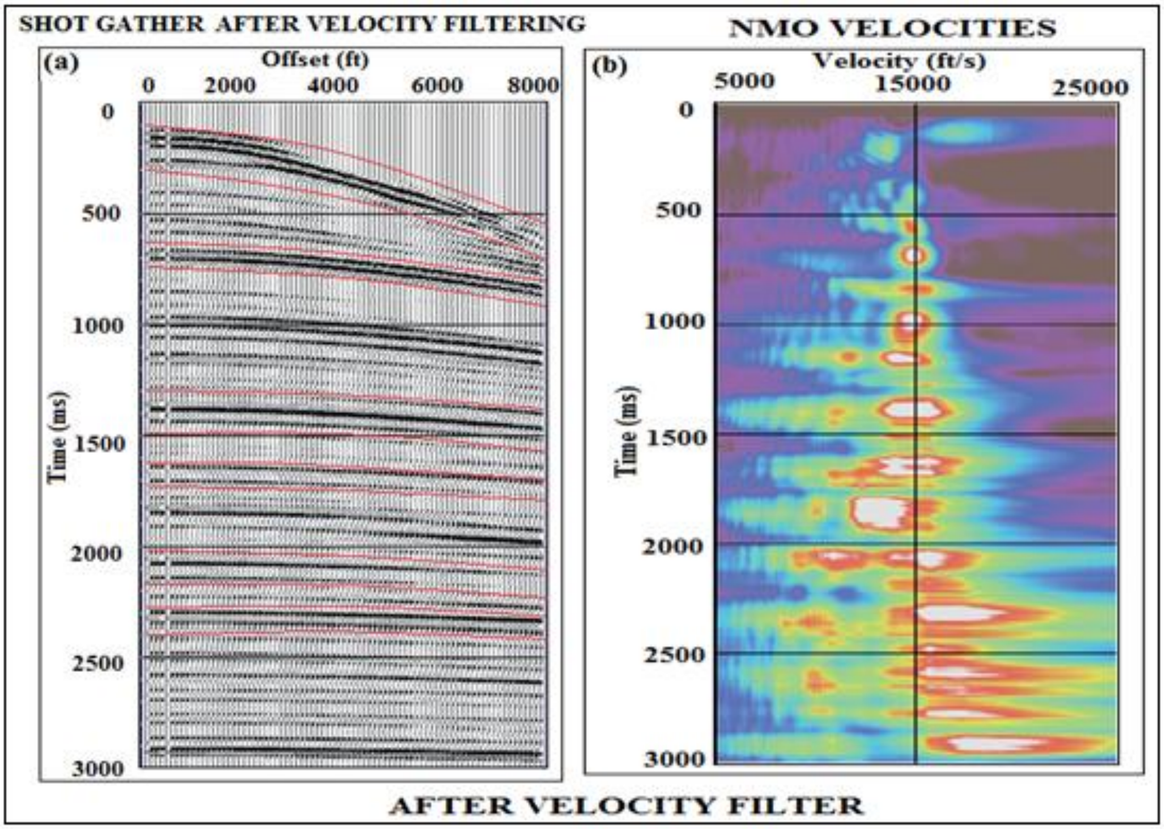

Figure 71: (a) Shot gathers of vertical-geophone data and (b) semblance panels displaying NMO velocity for pure compressional wave-mode (down-going P and up-going P wavefields) after velocity filtering.

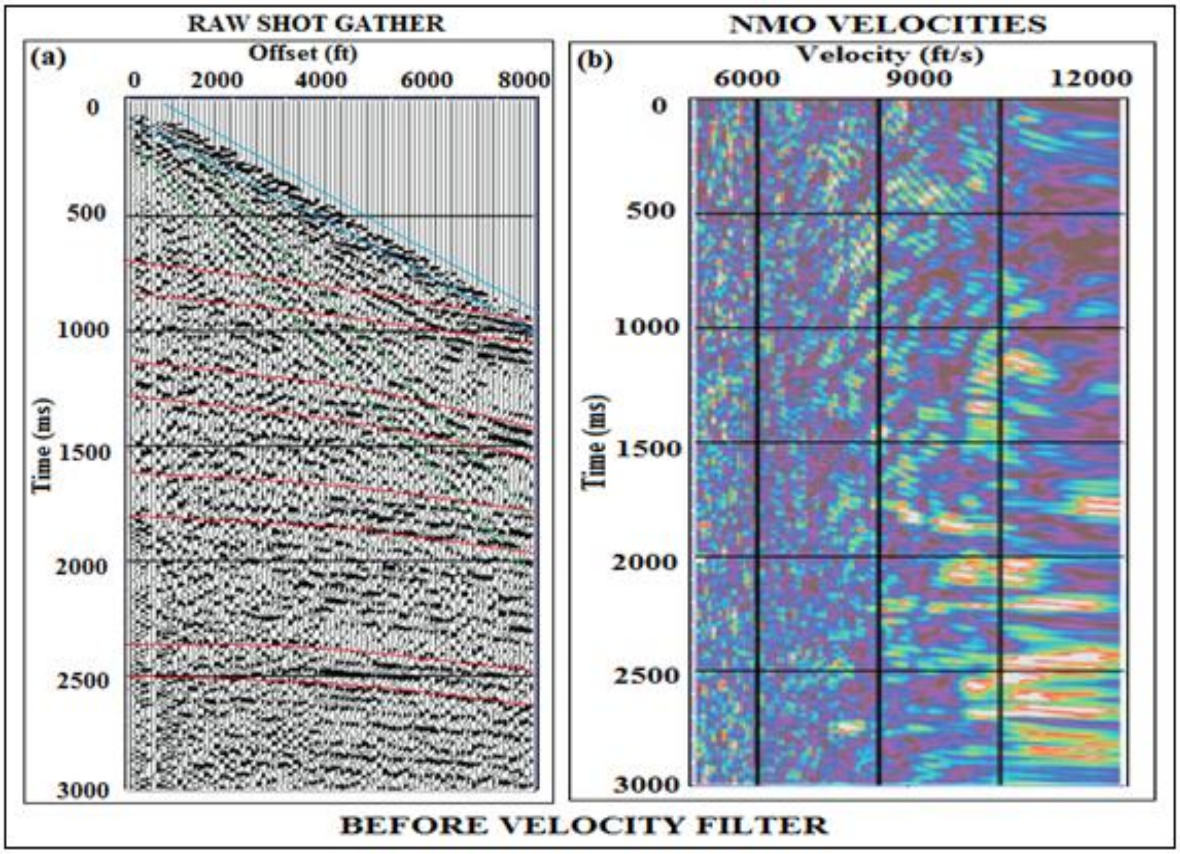

Figure 72: (a) Shot gathers of radial-geophone data and (b) semblance panels displaying NMO velocity for pure shear wave-mode (down-going SV and up-going SV wavefields) before velocity filtering.

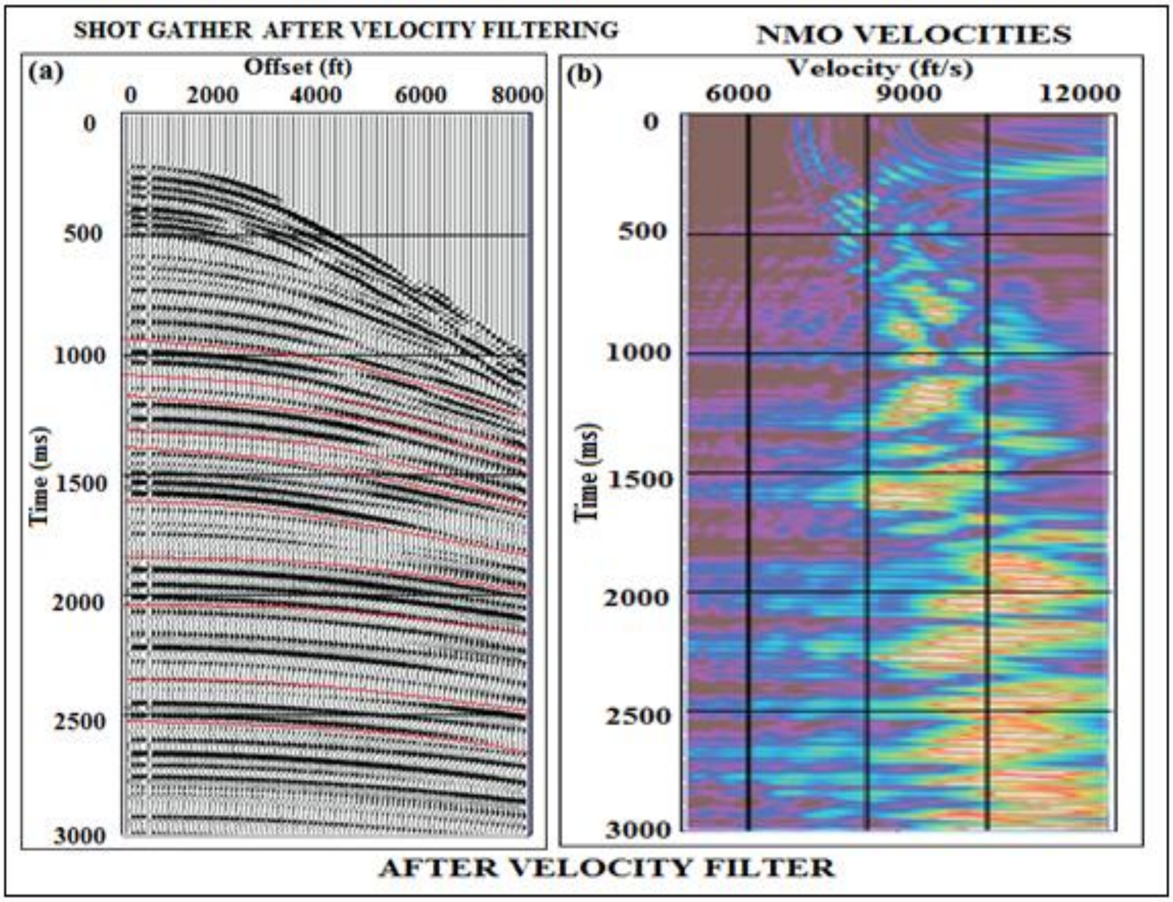

Figure 73: (a) Shot gathers of radial-geophone data and (b) semblance panels displaying NMO velocity for pure shear wave-mode (down-going SV and up-going SV wavefields) after velocity filtering.

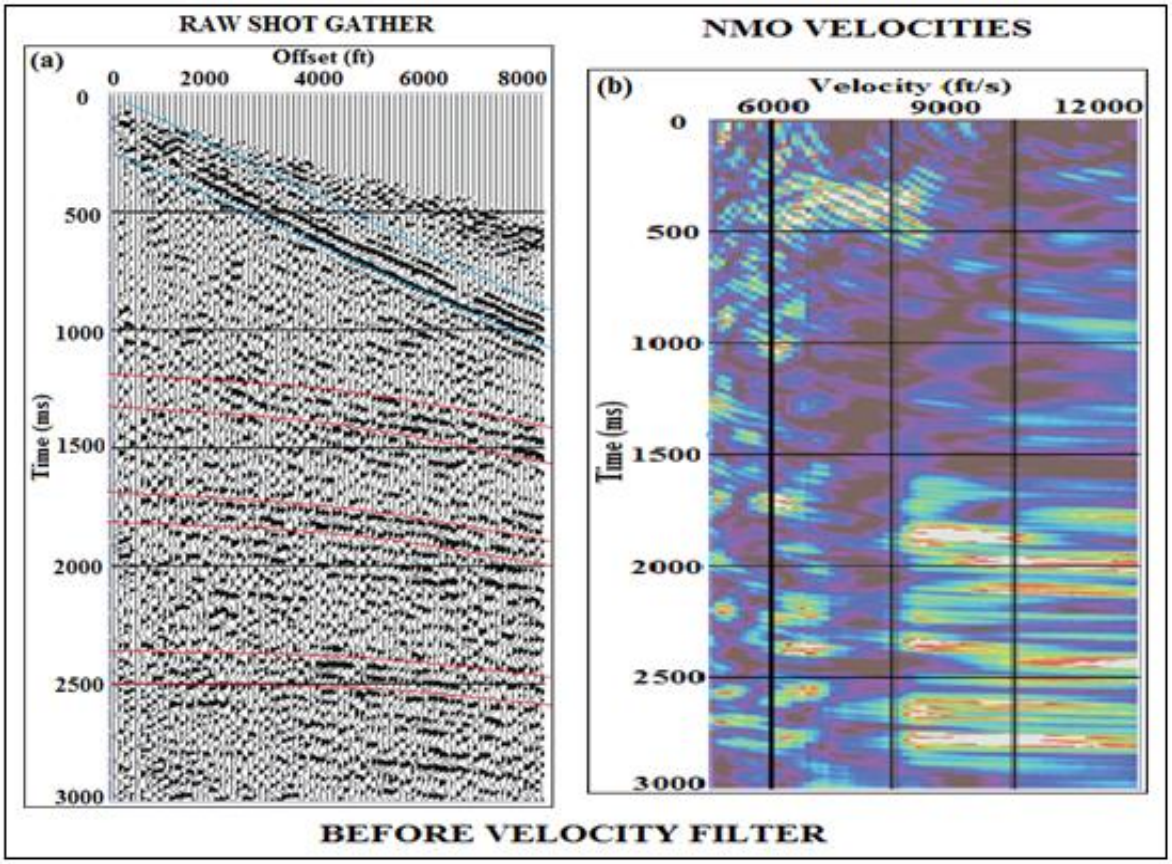

Figure 74: (a) Shot gathers of transverse-geophone data and (b) semblance panels displaying NMO velocity for pure shear wave-mode (down-going SH and up-going SH wavefields) before velocity filtering.

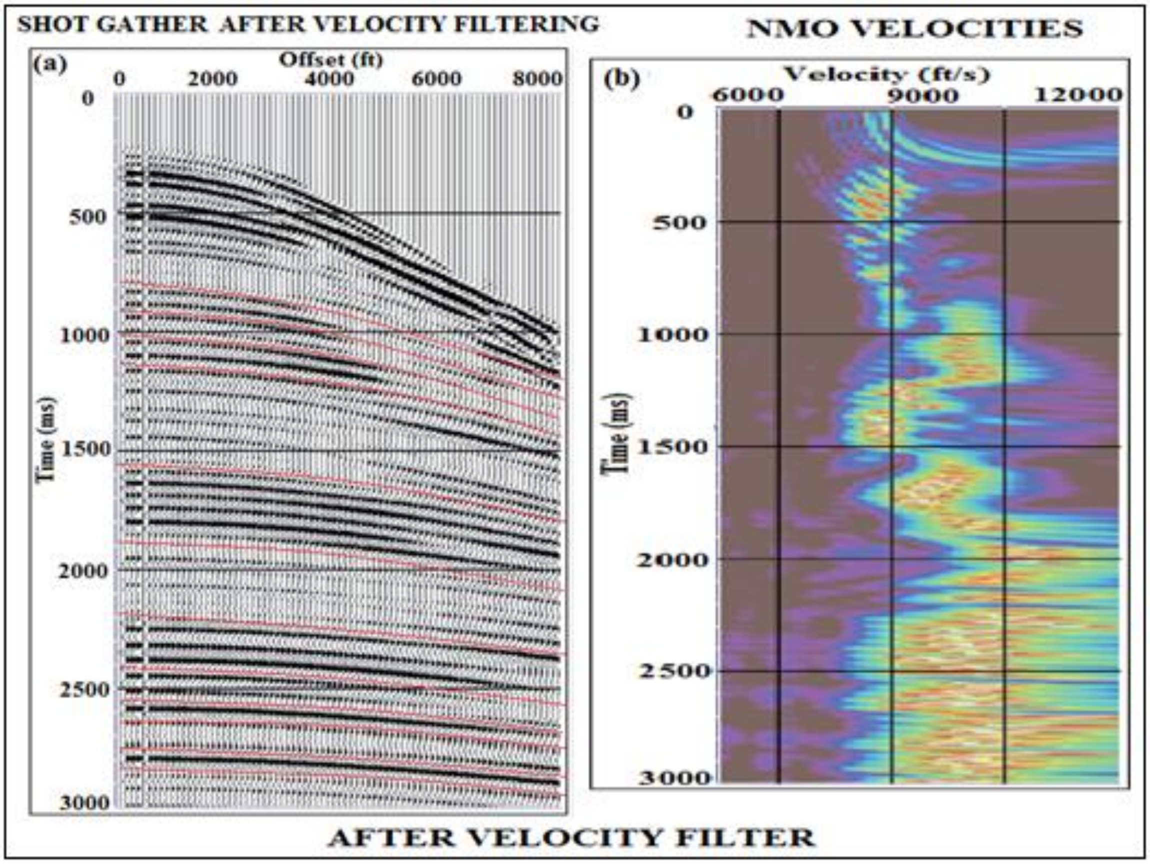

Figure 75: (a) Shot gathers of transverse-geophone data and (b) semblance panels displaying NMO velocity for pure shear wave-mode (down-going SH and up-going SH wavefields) after velocity filtering.

All velocities (P-P, P-SV, SV-P, SV-SV, SH-SH) that were used in figures 70 – 75 were derived from zero offset VSP. Based on the analysis of figures shown above (Figs. 70-75), I can list following observations:

- As demonstrated figures above, ratios of P and S NMO velocities are similar to P and S velocities obtained from log data.
- All reflections extend back to zero-offset, meaning SV and SH wave generated at source station.
- P-wave events occur in Figure 72a but not in Figure 74a.
- Surface waves in Figure 72 are not equal to surface waves in Figure 74.
- SH reflections differ from SV reflections as demonstrated in Figure 72 and 74.

Shot gathers of P-P, P-SV, SV-SV, SV-P, and SH-SH after velocity filtering are shown in Figs 76-80.

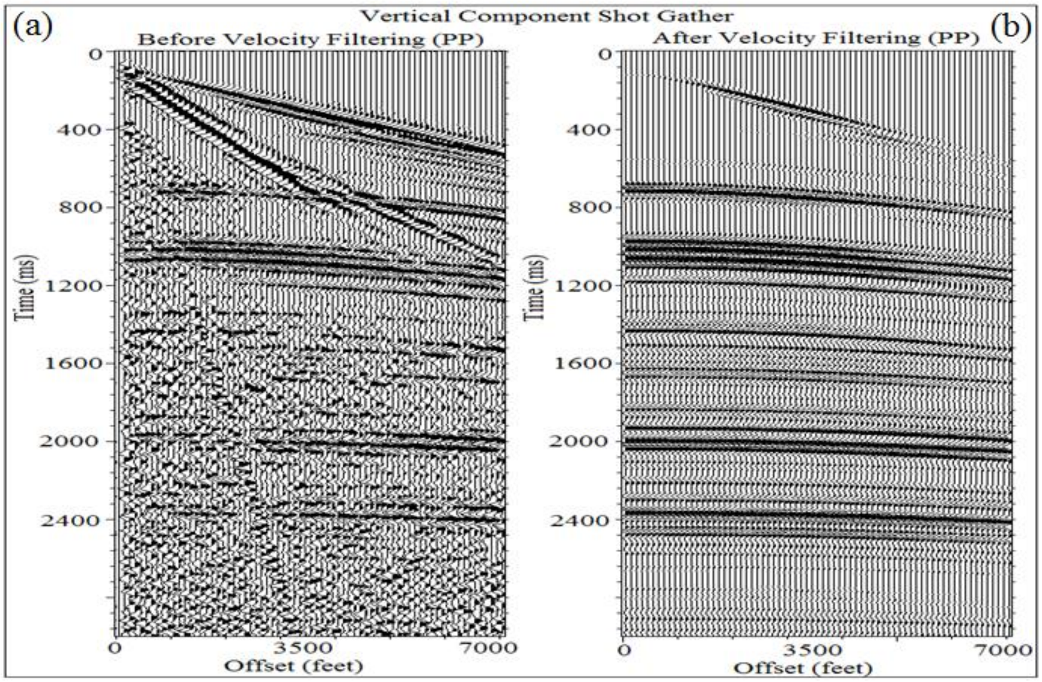

Figure 76: Shot gathers of vertical-geophone data before (a) and after (b) velocity filtering based on P-P velocity obtained from zero-offset VSP data.

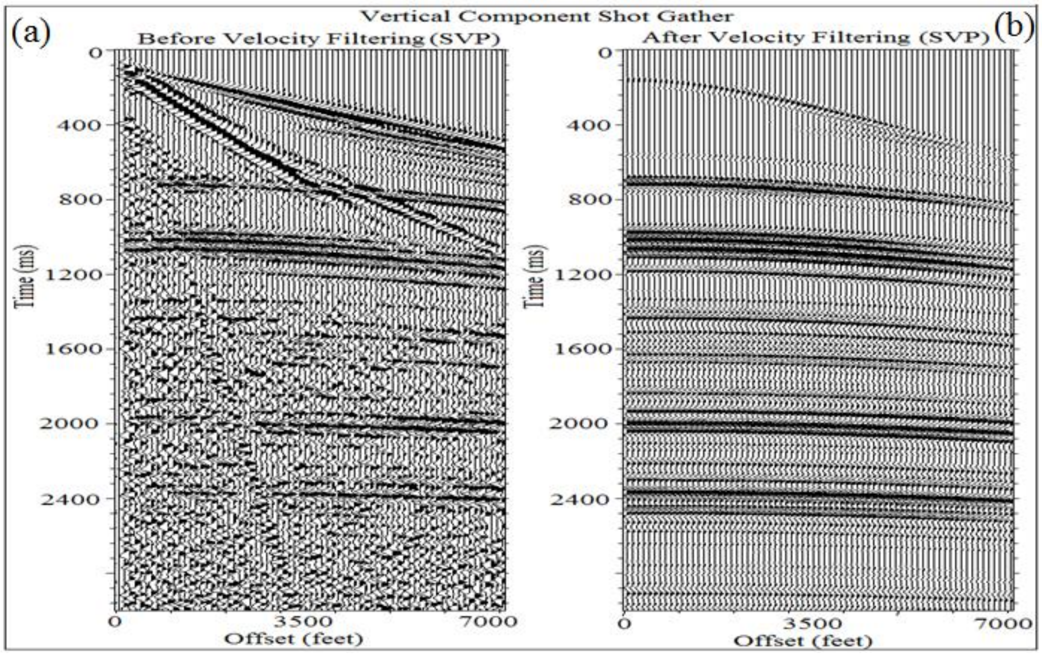

Figure 77: Shot gathers of vertical-geophone data before (a) and after (b) velocity filtering based on SV-P velocity obtained from zero-offset VSP data.

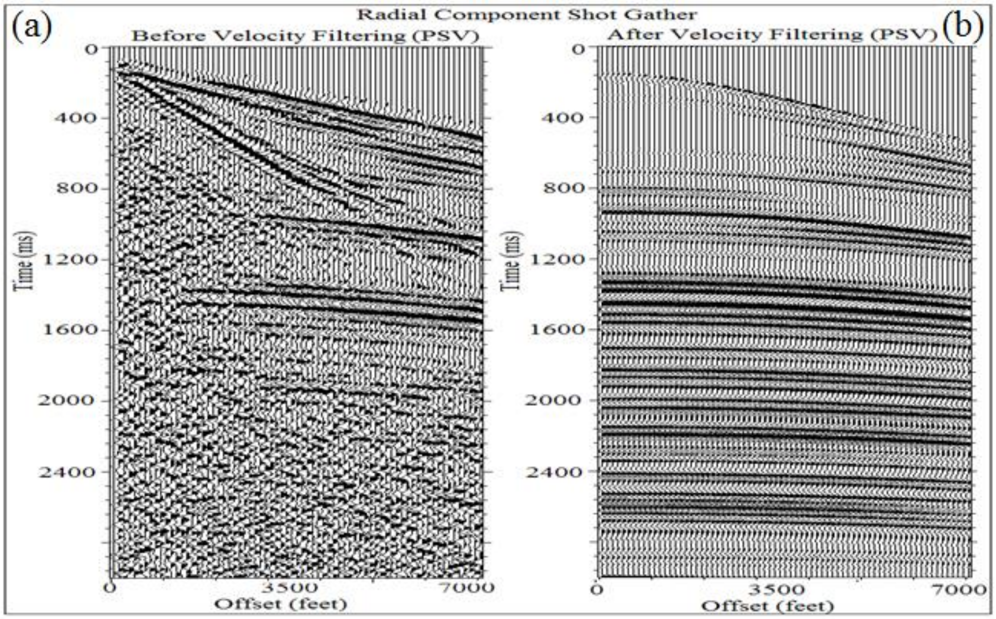

Figure 78: Shot gathers of radial-geophone data before (a) and after (b) velocity filtering based on P-SV velocity obtained from zero-offset VSP data.

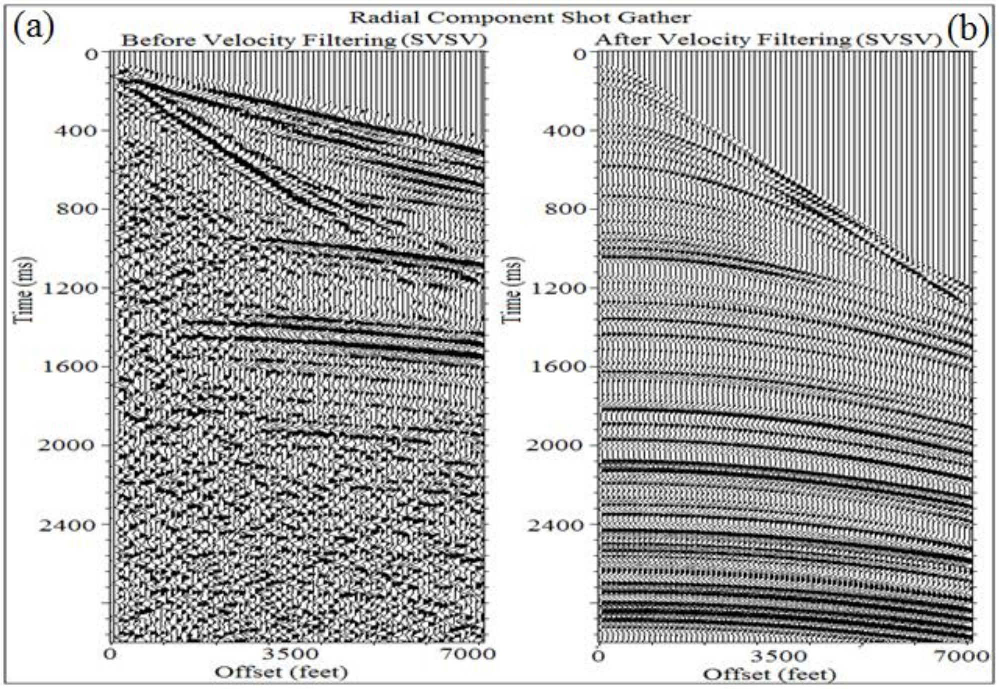

Figure 79: Shot gathers of radial-geophone data before (a) and after (b) velocity filtering based on SV-SV velocity obtained from zero-offset VSP data.

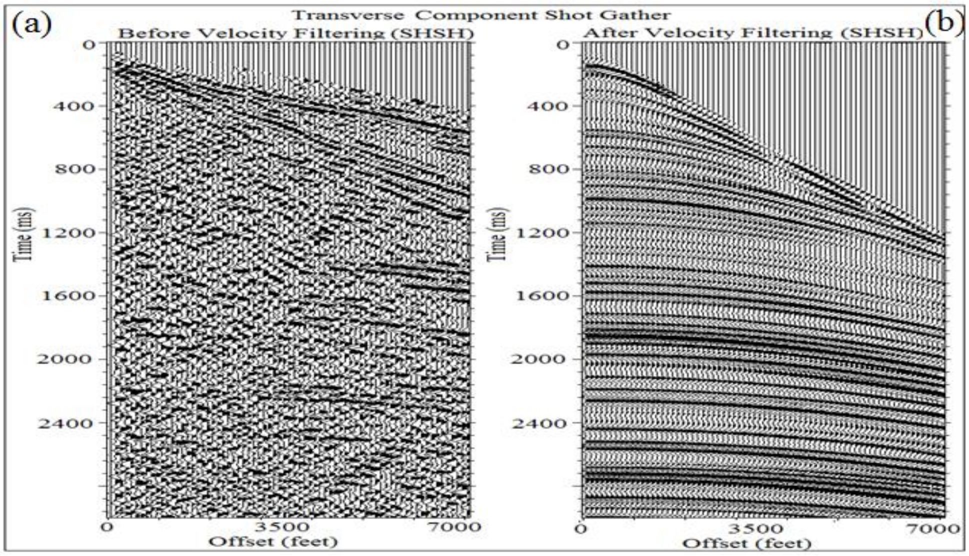

Figure 80: Shot gathers of transverse-geophone data before (a) and after (b) velocity filtering based on SH-SH velocity obtained from zero-offset VSP data.

Conclusions

Analysis of vertical-sections verified that the targeted Marcellus reservoir interval is imaged with high-quality data on both the P-P and the P-SV volumes. SV-SV data was generated and displayed in vertical section for an analysis. However this preliminary SV-SV data volume was not interpreted in this dissertation because additional processing is necessary to reach an acceptable level of image quality. The main difficulty in processing SV-SV data is picking SV refraction arrivals and calculating SV statics. Velocity behavior of SH and SV shear wave modes were compared by analyzing travel-time behavior along different take-off angle from a source-station. Results showed that SH and SV wave modes recorded by radial and transverse receivers propagate with different velocities at different take-off angles.

CHAPTER 5: INTERPRETATION OF MULTICOMPONENT SEISMIC DATA

Introduction

One of the goals of this PhD study is to apply 3D multi-attribute analysis techniques to various seismic volumes and create attribute maps that illustrate which seismic attributes are sensitive to reservoir parameters. 3D seismic attribute analyses have been widely used in industry and have proven to be valuable for characterizing geologic features such as faults and fractures (Chopra and Marfurt, 2005). In this chapter, I extend 3D seismic attribute analysis to multicomponent seismic data. The main reason for utilizing 3D multicomponent seismic attribute analysis is the ability to interpret images that show the areal extent of stratigraphic and structural features. Horizontal attribute slices provide detailed information about distinctive structural patterns and seismic amplitude changes associated with them that are not easily seen on vertical seismic section displays.

There are several examples of multicomponent seismic technology being applied to unconventional reservoir characterization and modeling (Cardona, 2001; Cardona et al., 2003; Lorenz et. al., 2004; Chopra and Marfurt, 2005; LaBarre and Davis, 2008; Singh et al., 2009). My research focuses on the Marcellus reservoir interval imaged by a high fold, full azimuth multicomponent seismic survey. These data allow many seismic attributes to be used to interpret the Marcellus Shale and related stratigraphy.

My goal is to discuss seismic attributes that are sensitive to changes in layer thickness, layer impedance, and fracture intensity, which are properties related to the geomorphology of Marcellus Shale reservoirs. With this information, I can address the orientations of stress fields and naturally occurring fracture networks within the Marcellus interval.

In this study, I demonstrate the value of analyzing poststack attributes such as amplitude and dip curvature, azimuth and coherency of faults, fracture networks, and stress field directions in the Marcellus Shale. I illustrate the value of elastic wavefield seismic stratigraphy by interpreting three different seismic volumes.

3D Multicomponent Seismic Attribute Analysis for the Characterization of Fractured Reservoirs

The more seismic wave types are included in a stratigraphic description of unconventional reservoirs, the better a seismic interpretation should characterize reservoir compartments and image stress fields and fracture orientation directions. Various attributes used to analyze Marcellus reservoirs and other formations will be discussed in this chapter.

The Marcellus reservoir is divided into two parts: the Lower and the Upper Marcellus, which are separated by the Cherry Valley Limestone. The base of the Lower Marcellus creates a strong reflection surface with the Onondaga Limestone. In addition to these units, the Tully Limestone, Tichenor siliciclastics, and Oriskany Sandstone will be analyzed using elastic wavefield stratigraphy. The first step is to identify significant seismic surfaces that best describe Marcellus reservoirs. Major seismic attributes that are considered include, but are not limited to, RMS, average, and maximum amplitude, coherency, curvature, frequency, dip, azimuth, and spectral decomposition. Geologic intervals identified from seismic sections were mapped for purposes of:

- Illustrating the value of elastic wavefield stratigraphy,
- Characterizing features and depositional settings of formations,
- Establishing well to seismic ties for characterizing the Marcellus reservoir interval, and
- Identifying naturally occurring fracture networks and stress field orientations.

Because structures are identified from seismic data, interpretation and evaluation of attributes were done using horizons representing main geologic formations. To get optimal results from attribute analyses, amplitude, spectral decomposition, coherency, and curvature attributes were created to provide detailed interpretations of Marcellus reservoirs and other intervals.

Amplitude extraction is the first step in quantifying attributes. Each amplitude attribute extracted from seismic data demonstrated different features of structures in the three seismic volumes (P-wave, fast and slow converted S-wave). Therefore, average and maximum amplitude attributes were extracted in addition to RMS amplitude. As demonstrated in later parts of this chapter, maximum or average amplitudes were better than RMS amplitudes for displaying differences among the images created by these three seismic wavefields.

The size of the analysis window that guides the position of the horizon in seismic data sections is crucial for interpretation accuracy and quality. In this study, the analysis window size was limited to 20 ms (10 ms above and 10 ms below each horizon) for amplitude analysis.

After completing attribute maps for selected horizons, well log data acquired in the survey area and VSP data will be analyzed to verify the accuracy of attributes represented in the maps. This process is followed by comparing attributes extracted from each seismic volume (compressional and shear wave volumes) to define the benefit of analyzing various wavefields when characterizing geologic settings.

This research does not cover all of the concepts of seismic interpretation, but it helps to understand how multicomponent seismic technology can be effective for determining characteristics of depositional facies and for developing reservoir architecture models.

A principle which multicomponent seismic technology enforces is that variations in seismic velocities and seismic attributes depend on rock features that change with azimuth direction. Figures 81 to 83 show consistent reflectors near the Marcellus reservoir and other formations, and also show the different reflectivity pattern observed between different datasets based on different elastic and acoustic responses of the rock formations. The S-wave reflectivity patterns seen in Figure 82 and 83 indicate intervals of continuity of reflectors and reflection dimming which are not obvious in P-wave data

(Fig 81). These S-wave features highlight critical structural features (faulting, fractures, etc).

Analysis of direct compressional wave (P-P) and converted shear wave (P-SV_1, and P-SV_2) data volumes showed shear-wave data volumes were more distorted by migration irregularities along the edges of image space than was the compressional wave volume. Migration artifacts observed on shear-wave volumes introduce fake structural dips and increase reflection smearing (Figures 82 and 83). Both of the migration-induced artifacts complicate S-wave data interpretation as horizons approach data-volume boundaries.

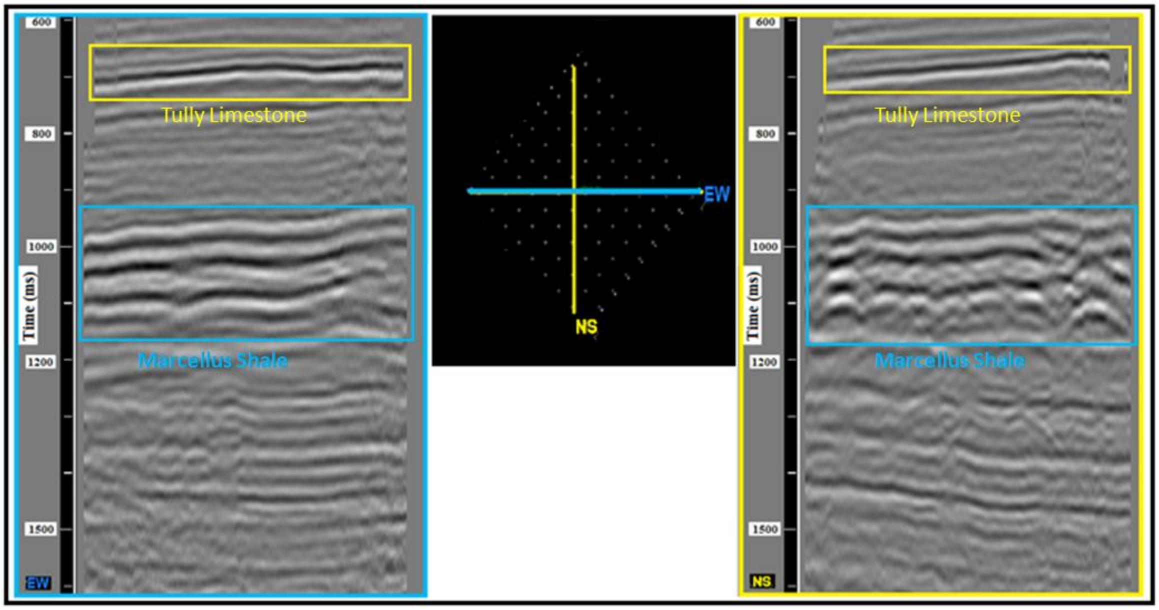

Figure 81: Compressional wave image: seismic line oriented East-West (left) and seismic line oriented North-South (right).

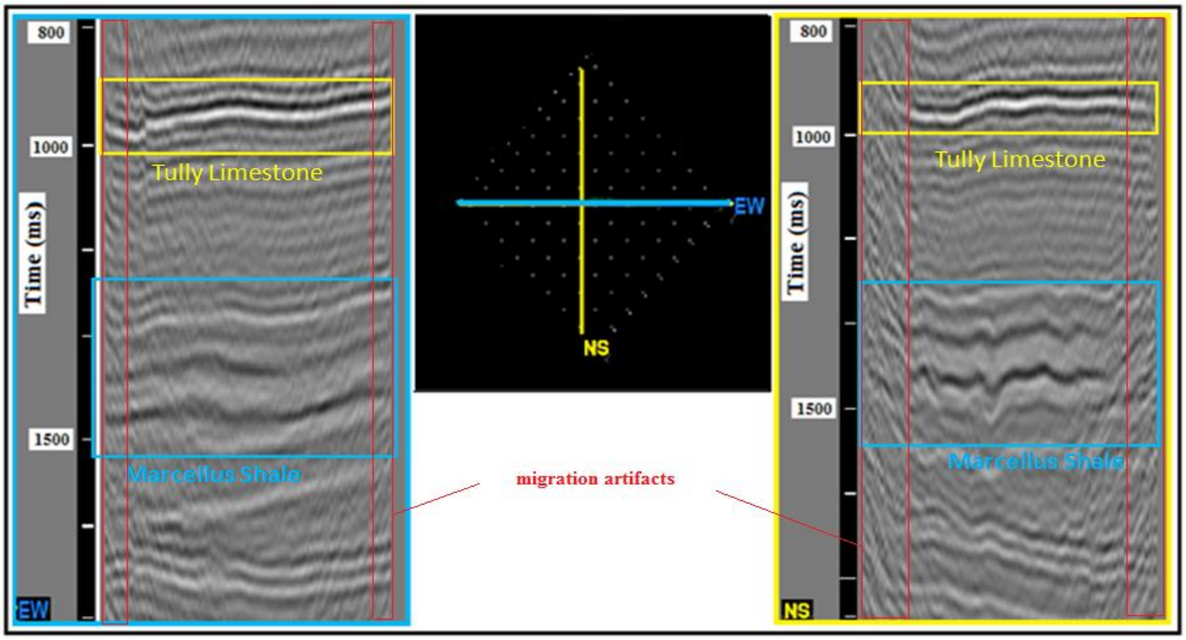

Figure 82: Fast shear wave image: seismic line oriented East-West (left) and seismic line oriented North-South (right). Red boundaries define where migration artifacts begin to effect data.

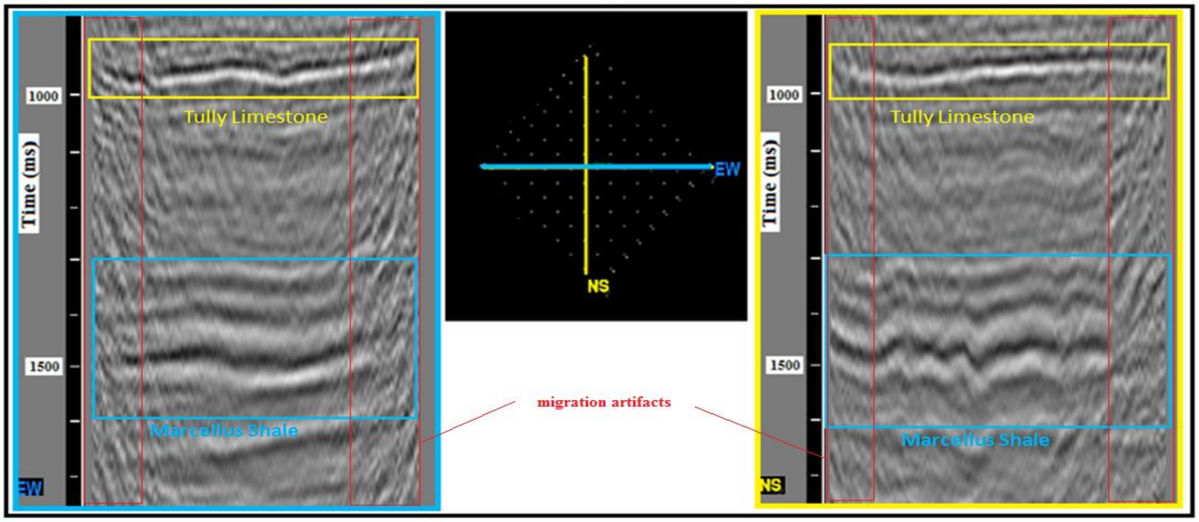

Figure 83: Slow shear wave image: seismic line oriented East-West (left) and seismic line oriented North-South (right). Red boundaries define where migration artifacts begin to effect data.

Seismic Attributes

One goal of my PhD project was to integrate available seismic and well-log data and interpret Devonian age formations within the Appalachian Basin in a stratigraphic framework that characterizes the Marcellus shale and other facies. The effects of azimuthal variations of seismic attributes such as amplitude, coherency, and dip/azimuth can be linked to geologic information to reveal rock anisotropy associated with fracture orientation and intensity within naturally fractured unconventional reservoirs.

Important geologic calibration data were recorded in a well positioned at the center of the seismic image space spanned by the 3D data volumes. A full suite of logs acquired at the center of the survey provided rock and fluid properties used for modeling P and S reflectivities.

Among these log data was a dipole-sonic log, which measured compressional (P), fast (P-SV_1), and slow shear (P-SV_2) velocities, and estimated S-wave anisotropy. These dipole-sonic data were used to generate P and S wave synthetic seismograms that aided depth registration of P and S data and identified key geologic targets in seismic images.

INTERPRETING P AND S HORIZONS AND LITHOLOGIC UNITS IDENTIFIED FROM GEOLOGICAL DATA

A geologic horizon interpreted along a seismic reflection event marks a chronostratigraphic surface (Hardage et al., 2011). When a reflection event has sufficient signal-to-noise character, there is increased confidence in the accuracy and validity of its associated interpreted horizon. These high-confidence horizons form the basis of a chronostratigraphic section that can be defined vertically and laterally throughout 3D seismic image space during interpretation. I interpreted chronostratigraphic surfaces along inline and crossline profiles separated by intervals that were usually every fifth profile in both the inline and crossline directions. This small line interval ensured that a selected horizon would not jump to an incorrect reflection event when switching interpretation analysis from one profile to another. Horizons spanning targeted stratigraphic intervals were interpolated between these interpreted profiles to generate a continuous horizon surface across seismic image space.

I mapped horizons identified from both compressional and shear wave data simultaneously to ensure geology was depth registered in both P and S image spaces and to establish optimal stratigraphic correlation between P and S data volumes. Mapping stratigraphic horizons at the edges of shear wave data volumes was difficult because of the migration inaccuracies illustrated on Figures 82 and 83. Therefore, seismic attributes generated near the edges of 3C3D image space appear less reliable than attributes calculated in the interior of a data volume where reliable selected horizons were interpreted. Interpretation of a selected S-wave horizon along inline and crossline profiles was terminated where the time structure of that horizon deviated significantly from its depth-equivalent P-wave horizon time structure. These continuous surfaces were used to guide calculations of depth-equivalent P and S seismic attributes.

Lithologic units analyzed in this section belong to the Hamilton Group, which extends from the top of the Onondaga Limestone to the base of the Tully limestone. The interval is divided into two Marcellus Shale formations and several related facies (Figure 84).

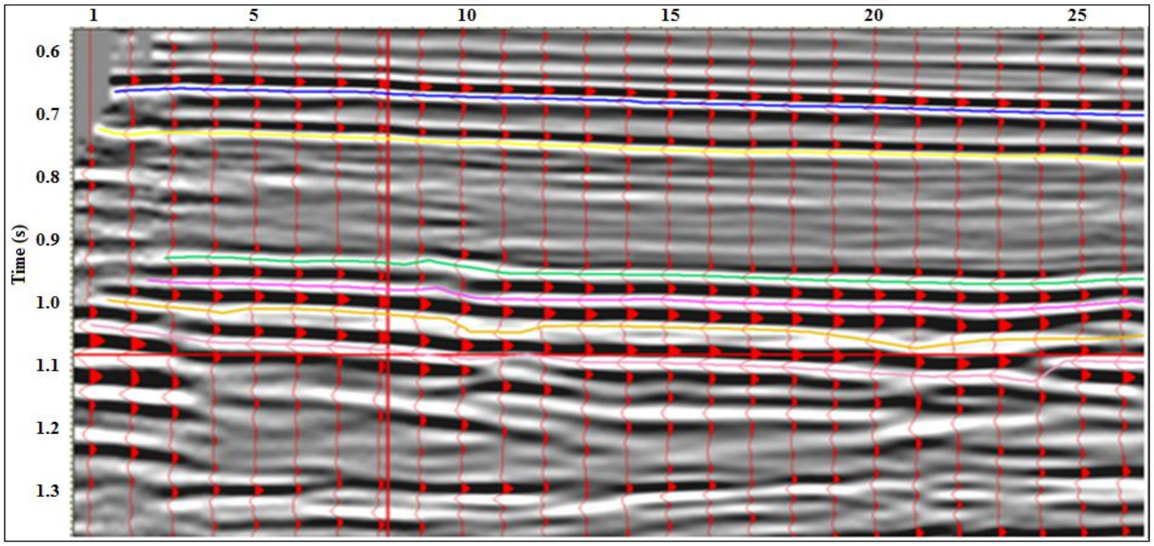

Figure 84: Six horizons identified from the P-P seismic volume. From top to bottom are the Tully Limestone (blue), Tichenor Limestone (yellow), Upper (green) and Lower Marcellus Shale (orange), Cherry Valley Limestone (pink), and Onondaga Limestone (purple).

It is essential to determine which reflection events correlate with key geologic horizons to be able to initiate seismic interpretation. Time-to-depth calibrations must be established for P-wave data and for each S-wave mode when interpreting multicomponent seismic data. Data acquired in the central-image calibration well allowed me to implement synthetic seismograms to establish time-to-depth correlations for the 3C3D Bradford County seismic data.

Velocity logs recorded in the central-image calibration well provided depth profiles of both P-wave velocity (V_P) and S-wave velocity (V_S). P-P and P-SV_1 synthetic seismograms were calculated by combining these velocity logs with the density log from the calibration well. These synthetic seismograms were my principal approach to defining depth-equivalent P and S reflection events as 3D P and S data volumes were interpreted. The correlations of seismic data and synthetic seismograms are shown on Figure 85 for P-SV$_1$ data.

Additional confirmations of the accuracies of correlations between geology and P and S images are shown in Figure 86 where the gamma-ray log recorded in the calibration well is displayed on compressional data (Figure 86a), fast shear data (Figure 86b), and slow shear data (Figure 86c).

Each significant change in gamma-ray magnitude correlates with a specific reflection event that allows depth-equivalent P and S horizons to be defined.

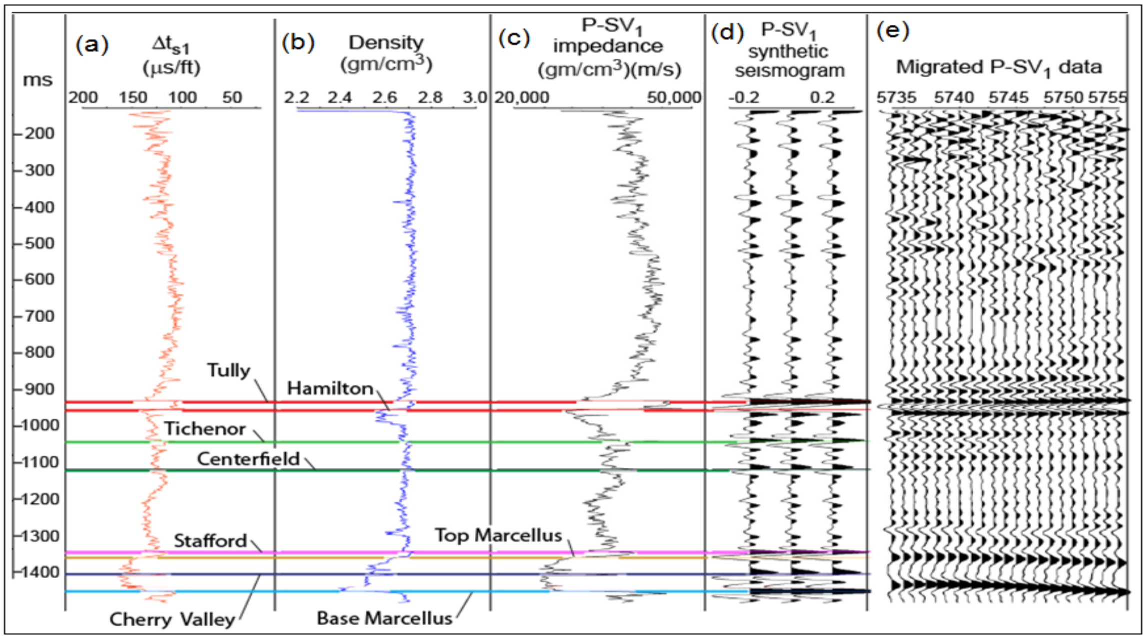

Figure 85: Shear wave sonic log (a), density log (b), P-SV$_1$ impedance (c), P-SV$_1$ synthetic seismogram (d), P-SV$_1$ seismic data (e).

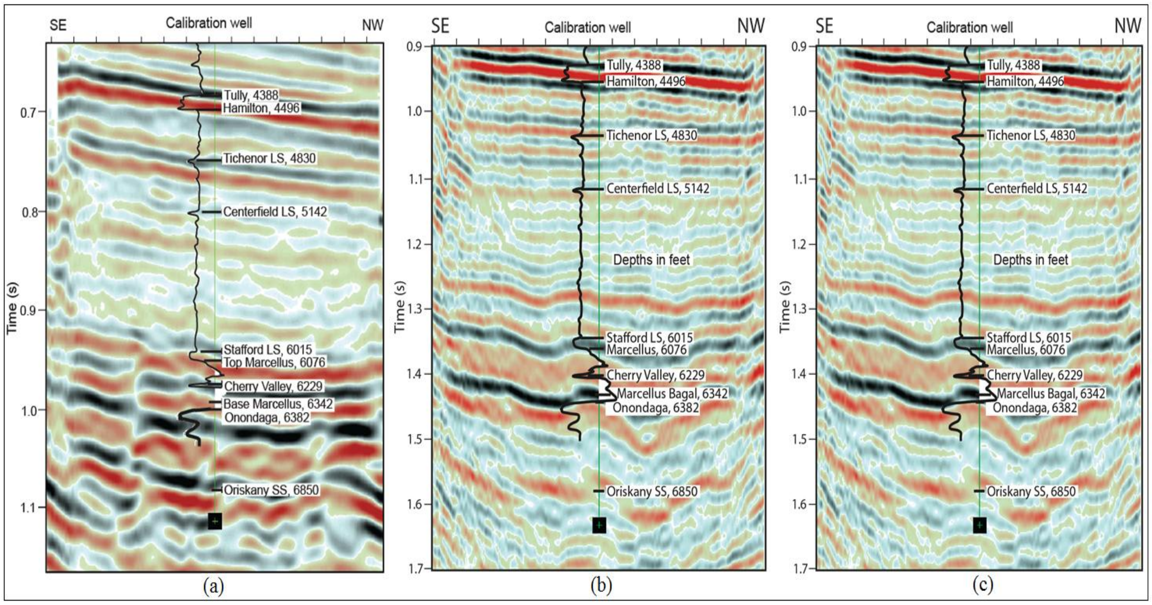

Figure 86: Gamma-ray log (black) recorded in the calibration well displayed on compressional (a), fast shear (b), and slow shear data (c).

A simple procedure was implemented to convert the Bradford County time-migrated P and S image volumes to depth (spatial wavelength) volumes. For each time-based volume, a single velocity function was calculated to convert image-time to depth across the entire 3D image space. Only one P-P time-to-depth conversion function was applied to the P-wave migrated-time volume. A spatially invariant V_P/V_S velocity ratio was then assumed and used to adjust this P-P time/depth relationship to create a P-SV time-to-depth conversion function. This single P-SV depth conversion was applied to both the P-SV$_1$ and P-SV$_2$ migrated-time data volumes.

Precise depth conversion requires several velocity functions, spaced at appropriate intervals across X-Y image space, be applied to a time-based seismic data volume. Because I used only a single time-to-depth conversion function across the entire image space of each data volume, my depth-converted data are only approximately correct.

However, these approximate-depth volumes are sufficiently accurate to allow important observations to be made about the relative vertical resolution of P and S seismic data.

Vertical slices through the P-P and P-SV_1 depth-converted data volumes are displayed on Figure 87. The vertical distances between the interpreted Tully and Marcellus horizons are labeled on each profile. By counting the number of peaks and troughs across a depth interval, these depth-domain profiles show P-SV_1 shear data have considerably better resolution than do P-P data. On average, P-SV_1 data have a dominant spatial wavelength of 200 ft over the depth range of 4,000 to 9,000 ft (5,000 ft divided by 25 wavelength cycles). In contrast, P-P data have a longer dominant wavelength of 250 to 280 ft depending on where the number of reflection cycles is counted across this 5,000-ft span. These depth resolution comparisons provide considerable confidence in the value of S-wave data for evaluating smaller geologic features associated with shale-gas plays.

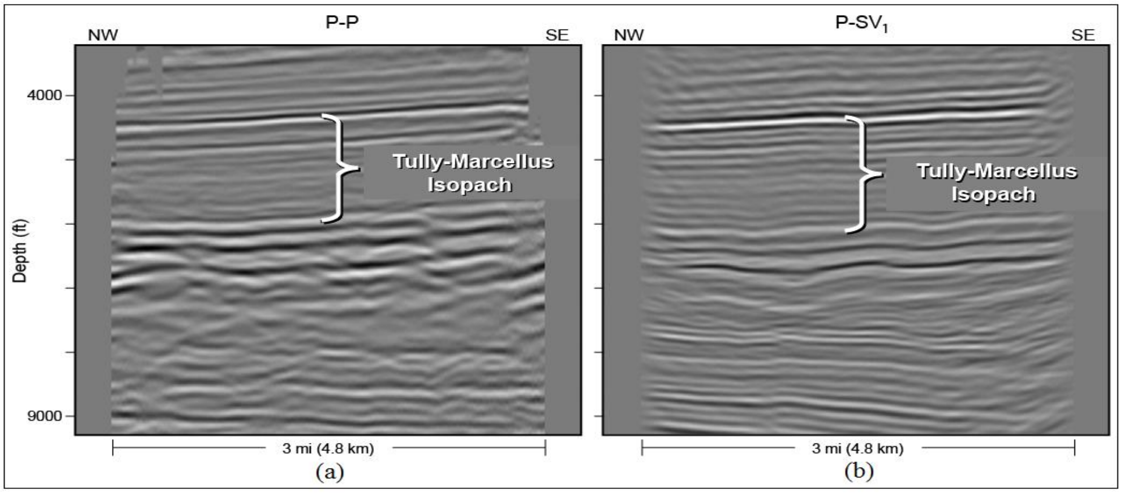

Figure 87: Equivalent profiles through depth-converted (a) P-P volume and (b) P-SV_1 volume.

Castagna et al., (2006) compared spectral decomposition methods such as DFT (discrete Fourier Transform), and CWT (continuous wavelet transform). Spectral analyses of depth-converted data volumes enforce wiggle-trace comparisons of P-P and P-SV$_1$ spatial wavelengths. Spectral comparisons of depth-based P and S data are displayed as Figure 88. These spectra show depth-converted P-P data (Fig. 88a) are dominated by wavelengths of 100 to 800 ft; whereas depth-converted P-SV$_1$ data (Fig. 88b) are dominated by wavelengths of 40 to 400 ft.

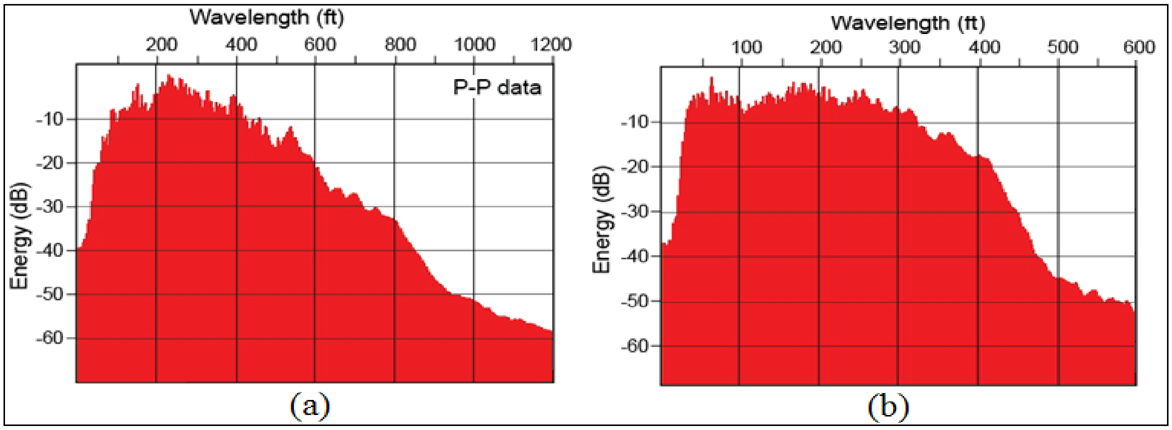

Figure 88: Spatial-wavelength spectrum of depth-converted P-P data (a) and P-SV$_1$ data (b).

Until depth-equivalent P and S horizons are established, P and S seismic attributes cannot be compared across targeted stratigraphic depth intervals to determine attribute combinations that optimize the detection of specific rock and fluid properties. Therefore it is essential for an interpreter to determine which S reflection is depth equivalent to a targeted P reflection event. Time-depth registration of P-P and P-SV data can be established using P and S traveltimes observed in VSP data acquired in the central-image calibration well. Each horizon was then extended from this well-control point across all of P-P and P-SV image space.

Away from the VSP calibration well, inline and cross-line sections of P-P and P-SV data were compared to define characteristic features that should be expected on both data sets and which would increase confidence that depth-equivalent horizons were being followed as interpretation proceeded farther from the VSP calibration well.

Geometric features such as stratigraphic terminations and lap-outs, if observed in both P and S image space, were important for deciding how to constrain the interpretation to depth-equivalent P and S horizons. However, shear wave seismic sequences often differ from compressional wave seismic sequences because of wave propagation physics.

One example of differences between P and S seismic sequences is demonstrated in Figure 89 and 90. Depositional and structural features can be imaged differently when observed in different directions (in-line and cross-line). As shown in Figure 91, P-wave inline and crossline sections present significantly different images for the same geologic horizon while shear wave volume images show similarity between inline and crossline sections.

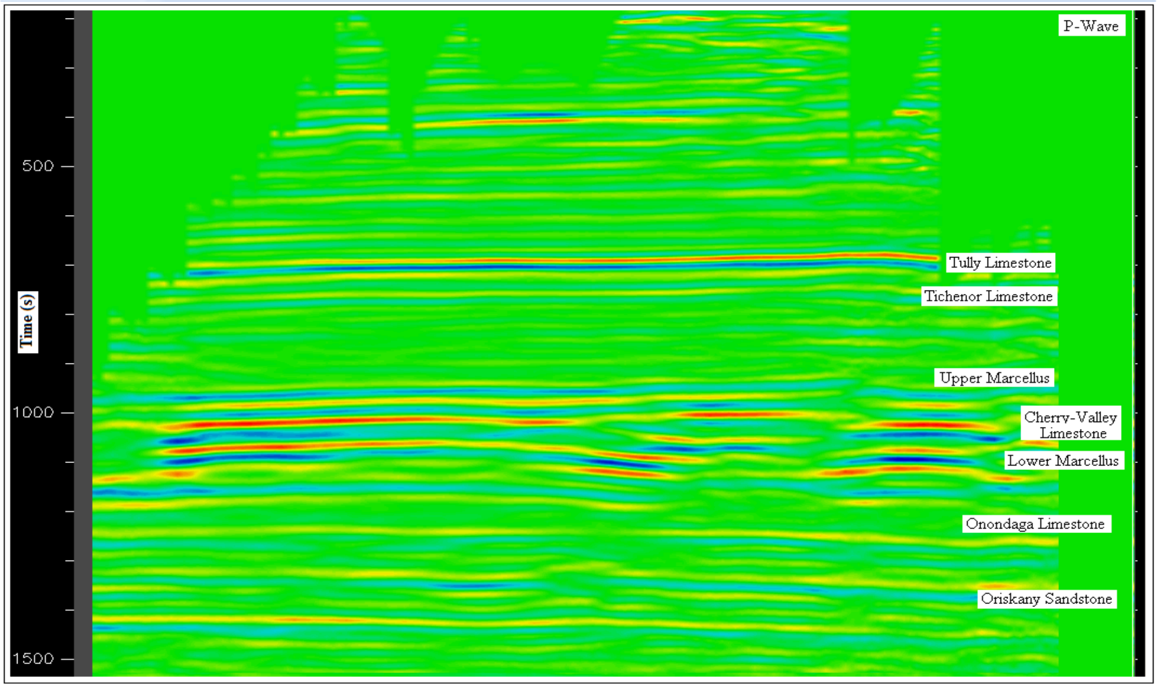

Figure 89: Horizons identified from P-wave data volume.

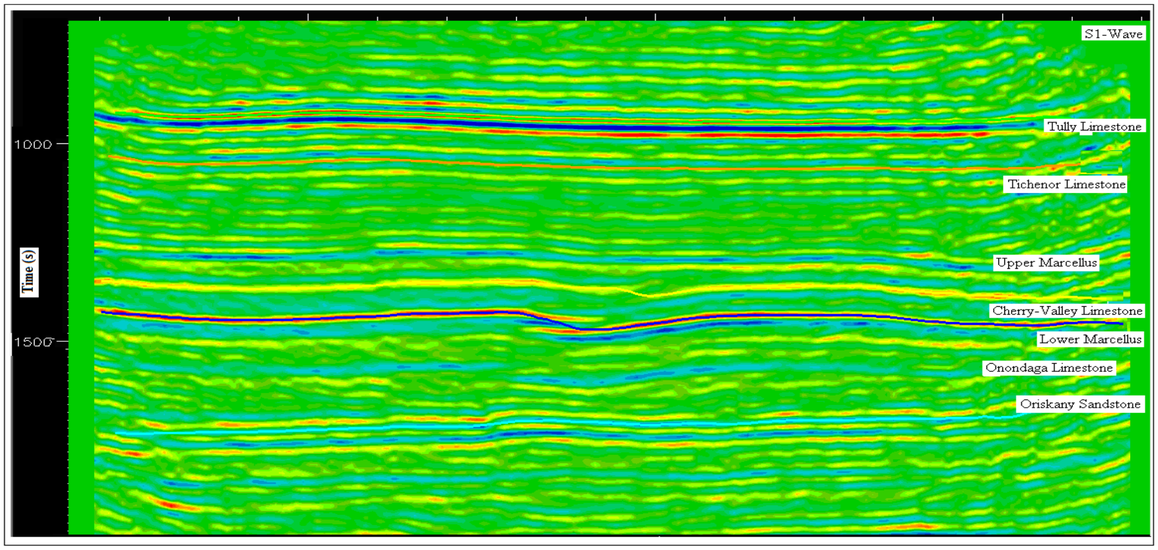

Figure 90: Horizons identified from fast shear wave (S1) data volume.

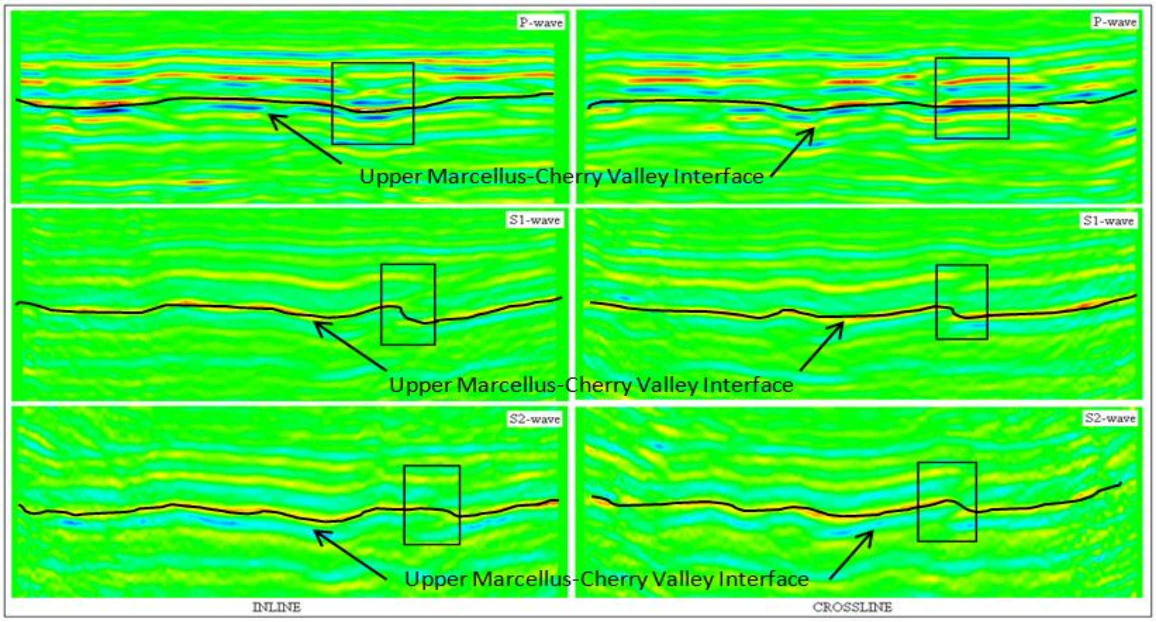

Figure 91: Structural comparison of Marcellus Shale - Cherry Valley Limestone interval among inline and crossline seismic volumes of compressional (top), fast-shear (middle) and slow-shear (bottom).

SEISMIC AMPLITUDE ATTRIBUTES

To identify features of geologic settings across the survey area, multiple seismic attributes were generated using three seismic volumes (P-P, fast-S, and slow-S). Average, maximum, and RMS amplitude values were mapped across the survey area using horizons identified on the seismic data. Within a time analysis window, an average amplitude attribute was calculated as the sum of squared amplitude values divided by the number of samples within an analysis window. A maximum-amplitude value is the maximum of the absolute value within the analysis window. A RMS-amplitude attribute is the square root of the mean squared values of amplitude for each sample in a targeted time window. All of these amplitude attributes, together with average amplitude, were mapped.

Seismic attributes were extracted from P and S seismic volumes using Landmark's PostStack Pal module. Multiple attributes were created from time windows centered on targeted horizons. Thin time analysis windows are better for calculating an attribute along a selected geologic horizon because narrow analysis windows minimize the possibility of including attributes belonging to different geology (Fig 92). In this study, time analysis windows were 20 ms thick (10 ms above and 10 ms below each targeted horizon).

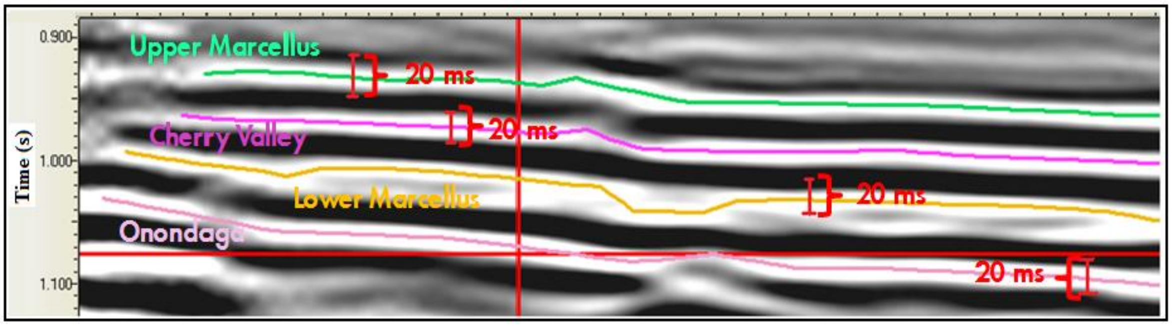

Figure 92: Marcellus interval time windows and their position on a seismic line.

Analysis of extracted attributes may determine the presence of fluid as well as indicate structural variations, conformities, and stratigraphic features such as folds, faults, and fracture networks. Anomalously high or low reflection amplitudes across a survey area may be indications of fluid contacts or channel features. Thus, analysis of several amplitude maps (RMS, average, and maximum amplitudes) may define lithological features that are imaged differently in various seismic volumes (P-wave, S1, and S2).

Figure 93 shows the variation of amplitude values for the Tully Limestone based on the type of amplitude attribute. Maximum and RMS amplitude maps provide evidence of geologic features that appear to be erosional effects (Figs. 93b, 93c). For most horizons, the presence of these features was not as clear on average-amplitude maps. The interpretational value of analyzing multiple amplitude maps is not limited to this example. Figures 94 and 95 show amplitude changes across two other horizons: the Upper and the Lower Marcellus. Average-amplitude maps show amplitude changes for the compressional-wave that are not observed for other modes. Likewise, maximum-amplitude maps for the slow-shear wave volume indicate facies distributions not seen in other images.

Figures 96 demonstrates why expanding the value of seismic stratigraphy beyond the constraints of compressional-wave data is crucial for determining the characteristics of depositional facies. These amplitude map examples indicate how each wave mode of an elastic wavefield (compressional, fast, and slow shear) image different aspects of stratal surfaces across the Tichenor interval. Combining these images helps to unravel various characteristics of depositional sequences within the survey area.

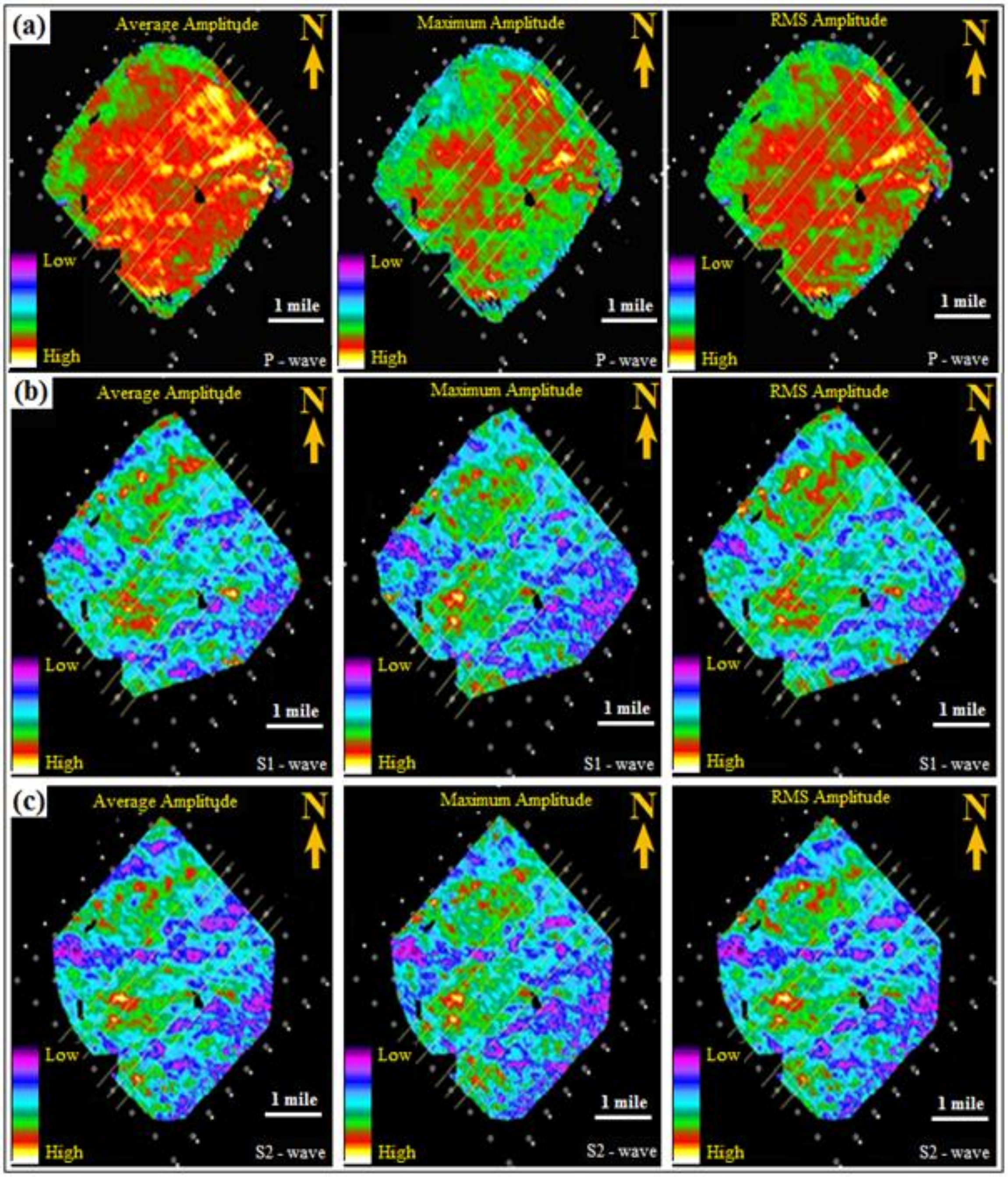

Figure 93: RMS, average, and maximum amplitude values extracted from (a) P-wave, (b) S1-wave, and (c) S2-wave seismic volumes for the Tully limestone formation.

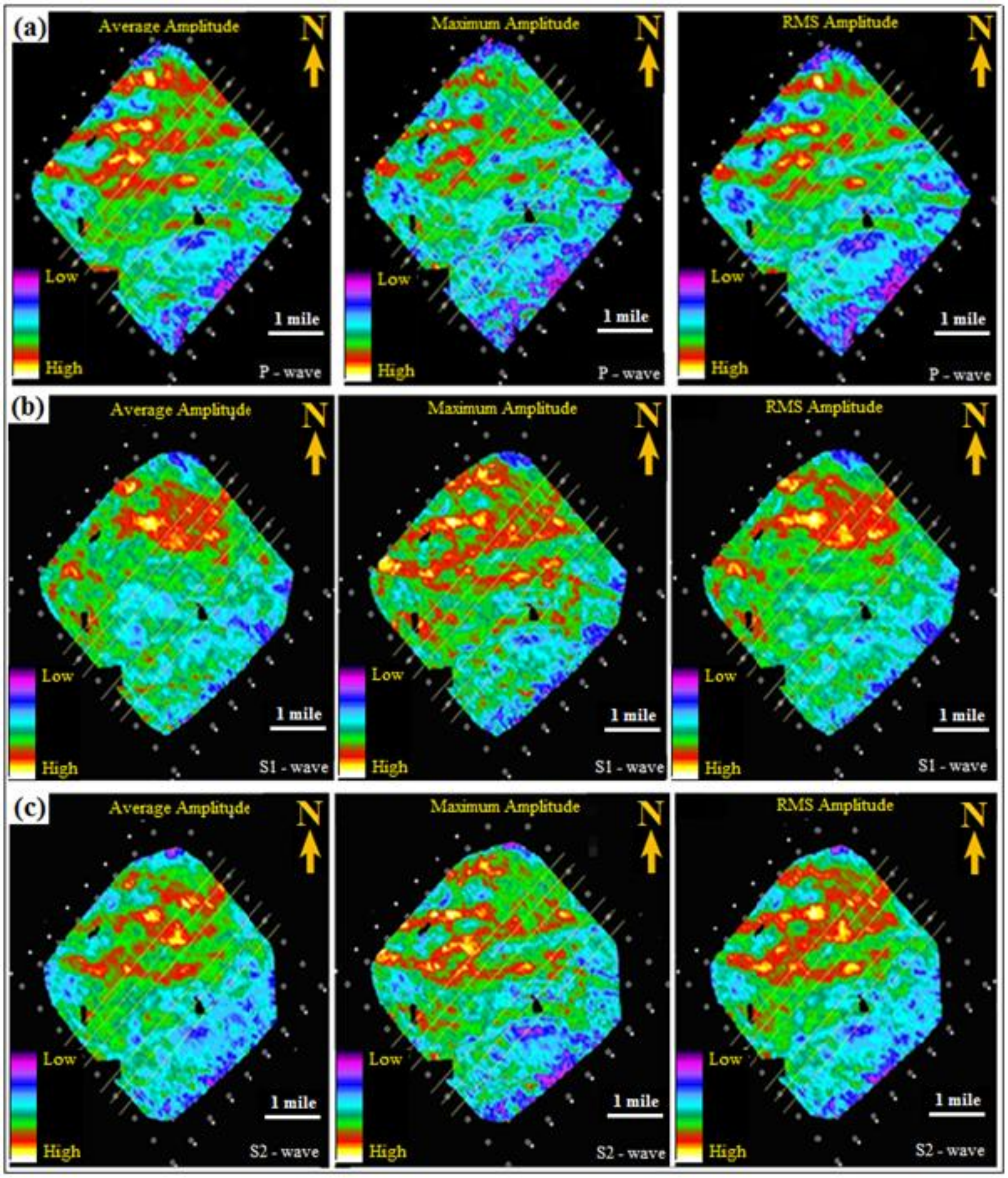

Figure 94: Average, maximum, and RMS amplitude values extracted from (a) P-wave, (b) S1-wave, and (c) S2-wave seismic volumes for the Upper Marcellus formation.

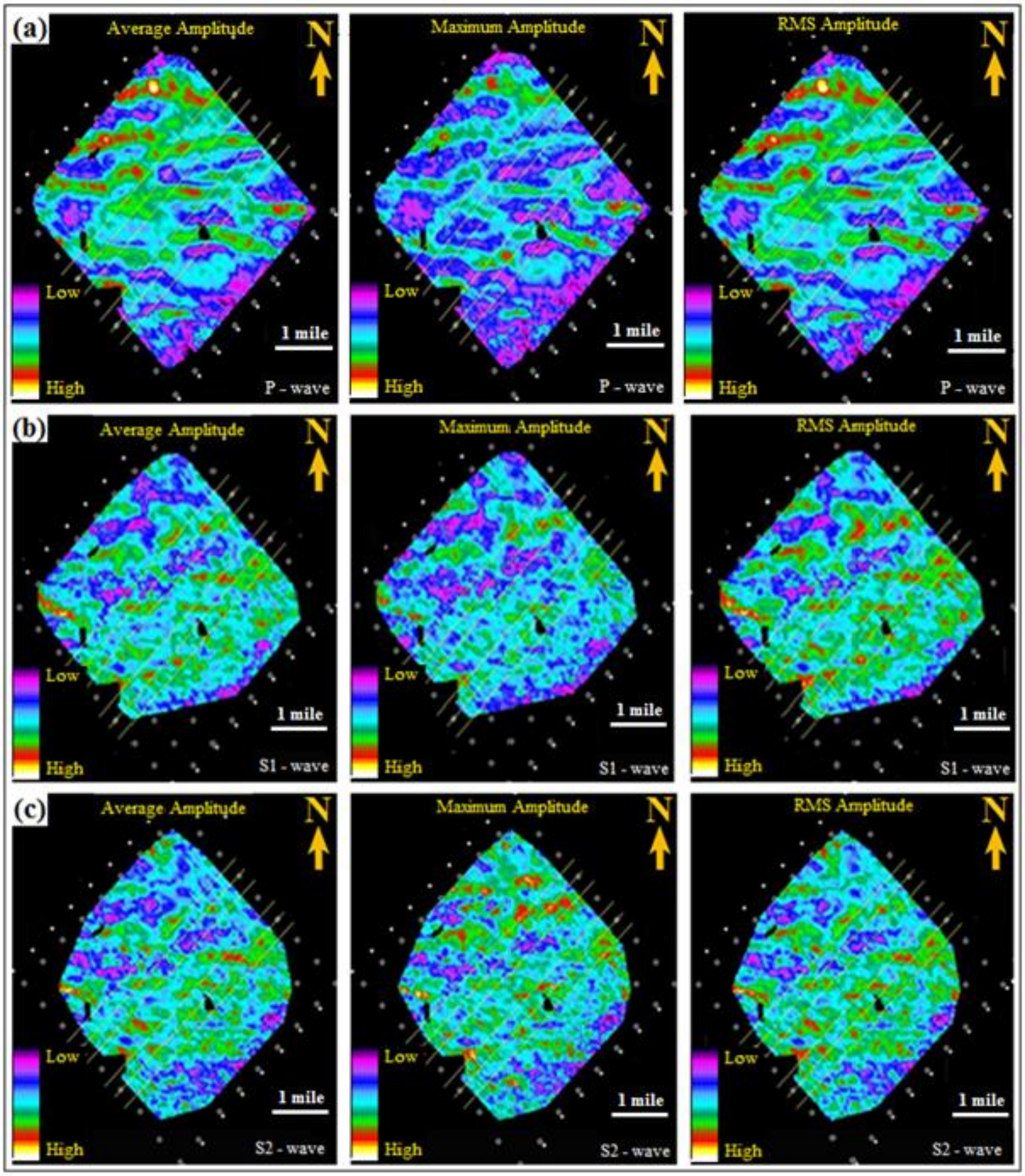

Figure 95: Average, maximum, and RMS amplitude values extracted from (a) P-wave, (b) S1-wave, and (c) S2-wave seismic volumes for the Lower Marcellus formation.

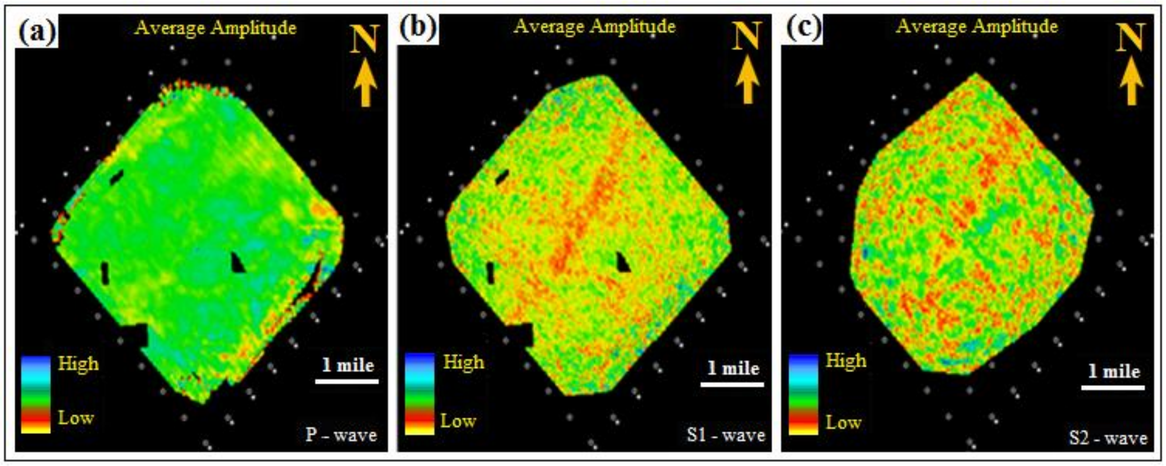

Figure 96: Average amplitude values extracted from (a) P-wave, (b) S1-wave, and (c) S2-wave volumes of the Tichenor interval. The southwest to northeast low amplitude (red) anomaly in (b) and (c) is absent in (a).

TIME AND HORIZON DISCONTINUITY ATTRIBUTES

Seismic facies parameters such as reflection strength and continuation vary according to the continuity of depositional sequences, and these variations often show depositional process-shaped stratification patterns within geologic intervals. Discontinuity attributes are valuable attributes for detecting faults and fracture systems. Coherency, dip curvature, and azimuth curvature are examples of attributes often used in fracture and fault analyses.

Curvature

There are several curvature attributes. Commonly used calculations are the magnitude and direction of minimum and maximum curvature along dip and strike directions of selected horizons. Curvature is an important parameter for fracture detection, and Gaussian curvature measurements have been used to predict fracture networks (Chopra and Marfurt, 2005; Chopra and Marfurt, 2007; Al-Dossary and Marfurt, 2006; Roberts, A., 2001; Marfurt et al, 1998).

Al-Dossary and Marfurt (2006) presented 3D volume curvature surfaces based on volumetric computations of dip and azimuth that represent the best choice for dip at each sample in a seismic volume. They demonstrated that geologic structures exhibit curvature attributes with different spatial wavelengths, and showed how curvature maps having different spatial wavelengths highlight different features of geological units. Curvature attributes with short wavelengths reveal information related to fracture systems, and longer wavelength curvature reveal larger-scale structural fracture not easily seen with other attributes. Volumetric curvature calculations often reveal mistakes made when horizon picking in areas where noise level is high and no consistent P-wave impedance contrast is present.

Figure 97 shows how curvature varies for different elastic wavefield volumes used in this study even though the data analysis interval is the same. Figure 97 (b) demonstrates that the Marcellus formations have a structural-fold fabric trending east-to-west. Also the curvature map extracted from S1 – wave on Figure 97 (c) shows the area where the unit that was identified as a channel feature is present.

As demonstrated in Figure 97, curvature attributes extracted from each wave mode provides different key information about geologic formation whereas this information was not provided by seismic data itself.

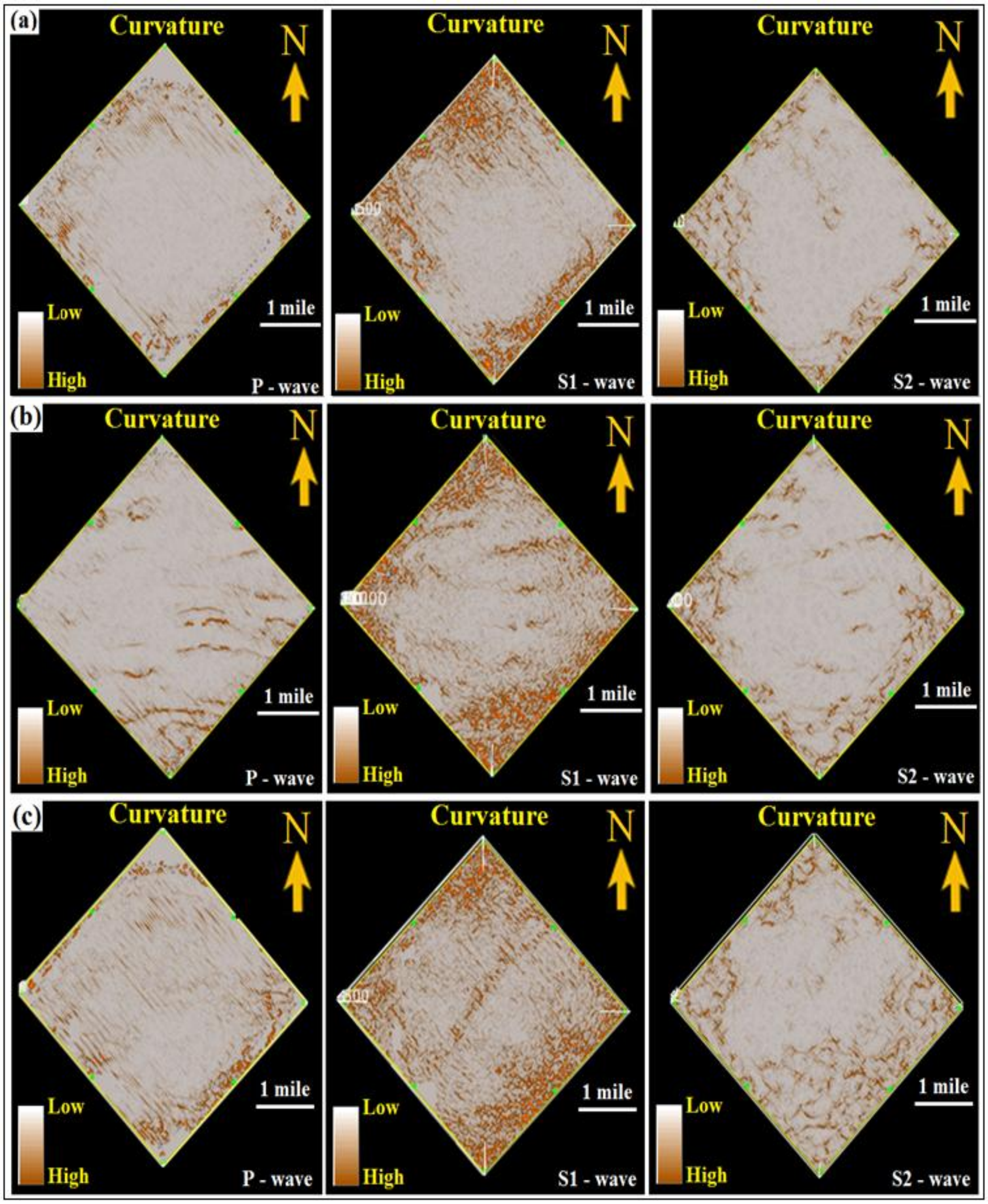

Figure 97: Curvature attribute maps extracted from P – wave, S1 – wave and S2- wave volumes for (a) Tully Limestone, (b) Marcellus Shale, and (c) a unit that was assumed to be a southwest to northeast channel. This anomaly is best seen on the S1 surface.

Coherency

Seismic coherency is described as a measure of similarity of seismic traces and measures lateral changes in impedance caused by structural or stratigraphic features, presence of fluid, or porosity changes (Marfurt et al. 1998). Coherency is best used to analyze the lateral continuity of seismic traces in a time analysis window centered on a horizon along which an attribute is mapped.

Several studies reported in the literature (Bahorich and Farmer, 1995, and Marfurt et al., 1998) demonstrate coherence attributes developed using techniques such as semblance, crosscorrelation, and eigen decomposition algorithms have provided valuable information about river channels, reefs, and other geologic features which have potential importance for oil and gas exploration.

As described by Bahorich and Farmer (1995) and Marfurt et al, (1998), a 3-D seismic coherency attribute provides important information for delineating faults and fracture systems when there are lateral changes in the seismic response. Coherency can also indicate subtle changes in stratigraphy, such as meandering channels, canyons, point bars, and other stratigraphic patterns. An important point to make here is that the accuracy of coherency maps depends on the quality of data and can be affected by noise level, resolution, and other imaging deficiencies. I focused not only the Marcellus reservoir interval, but also on limestone and a unit that was identified as a porous channel, so I could compare attribute analysis quality on horizons which were easily identified and which were distinctly different from reflectivity behaviors across Marcellus reservoirs.

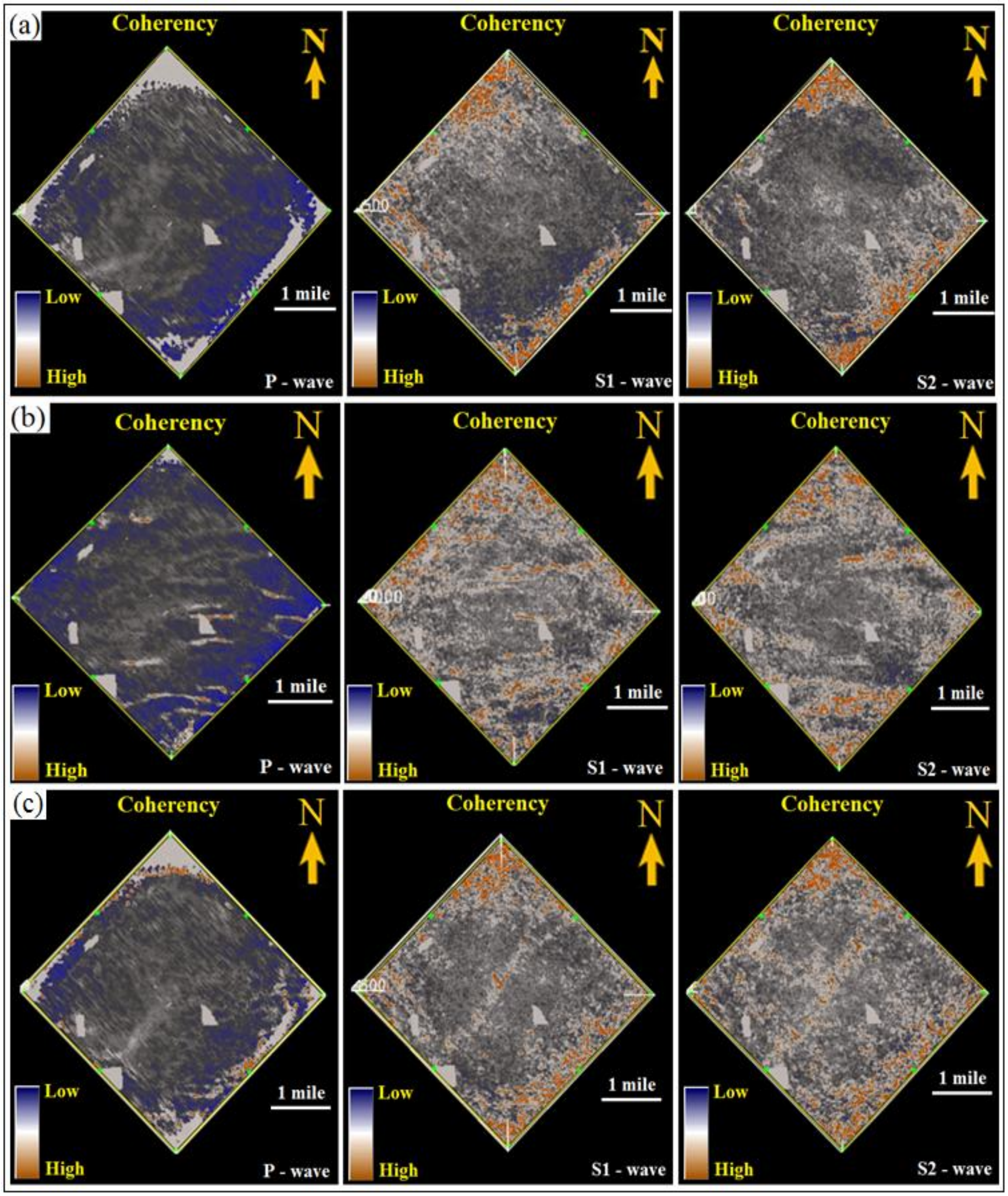

Figure 98: Coherency attribute maps extracted from P-wave, S1-wave, and S2-wave volumes for (a) Tully Limestone, (b) Marcellus Shale, and (c) a unit that was assumed to be a southwest to northeast channel. This anomaly is best seen on the S1 surface.

As indicated in Figure 97, curvature maps extracted from shear wave volumes demonstrate the area where the unit that has channel-like features is present. As shown in Figure 98, Marcellus formations have a strong structural-fold fabric trending east-to-west. These folds were also identified in attributes maps. As other seismic attributes, coherency also help interpreter to identify key geologic features that cannot directly be identified from seismic data wiggle-trace displays.

Some coherency volumes also use dip calculations, and combinations of coherency and dip are better for defining where fault patterns and fracture networks occur in formations.

Dip/Azimuth

Dip and azimuth attributes represent the magnitude of dip gradient and the direction of dip based on a best-fit surface among seismic traces in a time analysis window centered on a selected horizon. Rijks and Jaufred (1991) and Marfurt et al. (1998) demonstrate how faults with displacement offsets less than a seismic wavelet can be identified by dip and azimuth maps computed from seismic data.

Figure 99 and 100 display the dip and azimuth attribute maps extracted from P – wave, S1 – wave and S2 – wave. Although the geologic features that were clearly identified in some seismic attribute maps cannot be seen in dip and azimuth maps as easy as they were in curvature and coherency maps, these attributes (especially dip) can still be used to aid interpretation of geologic formations.

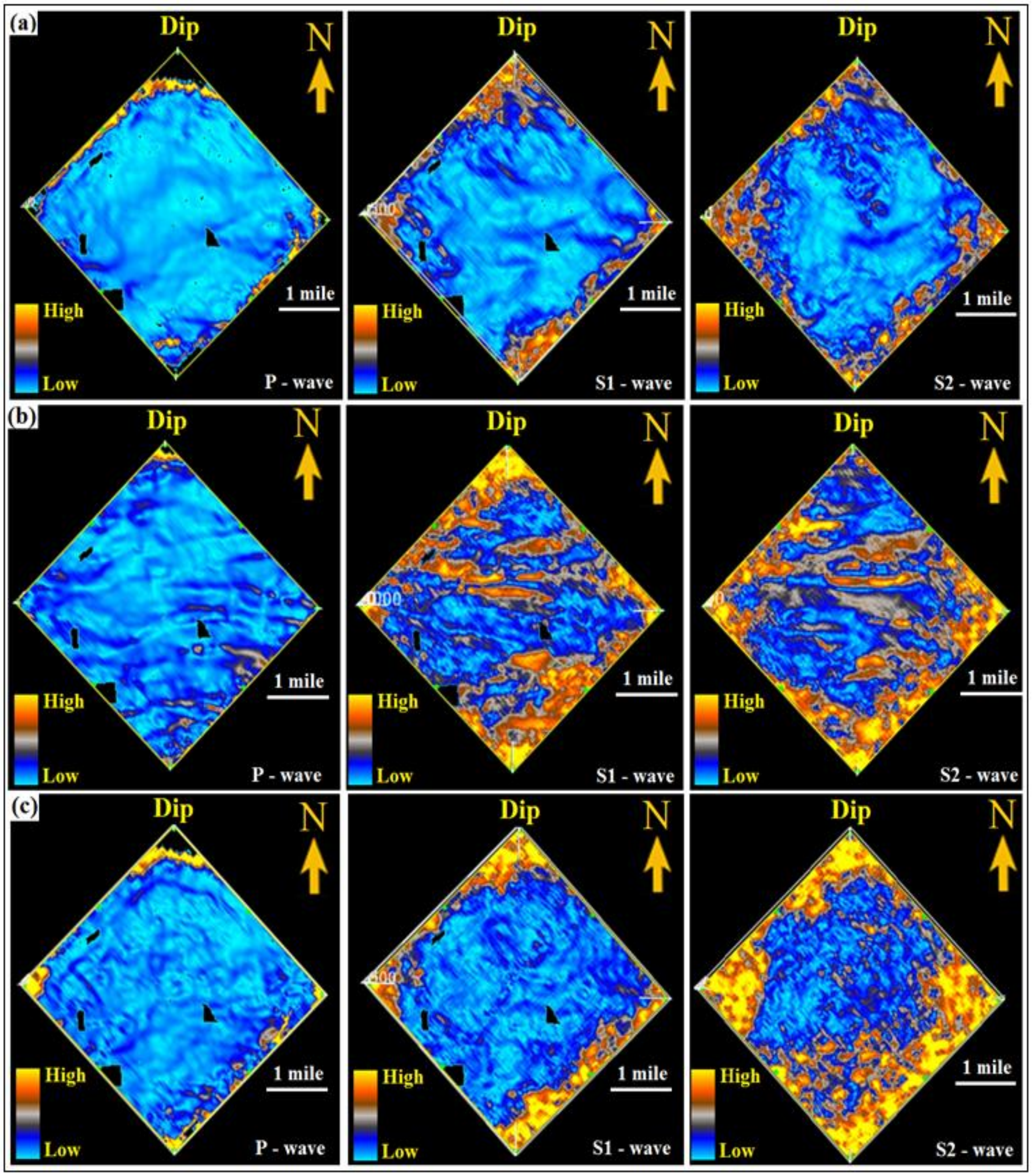

Figure 99: Dip attribute maps extracted from P-wave, S1-wave, and S2-wave volumes for (a) Tully Limestone, (b) Marcellus Shale, and (c) a unit that was assumed to be a southwest to northeast channel.

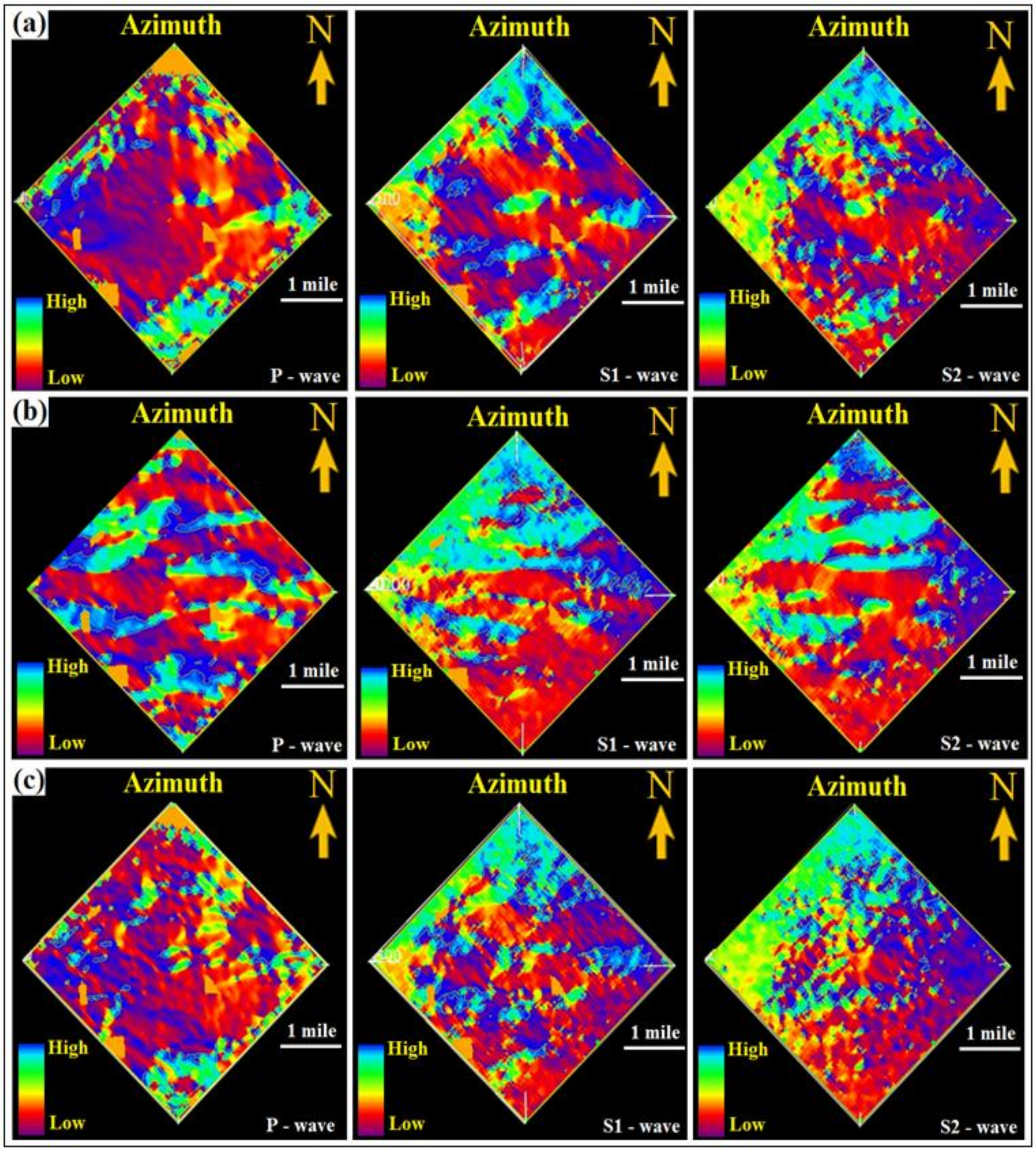

Figure 100: Azimuth attribute maps extracted from P-wave, S1-wave, and S2-wave volumes for (a) Tully Limestone, (b) Marcellus Shale, and (c) a unit that was assumed to be a southwest to northeast channel.

Spectral Decomposition

The goal of my seismic interpretation was to find any small changes that indicate subtle stratigraphic and structural areas of faulting and fracture networks. Amplitude analysis of seismic responses at specific ranges of frequencies may identify details that cannot be noticed from maps of amplitudes constructed from wide-band data. Attributes calculated with spectral decomposition represent seismic events within in each trace that are separated based on their frequency content. There are several methods to perform decomposition. Two common methods used in the literature are the Discrete Fourier Transform and the Continuous Wavelet Transform that yield higher resolution images in comparison with amplitude attribute mapping (Castagna et al., 2003, and 2006; Partyka et al., 1999; Sinha et al., 2005). Spectral decomposition is an effective and fast tool for providing detailed and accurate definitions of stratigraphic architecture and structural features from seismic data. Seismic interpretations are done for a range of frequency components that highlight different structural and stratigraphic details. Different geologic features that may not be noticed in some frequency ranges are better seen after the seismic traces are transformed into the time-frequency domain.

Although stacking removes information related to offset and azimuth due to averaging, post-stack attributes still express time and frequency relationships of data caused by impedance contrast and reflectivity, which aid in interpreting depositional environment and lithology. Frequency and bandwidth of seismic data play important role in such analyses.

By analyzing higher frequencies, thinner layering within the Marcellus interval (Upper Marcellus, Lower Marcellus, and Cherry Valley) can be identified. A broad frequency spectrum of fast-shear data results in a high-resolution image of the Cherry Valley formation as displayed in Figure 91.

Figure 101 illustrates the frequency spectrum of the three data volumes compared in this chapter. As seen in the figure, the fast-shear (S1) wave mode has a broader frequency spectrum than do P- and slow-shear (S2) wave modes. Figure 101 also demonstrates that slow-shear wave data have a rapid loss of high frequencies.

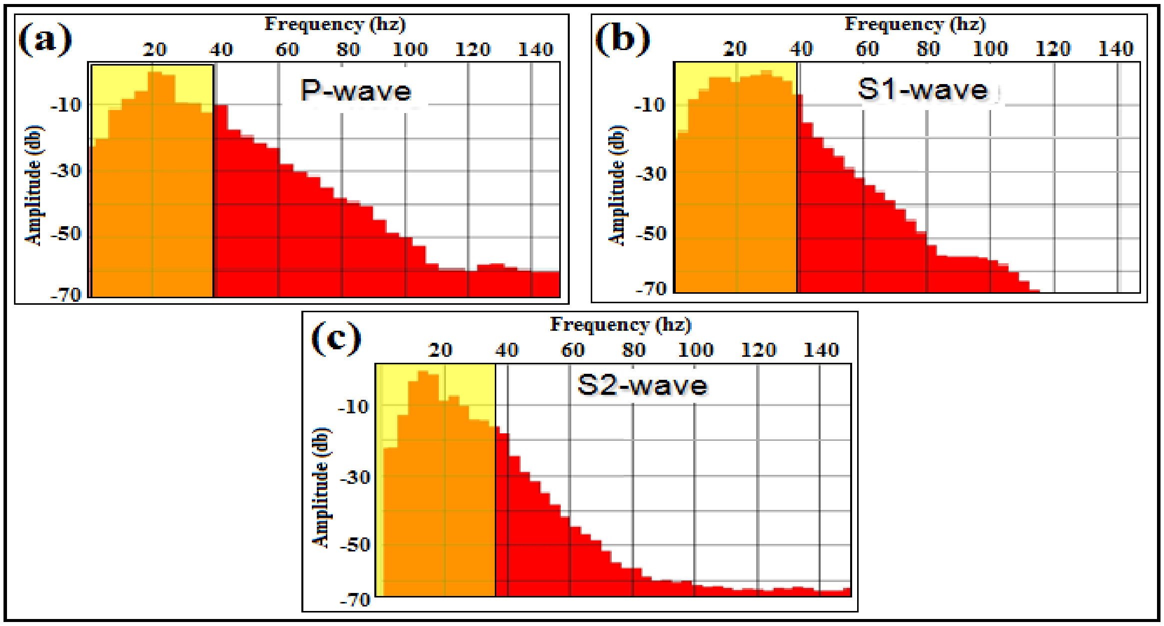

Figure 101: Spectral analysis of compressional (a) and converted shear waves (b) and (c) at the Marcellus interval.

Instantaneous Frequency and Instantaneous Phase

Final seismic volumes can be passed through a series of processing steps to unravel geologic information expressed by subsurface boundaries between different mediums that have different physical parameters. Any lithology change that results in a seismic reflection response may be measurable only when seismic attributes of multicomponent seismic data are calculated. Among complex trace statistics, instantaneous frequency and phase play key roles in detecting channels in attribute maps. These two attributes also provide important information about thicknesses of structures because they react to the maximum frequency present in an analysis window. Because instantaneous phase determines constant-phase surfaces of wavelets reflected within a medium, these phase surfaces can be used as indicators of lateral continuity to identify zones where fractures and faults occur within geologic formations.

Instantaneous frequency, being the time derivative of instantaneous phase, is particularly sensitive to seismic wave shape. Thus, instantaneous frequency can sometimes be used as an indicator of fractured zones if fractures cause any type of frequency anomaly. Hydrocarbon-filled fractures are of particular interest because hydrocarbon-bearing zones create low-frequency anomalies (Taner, 2001). For instantaneous frequency attributes to reflect physical meaning, data analysis windows should be selected carefully because noise affects the quality and robustness of this attribute.

Barnes (2007) described instantaneous amplitude as the maximum value a seismic trace can attain under a constant-phase rotation, and instantaneous phase as the phase angle required to rotate the trace to this maximum at any given specific time. A complex seismic trace $F(t)$ with reflection strength A, instantaneous phase θ, and instantaneous frequency $w(t)$ can be defined as in equations 1 to 4 (Taner, 2001; Vetrici and Stewart, 1996).

$$F(t) = f(t) + I f`(t). \qquad (1)$$

In this expression, $f(t)$ is the real a part of seismic trace, and $f`(t)$ is the imaginary part of seismic trace (Hilbert transform of the real trace).

$$A = |F(t)| \qquad (2)$$

$$\theta = \tan^{-1}[f(t)/f`(t)] \qquad (3)$$

$$w(t) = d\,\theta(t)/dt \qquad (4)$$

Figures 102 to 104 display instantaneous frequency and phase maps extracted from compressional, fast-shear and slow-shear wave volumes for horizons selected for the analysis. As demonstrated in Figure 102, a unit that was identified as a porous sand channel was clearly seen in instantaneous frequency and instantaneous phase maps extracted from shear wave data. The information provided by instantaneous frequency and instantaneous phase attribute maps agree with the information obtained from other attributes such as curvature, coherency and dip (Figures 97 (c) and 98 (c)).

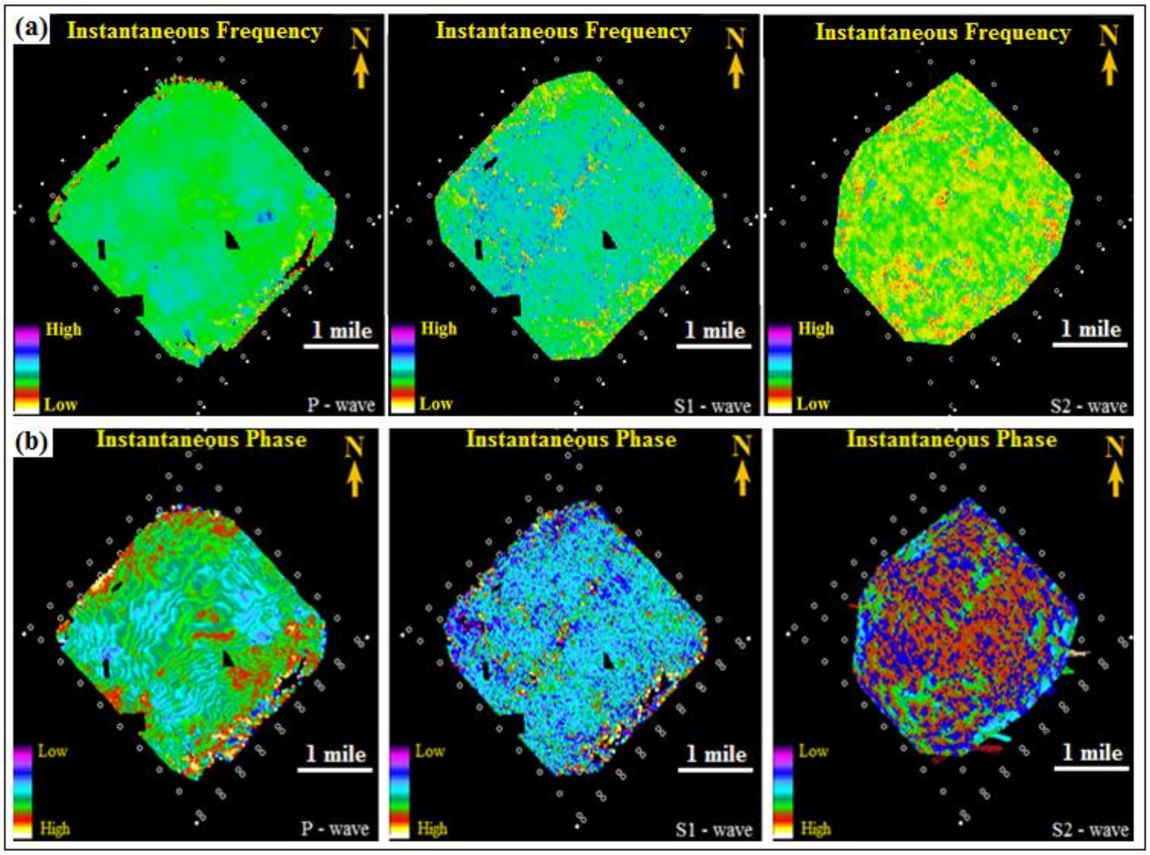

Figure 102: (a) Instantaneous frequency and (b) instantaneous phase maps extracted from P - wave, S1 – wave, and S2 - wave volumes for a unit that was assumed to be a southwest to northeast channel that is located just below Tully Limestone. The faint yellow trend in the S1-wave surface indicates this anomaly.

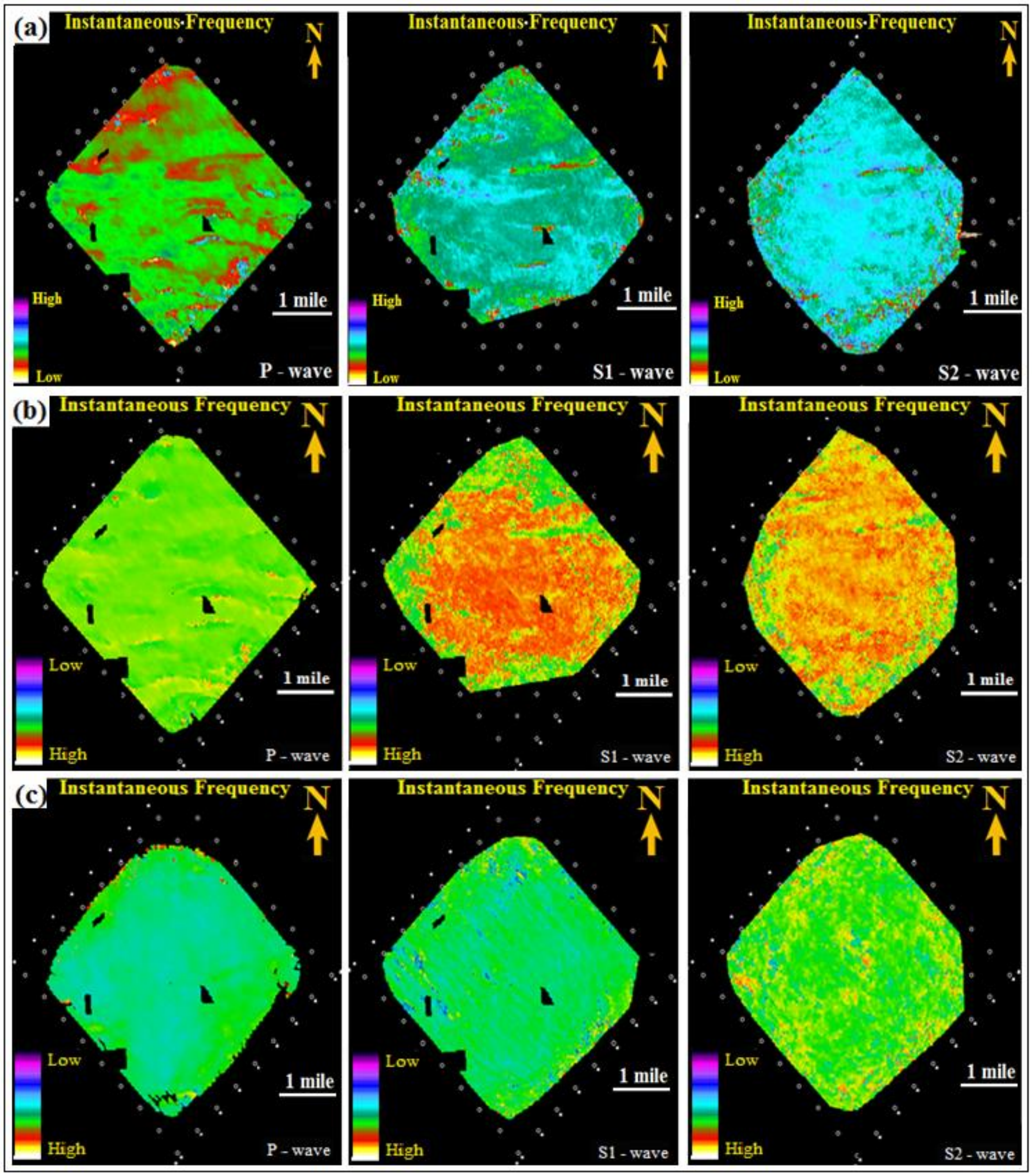

Figure 103: Instantaneous frequency maps extracted from P - wave, S1 – wave, and S2 - wave volumes for (a) Marcellus Shale, (b) Cherry Valley Limestone, and (c) Tully Limestone facies.

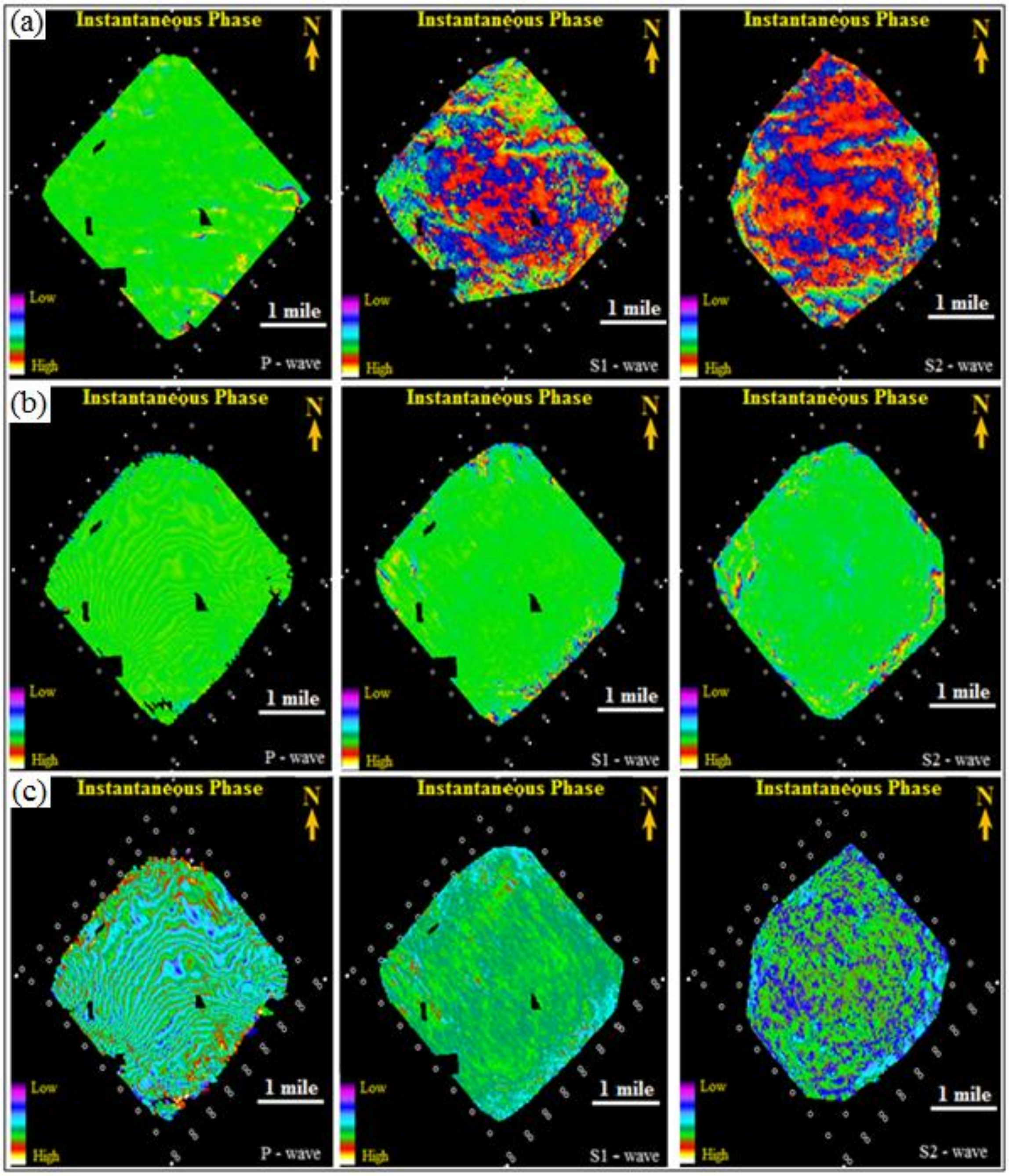

Figure 104: Instantaneous phase attributes extracted from P, S1, and S2 data volumes for (a) Marcellus Shale, (b) Cherry Valley Limestone, and (c) Tully Limestone facies.

Detection of Faulting Zones and Fracture Systems from Volume Analysis

All three data volumes confirmed that structural complexity increases within the Marcellus interval. Visual inspection of data volumes demonstrates that the Marcellus has a strong structural-fold fabric trending east-to-west. The analysis of multiple attributes generated from different data volumes led to better understanding of local effects of tectonic stress on the Marcellus. Although the natural fracture pattern within the Marcellus Shale is below the resolution of these post-stack seismic data, these structure maps provide a partial understanding of probable Marcellus fracture patterns. Understanding stress fields conditions within the unconventional shale reservoirs is useful for determining where natural fractures should be localized.

Complex structural zones such as fracture and fault systems are often poorly imaged because conventional seismic attributes may not provide valid information in some geological settings. In light of this fact, I will present a workflow to develop an analysis of seismic data acquired in a complex area such as Bradford County, Pennsylvania. The main strength of this analysis is to combine multiple seismic attributes to reveal a more detailed and clearer understanding of subsurface structures associated with the fractures and fault systems found in Marcellus Shale. There is often enough knowledge in single-component seismic data to identify main fault blocks by analyzing attributes generated from commercial software. However, my goal is not only to identify main fault blocks, but also to determine physical properties and connections between complex structures. This study is 3D-oriented, based on visual analysis of seismic dataset, and is formed in two stages:

- The first stage is to detect fault and fractured zones from seismic data from manually interpreted horizons.
- The second stage is to identify physical properties of these zones and to analyze how these faults and fracture systems connect to each other.

Geologic structures were extracted from the 3D seismic data using a Foster Findlay software demonstration license. The objective was to compare various attributes identified by Landmark Seisworks software in order to enhance and extract geological features imaged with multicomponent seismic data. Attribute volumes generated by Foster Findlay software contain valuable information required for a comprehensive understanding of characteristics of subsurface structures without involving any interpretation. My dataset is faulted and contains complex fracture systems as well as channels. Interpreting these features can require considerable time because it is difficult to understand these structurally complex features. Therefore Foster Findlay software was used to generate various attribute volumes in an attempt to gain a quicker understanding of these complex structures.

First, random noise attenuation was applied to the seismic data. The difference between volumes before and after filter application is demonstrated in Figure 105. Next, attribute volumes were generated by Foster Findlay software to provide a fast stratigraphic interpretation and rapid analysis of subsurface structures. Attribute volumes were generated to highlight areas where fractures and channel systems exist.

Results demonstrated that high amplitude events were easily identified in attribute volumes. Fault lineations and complex discontinuity systems interpreted as fracture systems were clearly identified in dip volume and in body volumes such as semblance (Figure 106 and 107). All attribute volumes provided strong correlations with reflectivity data; however, they revealed details which were not easily identified from conventional attributes such as coherency and curvature (Figure 108).

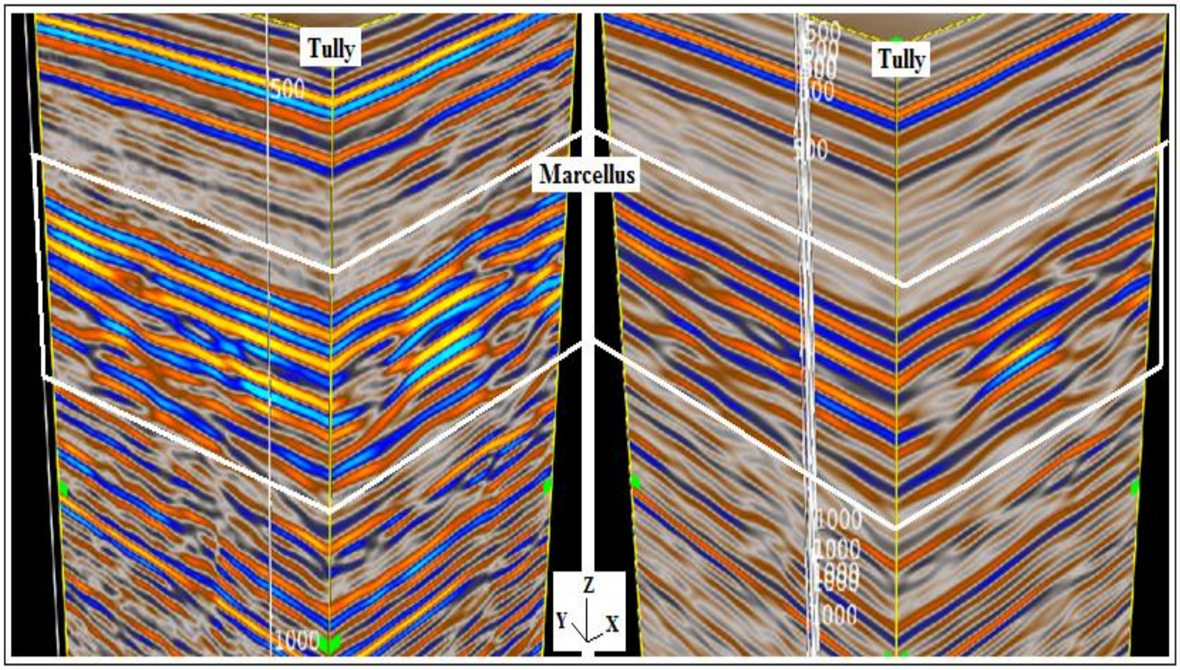

Figure 105: The appearance of P-wave data before (left) and after (right) random noise filter application.

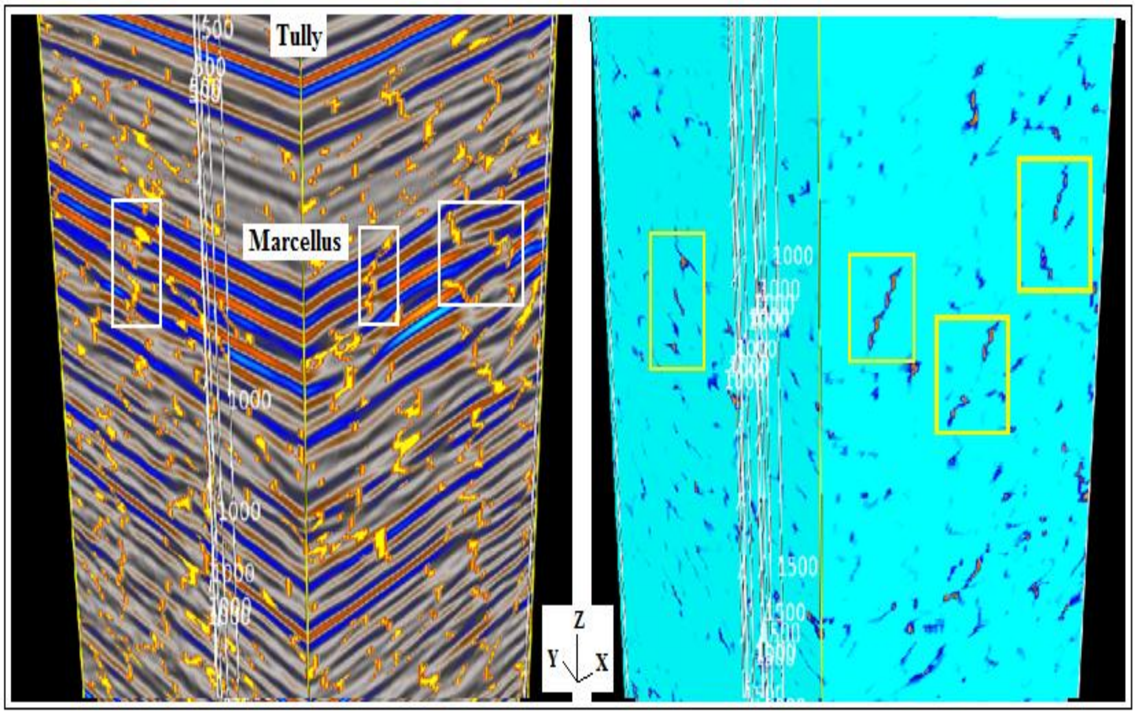

Figure 106: Discontinuities of seismic events identified by semblance (right), and discontinuity lines overlaid on P-wave data (left). White and yellow boxes indicate the zones where fracture and faults are interpreted.

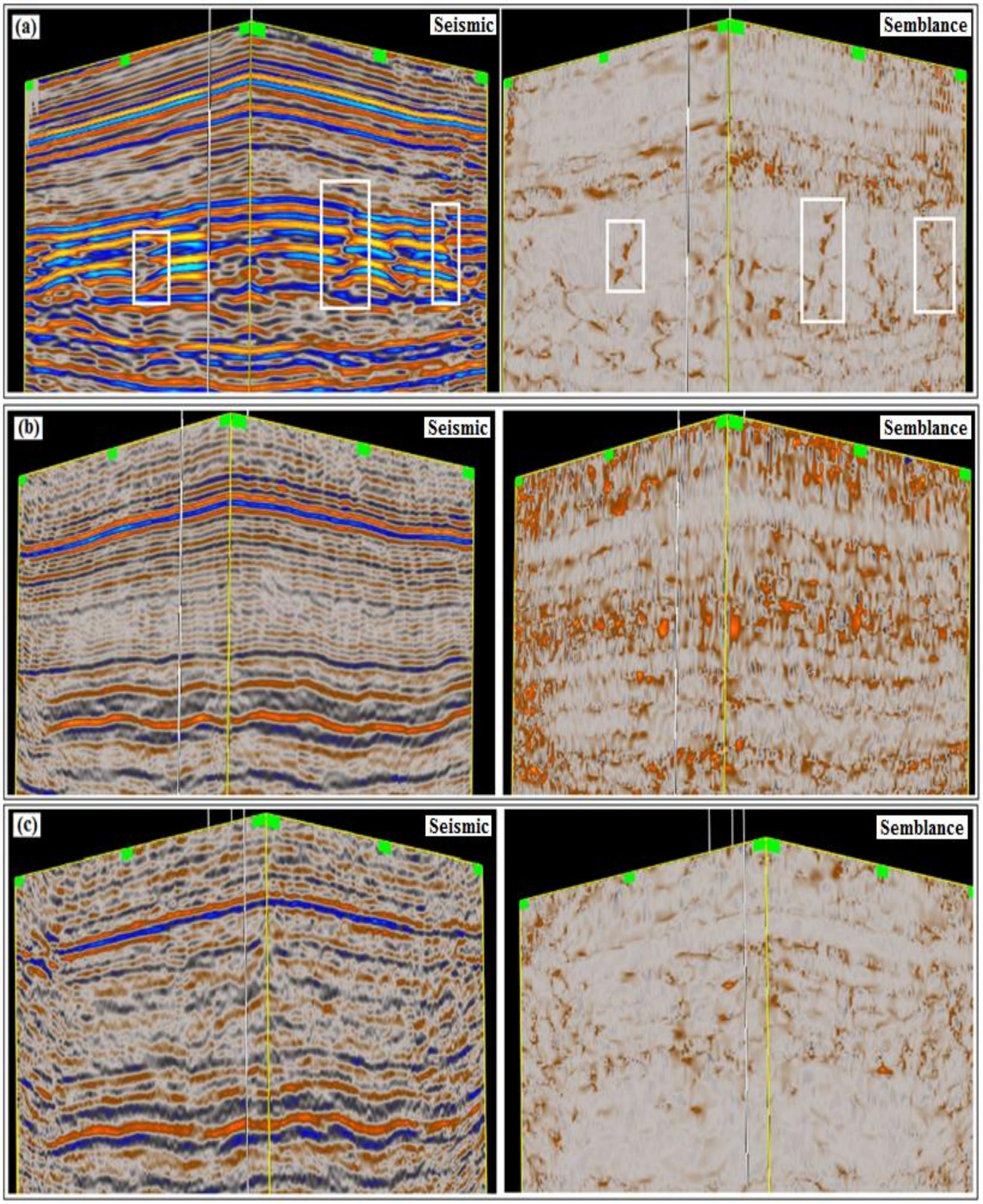

Figure 107: Semblance attributes generated from (a) P-wave, (b) S1-wave, (c) S2-wave seismic volumes. White boxes indicate the zones where fracture and faults are interpreted.

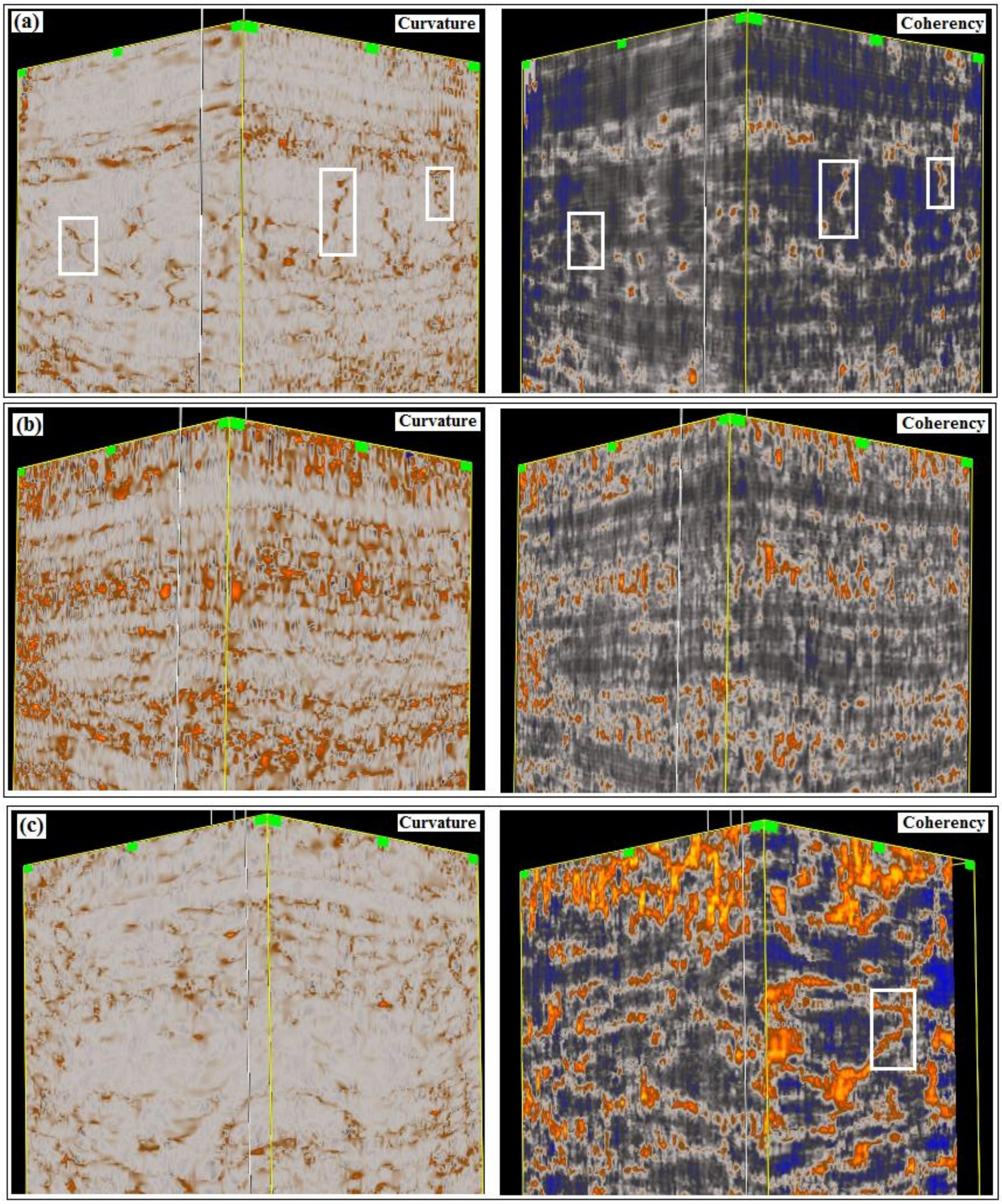

Figure 108: Curvature and coherency attributes generated from (a) P-wave, (b) S1-wave, (c) S2-wave seismic volumes. White boxes indicate the zones where fracture and faults are interpreted.

One of the goals of this study was to investigate and compare fracture and fault interpretations with various types of subsurface volumes. Foster Findlay attribute volumes such as Fault In and Fault Detect provided rapid stratigraphic interpretation by indicating the likelihood of fracture and fault systems from visual analysis to detect potential locations where complex features caused discontinuity of seismic reflection strength. As demonstrated in Figure 106, there was a good match between discontinuity surfaces detected from seismic data and the faulting/fracture networks identified from seismic data by Foster Findlay algorithms. Fault image volumes generated by software provided a detailed, efficient interpretation, highlighted potential zones where fault and fracture systems exist, and defined potential connections between possible fluid-flow channels within subsurface units.

Discontinuity surfaces highlighted with red/orange colored lines on dip volumes match discontinuity events identified from other attribute volumes (Figure 109).

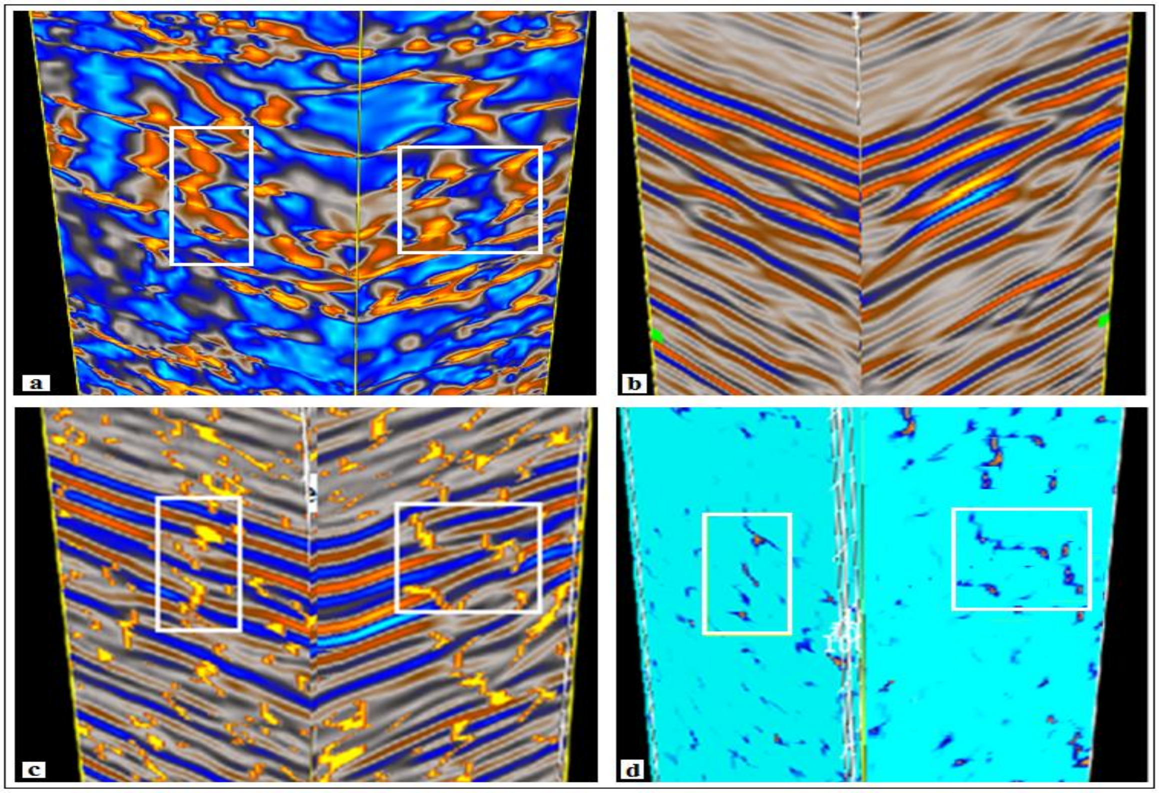

Figure 109: Discontinuity (c), dip (a) and semblance (d) volumes generated from P-wave seismic data (b). Each data display provides different details regarding faulting/fracture surfaces. White boxes indicate the zones where fracture and faults are interpreted.

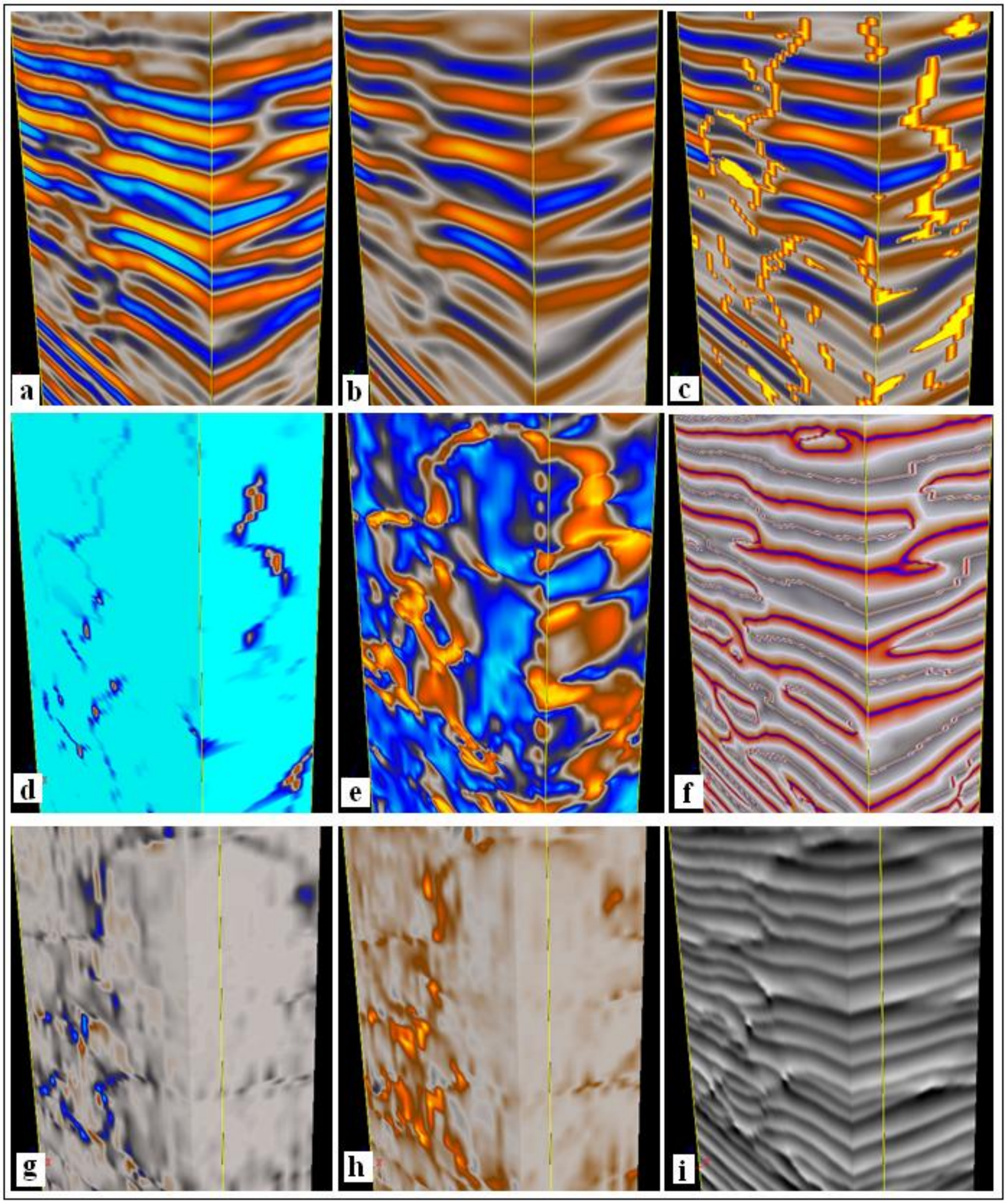

Figure 110: Seismic data volume before (a) and after (b) filtering, and various attributes indicating fault and fracture systems: fault line (c), instantaneous frequency (d), dip (e), phase (f), positive curvature (g), negative curvature (h), and energy (i). All examples are P-wave data.

Selected inline and cross-line profiles provided examples that illustrate how to identify complex features. Fault-line images (Fig. 110c) show high probabilities of faulting or the existence of fracture systems as yellow-shaded features. Other attribute volumes were utilized in addition to Foster Findlay volumes to provide comparison and to increase the accuracy of stratigraphic interpretation (Fig. 110). Potentially fractured zones and fault zones are interpreted where high amplitude reflectivity data correlate with a high level of instability in frequency decomposition volumes such as instantaneous frequency and instantaneous phase (Figs. 110d, 110f).

Curvature, a rate of change of direction of a curve on a multidimensional surface, indirectly infers fracture existence in layered media because a significant increase of curvature indicates increased strain values. As Roberts (2001) suggested, Hooke's Law requires stress to increase as Young's modulus increases. Therefore large curvature values with associated high Young's modulus indicate an increasing possibility of fracturing. These principles are described by the following equation:

$$\sigma = E\,e = E * (h/2) * K \tag{5}$$

$$e = (L_1 - L_o) / L_o \tag{6}$$

$$e = (h/2) / R = (h/2) * K \tag{7}$$

In equations 5 to 7, "E" represents Young's modulus of a layer, whereas "e" represents strain on the top of the layer and "K" represents maximum curvature of the layer. Young's modulus $E_b = \lambda + 2\mu$ is simply the P-wave modulus (Perez et al., 2011). The relationships defined above express how curvature can be used to estimate stress and strain in layered media. Although it is not easy to analytically calculate stress and strain from curvature because the top and the base of the fractured unit are difficult to define, fracture density of media can be estimated through curvature and stress-strain relationships. Figure 110 shows an example of positive and negative curvature values calculated from P-wave data displayed as volumes. Each attribute targets a different feature of the structure embedded in seismic data. Faults identified in semblance become clearer on fault-line volumes in which discontinuity zones are edged with boundaries to indicate possible faults or fractures. Figure 111 and 112 shows visual comparisons of reflectivity data, semblance, dip, discontinuity, detected fault and fault line attribute slices.

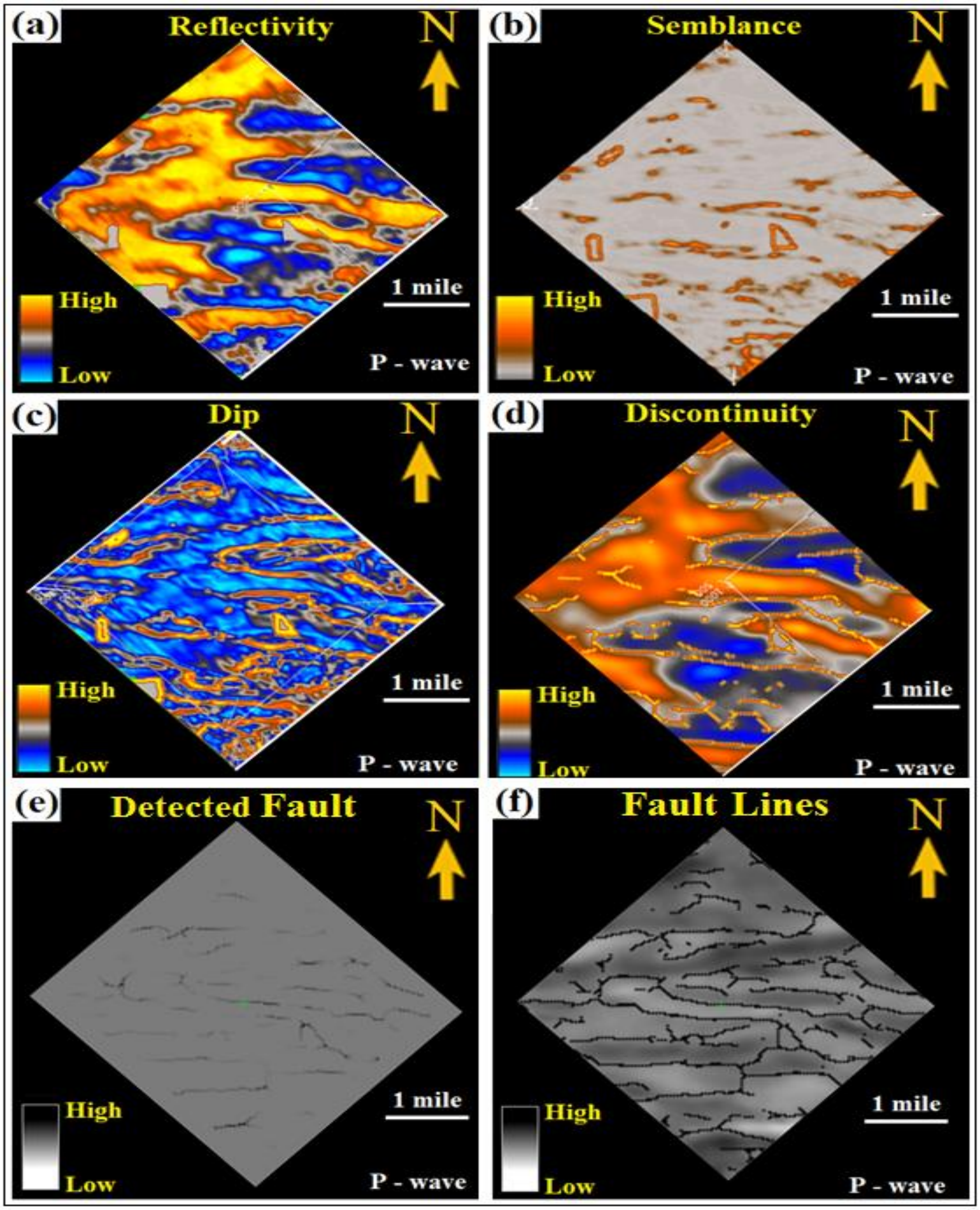

Figure 111: Visual comparison of reflectivity (a), semblance (b), dip (c), discontinuity (d), detected fault (e), and fault lines (f) attributes of Marcellus Shale interval. All examples are P-wave data.

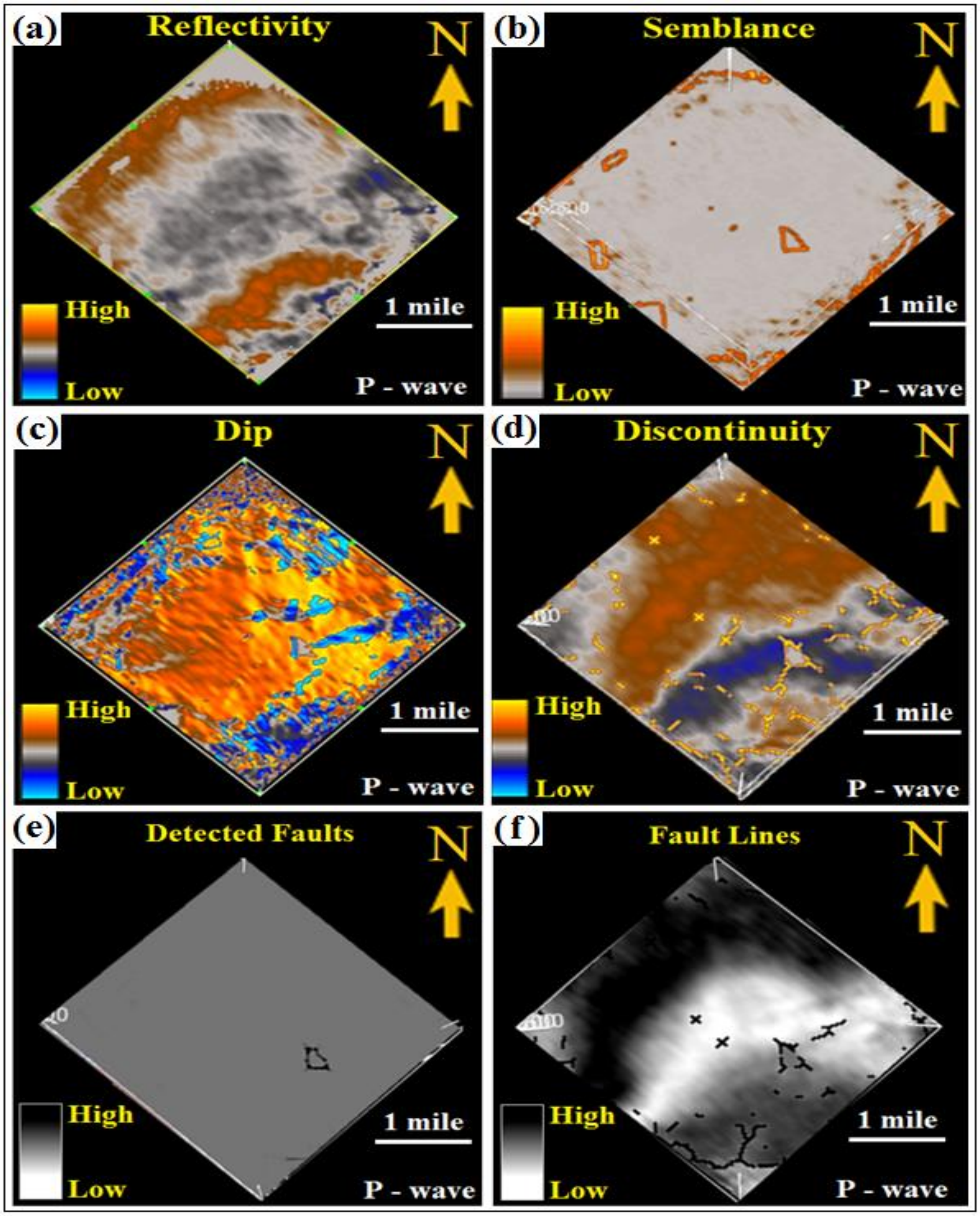

Figure 112: Visual comparison of reflectivity (a), semblance (b), dip (c), discontinuity (d), detected fault (e), and fault lines (f) attributes of Tully Limestone. All examples are P-wave data.

Figure 113 highlights the zones where potential fracture and fault systems caused strong amplitudes and significant patterns on various attributes. Each data panel displays the correlation between attributes for different inline and cross-line seismic sections.

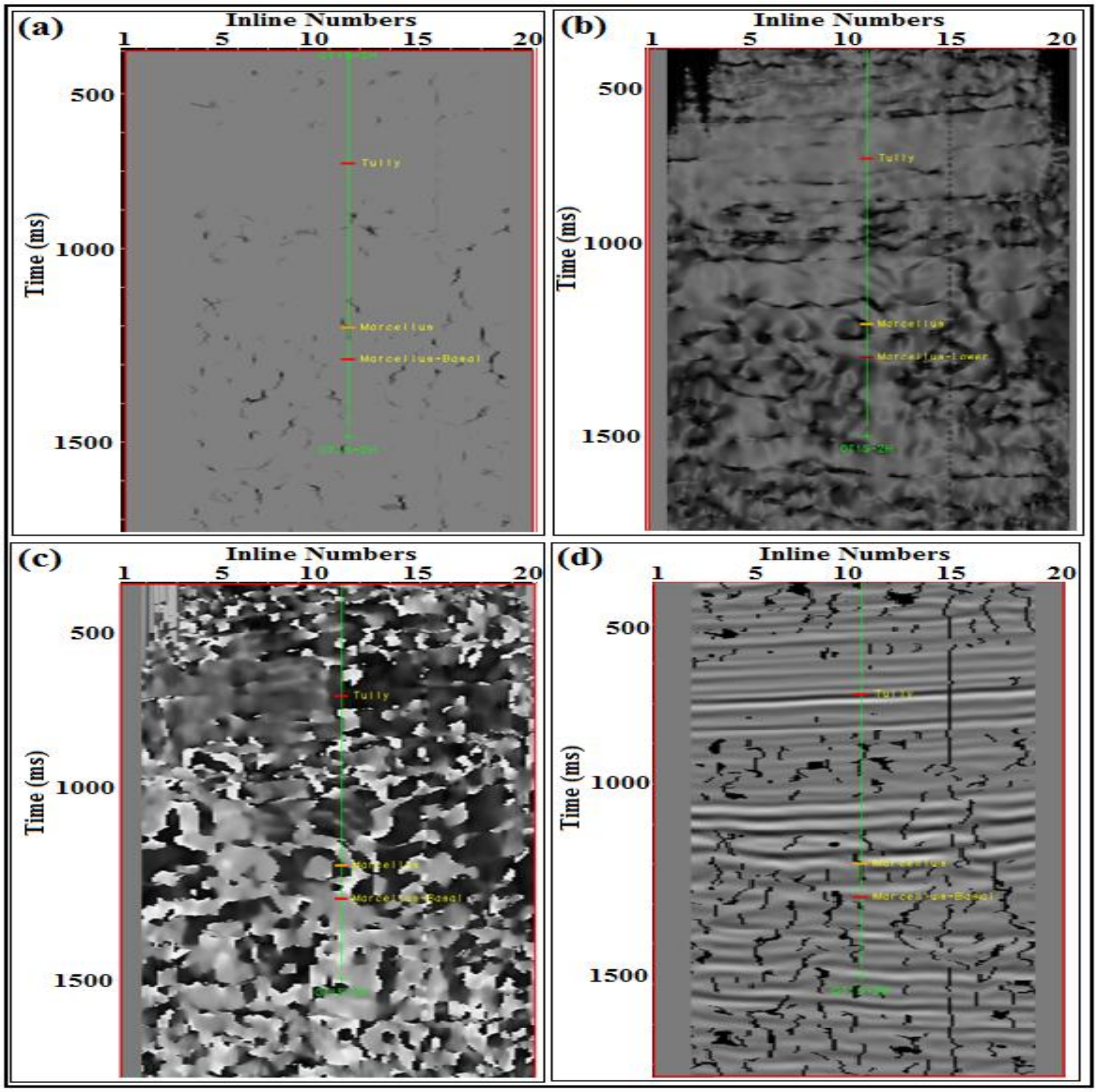

Figure 113: Visual comparison of reflectivity strength (a), dip (b), azimuth (c) and fault-line (d) attributes for inline seismic sections with formation tops displayed based on well data. All examples are P-wave data.

So far in this section, I have compared multiple seismic attributes for only compressional wave data (Figs. 107 through 113). When seismic attributes are generated from different seismic wave volumes (P, S1, S2), we observe major differences that highlight the importance of multicomponent seismic stratigraphy.

Multicomponent multi-attribute analysis demonstrated that lithology and pore-fluid content have significant influences on P- and S-wave velocities and their velocity ratios. Analysis of many seismic attributes demonstrated that some velocity changes are caused by pore pressure changes, and these variations can be detected on different volumetric attributes. Unconventional shale reservoirs typically have a velocity ratio (V_p/V_s) higher than 1.7. Overpressure conditions within an interval usually cause the velocity ratio to decrease. This indication of over-pressured zones within fractured shale reservoirs can be identified from analyses of seismic attributes. Identifying such geologic characteristics help overcome geologic production challenges such as low permeability, low porosity, and heterogeneity associated with natural fracture networks within overpressured reservoir intervals. P-wave seismic data alone cannot identify all such targets. Therefore multi-attribute analysis from multicomponent seismic data volumes are required to identify subtle fracture networks and faulted zones and lithological changes that may control gas production from unconventional reservoirs.

As demonstrated in Figures 114 – 118, some S-wave attributes such as discontinuity surfaces and semblance highlight faulted and fractured zones that cannot be identified from conventional P-wave seismic attributes such as coherency and curvature. Red boxes on Figures 114 – 115 point out the differences among the P, S1, and S2 wave images. Faults and fractures represented by vertical discontinuity surfaces identified from shear wave instantaneous bandwidth, instantaneous phase and instantaneous frequency volumes are not present in such volumes generated from compressional wave data.

Unlike shear wave instantaneous bandwidth, instantaneous phase and instantaneous frequency attributes, some attributes from conventional wave data show continuous reflectivity over the area where fractures and faults are interpreted from shear wave attributes (red boxes in Figs 114 and 115). However, some of the seismic attributes such as curvature, and discontinuity/fault line generated by compressional and shear wave images demonstrated similar behaviors within the Marcellus reservoir. These observations show us why multi-attribute analysis using multicomponent seismic data provide more details about geology.

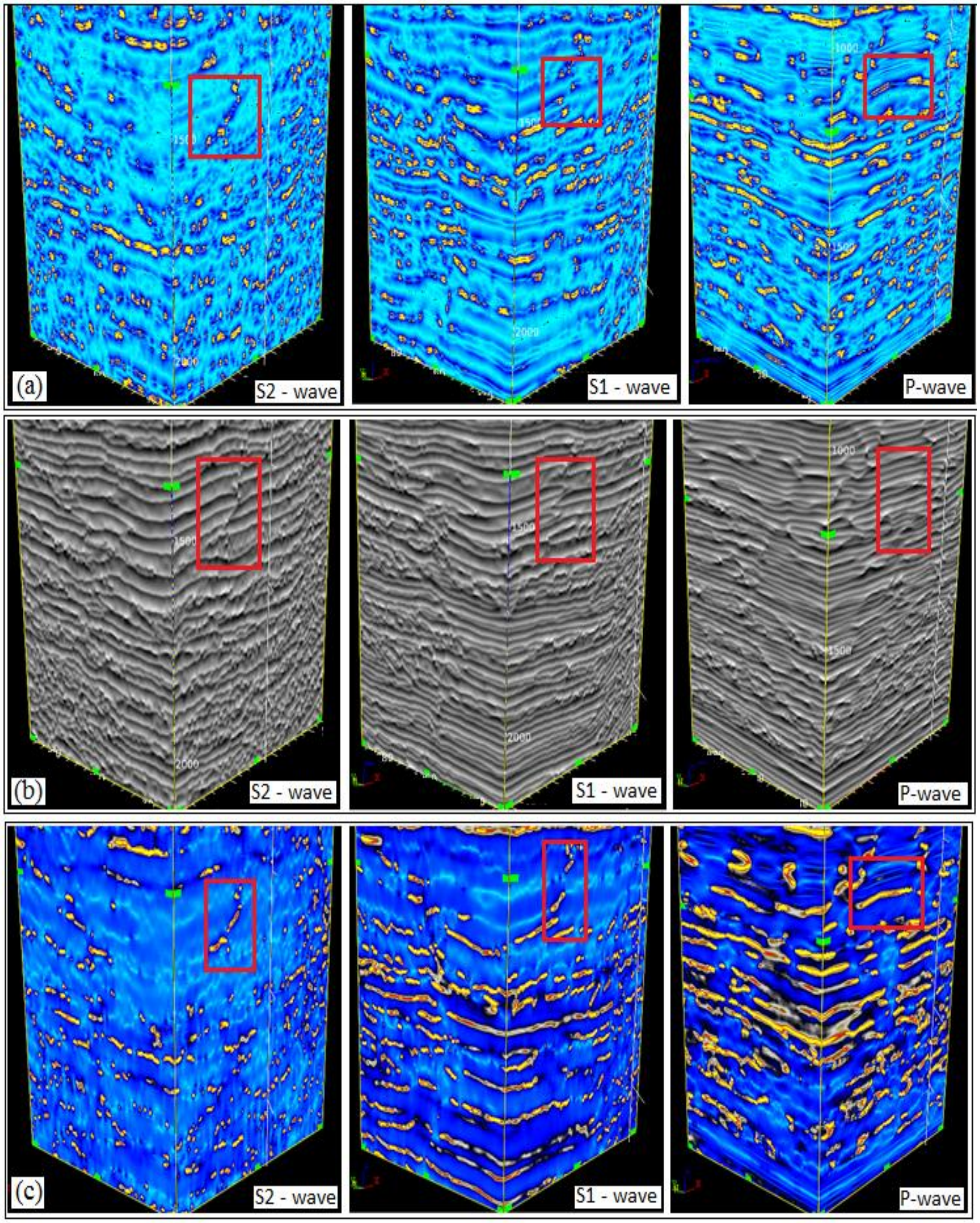

Figure 114: (a) Instantaneous bandwidth, (b) energy half time, and (c) instantaneous frequency attributes. Red boxes indicate zones where fracture and faults are interpreted.

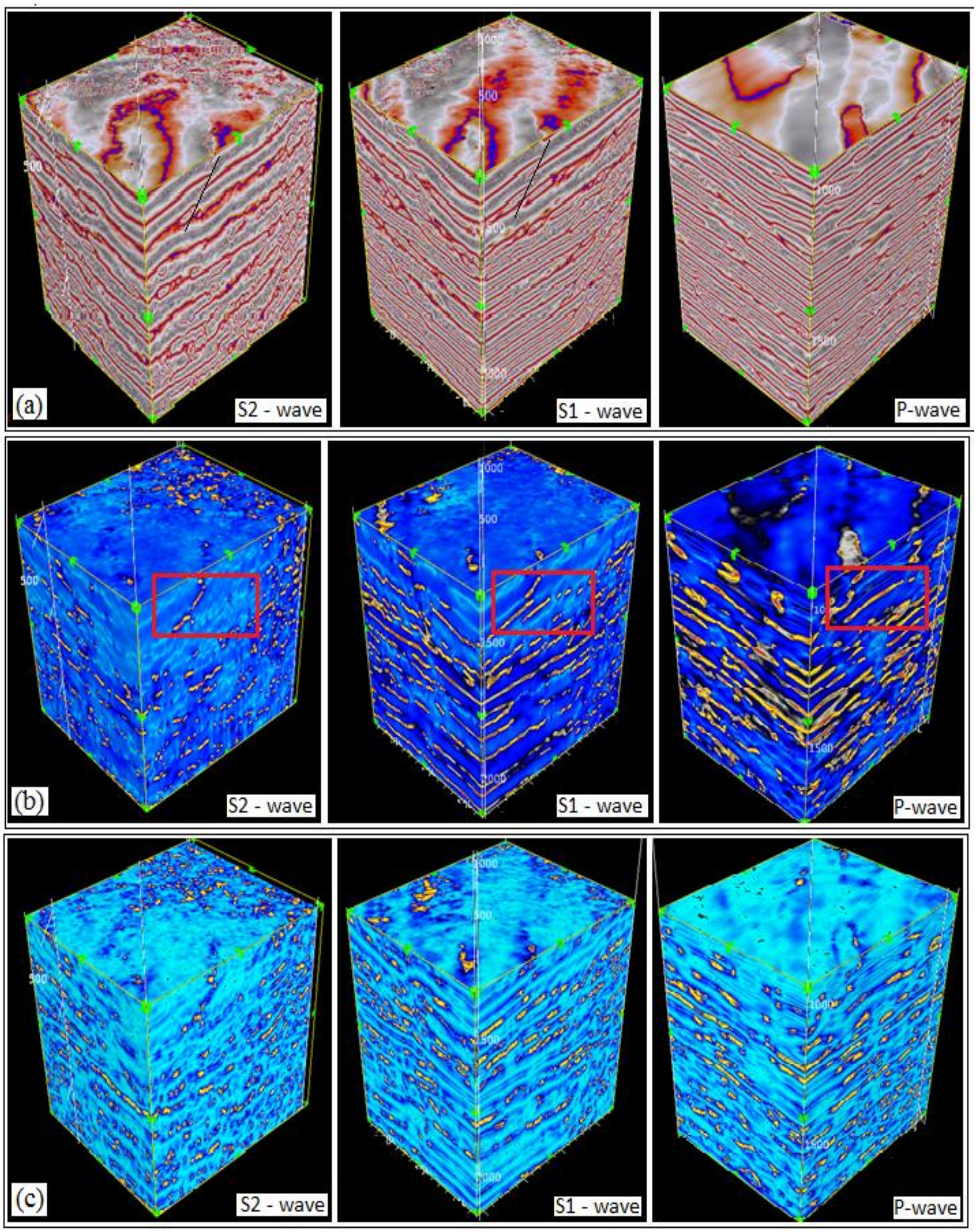

Figure 115: (a) Instantaneous phase, (b) instantaneous frequency, (c) instantaneous bandwidth attributes. Red boxes indicate zones where fracture and faults are interpreted.

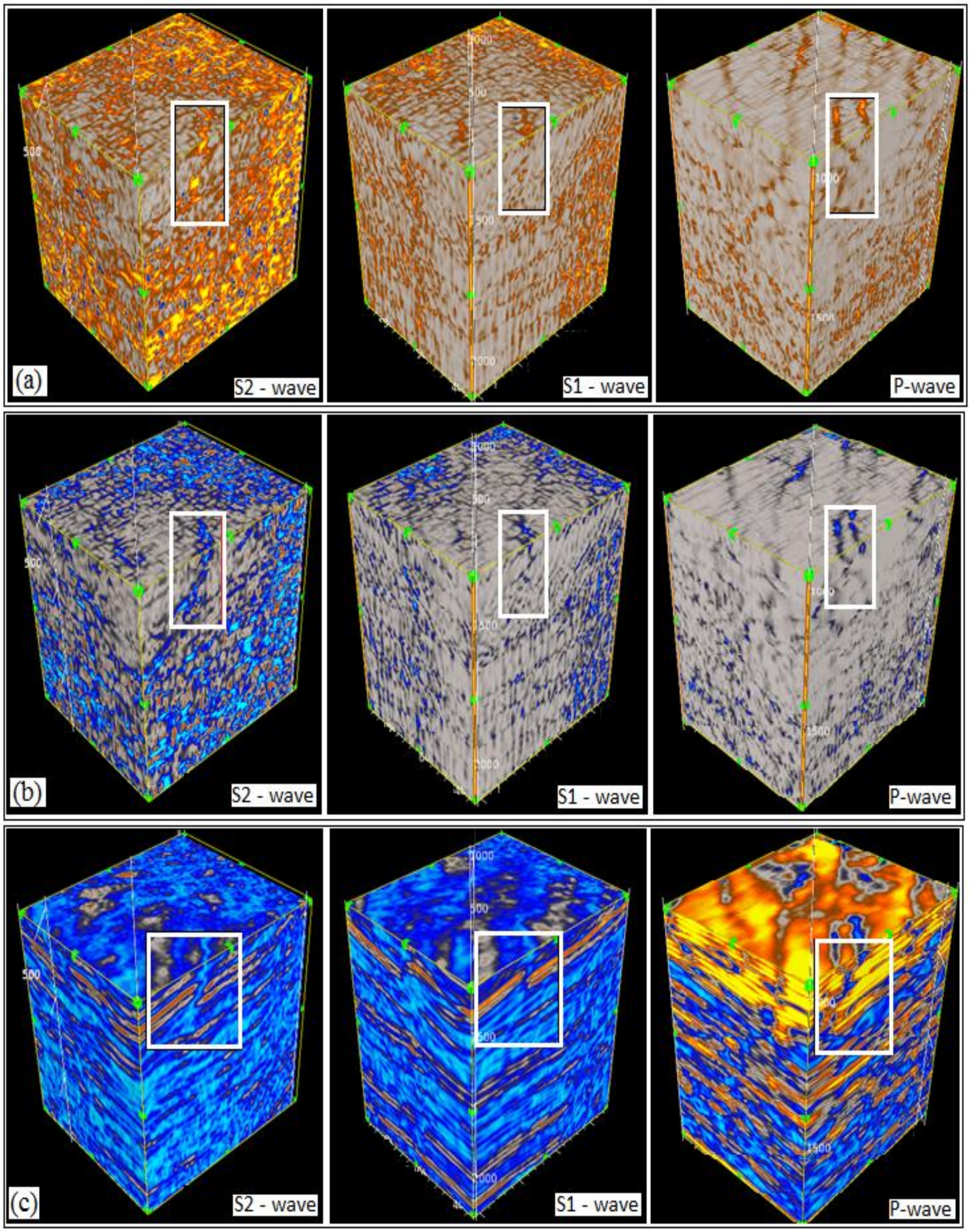

Figure 116: (a) Negative Curvature, (b) positive Curvature, (c) RMS amplitude attributes. White boxes indicate zones where fracture and faults are interpreted.

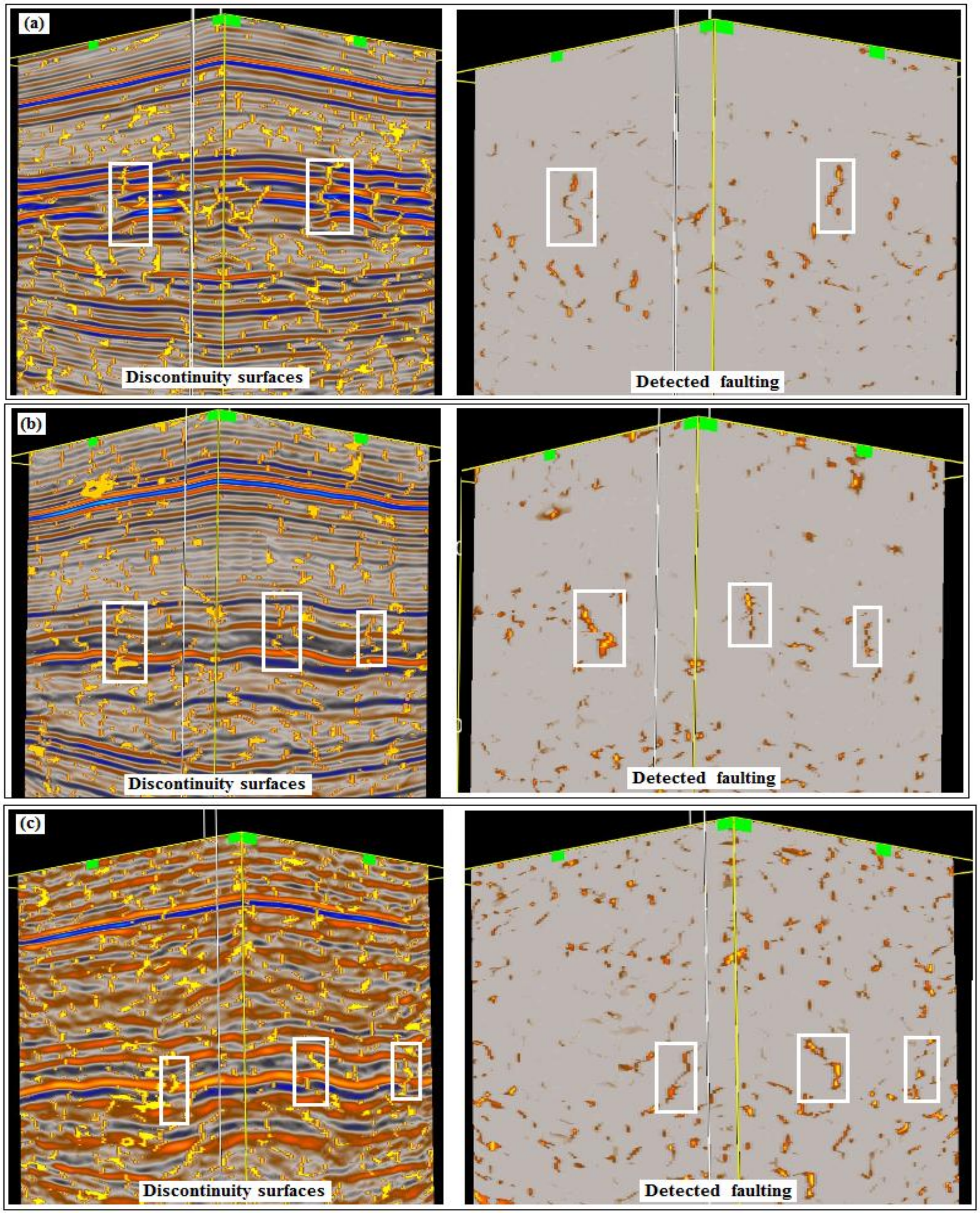

Figure 117: Discontinuity surfaces and detected faulting attributes generated from (a) P-wave, (b) S1-wave, (c) S2-wave volumes seismic volumes. White boxes indicate zones where fracture and faults are interpreted.

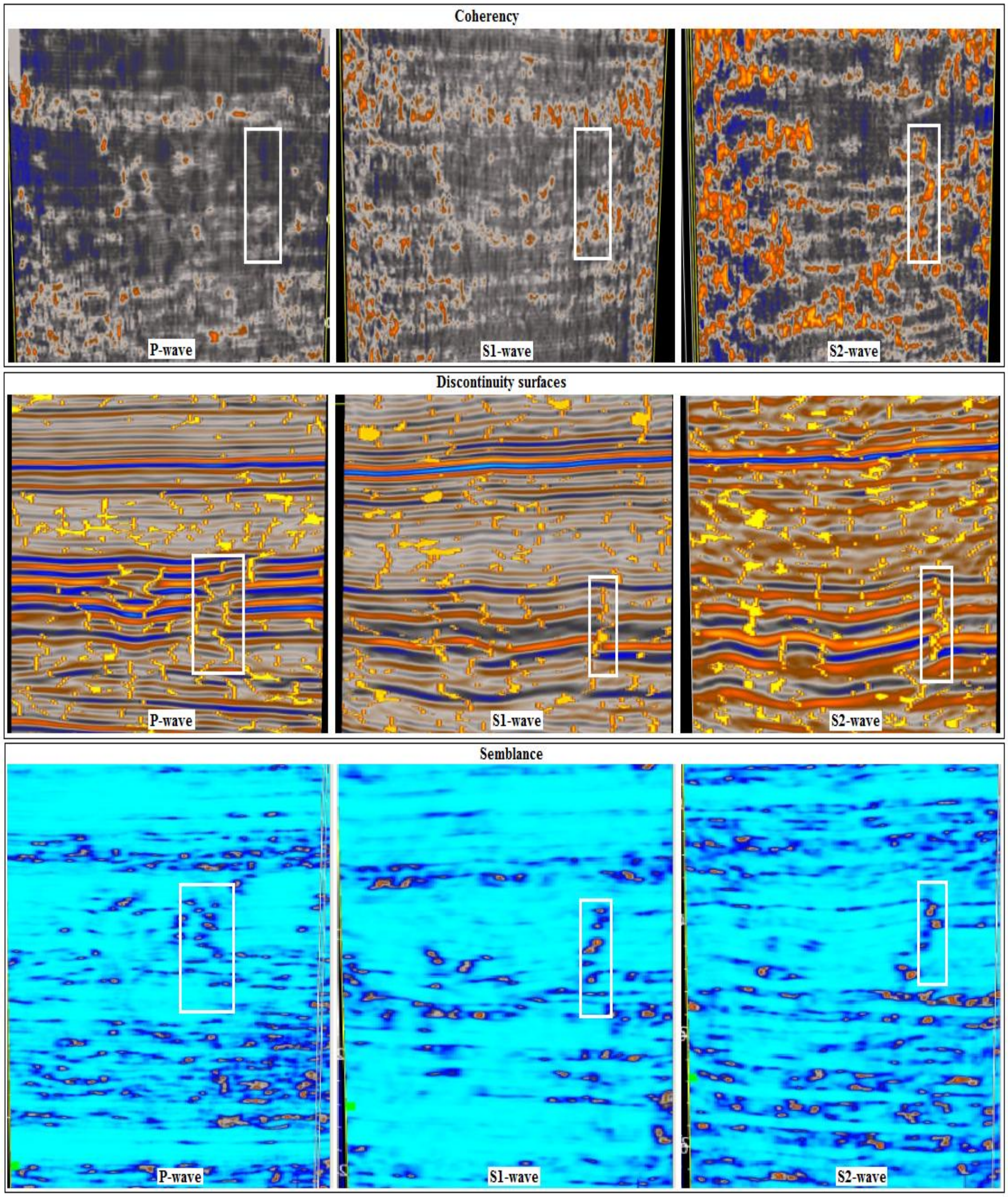

Figure 118: Discontinuity-surface, detected faulting, and coherency attributes generated from multicomponent seismic data. Semblance and discontinuity-surface attributes highlight faulted zones that cannot be identified on coherency attribute. White boxes indicate zones where fracture and faults are interpreted.

P-wave and S-wave Impedance Inversion for Geomechanical Analysis of an Intra-reservoir Anomaly and Marcellus Shale Formations

I generated impedance attributes with a model based inversion as described by Cooke and Schneider (1983). Such impedance inversion studies using multiple seismic wave-modes enable comparing borehole log data with multicomponent seismic data for quantitative reservoir analysis. The principal goal of impedance inversion is to transform seismic reflectivity data to impedances, which can then be linked to quantitative reservoir properties. Inversion also provides higher resolution and more accurate interpretations by removing the wavelet and de-tuning the data (Pendrel J., 2006; Pendrel et al., 2000).

P-wave and S-wave impedance inversion was done to (1) identify the extent of a porous Middle Devonian sandstone unit that was tentatively identified as a buried channel from seismic attribute analysis, and (2) evaluate the lateral continuity and changes in the reservoir texture of the Marcellus Shale. These inversion studies were performed using Hampson-Russell software. Model-based P-wave impedance inversion and bandlimited P-wave impedance inversion methods were performed on post-stack seismic data. The results of model-based inversion demonstrated that the background model strongly influences inversion results; whereas, bandlimited P-wave impedance inversion does not require a background model. Therefore, most of the inversion effort was based on bandlimited inversion.

Bandlimited impedance required that a zero-phase conversion be done by extracting a wavelet from well data acquired at the center of the seismic survey and then applying zero-phase wavelet deconvolution to the 3D seismic data. These zero-phase seismic traces were then integrated to generate a final impedance volume.

Multi-attribute analysis of multicomponent seismic data showed that fractures in the reservoir architecture and the organic content of shale units influence seismic reflection amplitude and other seismic attributes such as coherency and curvature (Figures 94, 95, 97 (b), and 98 (b)). Also attribute analysis (Figures 96, 97 (c), and 98 (c), and 99 (c)) showed a channel-like feature that was assumed to be a porous sandstone unit below the Tully Limestone formation. The objective of this section is to analyze this features using impedance inversion to provide additional information about its lithologic character.

The results of these impedance inversion analyses have improved the understanding of the extent of this geologic feature and can be used to evaluate the interval as a storage unit for flow-back water produced during hydrofracing operations. P-wave and S-wave impedance inversion results together with multi-attribute analysis suggest the thickness of this porous sand unit increases to the east, and may be filled with impermeable sediment that will decrease the porosity and permeability of this unit. This observation may have strong implications regarding the use of this sandstone interval as a water-storage unit.

IMPEDANCE INVERSION WORK FLOW

P-wave impedance and S-wave impedance studies were done using Hampson-Russell Software provided by the Exploration Geophysics Laboratory at the Bureau of Economic Geology. The inversion work involved several steps:

1) performing well-ties using P and S velocities recorded in the central-image calibration well for both compressional and shear data volumes,
2) extracting zero-phase and mixed-phase wavelets from the seismic dataset,
3) generating background models for P-wave and S-wave impedance inversions, and
4) applying inversion process on compressional and shear wave data volumes.

The project flow used to generate final impedance volumes is given in Figure 119. The input data used for an inversion consisted of a set of log data (density, sonic logs) acquired in the calibration well, the multicomponent seismic data (compressional and shear), and a series of seismic horizons picked from the seismic data volumes during interpretation. Well data were loaded into Hampson-Russell software via the GEOVIEW module that provided a database for entire project, and seismic horizons were imported into the database via the STRATA module.

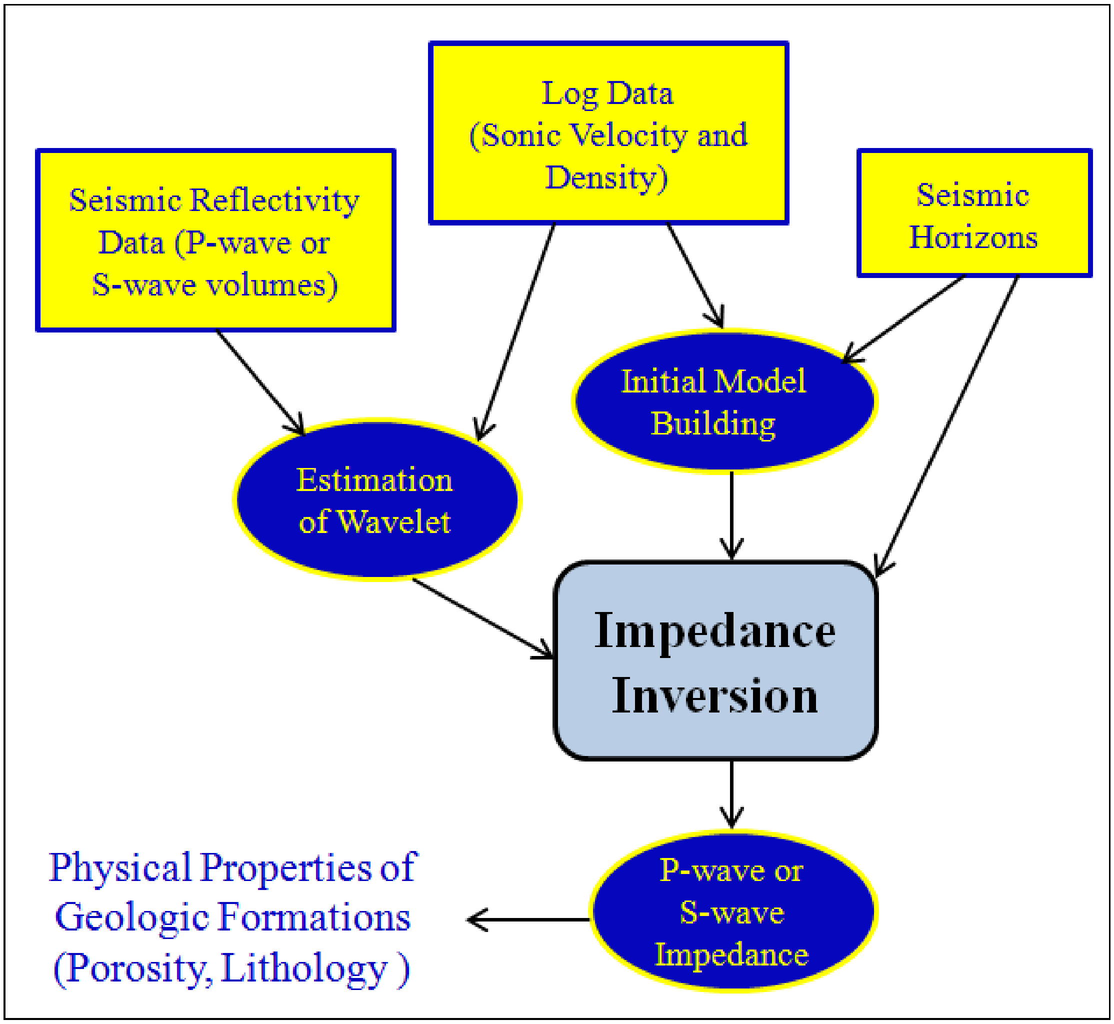

Figure 119: Flow chart used to generate final P-wave and S-wave impedance volumes.

My initial inversions integrated log data from the single calibration well, which is the only well within the seismic survey area that penetrates the entire Hamilton Group interval (Tully Limestone, Tichenor Limestone, Lower, and Upper Marcellus formations and Cherry Valley Limestone). I used the ELOG module to prepare and extract log data that were used in the inversion analysis. In addition to generating log cross plots, ELOG correlates well log data to multicomponent seismic data using synthetic seismic traces derived from calibration well data. ELOG provides multiple options for extracting a wavelet either from seismic data alone, or from well data in conjunction with seismic volumes. I extracted a wavelet using well log data in conjunction with seismic volumes (Fig. 120). STRATA uses log data to determine the amplitude and phase spectra of the wavelet and uses seismic traces to extract the wavelet via a coherency matching technique (White, 1980).

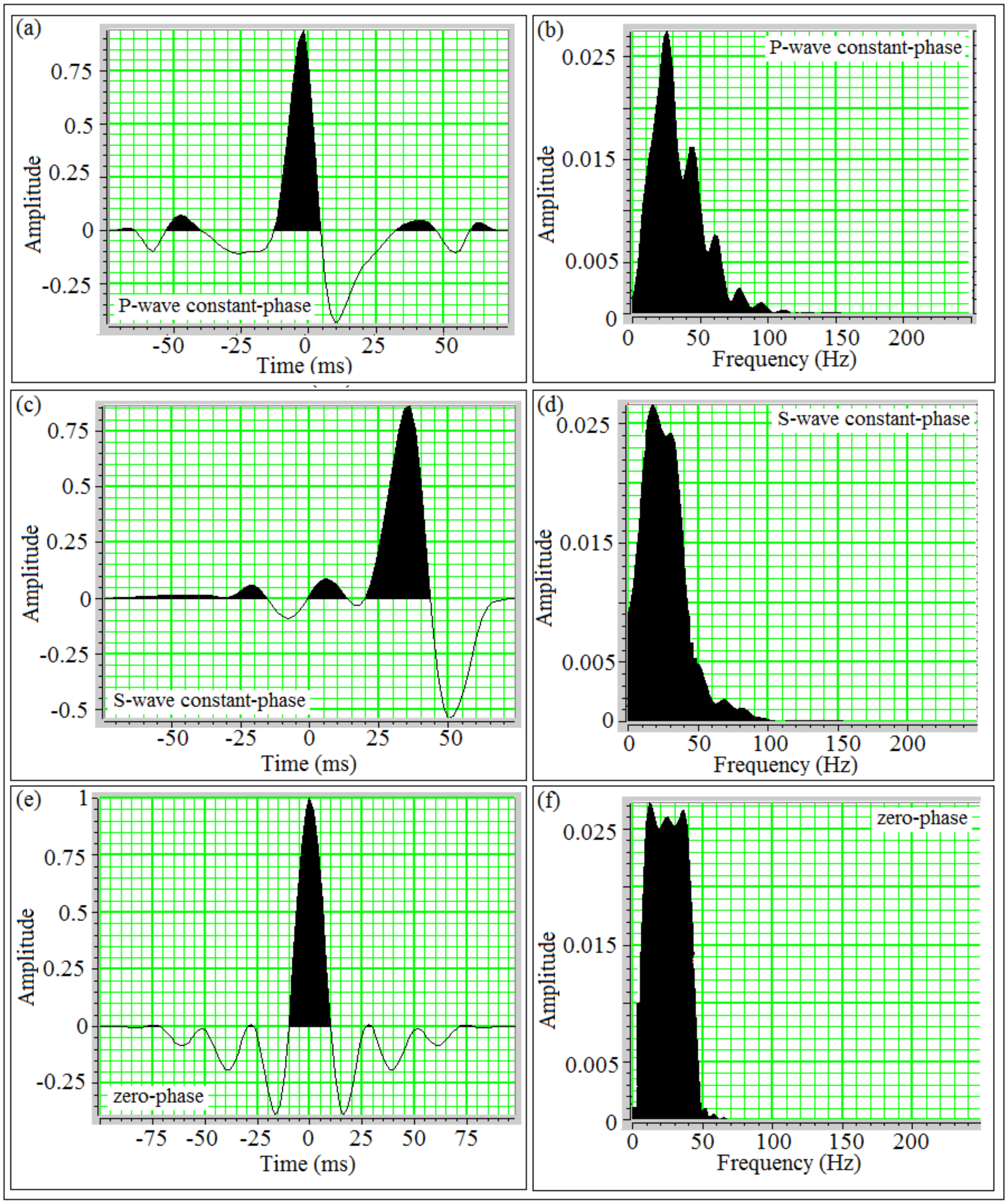

Figure 120: Wavelet and amplitude spectrum extracted under a constant phase (a-d) and zero-phase (e, f) assumptions. These wavelets were calculated using data from a 650 – 1050 ms window of in-line seismic section IL100 of the P-wave data (a, b) and S-wave data (c, d).

After incorporating well log impedance values into P-wave and S-wave impedance inversions of post-stack migrated multicomponent seismic volumes, I used the Hampson-Russell software module EMERGE to correlate these seismic impedance values with the distribution of lithologic units within the Hamilton Group (Tully Limestone to Lower Marcellus Shale formation). Because the log-derived synthetic seismic must correlate correctly with the multicomponent seismic data, manual corrections (squeezing and stretching the log) are required to optimize the best correlation in time between the log data and the seismic data volumes. The success of the correlation depends on estimating an accurate wavelet from well and seismic data, and is therefore contingent on both the quality of the log data and the seismic data.

Seismic lines IL100/XL90 and log data acquired in the calibration well at the center of the survey area were compared to consider seismic-to-well tie analysis. The well tie was analyzed by loading seismic data volumes and well data into Hampson-Russell Geoview, E-log, and STRATA modules. Compressional and shear wave logs and density measurements acquired in the borehole well were useful in estimating wavelets used for this inversion effort.

An amplitude spectrum and estimated wavelet were calculated for all traces of in-line IL100 over a time window spanning 650 ms – 1050 ms. These wavelets and spectra are shown in Figure 120. Note that the spectrum of the zero-phase wavelet is almost rectangular in character, and extends from 0 to 50 Hz. The estimated wavelet and its amplitude spectrum are similar to that of a Ricker wavelet. An initial 50 Hz Ricker wavelet was utilized for convolving with the well reflectivity series to create synthetic seismograms that were crosscorrelated with the compressional wave seismic data volume prior to wavelet extraction.

Five major horizons interpreted from seismic volumes were used to establish the match between seismic data and synthetic seismograms. As shown in the Figure 121, the tie between the seismic volumes and synthetic seismograms for Tully, Tichenor and Cherry-Valley Limestone units, Lower and Upper Marcellus Shale units were straightforward to establish.

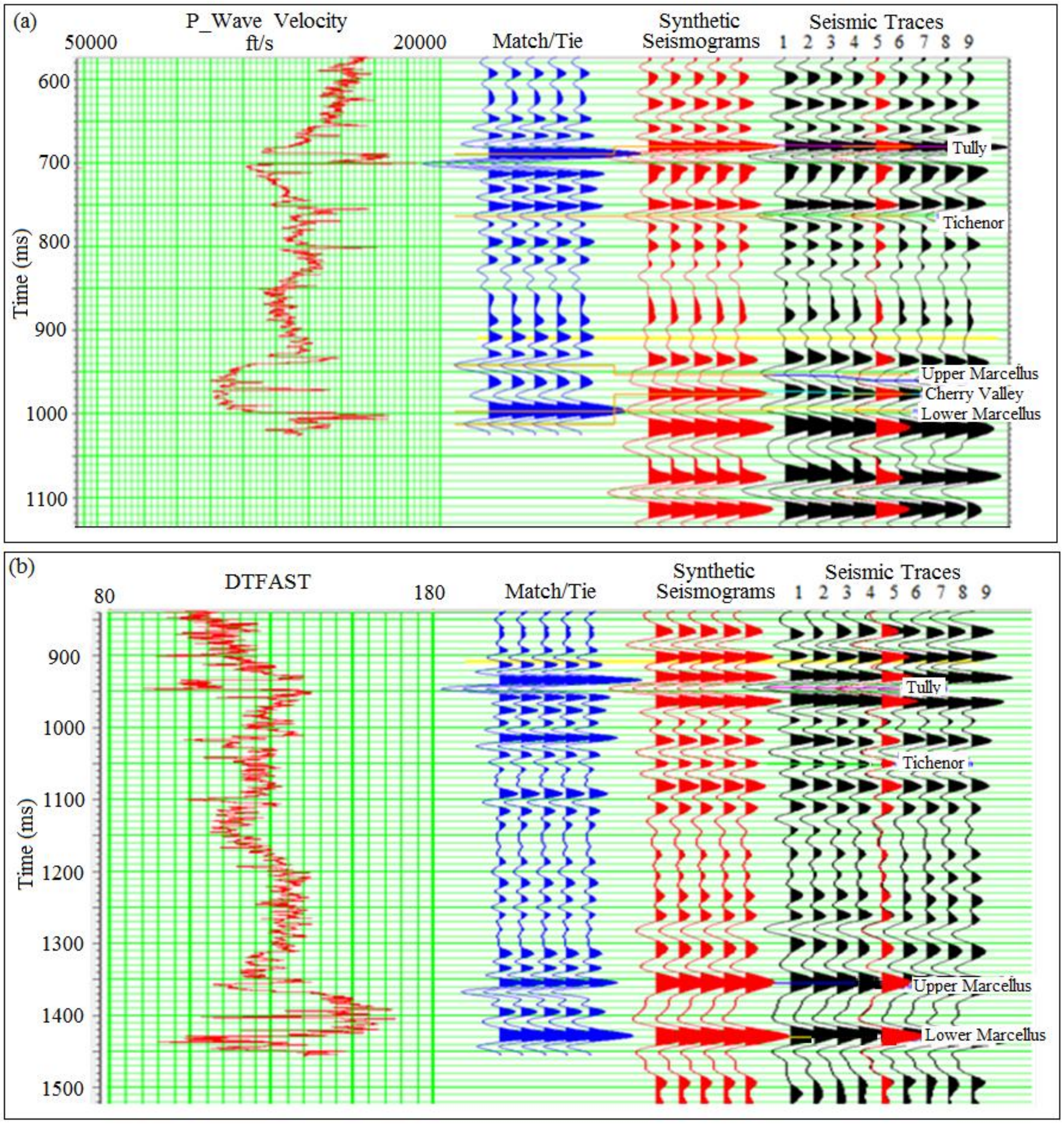

Figure 121: Seismic to well-tie analysis based on finding the best match between compressional seismic data and sonic compressional wave log data (a) and the match between shear seismic data and sonic shear data (b). Sonic wave velocity log data are shown on the left, and the compressional and shear wave seismic data along the inline direction which intersects the well location are shown on the right (black wiggles) on both figures. Synthetic seismograms (red wiggles) and the best match (blue wiggles) found between seismic and well data are shown in the middle on both figures.

INVERSION

In principle, bandlimited inversion is based on the assumption that a seismic trace is an approximation of the Earth's reflectivity; therefore, this approximated reflectivity can be inverted to produce the P-wave and S-wave impedance volumes representing Earth layering. Bandlimited inversion creates impedance volumes after the following steps are completed:

- building an initial low frequency Earth-layer model using sonic and density logs (Figure 122)
- inverting seismic traces using a recursive inversion procedure that creates a middle-frequency band of P-wave and S-wave impedance volumes.
- merging these low and middle-frequency volumes to produce a final impedance inversion volume

An important step required for building an initial Earth model is to provide main horizons picked from a seismic volume. Inversion software then creates the model by calculating interval velocities at selected points along these horizons, and interpolates these velocity values to produce a velocity volume in which each sample of each seismic trace that will be inverted has an associated velocity value. This velocity volume is blocky because of the interpolation along seismic horizons.

At the first stage, low-frequency components of impedance values are generated. Because seismic data generally do not contain useful energy below 10 Hz, the parameter that constrains the filter frequency was selected as 10 Hz. This parameter is important because bandlimited inversion techniques require a low-frequency limit be provided so a module can generate a model whose frequency is constrained between this low-frequency limit and the middle-frequency value that constrains the model the upper frequency limit of the estimation.

At the second stage, bandlimited inversion requires inverting the seismic traces to produce the middle-frequency range impedance estimates that are later merged with low-frequency range estimates. Although limiting inversion over a window is recommended to lower the processing time spent during inversion, I did not follow this approach because any window constrain used in inversion may create unrealistic inversion values at window edges and create differential bulk shifts from trace to trace on final impedance volumes.

At the last stage, the low-frequency model values are merged with the middle-frequency values (Figure 122 (a)).

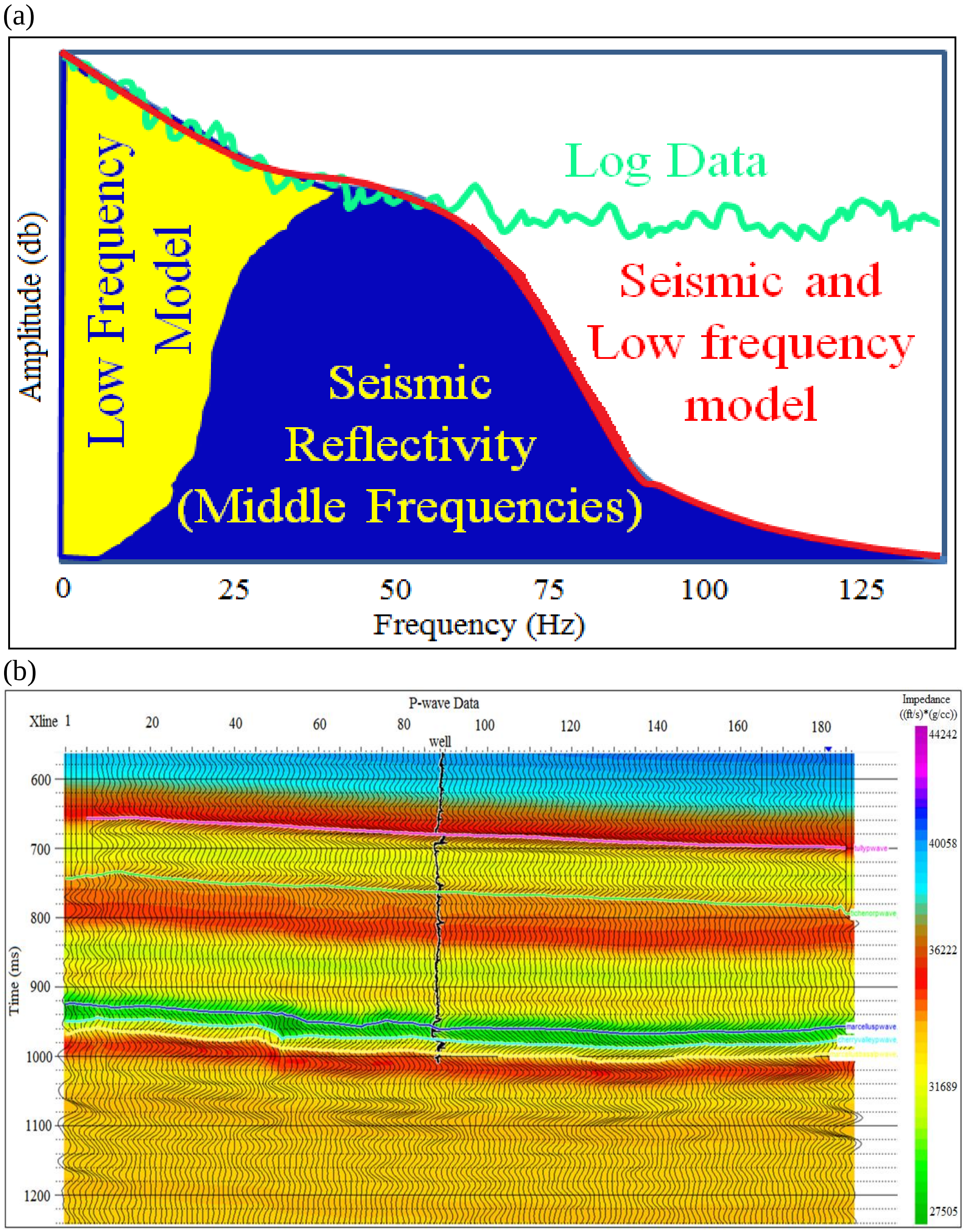

Figure 122: (a) Amplitude and frequency characteristics of seismic reflectivity data and log data integrated during impedance inversion process. (b) Initial background model generated for P-wave impedance inversion.

The initial low frequency background model uses high-cut filtered well impedance traces that have been interpolated laterally, using the five interpreted seismic horizons as a guide. This initial model (Fig. 122 (b)) shows rapid changes of impedance between these major horizons as a result of vertical changes in lithological characters.

A potential pitfall of the inversion is that each impedance value depends on all the reflection coefficients for shallower layers, thus residual errors shallower in each reflection coefficients are added onto deeper reflectivity estimates. This downward cascading of estimation errors raises a non-uniqueness problem in inversion in which there may be several combinations of reflection coefficients that minimize the error between model traces calculated from derived reflection coefficients and actual seismic traces. Adding constraints to layer-based inversion may heal this problem; however, this approach was not used in this study. A more sophisticated approach to this problem is to use a stochastic, or probabilistic, approach instead of a deterministic approach. This results in multiple realizations of the inversion product that span the solution space and theory address the issue of non-uniqness and give us a handle on uncertainty. Unfortunately such geo-statistical functionality was not suited to this dataset and is not offered by the Hampson-Russell software.

In these seismic data volumes, a peak represents a hard event resulting from an increase in acoustic impedance, whereas a trough represents a decrease in acoustic impedance. A strong negative correlation between impedance and porosity has been observed by past researchers, although the additional influence of sedimentation rate and compaction may complicate this relationship (Doyen, 1988; Verdin et al., 2008; and Koesoemadinata et al., 2008).

A channel feature composed of relatively unconsolidated, high porosity, sands would typically have a low impedance relative to its surrounding geology, and would therefore manifest itself as a negative seismic event (a trough), or, in the inverted seismic, as an area of low acoustic impedance.

Figure 123 shows the results of band-limited impedance inversion results obtained from compressional (Fig 123 (a)), and shear wave (Figure 123 (b)) data. As demonstrated in Figure 123 (b), a feature tentatively interpreted as a porous sandstone unit deposited in a channel is identified by the predominantly light blue colors just below the picked seismic horizon for the Tully Limestone and immediately next to the calibration well. P-wave impedance differences observed at the location where this channel feature is identified are not as obvious on P-wave data as it is on S-wave impedance values presented in Figure 123 (b). The Marcellus Shale is visible as continuous layers highlighted with yellow-green-yellow color sequences. The impedance values of the Marcellus Shale are quite different in the impedance volume generated using compressional wave data than it is when estimated from P-SV data. The Upper Marcellus - Cherry Valley - Lower Marcellus sequence also is represented by higher impedance values constructed using P-SV data than by values determined from P-wave data.

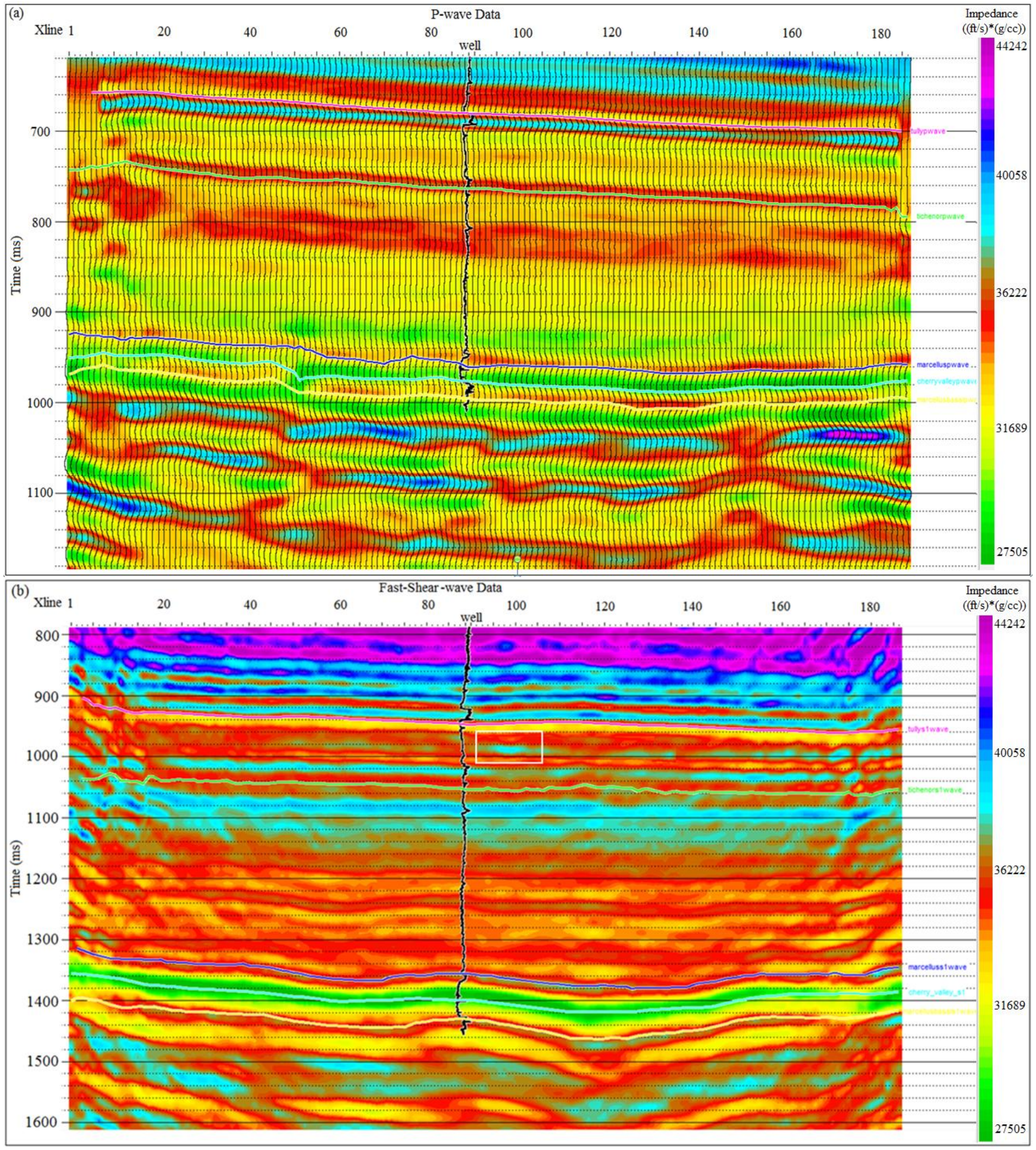

Figure 123: The results of impedance inversion obtained from compressional (a), and shear wave (b) data. An intra-reservoir anomaly (interpreted as a porous channel) is shown as the predominantly light blue color just below the picked seismic horizon for Tully Limestone (highlighted with rectangular white box).

ANALYSIS OF INTRA-RESERVOIR ANOMALY USING IMPEDANCE IMAGES

The multicomponent seismic data used in this study demonstrated that there is a channel feature positioned between the Tully Limestone and Tichenor Limestone units within the Hamilton group. There was no indication of any stratigraphic trap or any structural unit between these two major limestone units. The Tully and Tichenor Limestones created reflection events that did not show any folding or shape changes along inline and cross-line profiles. However, the unit that was identified as a channel feature demonstrated variation in P-SV reflection character as well as in P-SV amplitude attributes mapped over this region. This proposed porous sandstone unit is not identified in other parts of the image spaces. Providing an improved understanding of the nature of this channel unit from additional data is important.

In the P-wave impedance image (Fig 123 (a)), differences between impedance values recorded across the channel feature and those recorded around the surroundings units are approximately 1500-1800 ft/s * g/cc. In contrast, this value is almost 4000 ft/s * g/cc in the S-wave impedance image presented in Fig 123 (b). When analyses are done for a small data window focused on the channel feature, it is easier to see that impedance values calculated from P and S wavefields present quite different results. Figure 124 shows the map view of the area where the channel feature clearly was identified from interpreted amplitude attribute values and several in-line (blue lines ranged between IL40 - IL140) and cross-line sections (red lines ranged between XL70 - IL120) where I analyzed the P-wave and S-wave impedance differences.

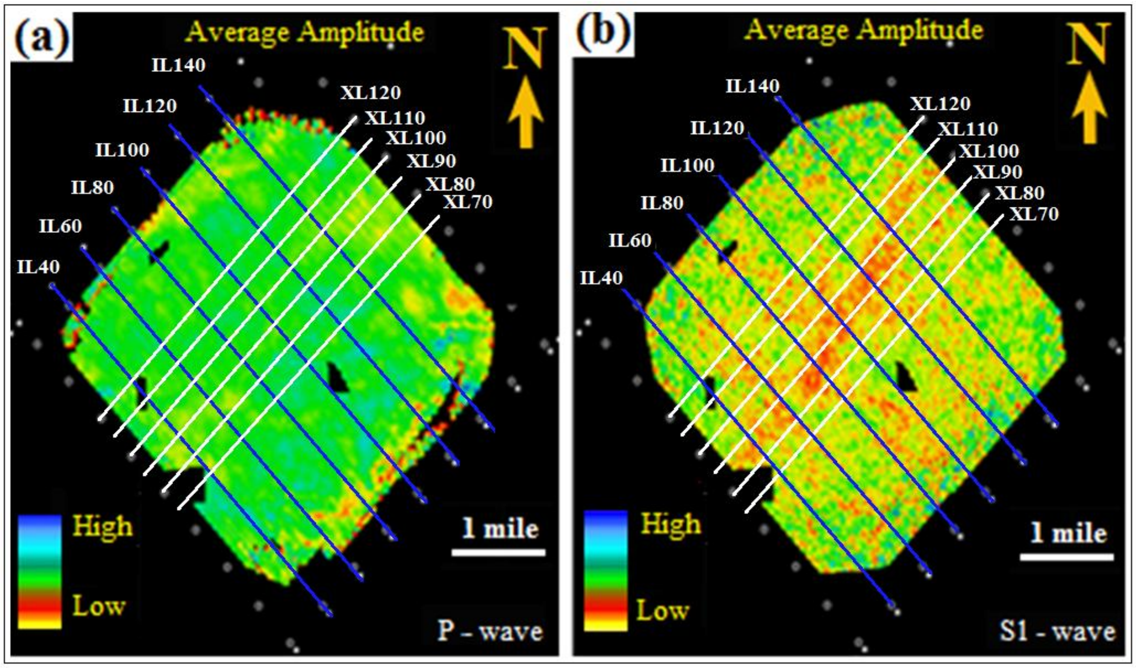

Figure 124: Amplitude attribute map extracted from (a) P-wave and (b) S-wave volumes for Tully – Tichenor interval. In-line (blue lines ranged between IL40 - IL140) and cross-line sections (white lines ranged between XL70 - IL180) passing through the channel feature where amplitude values are represented with red color which is quite lower compared to amplitude values of surrounding units represented by green and yellow colors.

To analyze impedance inversion results over the Tully-Tichenor interval, I narrowed my analysis window to a 900-1200 ms time interval and a 40-50 inline (or cross-line) spatial interval. With this smaller analysis window, it is easier to focus on impedance variation over the channel feature. Figure 125 shows S-wave impedance values calculated at inline impedance slices IL60, 80, 100, and 120, and Figure 126 compares P-SV impedance values presented on cross-line slices XL80, 90, 100, and 110.

The targeted unit is identified in both Figure 125 and 126 as the predominantly yellow/orange color just below the interpreted seismic horizon for the Tully Limestone. Color changes in impedance images are highlighted with white boxes in Figure 125 and 126. In addition to the target unit visible as yellow spots between 970-1000 ms time interval, the behavior of impedance values recorded over a time interval at 950-1000 ms throughout section varies when the target unit cuts into surrounding geology.

As shown in Figure 125, a lateral change was observed in S-wave impedance values just below the Tully Limestone unit as presented for inline sections IL60, 80, 100, 120. A similar lateral change can also be observed in Figure 126 that shows S-wave impedance variation below the Tully Limestone horizon as it was found on crossline sections XL70, 80, 90, 100.

The similar characteristic of impedance behavior over the area where this channel feature is present is that sudden drop in impedance values was repeatedly observed in different inline and crossline sections. This impedance difference between channel fill and surrounding geology along the inline direction is approximately 5000 (ft/s)*(g/cc) as demonstrated in Figure 125. This high difference seems logical when we think about the strong amplitude variation along the inline direction shown in Figure 124 (b) because inline sections cut through the feature where amplitudes and impedance values drop most suddenly. On the other hand, a crossline section is almost parallel to the channel direction, and does not transverse a large drop in impedance values at edges of feature. There is evidence of repeated changes in impedance values just below the Tully Limestone on crossline sections XL80, and XL90 because they cut through the feature

(Fig. 126). In contrast, changes in impedance values are not clear on crossline sections XL70, and XL100 which do not cross the feature.

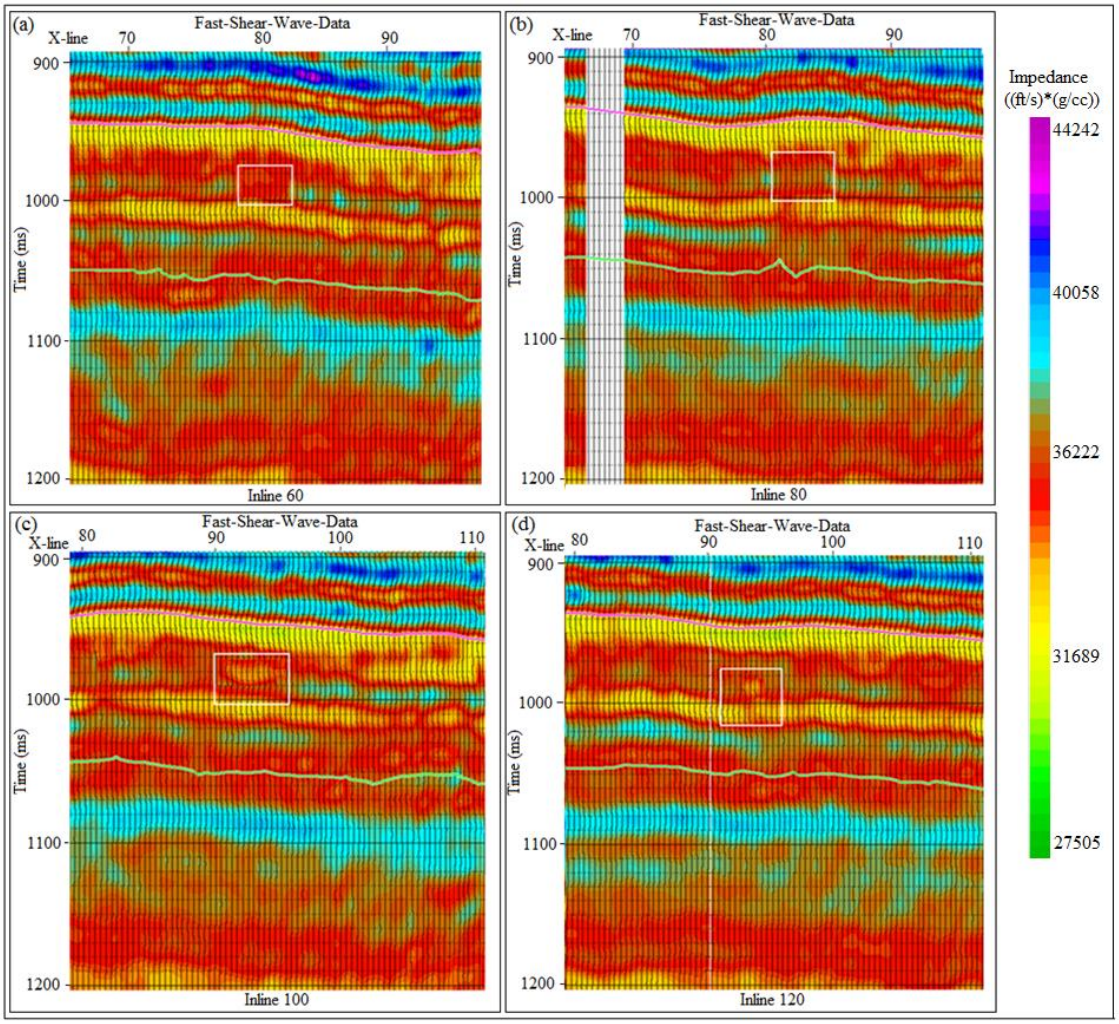

Figure 125: Display of the S-wave impedance values observed along inline directions 60 (a), 80 (b), 100 (c), and 120 (d) shown on Figure 124 (b). The targeted unit for study was interpreted on all four inline profiles and highlighted with white boxes. Pink and green lines represent the Tully and Tichenor Limestone events, respectively.

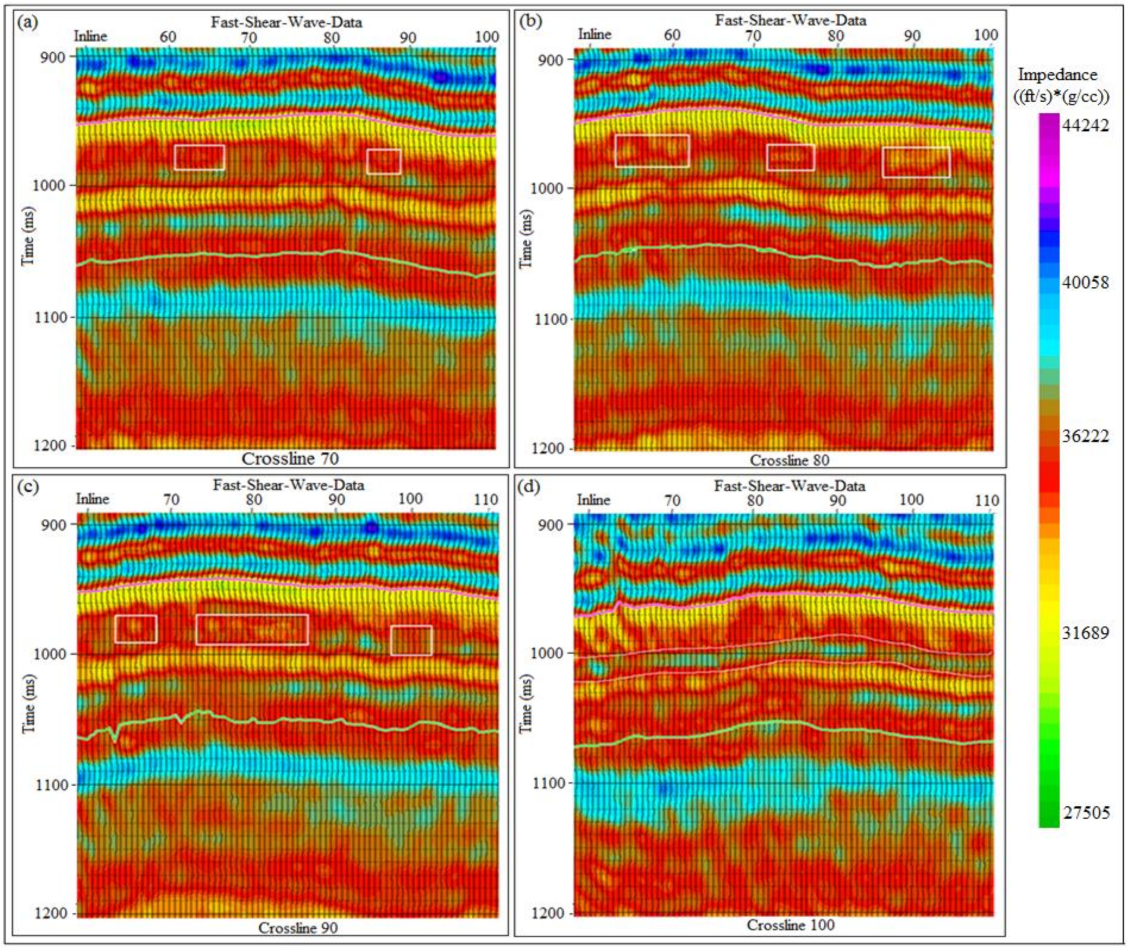

Figure 126: Display of the S-wave impedance values observed along cross-line directions 70 (a), 80 (b), 90 (c), and 100 (d) shown on Figure 124 (b). The targeted unit for study was highlighted as white boxes in inline profiles 70, 80, and 90 but it was difficult to identify this event on cross-line section 100. Pink and green lines represent the Tully and Tichenor Limestone events, respectively.

The lateral change that was observed in S-wave impedance images over the range of inline and crossline sections does not exist in the P-wave impedance images constructed using compressional wave seismic volumes. P-wave impedance values over the Tully-Tichenor interval (650 - 800 ms) are quite similar; therefore, there is no sign of any change in color scale over this time interval (Figures 127 and 128).

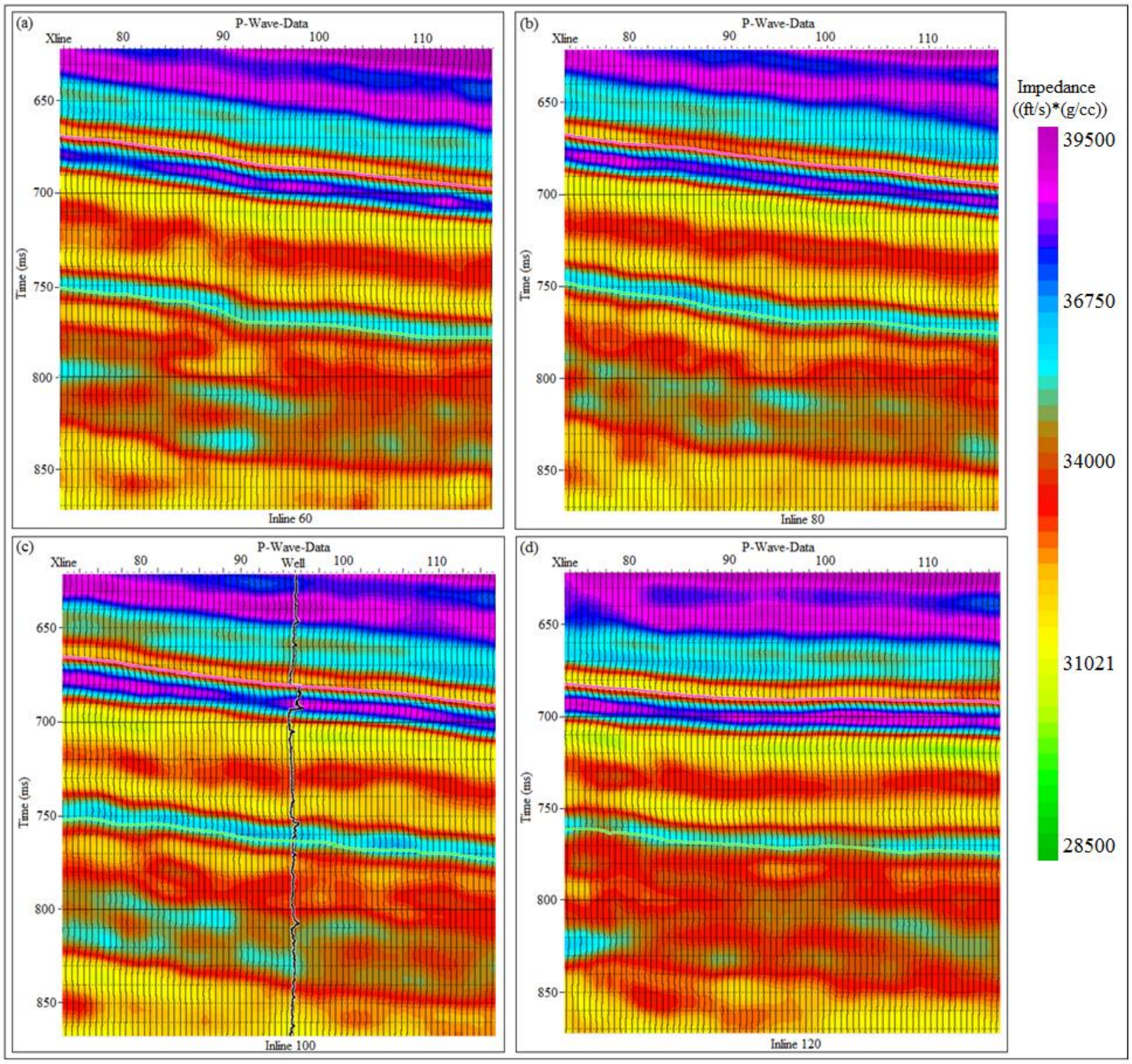

Figure 127: Display of P-wave impedance values observed along inline directions 60 (a), 80 (b), 100 (c), and 120 (d) shown on Figure 124 (a). There is no indication of the presence of an anomalous feature observed along these inline profiles. Pink and green lines represent the Tully and Tichenor Limestone events, respectively.

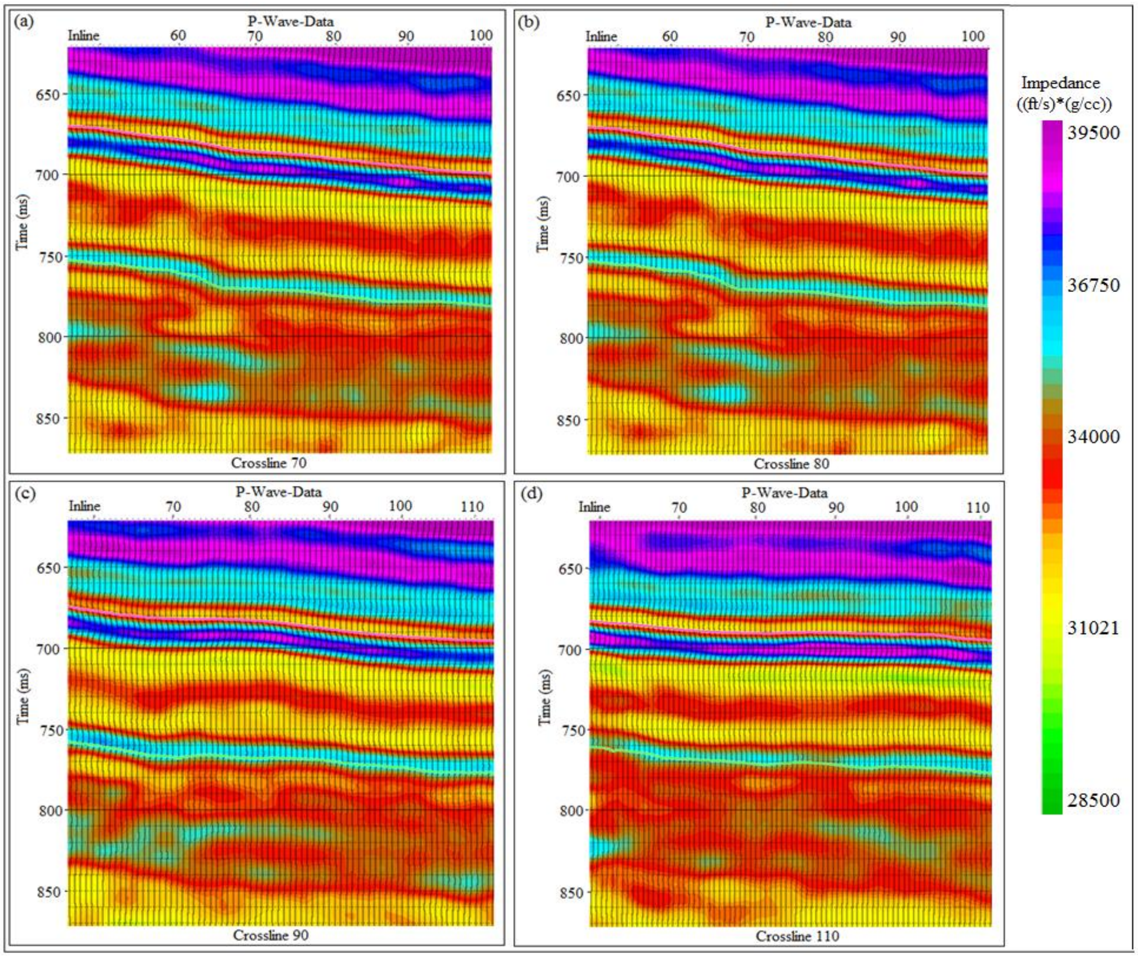

Figure 128: Display of the P-wave impedance values observed along cross-line directions 70 (a), 80 (b), 90 (c), and 110 (d) shown on Figure 124 (a). There is no indication of the presence of an anomalous feature observed along inline profiles. Pink and green lines represent the Tully and Tichenor Limestone events, respectively.

Inline and crossline profiles from the S-wave impedance volume illustrate the impedance variations within the porous sandstone unit located within the Tully-Tichenor interval and within the thin, overlying interval correlative with the channel sand feature that might be part of channel system (Figure 124 – 126). Intriguingly, low impedance values (yellow/orange impedance values) in the interval immediately below the Tully Limestone might prove to correlate with the targeted unit.

To have a better understanding of what these impedance values can tell us, I decided to display impedance volumes in 3D-volume view so that I could analyze structural features in multiple sections and slices simultaneously. Figure 129 shows S-wave impedance (a), and P-wave impedance (b) values presented in inline and crossline sections in addition to vertical impedance slices. Based on evaluation of these P-wave and S-wave displays, impedance values constructed from different elastic wavefields demonstrate quite different characteristics across this targeted interval as do other attribute values extracted using different elastic wavefield volumes. These observations confirm the additional value that elastic wavefield stratigraphy and multi-component seismic technology provide for reservoir characterization.

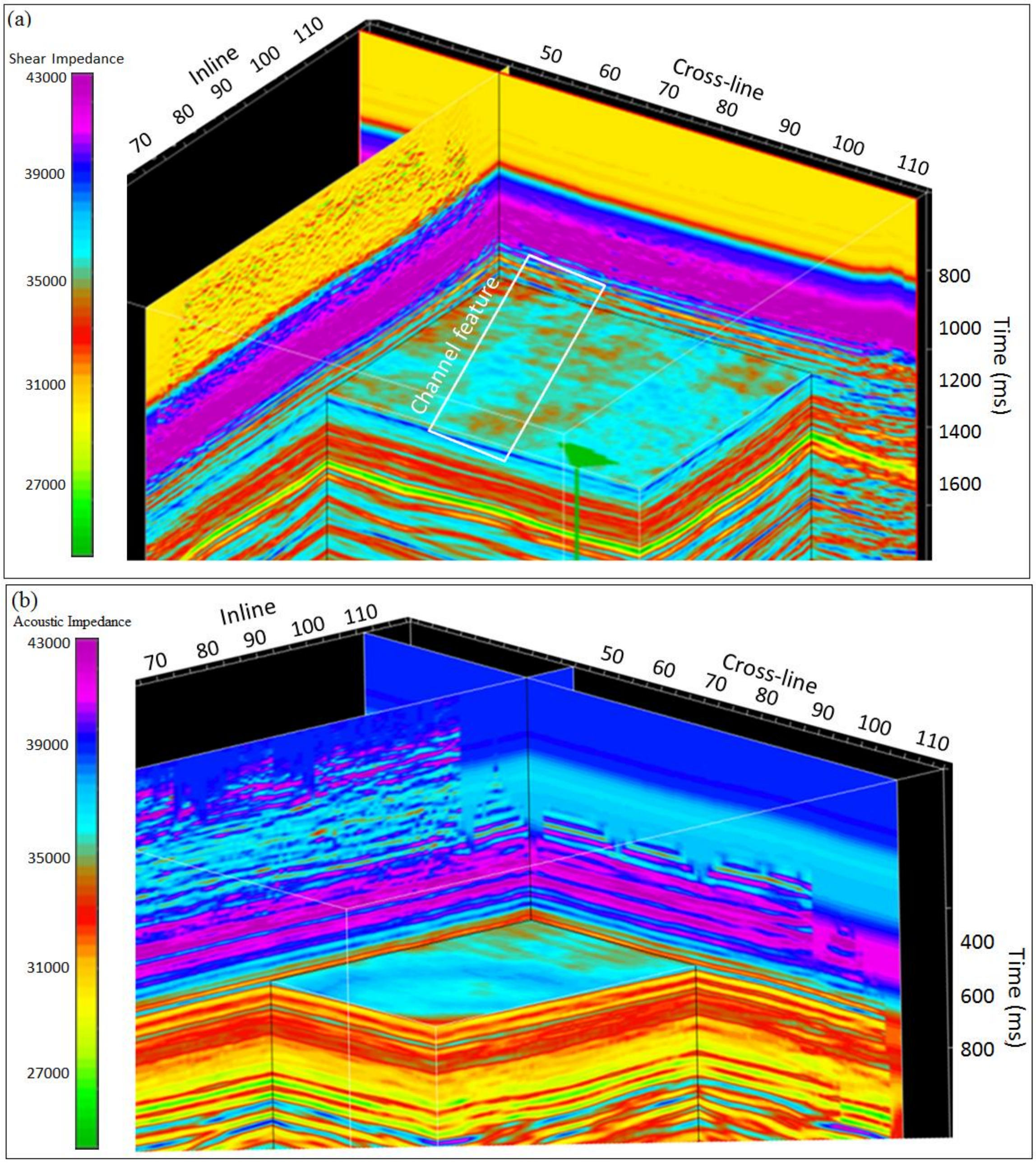

Figure 129: 3D volume view of the S-wave impedance (a) and P-wave impedance (b) values observed along inline and cross-line directions. 3D probe highlighted with white box (a) shows the channel feature whereas such a feature is not apparent on the P-wave impedance volume (b).

ANALYSIS OF MARCELLUS SHALE FORMATION USING IMPEDANCE IMAGES

The multi-attribute analysis of multicomponent seismic data demonstrated that there are several sections within the Marcellus Shale reservoir which seem quite different in images constructed using compressional and shear data. Log and seismic data suggested that reservoir architecture contains lateral variations of fractured/faulted zones which were identified in final image volumes. My goal in this section is to provide additional confidence in the presence of fractured zones within the Marcellus reservoir. Figure 130 shows the map view of the area where Marcellus is folded as interpreted for several in-line (blue lines ranged between IL40 - IL140) and cross-line sections (red lines ranged between XL70 - IL120) where I analyzed P-wave and S-wave impedances.

To analyze the impedance inversion results over Upper Marcellus - Cherry Valley – Lower Marcellus interval, I narrowed my analysis window to a data window of 900-1200 ms extending across 40 to 50 inlines and crosslines the center of the image space. In this way, it is easier to focus on impedance variation over the Marcellus interval where I expected to observe lateral difference in S-wave impedance values within the Marcellus than what occurs in surrounding formations.

The presence of fractures within the geologic formation reduces the stiffness of the rock formation, and therefore reduces the bulk modulus (K), and velocity. Because impedance is equivalent to the multiplication of velocity and density, the impedance value of an unfractured rock will be higher than the impedance value of fractured rock. Therefore, I expect to observe lower impedance values within the Marcellus interval where fractured zones exist.

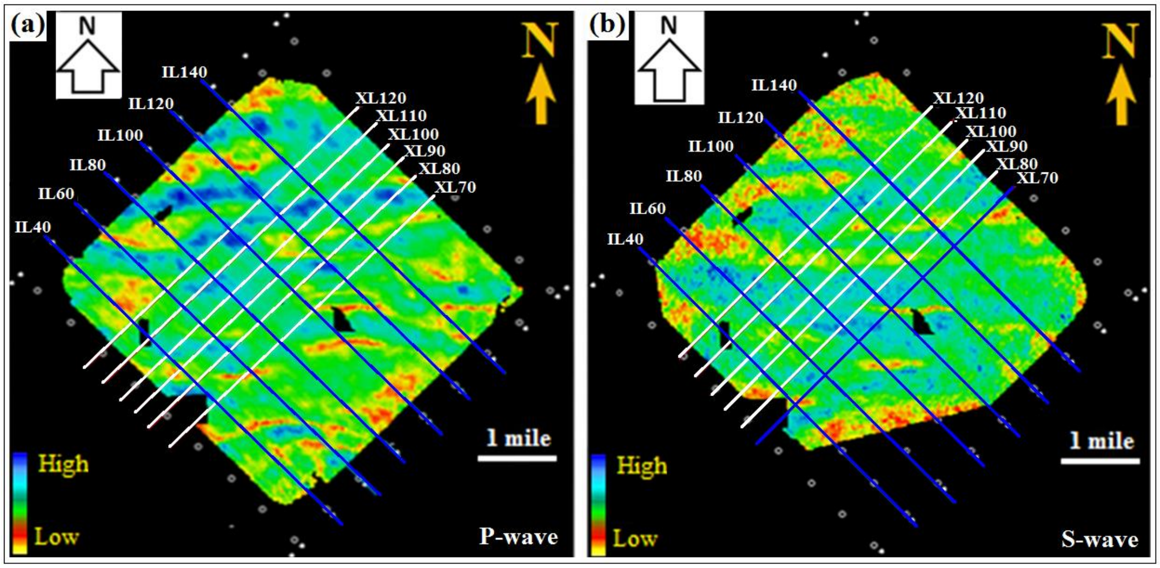

Figure 130: Amplitude attribute map extracted from compressional wave (a) and fast-shear wave (b) volumes for Marcellus Shale. In-line (blue lines ranged between IL40 - IL140) and cross-line sections (red lines ranged between XL80 - IL180) passing through the top of the Marcellus formation where amplitude values vary between red and blue colors which represent high (blue) and low (red-yellow) amplitude values, respectively.

Figure 131 shows the P-wave impedance slices selected at four different inline sections from the map shown in Figure 130 (IL60, 80, 100, and 120) in which impedance variations are observed in section views in the cross-line direction (XL70-110). Figure 132 compares impedance values calculated along four different cross-line sections from the map shown in Figure 130 (XL80, 90, 100, and 110) that illustrate impedance variations along the inline direction (IL60-120).

In both figures, certain zones within the Marcellus interval show lower impedance values where impedance values drop by approximately 2500-3500 (ft/s)*(g/cc) compared to surrounding areas. These locations are highlighted with white boxes in Figure 131 and

132. One hypothesis is to interpret these areas as locations where fractures exist. Inspection of the profiles shows that impedance values vary within the reservoir unit laterally from one inline (or crossline in Figure 132) to another inline section as presented in Figure 131. These differences in P-wave impedance images do not correlate with the differences in amplitude maps presented in Figure 130, which indicate locations where fold structures exist. Therefore, this interval indication of Marcellus rock fabric based on P-wave impedance images may be caused by many other reasons, one of which is the presence of fractures.

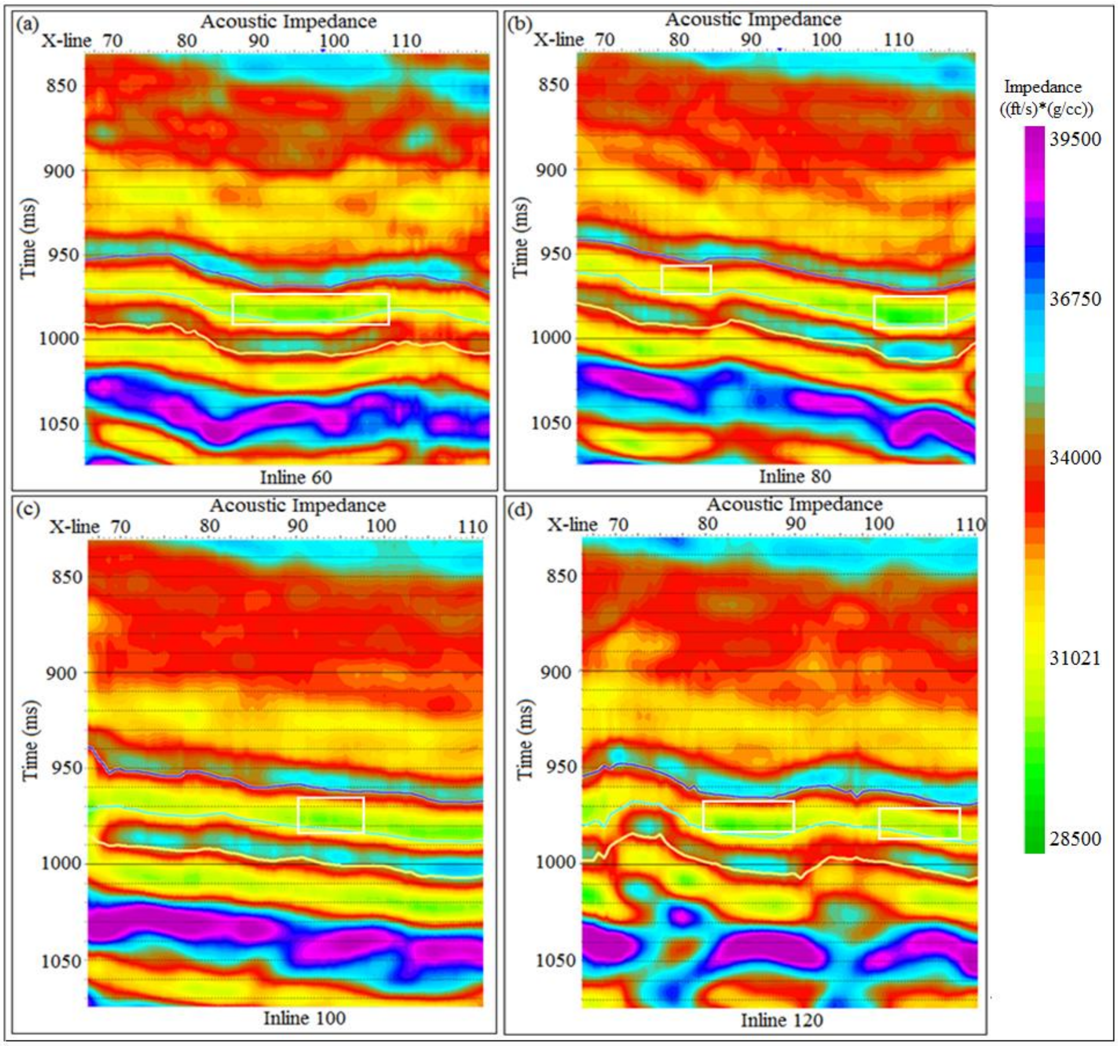

Figure 131: Display of the P-wave impedance values observed along inline directions 60 (a), 80 (b), 100 (c), and 120 (d) shown on Figure 130 (a). A minor lateral change observed in the P-wave impedance image of area above the Cherry Valley Limestone (highlighted with green) along the inline profiles may indicate the presence of possible fractured zones (areas highlighted with white rectangular boxes). Dark blue, green, and yellow lines represent the Upper Marcellus, Cherry Valley Limestone, and the Lower Marcellus events, respectively.

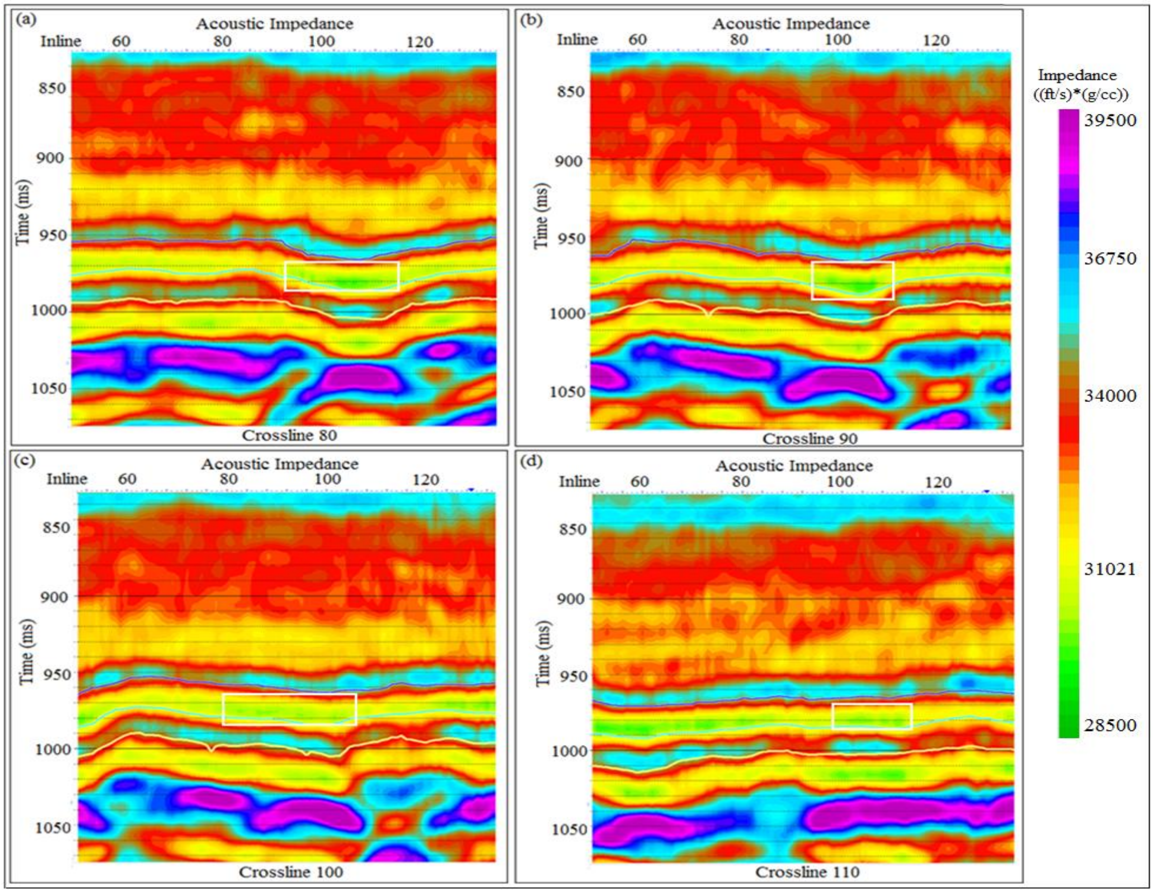

Figure 132: Display of the P-wave impedance values observed along cross-line directions 80 (a), 90 (b), 100 (c), and 110 (d) shown on Figure 130 (a). A minor lateral change observed in the P-wave impedance image of area above the Cherry Valley Limestone (highlighted with green) along the cross-line profiles may indicate the presence of possible fractured zones (areas highlighted with white rectangular boxes). Dark blue, green, and yellow lines represent the Upper Marcellus, Cherry Valley Limestone, and the Lower Marcellus events, respectively.

Figures 133 and 134 present S-wave impedance images calculated along the same inline and crossline sections where P-wave impedance values were. When the same analysis is done within the same window used to analyze P-wave impedance values, it is obvious that impedance behavior differ depending on the wave type used to construct the impedance volume.

The impedance behavior over the area where relatively low P-wave impedance values were observed in P-wave impedance images is not repeated in impedance images constructed using S-wave data.

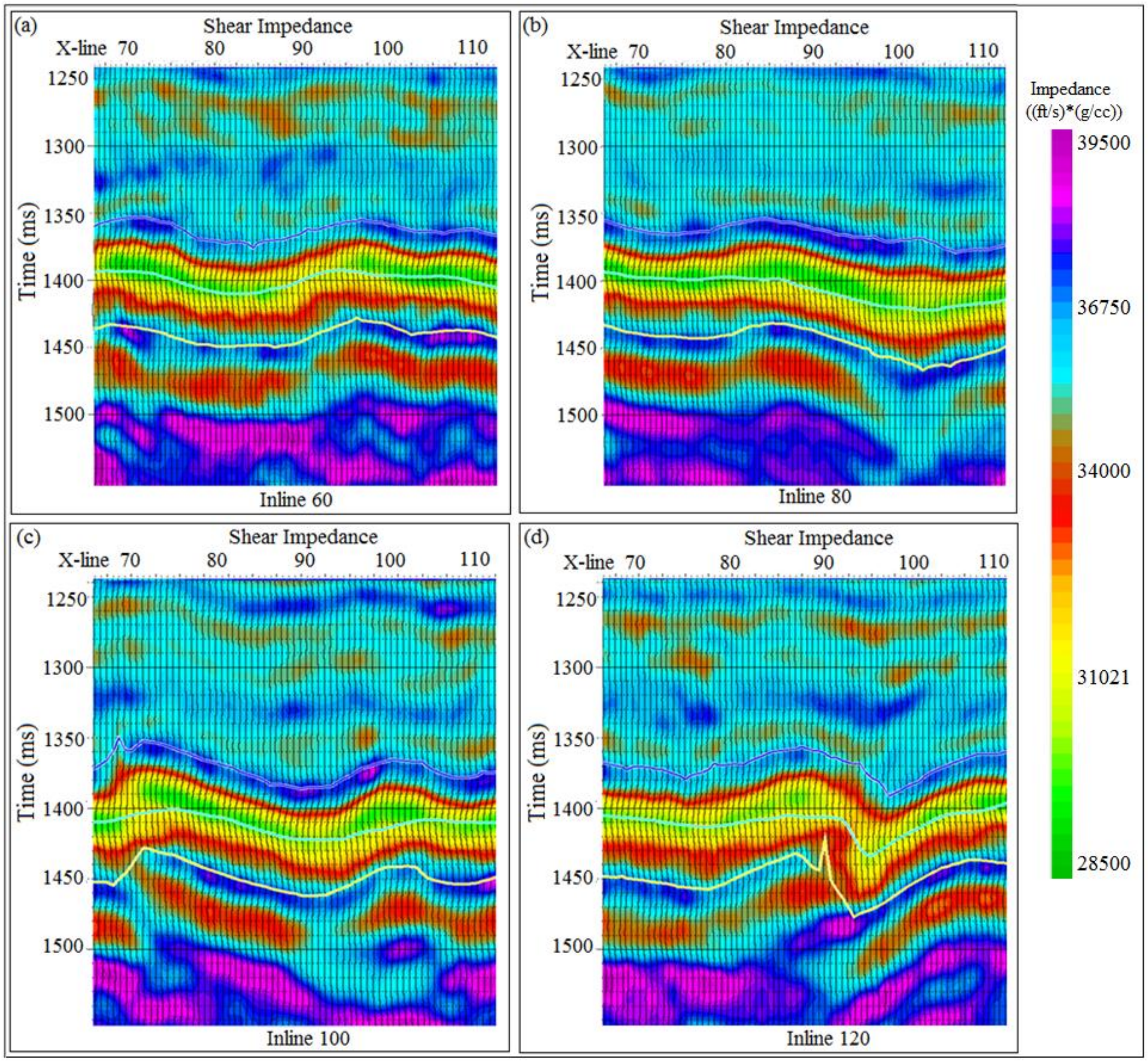

Figure 133: Display of the S-wave impedance values observed along inline directions IL60 (a), 80 (b), 100 (c), and 120 (d) that were selected from the amplitude map given in Figure 130 (b). There is no indication of the presence of any fractured zone observed in the S-wave impedance image along the inline sections. Dark blue, green, and yellow lines represent the Upper Marcellus, Cherry Valley Limestone, and the Lower Marcellus events, respectively.

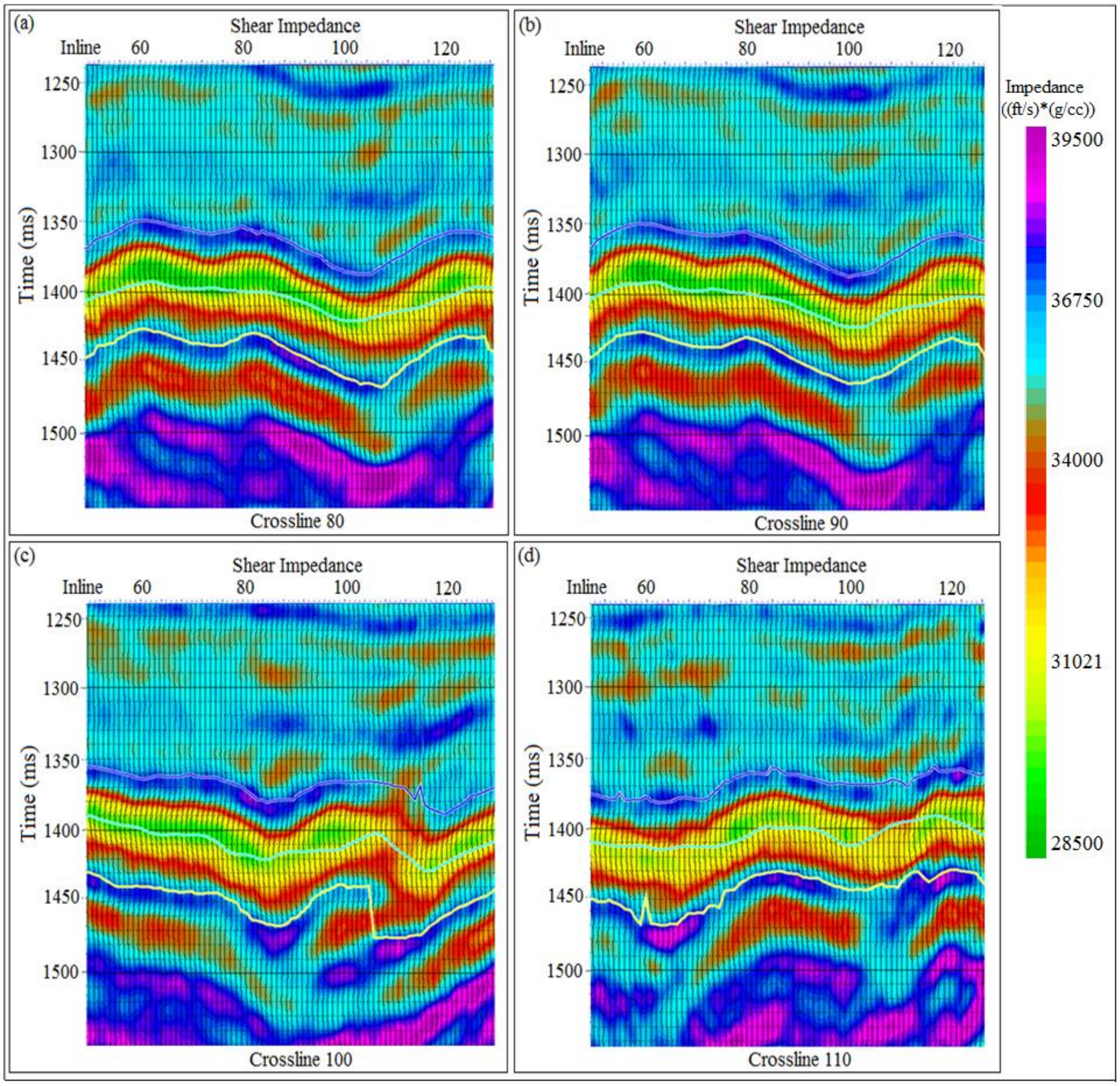

Figure 134: Display of the S-wave impedance values observed along cross-line directions IL80 (a), 90 (b), 100 (c), and 110 (d) that were selected from the amplitude map given in Figure 130 (b). There is no indication of the presence of any fractured zone observed in the S-wave impedance image along the cross-line sections. Dark blue, green, and yellow lines represent the Upper Marcellus, Cherry Valley Limestone, and the Lower Marcellus events, respectively.

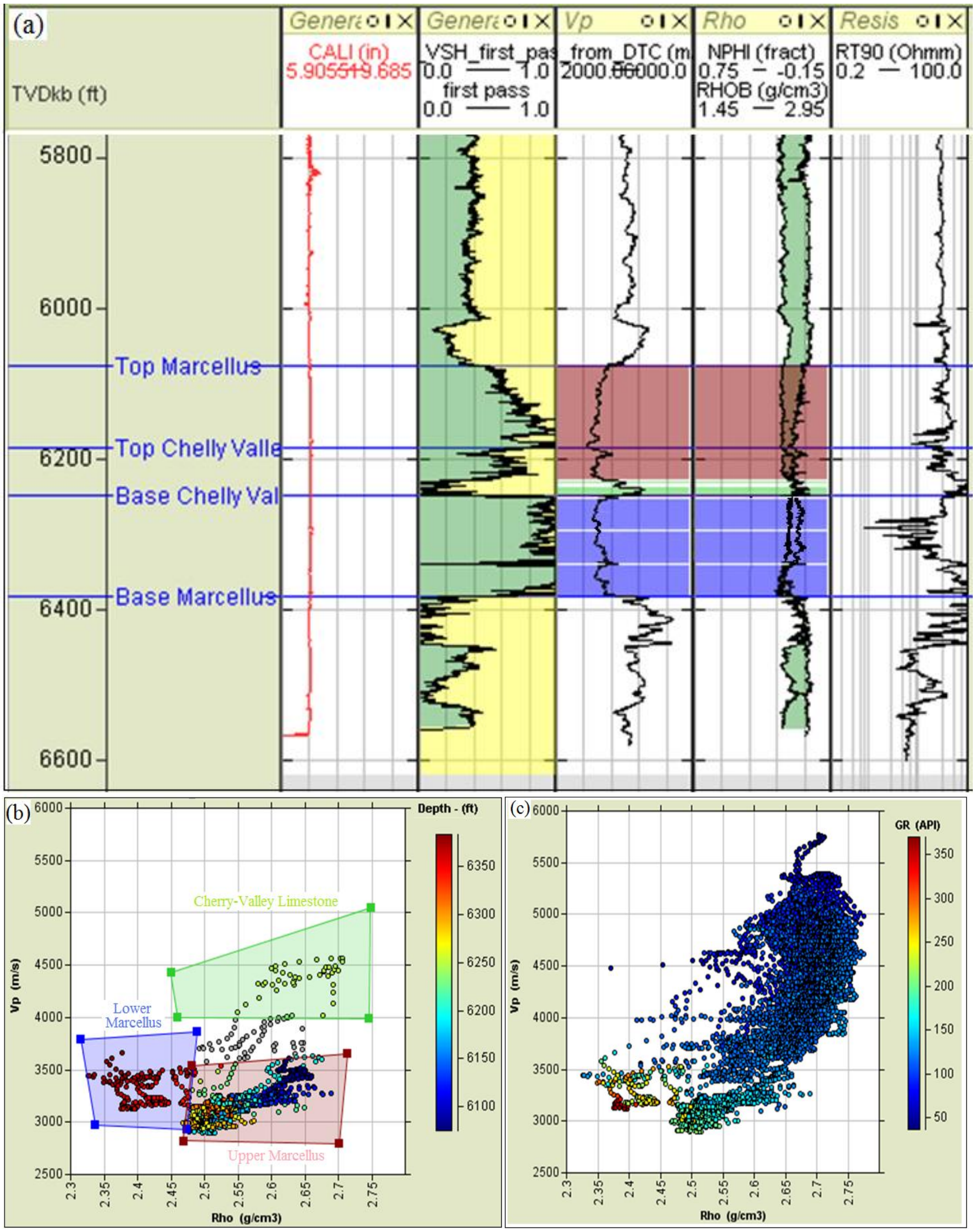

Figure 135: (a) Log section displaying log data for Marcellus interval. (b) P-wave velocity versus bulk density for only the Marcellus interval, with data points color-coded by depth. The Upper Marcellus and Lower Marcellus units are well delineated in this data space. (c) P-wave velocity versus bulk density for the entire logged interval, with data points color-coded by gamma-ray value.

Cross-plots of velocity and density log values were analyzed to understand the behavior of P-wave and S-wave impedance results. Figure 135 shows two density-velocity cross-plots. The first cross-plot (a) is color-coded by gamma-ray measurements; whereas, the second cross-plot (b), data values are color-coded by depth values.

As shown in the Figure 135, the Marcellus Shale is identified by high gamma-ray measurements which coincide with the depth values displayed in the figure. These data may indicate that the Lower Marcellus has higher organic content than the Upper Marcellus. In addition, the Lower Marcellus formation has lower velocity and lower density than the Upper Marcellus. In contrast, compaction-driven velocity-depth profile, the Lower Marcellus Shale has lower P-wave velocity values even though it is deeper than the Upper Marcellus. The difference between density values of Lower and Upper Marcellus formations is significant with the Upper Marcellus having greater density (Fig. 135). This differences in bulk density is postulated to be caused by iron (ferrite) being in the matrix of the Upper Marcellus (Diana Sava, BEG rock physicist – private communication).

Additional Research Findings

Based on multiple attributes and impedances volumes analyzed during this study, several geologic intervals were interpreted in detail.

TULLY-TICHENOR INTERVAL

Any hydrofrac operations involved in shale-gas exploration require water-storage units to store flow-back water. Because porous, brine-filled sandstones are good candidates for water-storage reservoirs, a detailed interpretation of the interval between the Tully Limestone and Tichenor Limestone formations was implemented to determine how seismic data generated from different wave modes reacted to these porous sandstone units commonly found in this interval.

In all data volumes the Tully Limestone formation is characterized by a strong reflection peak (black) immediately followed by a high-amplitude wavelet trough (red). Unlike the Tully Limestone, the Tichenor Limestone has lower amplitude responses in both the P-P (Figure 136 (a)), P-SV_1 (Fig. 136 (b)) and the P-SV_2 data volumes (Fig. 136 (c)).

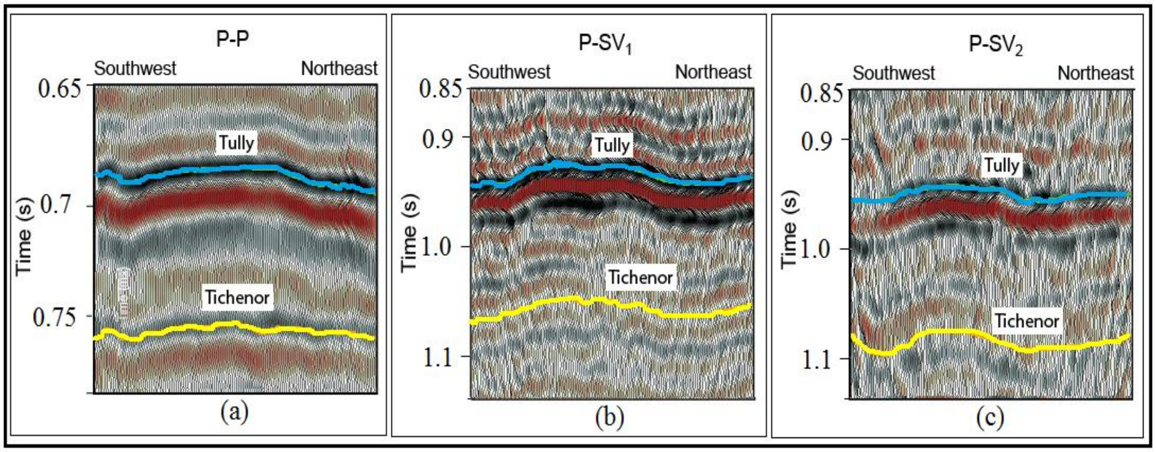

Figure 136: Seismic profiles comparing Tully Limestone (blue) to Tichenor Limestone (yellow) intervals in (a) P-P, (b) P-SV_1, and (c) P-SV_2 image spaces.

Because of improved spatial resolution of converted shear wave data compared to P-P data, P-P data show less reflection cycles across the sandstone interval relative to the number of reflection cycles that identified from P-SV_1 and P-SV_2 images (Fig. 136).

An important research finding is that P-SV_1 data imaged a southwest to northeast trending feature within the Tully-to-Tichenor interval (Figures 96, 97 (c), and 98 (c)) that appears similar to an eroded channel. These amplitude-attribute comparisons are an example of the increased geological information provided by elastic wavefield seismic stratigraphy (which is based on joint interpretation of both of P and S data) compared to the amount of information provided by traditional seismic stratigraphy (which uses only single-component P-wave data). Instantaneous frequency and instantaneous phase attributes (Figure 102) also demonstrate the presence of this channel feature as well as amplitude attributes. The detection of this depositional feature based on multi-attribute analysis has significant implications in evaluating water-storage reservoirs for hydrofrac flow-back waters.

Because the porous formation identified in multiple-attribute maps can contain units that could be storage reservoirs for hydrofrac flow-back waters, it is important to verify if the Tully Limestone formation lying immediately above these porous units have faulted zones which would provide a pathway allowing flow-back water to migrate upward into shallow aquifers. Multi-attribute analysis of any of the three seismic data volumes shows no evidence of any fault structures within the Tully Limestone.

MARCELLUS-SHALE INTERVAL

As shown in many seismic sections along different in-line and cross-line directions, the Marcellus Shale is divided into two major units: the Upper Marcellus and the Lower Marcellus. As identified from P and S volumes, the Cherry-Valley Limestone acts as a boundary between these two Marcellus units. All of the three data volumes showed that Marcellus formations have a strong structural-fold fabric trending east-to-west. These folds were also identified in attributes maps as well as on impedance sections (Figures 93, 94, 97 (b), 98 (b), 99 (b), 103 (a)).

In all data volumes, the top and bottom of the Marcellus formation are characterized by strong reflection events. Visual inspection of these profiles displayed on these figures implies P-SV$_1$ and P-SV$_2$ wave modes have a better vertical resolution across the Marcellus interval than do P-P wave mode. This result is another important research finding that emphasizes the benefit of using multicomponent seismic technology in shale-gas studies rather than relying on only traditional single-component P-P seismic data.

Identifying the Cherry-Valley Limestone formation was not as easy as identifying the Marcellus units because this thin limestone was not imaged as an individual reflection event in any of the three seismic data volumes. Instantaneous frequency, instantaneous phase, and discontinuity surface attributes were the best attributes to define the interfaces between the Cherry-Valley Limestone and its bounding Marcellus units.

Frequency spectra calculated in seismic windows dominated by the Marcellus interval confirm the frequency content of P-SV_1 data across the Marcellus Shale interval spans a broader range (10-40 Hz) than do P-P data (15-30 Hz). This analysis indicates shear-wave data provide improved resolution of prospect features within the shale reservoir formations.

Conclusions

Based on the examples presented in this chapter, I conclude that using combinations of P-wave and S-wave attribute and impedance volumes is an effective tool to:

(1) identify and analyze geometrical properties of complex depositional and structural features such as channels, fractures, and faults,

(2) investigate lateral and vertical depositional changes in layered media,

(3) extract more accurate and more detailed structural and stratigraphic information from seismic data, and

(4) improve geologic interpretations by characterizing, delineating, and classifying depositional facies.

As a consequence, incorporating multi-attribute volumes generated from various elastic wavefields increases the understanding of depositional systems, leads to better field development plans, improves resolution of small-scale complex fracture and fault zones, and facilitates the mapping of subtle units that may affect fluid flow. Amplitude, frequency, and phase attributes may be strongly affected by noise in the seismic data.

Careful post-stack impedance inversion always helps quantitative interpretation based on seismic attributes. Unfortunately, we have only a single control well to generate an accurate estimate seismic impedance model and a source wavelet to be used for P-wave impedance inversion process for our survey area.

Dip-magnitude and dip-azimuth maps provide useful information for identifying subtle features that may not otherwise be seen on seismic data. Curvature further points out details of these subtle features, and coherency highlights details of lateral stratigraphic contacts and facies changes.

In addition to conventional seismic attributes commonly used by the industry such as curvature, and coherency, instantaneous attributes (instantaneous phase, instantaneous frequency, and instantaneous bandwidth) also provide details that cannot be identified from curvature and coherency.

Seismic attributes that highlight discontinuities in seismic data are useful for fault and fracture characterization. Detected fault and discontinuity-surface/fault line attributes calculated by Foster Findlay software provide visually effective representations of fractured and faulted zones by highlighting discontinuities with colored surfaces. These highlights help interpreters understand depositional and structural properties of formations by allowing quick, effective visual comparisons among multiple seismic attributes. I demonstrated that while a coherence display is featureless in high coherence areas (gray), detected-fault and fault-line attributes delineate features in those areas.

Multiple attributes can be effectively displayed as vertical profiles, time-slice, and horizon-slice map views, or 3D volume displays. Different viewing techniques (2D vertical, map, or 3D volume views) need to be used to support analyses such as structural or stratigraphic interpretations, reconnaissance studies, and detailed reservoir-scale analyses. For a successful reservoir characterization, interpretation of unconventional shale reservoirs must rely on all of the analyses described in this chapter.

CHAPTER 6: CONCLUSIONS AND DISCUSSION

The fundamental objective in multicomponent seismic technology and elastic wavefield seismic stratigraphy is to reveal the nature of the subsurface. Ideally we aim to reveal the detailed geological nature of the subsurface, but in fact we can reveal only some aspect of its physical nature due to the limitations of seismic technology. While multicomponent seismic data may enable us to deduce the elasticity of shallow or deeply buried geologic formations, we know that we cannot directly obtain measurements regarding the geologic age or get a direct indication of the granular fabric of targeted rock layers. The items listed below summarize some of the information that a petroleum geologist may wish to know:

- To assess hydrocarbon reserves:
    - presence or absence of hydrocarbons
    - thickness of reservoir formation
    - porosity and permeability of reservoir
    - depth and areal extent of fluid contacts within the reservoir units
- To understand the nature of a prospect:
    - geological ages and type rock formations targeted by exploration
    - depositional environments, diagenetic and burial history of geologic formations
    - the nature of petroleum systems such as seal, source rock, and reservoir facies.
    - internal reservoir architecture and possible migration paths of hydrocarbon
    - overpressured zones

Unfortunately, geophysicists cannot directly address any one of these items. Upon identifying the properties of the subsurface that influence seismic reflection, a geophysicist can provide information such as: bulk modulus, density and rigidity (affecting compressional and shear velocities as well as P-wave impedance and reflection coefficients), reflection time and seismic absorption. In using multicomponent seismic technology, we seek to unravel the connection between seismic and geological properties of the subsurface formations. In real-life conditions, many elements impact the effectiveness of multicomponent seismic technology.

Some of these elements are:

- Data acquisition and survey design elements:
    - source and receiver spacing,
    - overall survey size,
    - number of source and receiver station deployed within a survey area,
    - survey equipment and recording systems
    - fold, offset, and azimuth distributions that can be obtained.
- Data processing elements are:
    - the resolution and bandwidth of the seismic wavelet,
    - frequency and phase content,
    - quality control of seismic data,
    - rotation of multicomponent seismic data to natural coordinates and wavefield separation,

  - shot-processing steps (noise attenuation, static corrections, gain compensation, etc.),
  - multiple attenuation and enhancement of major reflection events,
  - velocity analysis and modeling,
  - migration and imaging techniques,
  - post-processing steps.
- Data interpretation elements are:
  - enhancement of seismic events and noise level adjustment,
  - selection of seismic events and extraction of seismic amplitudes,
  - multi-attribute analysis of different seismic wavefields,
  - depth registration,
  - evaluation of different seismic responses and geologic events,
  - number of wells providing borehole data.

I attempted to address some of these factors during my PhD study. The data set that I utilized for this study demonstrated many challenges for seismic data processing and created difficulties due to the lack of log data from additional wells that could have been used for more accurate and detailed velocity model updates and could have guided me to more accurate seismic-to-geology tie analysis. Despite of all these challenges, I produced the following important research findings:

(1) Many examples from different multicomponent seismic analyses are presented to demonstrate the value of multicomponent seismic technology and elastic wavefield stratigraphy for evaluating shale-gas systems.

(2) I demonstrated that multicomponent seismic technology has greater value than single-component compressional-wave seismic technology for characterizing complex geologic targets. I presented evidence that describes the effect of the differences between the physics of compressional and shear wave propagation on interpreting geologic events from seismic data volumes.

(3) I demonstrated compelling examples to show how multicomponent seismic technology is effective for delineating unconventional reservoirs and for unraveling information regarding reservoir architecture.

(4) I provided information regarding stress field directions and fracture characteristics across the Marcellus interval.

(5) I analyzed an interval having porous Middle-Devonian Sandstone that can be used as storage for flow-back water produced by hydrofracing.

(6) I explained why the tectonic history and lithological characteristics of geologic formations can be related to in-situ stress variations that provides information about possible faulted and fractured zones within the reservoir formations.

(7) I evaluated the types of the data-acquisition equipment and recording systems that can be used to acquire seismic data across shale-reservoirs.

(8) I demonstrated differences in signal quality, frequency and phase content, and wave-mode amplitude distributions in seismic data acquired by different equipment.

(9) I presented examples that demonstrate that using MEMS accelerometer sensors provides improved signal-to-noise ratio as well reduced coherent noise, and most

importantly it enhances fidelity in recording multicomponent seismic data with increased bandwidth.

(10) My analysis comparing different recording systems showed that cable-free systems offer alternative ways to acquire multicomponent seismic data with similar quality to data acquired with cable-based systems.

(11) Finally as the most important research finding, I demonstrated that full-elastic wavefield data can be acquired using only vertical-force seismic sources. This research finding proposes a new approach to multi-component data acquisition and survey design projects because it eliminates the need to use both vertical-force and horizontal-force seismic sources to generate full-elastic wavefield directly at a source station data and simplifies multicomponent seismic data acquisition. Utilizing multiple wave modes such direct shear mode (SV-SV) generated by vertical-force sources enable additional S-wave images rather than only direct P and converted S images. Furthermore, the use of direct S mode from vertical-force source avoids converted-wave imaging challenges that are introduced by the asymmetry in compressional and shear wave raypaths in P-SV converted-wave data. Imaging with direct shear wave uses a CMP (common midpoint) based approach rather than a CCP (common conversion point) binning scheme.

By presenting these research findings, my PhD study proposes different approaches for characterizing unconventional shale reservoirs in analyzing complex geologic formations.

REFERENCES

- Aki, K.and Richards, P. G. (1980). Quantitative seismology: Theory and methods, v.l.

- Al-Anboori, A., Kendall, M., Raymer, D., and Jones, R. (2005). Microseismic monitoring and spatial variations in anisotropy, an example from Oman. 67th EAGE Conference and Technical Exhibition, Madrid, Spain, Expanded Abstracts, Paper P094.

- Al-Dossary, S. and Marfurt, K. (2006). 3D Volumetric multispectral estimates of reflector curvature and rotation. Geophysics, 71 (5).

- Alford, R. M. (1986). Shear data in the presence of azimuthal anisotropy: Dilley, Texas. 56th Annual Internat. Mtg., Soc. Expl. Geophys., Expanded Abstracts, 5, 476..

- Alkan, E. (2007). Multi-dimensional land seismic data acquisition techniques and random survey design: M.S. thesis in geological sciences, University of Texas, Austin.

- Avary, K.L. (2010) Geology of Marcellus Shale and Current Activity in West Virginia. West Virginia Water Conference, 2010.

- Bahorich, M. and Farmer, S. (1995). 3D seismic coherency for faults and stratigraphic features. The Leading Edge, 14 (10).

- Bale, R., Gratacos, B., Mattocks, B., Roche, S., Poplavskii K., Li., X. (2009). Shear wave splitting applications for fracture analysis and improved imaging: some onshore examples, First Break, v. 27, n. 9, p. 73- 83.

- Banik, N. C. (1987). An effective anisotropy parameter in transversely isotropic media: Geophysics, 52, 1654-1664.

- Bland H. C. (2006). An analysis of passive seismic recording performance. CREWES Research Report, 18, 1-9.

- Barnes, A.E. (2007). A tutorial on complex seismic trace analysis. Geophysics 72(6): W33-W43.

- Boyce, M.L., and Carr, T.R. (2010). Stratigraphy and Petrophysics of the Middle Devonian Black Shale Interval in West Virginia and Southwest Pennsylvanian: AAPG Search and Discovery Article #10265.

- Cardona, R. (2001). Shear wave velocity dependence on fluid saturation: SEG Expanded Abstracts 20, p. 1712.

- Cardona, R., Jenner, E., Davis, T.L. (2003). Fracture network characterization from P- and S-wave data at Weyburn field, Canada, 2003 SEG Annual Meeting Expanded Abstracts.

- Castagna, J. P., Sun, S., and Siegfried, R. (2003). Instantaneous spectral analysis: Detection of low-frequency shadows associated with hydrocarbons. The Leading Edge, 22, 127-129.

- Castagna, J. P., Sun, S. (2006). Comparison of spectral decomposition methods. First Break 24 (3), 75-79.

- Chapman, M. (2003). Frequency-dependent anisotropy due to meso-scale fractures in the presence of equant porosity, Geophys. prospect., 51, 369–379.

- Cooke, D.A. and Schneider W.A. (1983). Generalized Linear Inversion of Reflection Seismic Data, Geophysics, Vol. 48, No. 6. P. 665-676.

- Chopra, S., Marfurt, K. (2005). Seismic attributes -- A historical perspective, Geophysics, 70, 5, 3SO-28SO

- Chopra, S., Marfurt, K. (2007). Curvature attribute applications to 3D surface seismic data, The Leading Edge, 26, 404.

- Crampin, S. (1991). Effects of point singularities on shear-wave propagation in sedimentary basins: Geophysics. J. Int., 107, in press.

- Crampin, S., and Kirkwood, S.C. (1981). Velocity variations in systems of anisotropic symmetry: Geophysics., 49, 3542.

- Dankbaar, J.W.M. (1983). The wave-field generated by two vertical vibrators in phase and in counterphase: Geophysical prosp., 31,873-887.

- deWitt, Wallace, Jr., Roen, J.B., and Wallace, L. G. (1993). Stratigraphy of Devonian black shales and associated rocks in the Appalachian basin: U.S. Geological Survey Bulletin 1909B, p. B1-B57.

- DiSiena, J.P., Gaiser, J.E., and Corrigan, D. (1981). Three-component vertical seismic profiles – orientation for shear wave analysis. Paper S5.4, SEG Expanded Abstracts, 51st Annual International Meeting of SEG, 1990-2011.

- Doyen, P.M. (1988). Porosity from Seismic Data; a Geostatistical Approach. Geophysics. 53, no.10. 1263-1276.

- Dragoset, B. and Gabitzsch, J. (2007). Introduction to this special section: Low-Frequency seismic. The Leading Edge, 26(1), 34-35.

- Easley, D.T. (1992). Alternate description of wavefields generated by two vertical vibrators in counterphase: CREWES Res. Rep., 4, 2, 1-10

- Edelmann, H.A.K. (1981). Shover shear-wave generation by vibration orthogonal to the polarization. Geophy. Prospect., 29, 541-549.

- Engelder, T., and Geiser, P. (1980). “On the Use of Regional Joint Sets as Trajectories of Paleostress Fields During the Development of the Appalachian Plateau, New York”. Journal of Geophysical Research, Vol. 85, No.B11, p. 6319-6341.
- Engelder, T., Lash, G.G., Uzcategui, R.S. (2009). ”Joint sets that enhance production from Middle and Upper Devonian gas shales of the Appalachian Basin”. AAPG Bulletin, v.93., No.7, pp. 857-889.
- Evans, K.F., Oertel, G., Engelder, T. (1989). “Appalachian Stress Study 2. Analysis of Devonian Shale Core: Some Implications for the Nature of Contemporary Stress Variations and Alleghanian Deformation in Devonian Rocks”. Journal of Geophysical Research, Vol. 94, No.B6, p. 7155-7170.
- Evans, K.F., Engelder, T., Plumb, R.A. (1989). “Appalachian Stress Study 1. A Detailed Description of In Situ Stress Variations in Devonian Shales of the Appalachian Plateau”. ”. Journal of Geophysical Research, Vol. 94, No.B6, p. 7129-7154.
- Fertig, J. (1984). Shear waves by an explosive point-source – the Earth surface as a generator of converted P-S waves. Geophy. Prospect., 32, 1-17.
- Fertig, J., and Krajewski, P. (1989). Acquisition and processing of pure and converted shear waves generated by compressional wave sources: Surveys in Geophysics, 10, 103-132.
- Gross, M.R., and Engelder, T.A. (1991). A case for Neotectonic Joints Along the Niagara Escarpment, in Tectonics, Vol. 10, No.3, pp 631-641.

- Hardage, B.A. (2000). Vertical seismic profiling – principles. Third updated and revised edition, Pergamon, 552 pages (Editions 1 and 2 published in 1983 and 1985 by other publishing houses).

- Hardage, B.A. (2009). Horizontal wave testing. AAPG Explorer, 30, no. 12,
p. 26–27.

- Hardage, B.A. (2010). Vertical wave testing. AAPG Explorer, 31, no. 1, p. 32–33.

- Hardage, B. A. (2011). System and method for acquisition and processing of elastic wavefield data. U.S. Patent 8,040,754 B1.

- Hardage B. A., DeAngelo M., Murray P., Sava D. (2011). Multicomponent Seismic Technology, SEG Publications.

- Hill, D.G. and Lombardi, T.E. (2002). “Fractured Gas Shale Potential in New York”, The Report Prepared by TICORA Geosciences, Inc., for New York State Energy Research and Development Authority.

- Hons, M., Stewart, R., and Hauer G. (2008). Accelerometer vs. geophone response: A field Case History. CSPG CSEG CWLS Convention, 271-275.

- LaBarre, E.L., Davis, T.L. (2008). Fault and natural fracture identification from multicomponent seismic at Rulison Field, Colorado, 2008 SEG Annual Meeting Expanded Abstracts.

- Laine, J. and Mougenot, D. (2007). Benefits of MEMS based seismic accelerometers for oil exploration. Solid-state Sensors, Acuators and Microsystems Conference, 2007 (Transducers 2007), 1473-1477.

- Lansley M. (2012). Cabled versus cable-less acquisition: making the best of worlds in difficult operational environments. First Break, vol.30, pp 97-102.

- Lash, G., Loewy S., and Engelder, T. (2004). Preferential jointing of Upper Devonian black shale, Appalachian Plateau, USA: evidence supporting hydrocarbon generation as a joint-driving mechanish, Geological Society, London, Special Publications 2004; v.231; p.129-151.

- Levin, F. K. (1979). Seismic velocities in transversely isotropic media: Geophysics, 44, 918-936.

- Levin, F. K. (1980). Seismic velocities in transversely isotropic media II: Geophysics, 45, 3-17.

- Lewallen, K. T., Zou, R., Chen, G., Wu, X., and Todd, P. (2008). Seismic characterization of fractured tight gas reservoir, Piceance Basin. 78th Annual International Meeting, SEG, Expanded Abstracts, 27, 463-467.

- Li, X.Y., MacBeth, C., and Crampin, S. (1998). Interpreting non-orthogonal split shear waves for seismic anisotropy in multicomponent VSPs. Geophy. Prospect., 46, 1-27.

- Liu, E., Maultzsch, S., Chapman, M., and Li, X. (2003). Frequency-dependent seismic anisotropy and its implication for estimating fracture size in low porosity reservoirs, The Leading Edge, 22, 662–665.

- Loewy, S.L. (1995). The Post-Alleghanian Tectonic History of the Appalachian Basin Based on Joint Patterns in Devonian Black Shales, Masters of Science Thesis, Pennsylvania State University.

- Lorenz, J.C. (2004). Fracture Systems in the Piceance Basin: Overview and Comparison with Fractures in the San Juan and Green River Basins. Piceance Basin 2003 Guidebook: Rocky Mountain Association of Geologists, p 75-94.

- Lynn, H.B., and McCardle, M. (1990). Four 3-component VSPs from South Texas onshore – S-wave velocities for AVO and discussion of acquisition parameters. Paper BG3.2, SEG Expanded Abstracts, 9, 52-55.
- Koesoemadinata, A., Banik, N., Agarval, V., Singh, S., and Durrani, J. (2008). A Global Acoustic Impedance Inversion for Porosity and Lithology Prediction in Northern Gulf of Mexico. SEG Extended Abstracts.
- Marfurd, K.J., Kirlin, R.L., Farmer, S.L., and Bahorich. M.S. (1998). 3-D seismic attributes using a semblance-based coherency algorithm; Geophysics, vol.63, no.4, p.1150-1165.
- Maxwell, P., Tessman, J. and Reichert, B. (2001). Design through to production of a MEMS digital accelerometer for seismic acquisition. First Break, 19 (3), 141-144.
- Milici R.C., Swezey C.S., (2006). Assessment of Appalachian Basin Oil and Gas Resources: Devonian Shale – Middle and Upper Paleozoic Total Petroleum System. USGS Open-File Report Series 2006-1237.
- Miller, G. and Pursey H. (1954). The field and radiation impedance of mechanical vibrators on the free surface of a semi-infinite isotropic solid. Proceedings of the Royal Society of London, Series A, 223, no. 1155, 521–541.
- Mougenot, D. and Thorburn, N. (2004). MEMS-based 3C accelerometers for land seismic acquisition: Is it time? The Leading Edge, 23 (3), 246-250.

- Mougenot, D. (2005). Towards low frequencies: equipment and applications. 67th EAGE Conference & Exhibition, Expanded Abstract.

- Mougenot D. (2010). Land cableless systems: use and misuse, First Break, vol 28, pp 55-58.

- Partyka, G. J., Gridley, J., and Lopez, J. (1999). Interpretational applications of spectral decomposition in reservoir characterization. The Leading Edge 18, 353-360.

- Pendrel, J., Van Riel, P. (1997). Estimating Porosity from 3D Seismic Inversion and 3D Geostatistics. Presented at the 67th Annual International Meeting, SEG.

- Pendrel, J., Debeye, H., Pedersen-Tatalovic, R., Goodway, B., Dufour, J., Bogaards, M., Stewart, R. (2000). Estimation and Interpretation of P and S Impedance Volumes from the Simultaneous Inversion of P-wave Offset Data, CSEG Ann. Mtg. Abs. paper AVO 2.5.

- Pendrel, J. (2006). Seismic Inversion – A Critical Tool in Reservoir Characterization, Scandinavian Oil-Gas Magazine.No:5/6.

- Perez, M., Close, D., Goodway, B., and Purdue, G. (2011). Developing templates for integrating quantitative geophysics and hydraulic fracture completions data: Part I—Principles and Theory: 81st Annual International Meeting, SEG, Expanded Abstracts, 1794–1798.

- Plumb, R.A, Evans, K.F., Engelder, T. (1991). "Geophysical Log Responses and Their Correlation With Bed-to-Bed Stress Contrasts in Palezoic Rocks, Appalachian Plateau, New York". Journal of Geophysical Research, Vol. 96, No.B9, p. 14,509-14,528.

- Raikes, S. (1991). Shear-wave characterization of the BP Devine test site. Paper BG2.8, SEG Expanded Abstracts, 10, 65-68.

- Rijks, E. J. H., and Jauffred, J. C. E. M. (1991). Attribute extraction: An important application in any detailed 3D interpretation study: The Leading Edge, 10, 11-19.

- Roberts, A. (2001) Curvature attributes and their application to 3D interpreted horizons. First Break, 19 (2).

- Robertson, J.D. and Corrigan, D. (1983). Radiation patterns of a shear-wave vibrator in near-surface shale. Geophysics, 48, 19–26.

- Roen, J.B., and de Witt, Wallace, Jr. (1984). Stratigraphic framework of the Devonian black shales of the Appalachian basin: United States Geological Survey Open-File Report 84-111, 78 p., 31 oversized sheets.

- Sageman, B.B., Murphy, A.E., Werne, J.P., Ver Straeten, C.A., Hollander, D.J. and Lyons, T.W. (2003). A tale of shales: the relative roles of production, decomposition, and dilution in the accumulation of organic-rich strata, Middle-Upper Devonian, Appalachian basin: Chemical Geology, v. 195, p. 229-273.

- Sasaki, S.; Seki, T.; Imanaka, K.; Kimata, M.; Toriyama, T.; Miyano, T.; Sugiyama, S. (2007). Batteryless-Wireless MEMS Sensor System with a 3D Loop Antenna. Sensors, 2007 IEEE Conference.

- Simmons, J and Backus, M. (2001). Shear waves from 3-D-9-C seismic data. The Leading Edge, June 2001, 604-612.

- Singh P., Slatt, R. ,Borges, G., Perez, R., Portas, R., Marfurt, K., Ammerman, M., Coffrey, W. (2009). Reservoir Characterization of Unconventional gas shale reservoirs: Example from the Barnett Shale, Texas, U.S.A., Shale Shaker, Vol. 60, pp: 15-31.

- Sinha, S., Routh, P. S., Anno, P. D., and Castagna, J. P. (2005). Spectral decomposition of seismic data with continuous-wavelet transforms. Geophysics 70, 19-25.

- Singh, P.K., Williamson, P., Sadeghi, E., Boelle, J.L. (2009). A high-resolution shear wave anisotropy study of the Mesaverde tight gas reservoir, Rulison Field, Colorado, 2009 SEG Annual Meeting Expanded Abstracts.

- Smith, L.B., and Leone, J. (2010). Integrated Characterization of Utica and Marcellus Black Shale Gas Plays, New York State: AAPG Search and Discovery Article #50289.

- Stotter, Ch., Angerer, E. and Herndler, E. (2008). Comparison of single sensor 3C MEMS and conventional geophone arrays for deep target exploration. 78th SEG Annual Meeting, Expanded Abstract.

- Sun, Z., and Jones, M. J. (1993). Seismic wavefields recorded at near-vertical incidence from a counterphase source: CREWES Res. Rep., 4, 2, 1-10

- Taner, M.T. (2001). Seismic attribute. Canadian Society Exploration Geophysicists Record 26(7): 48-56.

- Thomsen, L. (1988). Reflection seismology over azimuthally anisotropic media: Geophysics, 53, 304–313.

- Thomsen, L., Tsvankin I., and Mueller, M.C. (1999). Coarse-layer stripping of vertically variable azimuthal anisotropy from shear-wave data: Geophysics, 64, 1126–1138.

- Thomsen, L. (2002). Understanding seismic anisotropy in exploration and exploitation: Distinguished Instructor Short Course (DISC), No. 5, SEG and EAGE.

- Tsvankin, I., and Grechka, V. (2011). Seismology of Azimuthally Anisotropic Media and Seismic Fracture Characterization. SEG Geophysical References Series No.17.

- Verdin C.T., and Ordaz, M.G. (2008). A Study To Assess The Value Of Post-Stack Seismic Amplitude Data In Forecasting Fluid Production From A Gulf-Of-Mexico Reservoir. Journal Of Petroleum Science And Engineering. 62. 1-15.

- Vetrici D.G. and Stewart R. R. (1996). 3-D Seismic Attributes. CREWES Research Report, Volume 8, 45 (1) – 45 (30).

- White, R.E. (1980). Partial Coherency Matching of Synthetic Seismograms with Seismic Traces. Geophysical Prospecting, Vol.28, Issue:3, 333-358.

- White, J. E. (1983). Underground sound—applications of seismic waves. Elsevier Science Publishers.

- Winterstein, D. F., and Meadows, M. A. (1991a). Shear-wave polarizations and subsurface stress directions at Lost Hills field: Geophysics, 56, 1349–1364.

- Winterstein, D. F., and Meadows, M. A. (1991). Changes in shear-wave polarizations azimuth with depth in Cymric and Railroad Gap oil fields: Geophysics, 56, 1349–1364.

- Wright, J.K., and Carpenter, E.W. (1962). The generation of horizontally polarized shear waves by underground explosions. J. Geophy. Res., 67, no. 5, 1957-1963.

- Yang, L., Zhang, Q., Bao, L., and Wei, X. (2007). Pure S-waves in land P-wave source VSP data. Applied Geophy. 4, no. 3, 173-182.

- Zagorski, W.A, Douglas, C.B., Emery, M., Wrightstone, G.R. (2011). “An overview of Some key factors controlling well productivity in core areas of Appalachian Basin”, AAPG Annual Conference and Exhibition.

- Zhou, R., Zhao, X., and Dushman, D. (2005). Shear-wave anisotropy from far-offset VSP. Paper MC4.2, SEG Expanded Abstracts, 24, 971-974.

VITA

Engin Alkan received the degree of Bachelor of Science from the Engineering Department at The University of Ankara, Turkey in 2003. In September, 2005, he entered the Graduate School at The University of Texas at Austin, and he received the degree of Master of Science from the Department of Geosciences in 2007. After working in the industry for 3 years, he entered the Graduate School at The University of Texas at Austin to earn the degree of Doctor of Philosophy in September, 2009. He has been working for Shell Exploration and Production Company in Houston, TX since January, 2011.

Permanent Address: 7122 Hollow Field Lane, Cypress, Texas 77433

This manuscript was typed by Engin Alkan.